Measurement of Beauty Quark Cross Sections in Photoproduction with the ZEUS Experiment at the Electron-Proton Collider HERA

Dissertation
zur Erlangung des Doktorgrades
des Fachbereichs Physik
der Universität Hamburg

vorgelegt von

Oliver Gutsche

aus Hamburg

Hamburg
2005

Gutachter der Dissertation:	Prof. Dr. R. Klanner Dr. A. Geiser
Gutachter der Disputation:	Prof. Dr. B. Naroska Dr. A. Geiser
Datum der Disputation:	10.03.2005
Vorsitzender des Prüfungsausschusses:	Prof. Dr. G. Heinzelmann
Vorsitzender des Promotionsausschusses:	Prof. Dr. G. Huber
Dekan des Fachbereichs Physik:	Prof. Dr. G. Huber

Abstract

The *Standard Model* of elementary particles has proven to be a big success over the last decades in describing the microscopic structure of matter. Despite this success, it still poses open questions to theory and experiment. In particular the heavy quark sector still shows discrepancies between measurement and theoretical prediction. This thesis presents measurements of beauty quark cross sections in the photoproduction regime in ep collisions with the ZEUS experiment at the HERA collider to contribute to the clarification of these questions.

The measurement of beauty quark cross sections requires a reliable identification of beauty quarks mostly exploiting their heavy mass or long lifetime. A well established procedure for the identification is the p_T^{rel} method which exploits statistically the harder spectrum of the transverse momentum of the muon from semi-leptonic beauty quark decays relative to the originating quark compared to lighter quarks. With the upgrade of the ZEUS detector in the course of the HERA II upgrade program 2000/2001, an additional method exploiting the long lifetime of the beauty quark became accessible. With the integration of a micro–vertex–detector in the ZEUS detector, a precise measurement of the impact parameter of the muon with respect to the interaction origin can statistically identify semi-leptonic beauty quark decays by their harder spectrum compared to lighter quarks. For both methods, jets experimentally represent the beauty quarks by their collimated shower of decay products and act as a reference for the p_T^{rel} and impact parameter methods. In this thesis, they also provide a hard scale for the perturbative calculation of theoretical predictions. This thesis measures photoproduction cross sections of semi-leptonically decaying beauty quarks into muons in dijet events:

$$ep \rightarrow eb\bar{b}X \rightarrow ejj\mu X$$

The p_T^{rel} method is used in pre– and post–upgrade running periods to identify beauty quarks. Afterwards, these results are used to explore the applicability of the impact parameter method in the post–upgrade running periods.

The technical task of this thesis consisted of the development of a new event display for the ZEUS detector incorporating the changes in the detector layout after the upgrade including the new micro–vertex–detector. The new solution providing event displays both for the pre– and post–upgrade running periods is presented by describing the visualisation concept and the implementation.

A global comparison of beauty quark production measurements from different experiments at different high energy particle colliders, carried out during a research stay at the University College London, describes the frame in which the cross section measurements of this thesis can be interpreted. Using leading order plus parton shower Monte Carlo generators for the comparison, the question of compatibility between the different results is of larger importance because the measurements under investigation do not provide a consistent picture about their compatibility to theoretical predictions.

In the following, a brief description of the structure of the cross section measurements and the study of the impact parameter method is given.
In the pre–upgrade running periods, a data sample of 110 pb^{-1} is used to measure cross sections with the p_T^{rel} method. A new general muon reconstruction is established to increase the statistics significantly. The experience from the pre–upgrade running periods is then transferred to the post–upgrade running periods to measure first beauty quark cross sections using the p_T^{rel} method with the upgraded detector in a data sample of 40 pb^{-1}. The comparison between pre– and post–upgrade results establishes a post–upgrade event sample with known beauty content which is suitable for comparisons of the two beauty quark identification methods. A first study of the applicability of the impact parameter method concludes the investigation of beauty quark production after the upgrade. In the end, future plans for measurements of beauty quark cross sections at ZEUS exploiting the long lifetime of the beauty quark are outlined.

Kurzfassung

Das *Standard Modell* der Elementarteilchenphysik hat sich über die letzten Jahrzehnte als großer Erfolg für die Beschreibung der mikroskopischen Struktur der Materie herausgestellt. Dennoch gibt es immer noch offene Fragen. Besonders der Bereich der schweren Quarks zeigt Unterschiede zwischen Experiment und theoretischen Vorhersagen. In dieser Arbeit werden *Beauty*-Quark-Wirkungsquerschnitts-Messungen im Photoproduktions-Bereich gemessen in *ep* Kollisionen am HERA Beschleuniger mit dem ZEUS Experiment vorgestellt, um zur Klährung dieser Unterschiede beizutragen.

Die Messung von *Beauty*-Quark-Wirkungsquerschnitten bedarf einer zuverlässigen *Beauty*-Quark - Identifikation meistens durch die Ausnutzung der hohen Masse oder der langen Lebensdauer der *Beauty* Quarks. Die p_T^{rel}-Methode stellt dabei ein etabliertes Verfahren zur statistischen Identifikation dar, indem sie das härtere Spektrum des transversalen Impulses von Myonen aus semi-leptonischen Zerfällen von *Beauty* Quarks relativ zum ursprünglichen Quark im Vergleich zu leichteren Quarks ausnutzt. Aber seit der Erweiterung des ZEUS Detektors während des HERA II Umbau-Programms 2000/2001 besteht die Möglichkeit der Anwendung einer weiteren Methode zur *Beauty*-Quark-Identifikation unter Ausnutzung der langen Lebensdauer des *Beauty* Quarks relative zu leichteren Quarks. Durch den Einbau des Mikro-Vertex-Detektors kann der Stoß-Parameter des Myons relative zum Ereignis-Ursprung mit genügender Genauigkeit bestimmt werden, um das resultierende ebenfalls härtere Spektrum vom semi-leptonischen *Beauty*-Quark-Zerfällen statistisch zur Identifikation auszunutzen. In dieser Arbeit repräsentieren experimentell Jets die Quarks durch den kollimierten Schauer ihrer Zerfallsprodukte und dienen als Referenz für die p_T^{rel}- und Stoß-Parameter-Methode. Zusätzlich definieren sie eine harte Skala für die pertubative Berechnung der theoretischen Vorhersagen. Diese Arbeit präsentiert *Beauty*-Quark-Wirkungsquerschnitts-Messungen im Photoproduktions-Bereich in Ereignissen mit zwei Jets und einem Myon:

$$ep \rightarrow eb\bar{b}X \rightarrow ejj\mu X$$

Die p_T^{rel}-Methode wird zur Identifizierung von *Beauty* Quarks in den Datennahmeperioden vor und nach dem Umbau benutzt. Danach werden diese Ergebnisse zur Studie der Anwendbarkeit der Stoß-Parameter-Methode in den Datennahmeperioden nach dem Umbau verwendet.

Der technische Teil der Arbeit umfasst die Entwicklung eines neuen *event displays* für den ZEUS-Detektor welches die Änderungen im Detektor-Aufbau nach dem Umbau und die Integration des Mikro-Vertex-Detektors widerspiegelt. Die neue Visualisierungs-Lösung bietet Ereignis-Visualisierungen für die Datennahmeperioden vor und nach dem Umbau und wird durch die Beschreibung des Konzepts und seiner Implementation vorgestellt.
Ein globaler Vergleich von *Beauty*-Quark-Wirkungsquerschnitts-Messungen von unterschiedlichen Experimenten an unterschiedlichen Beschleunigern, durchgeführt während eines Auslands-Studien-Aufenthalts am University College London, beschreibt den Rahmen in welchem die Messungen dieser Arbeit interpretiert werden können. Der Vergleich benutzt *leading order plus parton shower* Monte-Carlo-Simulationen und gibt eine Antwort auf die Frage nach der Kompatibilität zwischen den einzelnen Messungen. Die Beantwortung dieser Frage ist wichtig da die einzelnen Messungen keine einheitliche Antwort zur Kompatibilität zu theoretischen Vorhersagen geben.

Im Folgenden wird kurz der Aufbau der Wirkungsquerschnitts-Messungen und der Studie der Stoß-Parameter-Methode beschrieben. Zuerst wird ein Datensatz von 110 pb^{-1} der Datennahmeperioden vor dem Umbau benutzt, um Wirkungsquerschnitte mit der p_T^{rel}-Methode zu messen. Eine neue verbesserte Myon-Rekonstruktion wird etabliert, um die Statistik signifikant zu vergrößern. Anschließend werden die Erfahrungen aus den Datennahmeperioden vor dem Umbau auf den Datensatz von 40 pb^{-1} aus den neuen Datennahmeperioden übertragen, um erste *Beauty*-Quark-Wirkungsquerschnitte nach dem Umbau zu bestimmen. Ein Vergleich der Wirkungsquerschnitte zwischen den Datennahmeperioden vor und nach dem Umbau zeigt, dass der Datensatz aus der neuen Periode mit seinem durch die p_T^{rel}-Methode bestimmten *Beauty*-Quark-Anteil geeignet ist für den Vergleich der zwei Identifikations-Methoden. Daraufhin zeigt eine erste Machbarkeits-Studie die Anwendbarkeit der Stoß-Parameter-Methode. Am Ende werden zukünftige Pläne für *Beauty* -Quark-Wirkungsquerschnitts-Messungen mit dem ZEUS Detektor unter Ausnutzung der langen Lebensdauer der *Beauty* Quarks beschrieben.

Contents

1 Introduction **1**

2 Theoretical Overview **5**
2.1 The *Standard Model* . . . 5
2.2 High Energy *ep* Collisions in the *Standard Model* . . . 7
2.3 DIS Cross Sections and the Proton Structure . . . 11
2.4 Beauty Quark Photoproduction . . . 14
2.4.1 Beauty Quark Event Simulation with PYTHIA . . . 14
2.4.2 Next–To–Leading Order Calculation with FMNR . . . 20

3 Beauty Production in the Global Context **25**
3.1 Beauty Quark Identification Techniques . . . 25
3.2 From Fixed Target to Collider Experiments . . . 26
3.3 Beauty Quark Production at the $Sp\bar{p}S$ . . . 27
3.4 Beauty Quark Production at the Tevatron . . . 29
3.5 Beauty Quark Production at HERA . . . 31

4 Global Comparison with JetWeb **35**
4.1 JetWeb and HZTOOL . . . 35
4.2 Comparison of Beauty Quark Cross Sections from UA1, D0 and ZEUS . . . 37

5 The ZEUS Detector at HERA **41**
5.1 The HERA Collider . . . 41
5.2 The ZEUS Detector . . . 43
5.2.1 The Central Tracking Detector . . . 45
5.2.2 The Silicon–Strip Micro Vertex Detector . . . 46
5.2.3 The Uranium–Scintillator Calorimeter . . . 47
5.2.4 The Muon Detectors . . . 49
5.2.5 The Backing Calorimeter . . . 51
5.2.6 The Luminosity Measurement . . . 52
5.2.7 The ZEUS Trigger System . . . 53
5.3 ZEUS Detector Simulation . . . 54

6 Event Visualisation for the ZEUS Experiment **55**
6.1 ZeVis - the new ZEUS Event Display . . . 55
6.2 The Client–Server Event Display Concept . . . 56
6.3 ZeVis - Server Side . . . 57
6.4 ZeVis - Client Side . . . 60

7 Event Reconstruction **67**
7.1 Track Reconstruction in the Inner Tracking Detectors . . . 67
7.1.1 Track Reconstruction with the CTD . . . 68
7.1.2 Track Reconstruction with the MVD and the CTD . . . 68
7.1.3 Resolution . . . 69
7.2 Reconstruction of Calorimetric Variables . . . 70
7.3 Muon Reconstruction . . . 71
7.3.1 Muon Reconstruction Algorithms . . . 72

7.3.2 GMuon - A General Muon Reconstruction . . . 75
7.4 Reconstruction of the Hadronic System . . . 81
7.4.1 Reconstruction of Energy Flow Objects . . . 81
7.4.2 Correction of the Cone Islands . . . 83
7.4.3 Corrections for the Presence of a Muon . . . 84
7.5 Jet Reconstruction . . . 85

8 Event Selection **87**
8.1 Data and MC Samples . . . 87
8.2 Trigger . . . 89
8.2.1 Trigger Corrections for Post–Upgrade Running Periods . . . 90
8.3 Photoproduction Selection . . . 90
8.3.1 Veto on Reconstructed Electrons . . . 90
8.3.2 Veto on the Inelasticity with the Jacquet-Blondel Method . . . 91
8.4 Muon Selection . . . 92
8.4.1 Muon Efficiency Correction Systematics . . . 96
8.5 Jet Selection . . . 97
8.6 Jet-Muon Association . . . 100
8.7 Additional Cuts . . . 100
8.8 Summary . . . 101
8.8.1 Control Distributions . . . 102

9 Beauty Quark Identification **105**
9.1 p_T^{rel} Method . . . 105
9.1.1 Background $p_T^{rel,jet-\mu}$ and p_T^{rel} Shape Corrections . . . 108
9.2 Impact Parameter Method . . . 110
9.2.1 Background Impact Parameter Shape Corrections . . . 111

10 Beauty Quark Cross Sections **113**
10.1 Pre–Upgrade Cross Sections . . . 114
10.1.1 Shape Comparison between Data and MC . . . 114
10.1.2 Comparison to Leading Order plus Parton Shower MC . . . 119
10.1.3 Systematic Errors . . . 122
10.1.4 Comparison to NLO QCD Predictions . . . 124
10.2 Post–Upgrade Cross Sections . . . 126
10.2.1 Shape Comparison between Data and MC . . . 126
10.2.2 Comparison to MC and NLO QCD Predictions . . . 128
10.2.3 Comparison between Pre– and Post–Upgrade Running Periods . . . 131
10.3 Impact Parameter Method in Post–Upgrade Running Periods . . . 133
10.3.1 Outlook for the Post–Upgrade Beauty Quark Cross Section Measurements . . . 134

11 Conclusions and Outlook **137**

A JetWeb - a WWW MC Comparison Database **139**
A.1 An Introduction to JetWeb . . . 139

B ZeVis - a Technical Description **141**
B.1 The Single Event Mode of the ZeVis Event Display . . . 141
B.2 The GUI of the ZeVis Event Display . . . 143
B.3 The MVD in the ZeVis Event Display . . . 147
B.3.1 ROOT Drawing Capabilities . . . 147
B.3.2 The Implementation of the MVD Geometry . . . 148
B.3.3 The Implementation of the MVD Hits . . . 153

C Monte Carlo Samples **155**
C.1 Beauty Quark MC Samples . . . 155
C.2 Charm Quark MC Samples . . . 156
C.3 Lighter Flavour MC Samples . . . 156

D Numbers of Selected Events **159**
D.1 Pre–Upgrade Event Numbers . . . 159
D.2 Post–Upgrade Event Numbers for $p_T^\mu \geq 1.5$ GeV . . . 160
D.3 Post–Upgrade Event Numbers for $p_T^\mu \geq 2.0$ GeV . . . 160

E Trigger Selection **161**
E.1 Pre–Upgrade Trigger Selection . . . 161
E.1.1 Barrel/Rear Muon Trigger: TLT EXO 11/12 . . . 161
E.1.2 Low E_T Dijet: TLT HPP 14 . . . 161
E.1.3 Semi-Isolated Muon with the Barrel/Rear Muon Chambers: TLT MUO 3 . . . 161
E.1.4 Muon plus Dijets for Running Periods 1999-2000: TLT HFL 1 . . . 162
E.2 Post–Upgrade Trigger Selection . . . 162
E.2.1 Inclusive Dijets: TLT HFL 5 . . . 162
E.2.2 Inclusive Semi-Leptonic Muon: TLT HFL 13 . . . 162
E.2.3 Muon plus Dijets: TLT HFL 25 . . . 162

F Comparison with Previous Results **163**

G Detailed Systematic Errors **167**
G.1 Pre–Upgrade Systematic Errors . . . 167
G.2 Post–Upgrade Systematic Errors for $p_T^\mu \geq 1.5$ GeV . . . 169
G.3 Post–Upgrade Systematic Errors for $p_T^\mu \geq 2.0$ GeV . . . 171

References **179**

List of Figures **184**

List of Tables **186**

Chapter 1

Introduction

The question about the fundamental structure of matter is a longstanding problem in the history of mankind and many attempts have been made to give a complete and consistent answer. Developed over the last century, the *Standard Model* represents the current knowledge about the microscopic structure of matter. It describes this structure by 12 elementary particles, their anti–particles and three fundamental interactions acting between them. The elementary particles are divided up into two groups, the leptons and the quarks.
Quarks are not observable on their own due to the strong force acting between them. The strong force, linearly increasing with the distance between two quarks, binds the quarks into observable bound states (*hadrons*). The *charm*, *beauty* and *top* quarks are called *heavy quarks*. They have masses heavier than the energy scale at which quarks are confined into hadrons ($\Lambda \sim 250$ MeV). The remaining three quarks are called *light flavour* quarks.
Heavy quarks are produced only in high energy collisions, for example in cosmic rays interacting with ordinary matter. Because hadrons containing heavy quarks decay in a fraction of a second, the study of their properties requires their controlled production and the detection of their decay products. This is nowadays achieved at elementary particle accelerators where large detector systems detect the decay products of particle interactions.

The study of the production of the beauty quark still has open questions and the description of beauty quark production by the *Standard Model* is not yet consistent. Several experiments have studied beauty quark production in high energy hadronic interactions amongst which are the UA1 experiment at the $Sp\bar{p}S$ collider at CERN, the DO and CDF experiments at Fermilab and the H1 and ZEUS experiments at HERA. Most of the experiments confirmed the compatibility of their beauty quark production measurements with predictions of the *Standard Model*. Others showed some differences which could not be fully explained. Newer results tend to agree with the theoretical predictions which have also been refined in recent time.

The goal of this thesis is to contribute to the solution of the remaining discrepancies between theory and experiment in the field of beauty quark production. Therefore, high energy ep collisions are investigated with the ZEUS detector at the HERA collider at DESY to measure beauty quark cross sections in the photoproduction regime.

The measurement of beauty quark cross sections requires the reliable identification of beauty quarks by their decay products. Several techniques exist which mostly exploit the heavy mass or the long lifetime of the beauty quark compared to lighter quarks.
A well established procedure exploiting the heavy beauty quark mass is the p_T^{rel} method. The spectrum of the transverse momentum of a muon from a semi-leptonic decay of a beauty quark relative to the originating quark (p_T^{rel}) is harder than the p_T^{rel} of a muon from a lighter quark and can be used on a statistical basis to identify beauty quarks. Experimentally, quarks are represented by particle jets which can be measured by the detector. They act as the reference for the p_T^{rel} method which is experimentally defined as the transverse momentum of the muon relative to the jet containing the muon. Two jets are required in photoproduction events to provide a hard scale for a reliable perturbative calculation of theoretical predictions. First measurements of beauty quark photoproduction cross sections from ZEUS with the p_T^{rel} method in dijet plus muon events:

$$ep \rightarrow eb\bar{b}X \rightarrow ejj\mu X \tag{1.1}$$

already exist and result in cross sections compatible with *Standard Model* predictions.

But since the upgrade of the ZEUS detector in the course of the HERA II upgrade program, a different identification method became available. By the integration of the micro–vertex–detector (MVD), the ZEUS track reconstruction is sufficiently accurate to exploit the long lifetime of the beauty quark by measuring the impact parameter of the muon with respect to the primary interaction vertex. The impact parameter spectrum of muons from beauty quarks is harder than for muons from lighter quarks and can also be exploited statistically to identify beauty quarks.

One of the overall goals of the post–upgrade beauty quark program of the ZEUS collaboration is to measure beauty quark cross sections using a different method than the p_T^{rel} method and hence with different systematics. The aim of this thesis is to study the applicability of the impact parameter method in the post–upgrade running periods by a comparison to the well established p_T^{rel} method in dijet plus muon events.

Two considerations guide the presented analysis. The available data sample from the post–upgrade running periods after the upgrade was limited due to the complicated starting phase of the upgraded HERA collider. But for significant cross section measurements, sufficient statistics is required. Fortunately, the impact parameter method promises a higher background separation than the p_T^{rel} method. Therefore, the goal is to increase first the statistics by improving the muon reconstruction. The development of a new general muon reconstruction will increase the statistics but is also expected to increase the selection of background which will be then compensated by the higher background rejection of the impact parameter method.

The new general muon reconstruction will be established first on the well known pre–upgrade data sample and then used to make measurements of beauty quark photoproduction cross sections in dijet plus muon events using the p_T^{rel} method. Here, measured cross sections will be compared to the previous results and new cross sections will be measured exploiting the increased statistics. The measured cross sections will be compared to theoretical predictions to investigate the description of beauty photoproduction in the *Standard Model*.

The experience gained in the analysis of the pre–upgrade running periods will then be transferred to the post–upgrade running periods. The measured cross sections using the p_T^{rel} method will be compared to theoretical predictions and to the cross sections of the pre–upgrade running periods. This will establish a suitable dijet plus muon sample with known beauty quark content identified by the p_T^{rel} method. This sample will be used afterwards to study the applicability of the impact parameter method.

The structure of this thesis is presented in the following.
Chapter 2 introduces the theoretical concepts of the *Standard Model* needed for the measurement of beauty quark photoproduction cross sections. The simulation approach and the currently most accurate theoretical predictions are discussed.
Chapter 3 gives an overview of already published beauty quark production cross section measurements.
Chapter 4 presents a global comparison study carried out during a research stay at the University College London using the JetWeb facility. Here, the direct compatibility of beauty quark cross section measurements from different experiments at different colliders is investigated. The comparison is of larger importance as the different results do not give a consistent answer about their compatibility to *Standard Model* predictions.
Chapter 5 introduces the experimental setup of the ZEUS detector with emphasis on the detector components used in this analysis.
Chapter 6 introduces the new event display for the ZEUS detector which was developed in the course of the technical task of this thesis to integrate the new detector components and the changes in the detector geometry after the upgrade.
Chapter 7 describes the reconstruction of the different final state quantities like jets and muons with emphasis on the new general muon reconstruction.

Chapter 8 introduces the dijet plus muon event selection applied to the pre– and post–upgrade data samples and the corresponding simulation and presents control distributions to investigate the correspondence of the simulation to the data.
Chapter 9 introduces the two beauty quark identification methods: the p_T^{rel} method and the impact parameter method.
Chapter 10 presents the beauty quark cross section measurements with the p_T^{rel} method separately for the pre– and post–upgrade running periods and ends with a first applicability study of the impact parameter method using the post–upgrade dijet plus muon sample.
Chapter 11 concludes the cross section measurements and gives an outlook on future plans for the measurement of beauty quark photoproduction measurements with the ZEUS detector.

Chapter 2

Theoretical Overview

This chapter introduces the theoretical description of beauty quark production in the photoproduction regime.
The *Standard Model* is introduced and the basic theoretical concepts are described.
Afterwards, the focus is shifted to *ep* collisions, their kinematics is described and the calculation of the *ep* cross section is presented.
One of the main results from HERA is the determination of the proton structure. The concept of the proton structure and the determination from HERA measurements is described in more detail.
To compare *Standard Model* cross section predictions to the measurement of beauty photoproduction, the calculation of the beauty cross sections is introduced. The characteristics of the event simulation approach used in this thesis for acceptance calculations is described by the introduction of the simulation program *PYTHIA*. In the end, the implementation of the beauty cross section calculation in the program *FMNR* is discussed and systematic changes in the calculation with regard to the cross sections measured in this thesis are investigated.

2.1 The *Standard Model*

One of the longstanding questions of mankind about the nature of matter has come a long way since the discovery of the atoms and their clustering into molecules. Soon after the discovery of the description of an atom by its electron cloud orbiting the core, the nucleus itself was found to be made of protons and neutrons. But in the sequence *molecules* → *atoms* → *nucleus* → *nucleons*, the elementary structure had not been reached. By the discovery of the subnuclear structure of matter, the next step to the elementary description of matter had been made.
Nowadays, the structure of matter is described by elementary particles and their fundamental interactions [1]. There are three generations of elementary particles (*fermions*) divided into two groups of *leptons* and *quarks* listed in Tab. 2.1. The charm (c), beauty (b) and top (t) quark are categorised as *heavy flavour quarks* whereas the up (u), down (d) and strange (s) quarks belong to the category of *lighter flavour* quarks. Each elementary particle has an anti-particle as partner with oppositely signed *charge-like* quantum numbers.

	Generations			Q_{EM}	Interactions el.magn.	weak	strong
Quarks	$\begin{pmatrix} u \\ d \end{pmatrix}$	$\begin{pmatrix} c \\ s \end{pmatrix}$	$\begin{pmatrix} t \\ b \end{pmatrix}$	$+2/3$ $-1/3$	yes yes	yes yes	yes yes
Leptons	$\begin{pmatrix} \nu_e \\ e \end{pmatrix}$	$\begin{pmatrix} \nu_\mu \\ \mu \end{pmatrix}$	$\begin{pmatrix} \nu_\tau \\ \tau \end{pmatrix}$	0 -1	no yes	yes yes	no no

Table 2.1: The elementary fermions in the *Standard Model* ordered in three generations. The value of the electromagnetic charge Q_{EM} is given in multiples of the elementary charge unit.

These particles interact by three fundamental interactions indicated in Tab. 2.1. The gravitational force

is currently not incorporated in the *Standard Model*. The interactions between the elementary particles are mediated by (virtual) gauge vector bosons representing the fundamental interactions given in Tab. 2.2. The strength of the interactions is given in terms of couplings α_i.

Interaction	boson	Q_{EM}	related group	typical coupling α_i
weak	$\begin{cases} Z^0 \\ W^\pm \end{cases}$	$\begin{matrix} 0 \\ 1 \end{matrix}$	$SU(2)_L \times U(1)_Y$	10^{-6}
electromagnetic	γ	0	$SU(2)_L \times U(1)_Y$	10^{-2}
strong	8 gluons g	0	$SU(3)_C$	1

Table 2.2: The fundamental interactions in the *Standard Model*. The value of the electromagnetic charge, Q_{EM}, is given in multiples of the elementary charge unit. The strength of the interactions is given by their couplings α_i at very low energies $E \ll m_p$.

The framework of renormalisable gauge field theories is used for the mathematical description of the composition of matter from leptons or *hadrons* (groups of two quarks (*mesons*) or three quarks (*baryons*)). The exchange bosons of the interactions are related to symmetries of the fields and described by the group structure of the *Standard Model*:

$$SU(3)_C \times SU(2)_L \times U(1)_Y, \tag{2.1}$$

where $U(n)$ denotes the group of all unitary $n \times n$ matrices and $SU(n)$ is the group of all unitary $n \times n$ matrices with determinant 1.
The *weak and electromagnetic interactions* (called electroweak interactions) are unified in the gauge group $SU(2)_L \times U(1)_Y$. Through *spontaneous symmetry breaking*, the bosons of the weak interactions (Z^0, $W^\pm$) acquire masses ($M_W = 80.41$ GeV, $M_Z = 91.187$ GeV) whereas the photon remains massless.
The strong interaction which mediates the forces between the quarks is described by *quantum chromodynamics* (QCD) as an exact $SU(3)_C$ gauge symmetry. The exchange bosons carrying the colour charge are massless gluons forming a colour octet. Each quark can be assigned one of the three colours forming a $SU(3)_C$ triplet. Quarks are not individually observable due to the strong force linearly increasing with the distance between two quarks. Due to this *confinement* any single quark in the final state of an elementary interaction produces a jet of observable hadrons.
The predictions of the *Standard Model* for particle interactions can be expressed as power series expansions in coupling constants α_i, if $\alpha_i \ll 1$. A graphical representation of this perturbative calculation approach is given by *Feynman diagrams* where the interacting, intermediate and produced particles are represented by lines. Each order of a coupling constant from the expansion is represented by a corresponding vertex. If the expansion series converges, the series can be discontinued at an appropriate order and the following orders can be neglected. The resulting calculation of an interaction is characterised by the order after which the expansion is stopped.

2.2 High Energy *ep* Collisions in the *Standard Model*

High energy *ep* collisions[1] are a unique source of very high energy lepton-proton scattering interactions and continue the line of former scattering experiments in fixed target and collision interactions.
The kinematics of *ep* collisions are introduced by the generic diagram of an electron–proton interaction shown in Fig. 2.1.

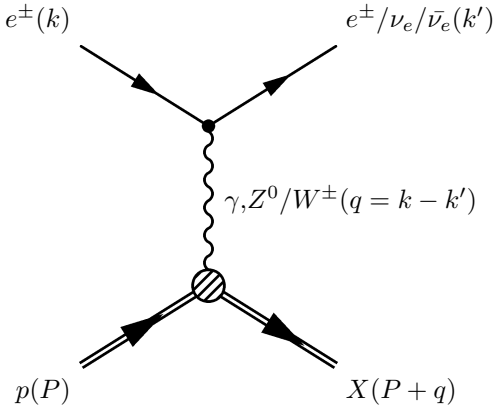

Figure 2.1: Generic diagram of electron–proton scattering. The four vectors of the particles are given in parentheses.

The incoming electron ($e^{\pm}$) interacts with an incoming proton (p) by the exchange of a vector boson. In *charged current* interactions (CC), a $W^{\pm}$ boson is exchanged and the flavour of the incoming lepton is changed to a neutrino. In *neutral current* interactions (NC), the exchanged boson is a photon or a neutral Z^0 boson.
The four–vectors of the initial and final states are given by $k = (E_{e^{\pm}}, \vec{k})$, $P = (E_p, \vec{P})$ and $k' = (E', \vec{k'})$, $P' = (E_X, \vec{P'})$ where $E_{e^{\pm}}$ and $\vec{k}$ are the energy and momentum of the incoming lepton and E_p, $\vec{P}$ are the energy and momentum of the incoming proton. For the outgoing lepton or neutrino and hadronic system X, the energy and momentum are given by E', $\vec{k'}$ and E_X, $\vec{P'}$ respectively. The four–vector q of the exchanged boson is given by

$$q = k - k' \tag{2.2}$$

The following Lorentz invariant variables describe the event kinematics[2]:

$$\begin{aligned}
s &= (k + P)^2 \simeq 2k \cdot P && (2.3)\\
Q^2 &= -q^2 = -(k - k')^2, \quad 0 \leq Q^2 \leq s. && (2.4)\\
W^2 &= (q + P)^2 \simeq -Q^2 + ys && (2.5)\\
x &= \frac{Q^2}{2P \cdot q}, \qquad 0 \leq x \leq 1 && (2.6)\\
y &= \frac{q \cdot P}{k \cdot P} \simeq \frac{2P \cdot q}{s}, \qquad 0 \leq y \leq 1 && (2.7)
\end{aligned}$$

The square of the centre–of–mass energy s is related to the *Bjorken scaling variables* x and y and the virtuality of the exchanged boson Q^2 by the following equation[3]:

$$Q^2 = sxy. \tag{2.8}$$

The proton is a compound object and known to be made up from partons (quarks and gluons). This substructure has to be taken into account for the description of *ep* collisions.
In the simplest picture, the *quark parton model* (QPM), the proton consists of three *valence quarks* which are regarded as quasi freely moving by describing the proton in the *infinite momentum frame* moving

[1] Electron and e denotes both electrons and positrons if not indicated differently.
[2] The relations 2.3, 2.5 and 2.7 are obtained neglecting the proton and lepton mass.
[3] At HERA, the centre–of–mass energy s is fixed at 318 GeV (300 GeV till 1998, see chapter 5). Hence only two of the four variables are independent.

with infinite momentum. In this picture, the basic description of *ep* collisions is given by the interaction of a quark of the proton directly with the electron by exchange of a photon (Fig. 2.2).

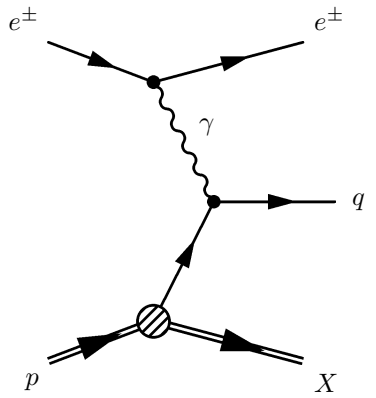

Figure 2.2: Feynman diagram of an electron–proton interaction in the *quark parton model* (QPM). The interaction takes place between a quasi–free quark (q) and the electron ($e^{\pm}$) by exchange of a photon (γ).

Using the QPM picture of the proton to describe *ep* interactions, the *inelasticity* y specifies the fraction of the lepton energy transferred to the interaction whereas the Bjorken scaling variable x denotes the fraction of the proton energy transferred to the interaction. The virtuality Q^2 corresponds to the resolution of the probe[4] and W is the invariant mass of the system recoiling against the scattered electron and can be interpreted as the centre of mass energy of the virtual boson–proton system.
The composition of the proton is currently not yet calculated from first principles and has to be determined by experiment. It is quantified by *parton density functions* $f_i(x, Q^2)$ (PDF's) which give the probability to find a parton i of the momentum fraction x in the proton at a given scale Q^2. The general form of the electron–proton cross section is given by:

$$d\sigma \sim L_{\mu\nu} W^{\mu\nu} \tag{2.9}$$

where $L_{\mu\nu}$ and $W^{\mu\nu}$ are the leptonic and hadronic tensors [1]. The non-perturbative structure of the proton is included in the hadronic tensor which can be expressed in the limit of large Q^2 by means of *structure functions* $F_i(x, Q^2)$. In the QPM, the structure functions are independent of Q^2 (*Bjorken scaling*) and are directly related to the PDF's by:

$$F_2(x) = xF_1(x) = \sum_i e_i^2 x f_i(x) \tag{2.10}$$

where i is the sum over the partons and e_i the charge or parton i.
Taking into account the QCD description of the strong forces between quarks, the simple proton picture of the QPM has to be modified. In detail, the representation of the proton by freely moving quarks quantified by their PDF's is too simple and the internal dynamic structure of the proton has to be taken into account: the proton description has to include the gluons in the proton. In addition to the QPM contributions (Fig. 2.2), diagrams with a gluon from the proton interacting with the electron have to be included. One of the *leading–order* contributions[5] in α_s is given by the diagram of *boson–gluon–fusion* (see (a) in Fig. 2.3). This graph can be described as the fluctuation of a gluon from the partonic substructure of the proton into a quark/anti–quark pair. One of the quarks interacts electromagnetically with the electron by exchange of a photon.
But the BGF graph doesn't display the only leading order α_s contribution to the electron–proton cross section. The *QCD Compton* graph (QCDC) (see (b) in 2.3) where a quark which interacts by the exchange of a photon with the electron radiates a gluon after the interaction contributes to the cross section as well. Also gluon radiation before the interaction has to be taken into account.
As mentioned in the description of the QPM, the individual distributions of partons in the proton can currently not be calculated from first principles. In the *factorisation* approach [2], where the calculable

[4] To date, HERA data covers a Q^2 range up to 40000 GeV^2. The upper Q^2 limit corresponds to a resolution of $\lambda \approx \hbar c/\sqrt{Q^2} = 10^{-18}$ m, 1/1000 of a proton radius.
[5] *Leading–order* depicts the first non-vanishing order in the perturbation series.

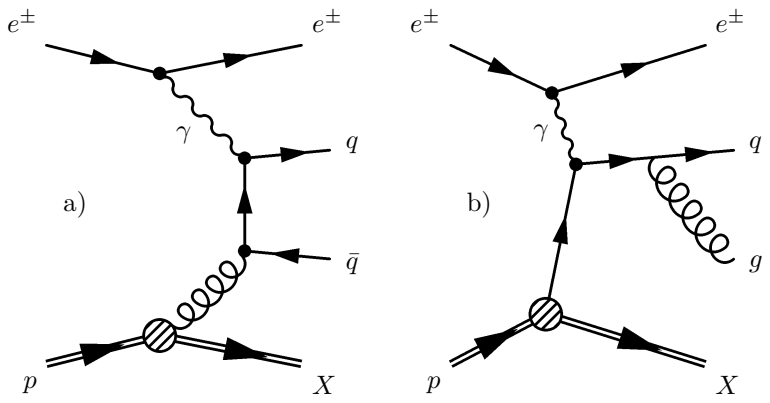

Figure 2.3: Leading order diagrams for *boson–gluon–fusion* (BGF) (a) and QCD Compton scattering (b) where the quark radiates a gluon after the interaction.

short-range part (hard process) is separated from the non-calculable long-range part (soft process), the structure function $F_2(x, Q^2)$ has the form:

$$F_2(x, Q^2) = \sum_i \int_x^1 \frac{dx'}{x'} C_{2,i}(x/x', Q/\mu, \alpha_s(\mu)) f_i(x', \mu) \tag{2.11}$$

where i sums over all partons and $C_{2,i}$ are the hard scattering functions (or Wilson coefficients). The factorisation scale μ defines the scale below which gluon radiation is absorbed in the PDF's to avoid divergences rather than treated in the perturbative calculation of the hard subprocess.
The same approach as for the proton structure description can also be applied to the photon. The photon flux from the electron has a finite probability to fluctuate into a hadronic system before interacting with the proton. The analogous description of the partonic photon structure by *photon structure functions* leads to the separation of the cross sections in two contributions. This separation is arbitrary and it is shown in the following that only the sum of the two components has a physical meaning.
In more detail, the photon has to be regarded on the one hand as a single particle (*pointlike component*), on the other hand the hadronic structure of the photon has to be taken into account (*hadronic component*). As mentioned above, the photon has a probability to fluctuate into a hadronic state. In this case, a quark or a gluon of the hadronic structure of the photon can interact with the hadron and contribute to the cross section (Fig. 2.4).

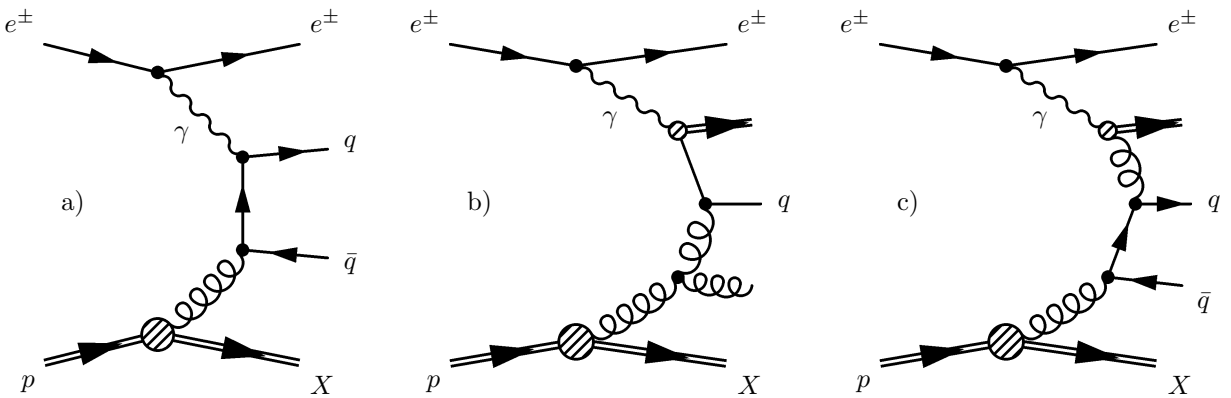

Figure 2.4: Leading order Feynman diagrams for the pointlike and hadronic components of photoproduction processes : a) pointlike boson–gluon–fusion b) hadronic boson–gluon–fusion with interaction of a quark from the hadronic structure of the photon with the hadronic structure of the proton and c) hadronic boson–gluon–fusion with interaction of a gluon from the hadronic structure of the photon with the hadronic structure of the proton.

In analogy to the proton PDF's, a factorisation scale μ_γ is introduced. It sets the scale where collinear light parton emissions from the photon are not included anymore in the photon PDF's and are treated

by the hard subprocess.
The differential photon–hadron cross section at HERA[6], calculated by [3] and confirmed by [4], can be separated into a pointlike and hadronic contribution [5]:

$$d\sigma^{(\gamma H)} = d\sigma^{(\gamma H)}_{point}(P_\gamma, P_H) + d\sigma^{(\gamma H)}_{hadr}(P_\gamma, P_H) \tag{2.12}$$

where P_H and P_γ denote the parton probability distributions in the proton or photon respectively.
The factorisation theorem allows to separate the cross sections in a calculable (hard) and a non–calculable (soft) part, regarding the cross section as a convolution of photon-parton and parton-parton cross sections folded by the parton densities in photon and proton respectively:

$$d\sigma^{(\gamma H)}_{point}(P_\gamma, P_H) = \sum_j \int dx f_j^{(H)}(x, \mu_f) d\hat{\sigma}_{\gamma j}(P_\gamma, xP_H, \alpha_s(\mu_R), \mu_R, \mu_F, \mu_\gamma) \tag{2.13}$$

$$d\sigma^{(\gamma H)}_{hadr}(P_\gamma, P_H) = \sum_{ij} \int dx dy f_i^{(\gamma)}(x, \mu_\gamma) f_j^{(H)}(y, \mu'_F) d\hat{\sigma}_{\gamma j}(xP_\gamma, yP_H, \alpha_s(\mu'_R), \mu'_R, \mu'_F, \mu_\gamma) \tag{2.14}$$

The parton densities in the photon and the proton are given by $f_i^{(\gamma)}$ and $f_i^{(H)}$. The renormalisation scales are given by μ_R and μ'_R, the factorisation scales for the hadron are given by μ_F and μ'_F and the factorisation scale for the photon by μ_γ. These universal parton densities are not perturbatively calculable but their evolution with the renormalisation scale obeys the Altarelli–Parisi equations (DGLAP) [6] in the case of the proton:

$$\frac{df_i(x, \mu_F)}{dlog\mu_F^2} = \frac{\alpha_s}{2\pi} \int \frac{dy}{y} p_{ki} f^k(\frac{y}{x}, \mu_f). \tag{2.15}$$

The renormalisation scale for the photon obeys an renormalisation group evolution equation [7] which can be obtained by slightly modifying the DGLAP equations:

$$\frac{\delta f_i^{(\gamma)}}{\delta log\mu^2} = \frac{\alpha_{em}}{2\pi} P_{i\gamma} + \frac{\alpha_s}{2\pi} \sum_j P_{ij} \otimes f_j^{(\gamma)}. \tag{2.16}$$

The first term, the main difference to the hadron evolution equations, is due to the direct coupling of the photon and the quarks.
To investigate the relation of the hadronic with the pointlike component of the cross section, the partonic cross sections for the processes with generic partons i and j:

$$\gamma + j = Q + \bar{Q} + X \tag{2.17}$$

$$i + j = Q + \bar{Q} + X \tag{2.18}$$

are calculated and renormalised for ultraviolet divergences. The resulting cross sections $d\sigma_{\gamma j}$ and $d\sigma_{ij}$ still contain the divergences due to the collinear emission of a massless final–state parton from one of the incoming partons and are subtracted through factorisation. The next–to–leading order (NLO) expansion of the partonic cross section is given by:

$$d\sigma_{\gamma j} = \alpha_{em}\alpha_s d\sigma^{(0)}_{\gamma j} + \alpha_{em}\alpha_s^2 d\sigma^{(1)}_{\gamma j} \tag{2.19}$$

$$d\sigma_{ij} = \alpha_s^2 d\sigma^{(0)}_{ij} + \alpha_{em}\alpha_s^3 d\sigma^{(1)}_{ij} \tag{2.20}$$

which can be written using a dimensional regularisation of $d = 4 - 2\epsilon$ using the subtracted partonic cross sections $d\hat{\sigma}_{\gamma j}$ and $d\hat{\sigma}_{ij}$ in the $\overline{MS}$-scheme [5]:

$$d\hat{\sigma}^{(0)}_{\gamma j}(p_1, p_2) = d\sigma^{(0)}_{\gamma j}(p_1, p_2) \tag{2.21}$$

$$d\hat{\sigma}^{(0)}_{ij}(p_1, p_2) = d\sigma^{(0)}_{ij}(p_1, p_2) \tag{2.22}$$

[6] A suited description approach of the photon flux from the electron has to be used to transform the photon–hadron cross section to an electron–hadron cross section (see Sec. 2.4.2).

$$
\begin{aligned}
d\hat{\sigma}^{(1)}_{\gamma j}(p_1,p_2) &= d\sigma^{(1)}_{\gamma j}(p_1,p_2,\frac{1}{\bar{\epsilon}}) + \\
&\frac{1}{2\pi}\sum_k \int dx \left(\frac{1}{\bar{\epsilon}} P_{k\gamma}(x)\right) d\sigma^{(0)}_{kj}(xp_1,p_2) + \\
&\frac{1}{2\pi}\sum_k \int dx \left(\frac{1}{\bar{\epsilon}} P_{kj}(x)\right) d\sigma^{(0)}_{\gamma k}(p_1,xp_2) \qquad (2.23)\\
d\hat{\sigma}^{(1)}_{ij}(p_1,p_2) &= d\sigma^{(1)}_{ij}(p_1,p_2,\frac{1}{\bar{\epsilon}}) + \\
&\frac{1}{2\pi}\sum_k \int dx \left(\frac{1}{\bar{\epsilon}} P_{ki}(x)\right) d\sigma^{(0)}_{kj}(xp_1,p_2) + \\
&\frac{1}{2\pi}\sum_k \int dx \left(\frac{1}{\bar{\epsilon}} P_{kj}(x)\right) d\sigma^{(0)}_{ik}(p_1,xp_2). \qquad (2.24)
\end{aligned}
$$

The relation between the pointlike and the hadronic component is shown by the appearance of the term $P_{k\gamma}(x)$ in Eq. 2.23 which is related to the direct coupling of the photon with the quarks (pointlike component). This means that the divergences due to the collinear emission of quarks from the incoming photon in the pointlike component (Eq. 2.19) are reabsorbed into the partonic densities in the photon appearing in the hadronic component (Eq. 2.20). This shows that the pointlike and hadronic components of the photoproduction cross section are very closely related and that only their sum has a physical meaning. As a result, the separation of the cross section into a pointlike and a hadronic component is ambiguous for NLO and higher–order calculations.

Nevertheless, this separation can be defined safely for leading–order calculations to get a physical picture. These calculations including the separation are commonly used in simulations (see Sec. 2.4.1).

2.3 Deep Inelastic Scattering Cross Sections and the Structure of the Proton

HERA processes are distinguished by the virtuality of the exchanged boson Q^2 and the invariant mass of the virtual photon–proton system W^2. An interaction where the boson virtuality is larger than the proton mass ($Q^2 \gg M_p^2$) is denoted as *deep* and an interaction where the invariant mass of the virtual photon–proton system is larger than the proton mass ($W^2 \gg M_p^2$) is denoted as *inelastic*, an interaction with both $Q^2 \gg M_p^2$ and $W^2 \gg M_p^2$ therefore *deep inelastic scattering* (DIS) in the case of the exchange of a γ, Z_0 or $W^{\pm}$ boson. The case of a quasi–real exchanged boson which can only be a photon due to the available energy content of the exchange is named *photoproduction* (PHP) and is discussed later (see Sec. 2.4).

The calculation of NC and CC deep inelastic scattering cross sections in the QPM plus leading–order corrections (see Sec. 2.2) takes into account BGF and QCDC diagrams (Fig. 2.3) in addition to the QPM diagrams (Fig. 2.2). The unpolarized CC and NC cross sections in DIS in the QPM [8] are shown in Eq. 2.25 and 2.26:

$$
\begin{aligned}
\frac{d^2\sigma_{NC}(e^{\pm}p \to eX)}{dxdy} &= \frac{4\pi\alpha_{em}^2}{xyQ^4}\left[\left(1-y-\frac{x^2y^2M^2}{Q^2}\right)F_2^{NC} + y^2xF_1^{NC} \mp \left(y-\frac{y^2}{2}\right)xF_3^{NC}\right] \qquad (2.25)\\
\frac{d^2\sigma_{CC}(e^{\pm}p \to \nu X)}{dxdy} &= \frac{4\pi\alpha_{em}^2}{xyQ^4}(1\pm\lambda^2)\frac{1}{2}\left(\frac{G_F M_W^2}{4\pi\alpha_{em}}\frac{Q^2}{Q^2+M_W^2}\right)^2 \\
&\left[\left(1-y-\frac{x^2y^2M^2}{Q^2}\right)F_2^{CC} + y^2xF_1^{CC} \mp \left(y-\frac{y^2}{2}\right)xF_3^{CC}\right] \qquad (2.26)
\end{aligned}
$$

where α_{em} is the fine structure constant and G_F the Fermi constant. The charged current *structure functions* F_1^{CC}, F_2^{CC} and F_3^{CC} derive exclusively from the W exchange and the neutral current structure functions F_1^{NC}, F_2^{NC} and F_3^{NC} are determined by photon and Z exchange and by their interference.

The ep cross section is expected to be dominated at $Q^2 \ll M_Z^2$ by photon exchange.

The exchange of Z^0 and $W^{\pm}$ is suppressed by a factor:

$$\frac{\sigma(Z^0, W^{\pm})}{\sigma(\gamma)} \sim \left(\frac{Q^2}{Q^2 + M^2_{Z^0, W^{\pm}}} \right)^2 \tag{2.27}$$

due to the large mass of the exchange bosons. Latest measurements from the ZEUS and H1 collaborations of the CC and NC deep–inelastic scattering cross sections [9] show the suppression of the CC cross section with respect to the NC cross section at lower Q^2 values than the $W^{\pm}$ mass (Fig. 2.5).

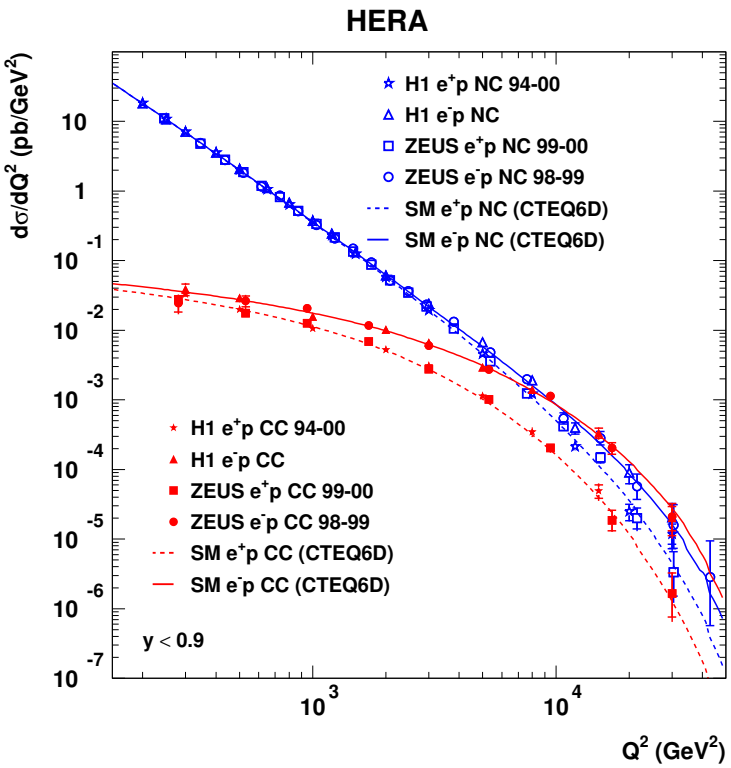

Figure 2.5: Inclusive differential charged current (CC) and neutral current (NC) cross sections as a function of Q^2 from the ZEUS and H1 collaborations [9]. The *Standard Model* predictions for NC and CC DIS are shown in solid and dashed lines respectively. The suppression of the CC cross section with respect to the NC cross section is clearly shown at Q^2 values lower than the $W^{\pm}$ mass squared.

The measured structure functions $F_2(x, Q^2)$ [9] (Fig. 2.6) show an approximate independence from Q^2 for $x \geq 0.1$ and therefore look the same for all values of the probe resolution. Here, the proton structure is dominated by the valence quark contents and the *Bjorken scaling* expected in the QPM picture is approximately valid.

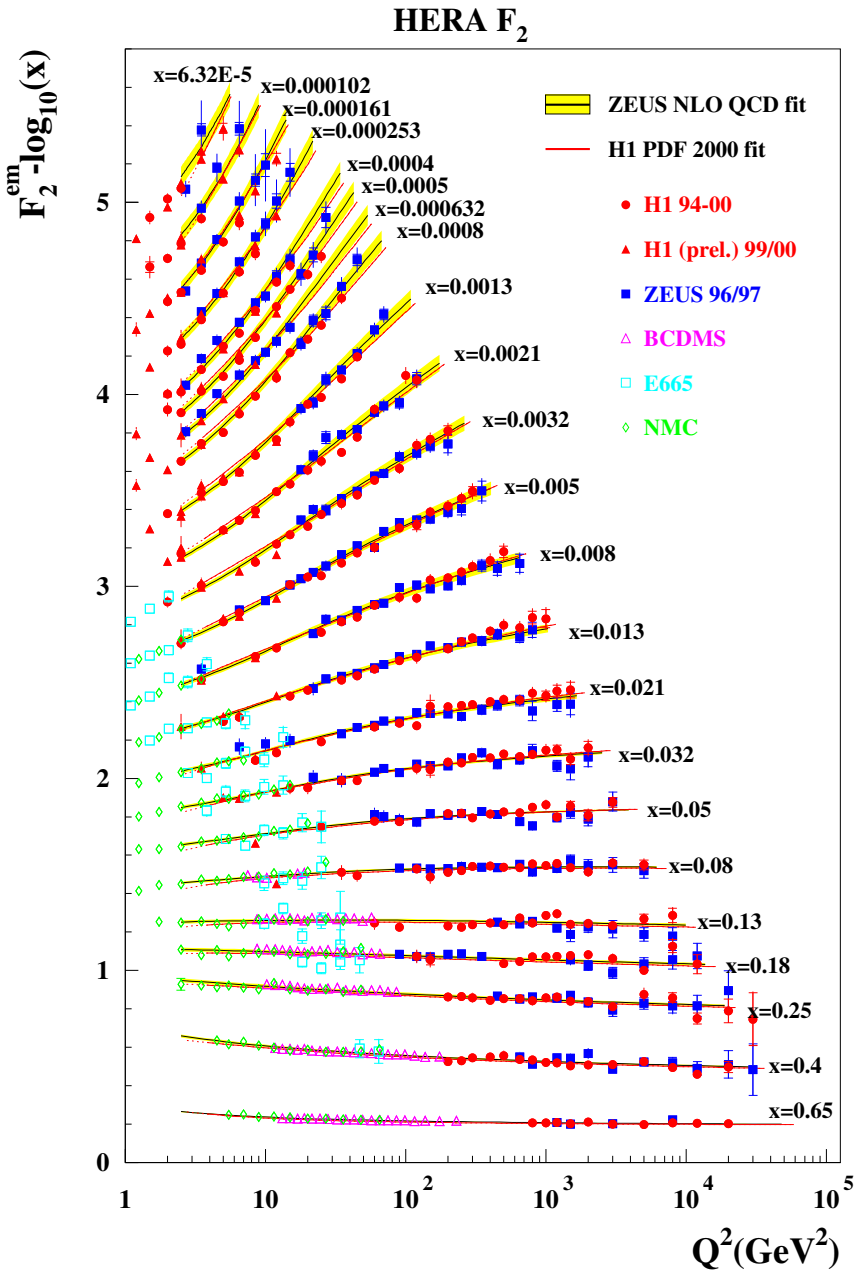

Figure 2.6: Dependence of the proton structure function $F_2^{em}(x, Q^2)$ from Q^2 at fixed values of x. For $x \geq 0.1$, the structure function is independent of Q^2. For $x \ll 0.1$, the number of partons sharing the proton momentum increases with Q^2.

For $x \ll 0.1$, the structure functions increase with Q^2. This indicates that at higher Q^2 the proton momentum is shared by more partons than at lower Q^2 mainly due to the contribution by the gluons in the proton splitting into $q\bar{q}$ pairs.

Although the gluon density cannot be directly determined from the structure functions using the factorization theorem, the increasing slope of the structure functions compared to the expected independence of Q^2 provides a possibility to extract them. Due to this indirect determination, the error on the gluon PDF is large compared to the error of the quark PDF's which is shown in Fig. 2.7.

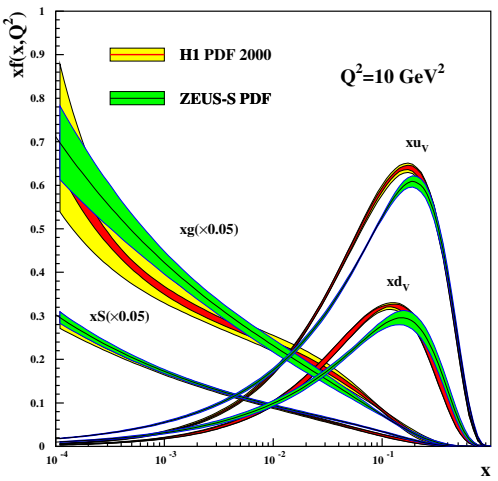

Figure 2.7: Proton density functions for u, d and s quarks and gluons extracted from NLO calculations by the ZEUS and H1 collaborations [10] at $Q^2 = 10$ GeV^2. The dominance of the valence quarks at higher x is changed at lower x, where the probability to find a gluon in the proton increases due to the gluon radiation of the quarks before the interaction. Due to the indirect determination of the gluon PDF from the increasing slope of the structure functions at low x, the error on the gluon PDF is larger than the error of the quark PDF's.

2.4 Beauty Quark Production in the Photoproduction Regime

The dominant contribution of the HERA cross section is the photoproduction regime defined by the virtuality to be $Q^2 < M_p^2$.
The exchange of a Z^0 or $W^{\pm}$ boson is largely suppressed due to the small transfered momentum between the electron and the proton. In ep collisions, a finite probability exists for the lepton to emit an almost on-shell photon which interacts with the hadronic structure of the proton. As presented in Sec. 2.2, the contribution can be taken into account in the cross section calculation by dividing the calculation into a pointlike part where the photon directly interacts with the partonic substructure and a hadronic part where the photon fluctuates into a hadronic system before the hard interaction. But for heavy quark production and in particular for beauty production, the contribution from the hadronic component is small if the scale used to separate the two components is less than $2m_b$.
In the next sections, the leading order simulation approach using the PYTHIA event generator is introduced followed by the description of the theoretical concepts of the next–to–leading order calculation for beauty quark production with special emphasis on the dijet final state used in this thesis.

2.4.1 Beauty Quark Event Simulation with PYTHIA

The detailed simulation of the final states of ep interactions is an important ingredient needed for the cross section measurement. Not only efficiencies and acceptances of the measurement including detector effects are determined using a detailed simulation. Also the separation of the signal from the background can be performed using simulations (see Chap. 9).
The simulation process is divided into two stages. The first stage consists of the simulation of the final state of an ep interaction. The partons from the hard subprocess are evolved to the hadron level as if they had been measured with a perfect detector. Stage 2 simulates the impact of a realistic detector on that final state. The so called *detector simulation* is described later in Sec. 5.3.

In this thesis, the *PYTHIA* [11] Monte Carlo (MC) event generator is used to simulate *ep* collisions. PYTHIA is a multi-purpose high energy particle collision simulator capable of simulating e^+e^--, *pp*- and *ep* collision. The general structure of PYTHIA to simulate an event is based on leading order calculations of the hard subprocess supplemented by parton showering in the initial and final state as explained before. Next–to–leading order simulations are not yet suited for reasonably fast event simulation and therefore not available yet. The soft contributions to the final state are simulated using phenomenological approaches. The general structure of the PYTHIA MC generator as a leading order plus parton shower simulation is shown in Fig. 2.8

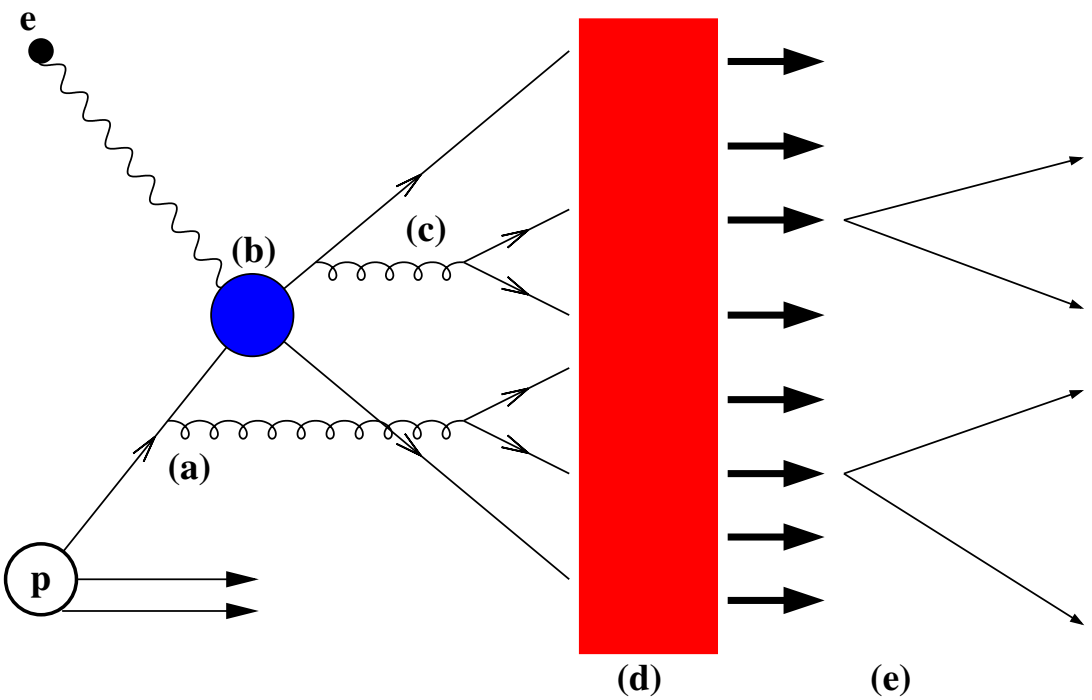

Figure 2.8: General structure of the leading order plus parton shower MC generator PYTHIA. Radiation from initial (a) and final (c) partons (*parton showers*) and partons from the hard subprocess (b) transform in the fragmentation/hadronisation stage (d) to unstable hadrons which in the end decay into stable hadrons (e).

and consists of the following stages:

Stage 1: Incoming parton distributions: The initial input of the PYTHIA event generator are the parton distributions of the colliding particles (see Sec. 2.2 and 2.3). In particular, he Weizsäcker-Williams spectrum [12] is used to describe the photon flux from the lepton.

The partonic structures are used in the *massive scheme* where only lighter flavours are active in the proton and the photon. Heavy flavours have to be produced by gluon splitting. Therefore, beauty photoproduction is dominated by LO BGF processes. As presented before, the photon can interact directly with a gluon from the proton. In PYTHIA terminology, theses processes are called *direct* (see (a) in Fig. 2.4). The interaction of the partonic photon structure with a gluon from the proton are called *resolved* processes (see (b) in Fig. 2.4). A suited separation of direct and resolved processes uses x_γ, the momentum fraction of the virtual photon transferred to the hard subprocess. Direct processes transfer the complete momentum of the virtual photon to the subprocess and therefore follow $x_\gamma = 1$. Resolved processes only transfer a fraction of the photon momentum and therefore have $x_\gamma < 1$. In the experimental final state of this analysis, x_γ can be approximately determined from the two highest transverse energy jets in the event:

$$x_\gamma^{jets} = \frac{(E - p_z)^{jet_1} + (E - p_z)^{jet_2}}{E - p_z} \tag{2.28}$$

if no further jets are present. Due to the massive scheme calculation, the missing contributions from heavy *excitations* from proton and photon where a heavy quark directly from the partonic substructures enters the hard subprocess have to be simulated separately. For this purpose, the heavy quark is extracted in the massless scheme from the partonic substructure by splitting a gluon from the substructure into a $b\bar{b}$ pair.

Stage 2: Hard subprocess: The LO calculation of the hard subprocess (see (b) in Fig. 2.8) sets the overall kinematics and the cross section of the simulated event (see Sec. 2.2 for the description of the NLO cross section calculation) and represents the core of the event simulation.

Stage 3: Parton shower: Higher order corrections to the event topology not taken into account by the LO hard subprocess have to be included using phenomenological approaches. In the *parton shower model* (PS), the partons from the partonic structure of the incoming particles and the partons originating from the hard subprocess can radiate gluons ($q \to qg$, etc.) or split into $q\bar{q}$ pairs ($g \to q\bar{q}$), also called initial (see (a) in Fig. 2.8) and final (see (c) in Fig. 2.8) state radiation. The PS is explained in more detail in Sec. 2.4.1.1.

Stage 4: Fragmentation/hadronisation: Due to confinement, observable hadrons can only exist in colour singlet states. Partons carry a net colour charge, so they have to be transferred to a colour singlet state. This hadronisation process (see (d) in Fig. 2.8) is not perturbatively calculable. The *string model* or *Lund model* mainly used in PYTHIA describes the non-perturbative hadronisation process using the linear confinement picture (see Sec. 2.4.1.2).

Stage 5: Decay of unstable hadrons: The hadrons produced in the hadronisation stage don't have to be stable. They can be unstable and decay in this last stage to stable hadrons (see (e) in Fig. 2.8 and Sec. 2.4.1.3).

The philosophy of PYTHIA is to simulate the fragmentation/hadronisation of the partons as detailed as possible.
In the following the initial and final state radiation stage, the fragmentation/hadronisation stage and the decay of unstable hadrons with emphasis on beauty flavoured hadrons are described in more detail.

2.4.1.1 Parton Shower

The stages of initial and final state radiation and gluon splitting have to simulate bremsstrahlung radiation from the lepton and gluon radiation from the partons before and after the hard subprocess. Therefore it has to be decided if and when one of the following branchings $a \to bc$ occurs:

$$e^{\pm} \to e^{\pm}\gamma \tag{2.29}$$
$$\gamma \to q\bar{q} \tag{2.30}$$
$$q \to qg \tag{2.31}$$
$$q \to q\gamma \tag{2.32}$$
$$g \to gg \tag{2.33}$$
$$g \to q\bar{q} \tag{2.34}$$

The hadronisation/fragmentation process is separated due to the different treatment in an initial and a final stage. Both are started at a scale Q^2_{max} which defines the transition between the initial and final state radiation and the hard subprocess.
In the initial stage, the radiation before the hard subprocess has to be simulated although the following hard subprocess sets the overall event kinematics. The simulation is carried out in the *backward evolution scheme* starting from the scale Q^2_{max}. It is based on the usage of the DGLAP evolution equations [6]. Starting from the two incoming partons to the hard subprocess, the backward evolution traces the showers backward in time in a sequence of decreasing spacelike virtualities Q^2 and increasing momentum fractions x and y down to the point where a cutoff $Q^2_0 \approx 1$ GeV is reached.
On the other hand, the final state radiation splits the final state partons into timelike showers starting at Q^2_{max}. The similar evolution ends at Q^2_0.
Branchings on both sides are interleaved in a common sequence of decreasing Q^2 values. At each Q^2 value, the splitting kernels $P_{a\to bc}(z)$ of the DGLAP equations characterise the splitting process with z giving the energy sharing between a and b.

2.4.1.2 Fragmentation/Hadronisation

The fragmentation of partons into hadrons is described in analogy to the description of the partonic structure of the proton. *Fragmentation functions* $D(z)$ give the probability that a parton fragments into a hadron with momentum fraction z of the original parton.
The picture of asymptotic freedom at short distances and confinement at large distances in QCD is a widely accepted picture of the strong force in hadrons. It characterises the strong force between partons to increase linearly with distance. The linear confinement picture is the basis of the string fragmentation of the Lund model which is the basis of the hadronisation simulation of PYTHIA.
In this picture, the energy in the colour dipole field between a colour charge and an anti–colour charge increases linearly with their distance. An uniform colour flux tube with transverse dimension of typical hadronic sizes (1 fm) represents the linearly rising potential between the colour charges. If the charges move apart, the potential increases and the string can break up producing a new $q'\bar{q}'$ pair. The original system splits into two colour singlet systems and further breaking can occur if the invariant mass of a system is large enough. The string break-up generates the new $q\bar{q}$ pair through quantum mechanical tunneling $\sim exp(-\pi m_{q,\perp}^2/\kappa^2)$ with $\kappa \approx 1$ GeV/fm as the string tension. This leads to a flavour-independent Gaussian transverse momentum spectrum. It has to be locally compensated between the two quarks since the string has no transverse excitation. The transverse momentum of the resulting hadron is the summed momenta of the quarks forming it. An additional consequence of the tunneling is the suppression of heavy quark production in the hadronisation due to the high heavy quark mass. The heavy quark higher order corrections are only included via parton showers.
In the string fragmentation, the momentum fraction $z = (E + p_\parallel)_h/(E + p)_q$ with $p_\parallel$ the momentum of the formed hadron h along the direction of the quark q is given by the string fragmentation function:

$$f(z) \sim \frac{1}{z}(1-z)^a exp\left(-\frac{bm_{h,\perp}^2}{z}\right) \tag{2.35}$$

with the free parameters a and b. The parameters have to be determined from measurements.
The string fragmentation describes the fragmentation of light quarks but has deficits in describing heavy quark fragmentation.
The heavy quark fragmentation functions are expected to peak near 1 because the produced hadron should retain a large fraction of the initial quark momentum. Nevertheless, the perturbatively calculable part of heavy quark fragmentation functions has to be supplemented with a phenomenological non-perturbative form to include higher order corrections which are expected to be large in heavy flavour fragmentation. One of the popular parametrisations is the *Peterson* fragmentation function [13]:

$$D(z) \propto \frac{1}{z}\left(1 - \frac{1}{z} - \frac{\epsilon}{1-z}\right)^{-2} \tag{2.36}$$

where the parameter ϵ depends on the heavy flavour considered. The parameter fitted for beauty quark production is determined from a fit to a measurement of B mesons in e^+e^- collisions [14] using :

$$\epsilon \approx 0.003 \tag{2.37}$$

The PYTHIA MC was used with the string fragmentation approach for light flavours and with the Peterson fragmentation in the case of heavy flavours. A more detailed overview of the used PYTHIA MC samples can be found in Sec. 8.1.

2.4.1.3 Decay of Unstable Hadrons

The description of the decay of unstable hadrons is restricted to semi-leptonic beauty–flavoured hadrons into muons according to the investigated beauty quark decay channel. Although beauty–flavoured hadrons are long–lived compared to other strongly decaying particles, their decay time–scale of $10^{-12}s$ is too short to observe beauty hadrons directly. Only the decay products are experimentally accessible and the MC generator has to reflect this behaviour.
The most simple picture of the decay of beauty–flavoured hadrons is given by the *spectator model* (see Fig. 2.9). The hadron decay is treated as the decay of a free beauty quark. The other partons within the hadron don't play a role in the decay.

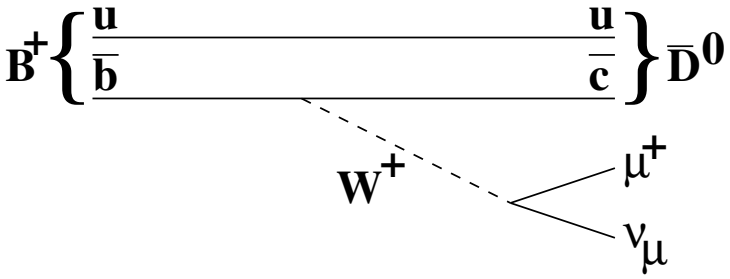

Figure 2.9: Hadron decay $B^+ \rightarrow \mu^+ \nu_\mu \bar{D}^0$ in the spectator model.

Beauty quarks predominantly decay into charm quarks via the emission of a virtual W boson. The W boson produces two fermions $f\bar{f}'$. With a probability of $10.57 \pm 0.22\%$ [8], these are a muon μ and a muon–neutrino ν_μ (see (a) in Fig. 2.10). In addition to these *prompt* decays, muons can be produced from beauty quark decays also through *cascade processes* where the charm quark resulting from the beauty decay decays semi-leptonically into a muon (see (b) in Fig. 2.10).

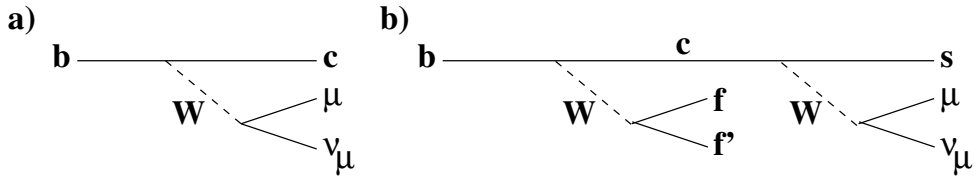

Figure 2.10: Beauty quark decay: *a): prompt* decay, *b): cascade* decay via a charm quark.

The decays are implemented in PYTHIA by the respective measured branching ratio. The compatibility of the decay spectrum of muons implemented in PYTHIA to measurements by BaBar and Belle is investigated in the following.
The Belle and BaBar collaborations measured the momentum spectrum of electrons in the beauty–flavoured hadron rest–frame [15]. Fig. 2.11 shows that the measurement is compatible to the prediction from PYTHIA [16] and that PYTHIA can be reliably used to simulate semi-leptonical beauty–flavoured hadron decays.

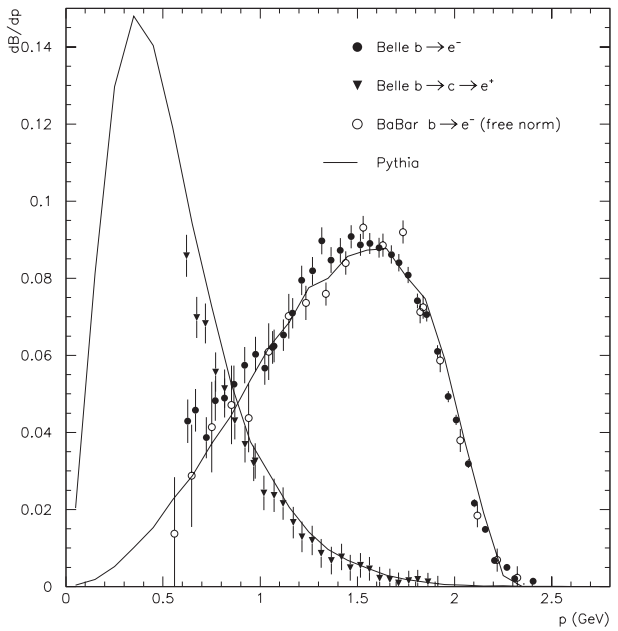

Figure 2.11: Differential branching ratio dB/dp for the electron momentum in the B hadron centre–of–mass system as measured by Belle for direct (circles) and indirect (triangles) B-meson decays compared to the PYTHIA prediction (line). The momentum distribution by BaBar is shown with arbitrary normalisation (empty circles).

Fig. 2.12 compares the electron spectrum of the B hadron mixture at the $\Upsilon(4s)$ resonance (BaBar/Belle centre–of–mass energies) with the muon spectrum of the B hadron mixture at LEP centre–of–mass energies. The two distributions are very similar. The lepton spectrum from B hadrons is quite independent from the B hadron mixture and the lepton flavour and can be considered valid for muons at HERA.

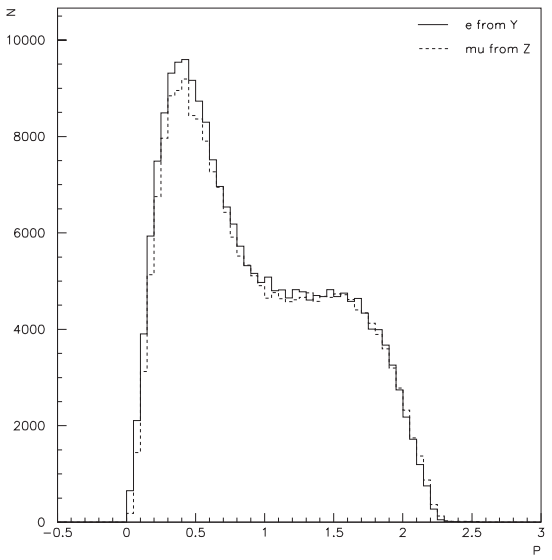

Figure 2.12: PYTHIA prediction for the electron momentum distribution of the B hadron mixture at the $\Upsilon(4s)$ resonance (BaBar/Belle centre–of–mass energies) with the muon spectrum of the B hadron mixture at LEP centre–of–mass energies.

2.4.2 Next–To–Leading Order Calculation with FMNR

This section describes the calculation of hadron–level dijet plus muon photoproduction beauty quark cross sections in next–to–leading order for the comparison with the measurements of this thesis.

The next–to–leading order calculation of the γp photoproduction cross section follows the approach presented in Sec. 2.2 of separation of the cross section into a pointlike and a hadronic component (Fig. 2.4).
The calculation is implemented in the program by **F***rixione*–**M***angano*–**N***ason*–**R***idolfi (FMNR)* [17] which is used in this thesis to calculate cross sections.
FMNR is a parton generator which provides two- and three-parton final states and calculates photoproduction cross sections. The calculation is performed in the *massive approach* where only light quarks (up to the mass of the strange quark) and gluons are active partons in the initial state. This is implemented using a modified version of the $\overline{MS}$ subtraction scheme [18] in which heavy quark effects decouple in processes involving momenta much smaller than the heavy quark mass. This approach was favoured over the *massless approach*, where the heavy flavours are treated as active massless initial partons above some energy thresholds.
FMNR generates sequences of correlated events. These sequences are chosen to cancel out divergences in the cross section calculation.
For the calculation of *ep* collisions, the *Weizsäcker-Williams function* [12] is used to simulate the energy distribution of the quasi-real photon flux from the electron which is afterwards used by the FMNR calculation.

To extract dijet plus muon photoproduction beauty quark cross section predictions, a dijet plus muon final state is selected by application of the KTCLUS jet finder algorithm (see Sec. 7.5) to the partonic final state of the FMNR calculation.
The muon selection requires the fragmentation/hadronisation of the parton final state. This is done in analogy to the approach chosen in the Monte Carlo event simulation (for more details see Sec. 2.4.1). The fragmentation/hadronisation of beauty quarks is carried out according to the *Peterson fragmentation* [13]. The subsequent decay of the B hadrons into muons is performed according to the total $B \to \mu X$ branching ratio where the muon momentum in the B hadron rest frame is extracted from PYTHIA.
The following parameter set is used for the calculation:

- Proton PDF: CTEQ5M
- Photon PDF: GRV-HO
- beauty quark mass: 4.75 GeV
- factorisation and renormalisation scales are set to the transverse mass of the beauty quark pair which is proposed by the authors for $b\bar{b}$ cross sections:

$$\mu_R = \mu_F =< m_T >= \sqrt{\frac{1}{2}\left((p_T^b)^2 + (p_T^{\bar{b}})^2\right) + m_b^2} \tag{2.38}$$

  where $p_T^{b(\bar{b})}$ is the transverse momentum of the beauty (anti-beauty) quark in the laboratory frame. The scale μ_γ was set to ~ 1 GeV because the *massive approach* does not contain active heavy flavours in the initial state.
- $\Lambda^{(5)}_{QCD} = 0.226$ GeV according to the value of α_s used in the CTEQ5M PDF
- Peterson fragmentation with $\epsilon = 0.0035$
- B hadron branching ratio into muons: 0.217 (shape is taken from PYTHIA, see Sec. 2.4.1.3)

The influence of the chosen hadronisation and renormalisation scales is investigated by changing the input parameters for beauty quark mass and scales simultaneously:

-: $m_b = 4.5$ GeV, $\mu_R = \mu_F = \frac{1}{2} < m_T >$

+: $m_b = 5.0$ GeV, $\mu_R = \mu_F = 2 < m_T >$

The reduction of the scales and the mass results in a +24.8% increase in the total dijet plus muon beauty quark photoproduction cross section whereas the increase yields a −24.7% decrease. The influence on the photoproduction cross section differential in the transverse momentum of the muon p_T^μ is shown in Fig. 2.13

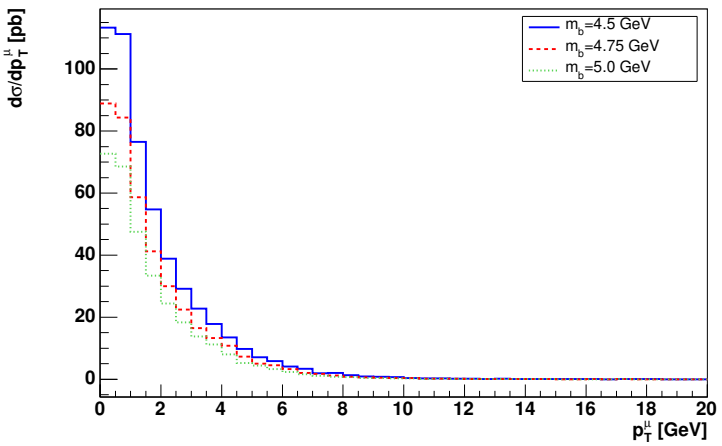

Figure 2.13: Changes in the differential NLO QCD cross section predictions in p_T^μ from FMNR by changing the beauty quark mass and the renormalisation and fragmentation scales simultaneously. The dijet plus muon selection is applied to the generated events by FMNR and the muon pseudo-rapidity is restricted to $-2 \leq \eta^\mu \leq 2.5$.

The change in beauty quark mass and renormalisation and hadronisation scales has also a significant influence on the cross section differential in the pseudo-rapidity[7] of the muon η^μ shown in Fig. 2.14.

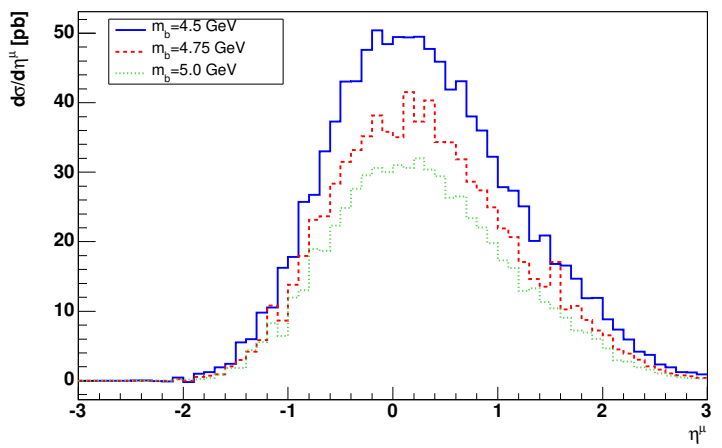

Figure 2.14: Changes in the differential NLO QCD cross section predictions in η^μ from FMNR by changing the beauty quark mass and the renormalisation and fragmentation scales simultaneously. The dijet plus muon selection is applied to the generated events by FMNR and the muon transverse momentum is restricted to $p_T^\mu \geq 1.5$ GeV.

[7] $\eta = -ln\left(tan\left(\frac{\theta}{2}\right)\right)$

The influence of the change of the chosen proton PDF CTEQ5M to MRST results in a decrease of the total dijet plus muon beauty quark photoproduction cross section of -1.4% which is consistent with the relative change in the cross sections differential in p_T^μ and η^μ shown in Fig. 2.15.

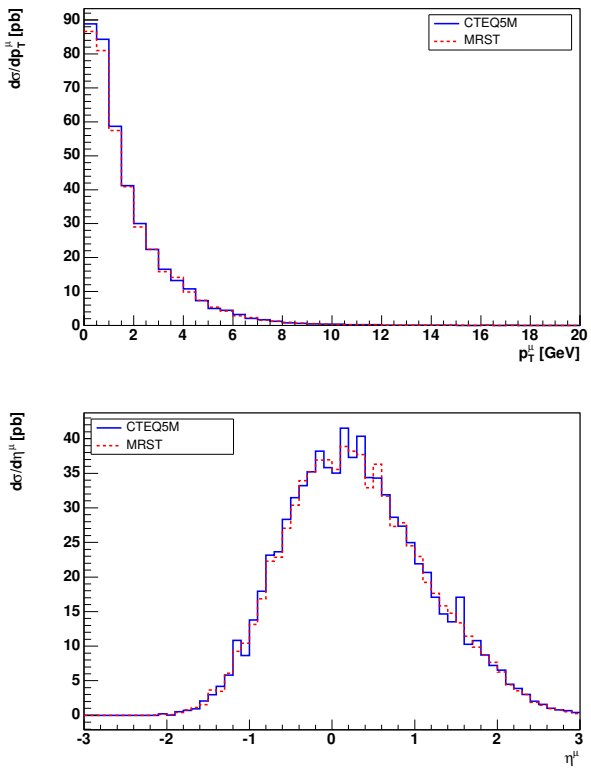

Figure 2.15: Changes in the differential NLO QCD cross section predictions from FMNR by changing the proton PDF from CTEQ5M to MRST. Shown are the differences in the cross sections differential in the transverse momentum of the muon p_T^μ (*top*) and the pseudo-rapidity of the muon η^μ (*bottom*).

The influence of the change of the proton PDF is negligible compared to the influence of the beauty quark mass and the scales.

The fragmentation of the beauty quark plays a significant role in the extraction of the dijet plus muon cross section predictions by FMNR. The effect of the fragmentation is investigated by changing the input parameter to the Peterson fragmentation and in addition changing the fragmentation to the Kartelishvili (k) fragmentation function [19]:

-: $\epsilon = 0.0020$

+: $\epsilon = 0.0053$

k: $\alpha = 13$

The influence on the total cross section is $+2.1\%$ for decreasing the Peterson fragmentation parameter and -1.7% for increasing it. The change of the fragmentation function to the Kartelishvili function yields a $+2.3\%$ change. The influence of the fragmentation is negligible compared to the influence of the scales and the beauty quark mass which is confirmed by the relative change of the cross sections differential in p_T^μ and η^μ (see Fig. 2.16).

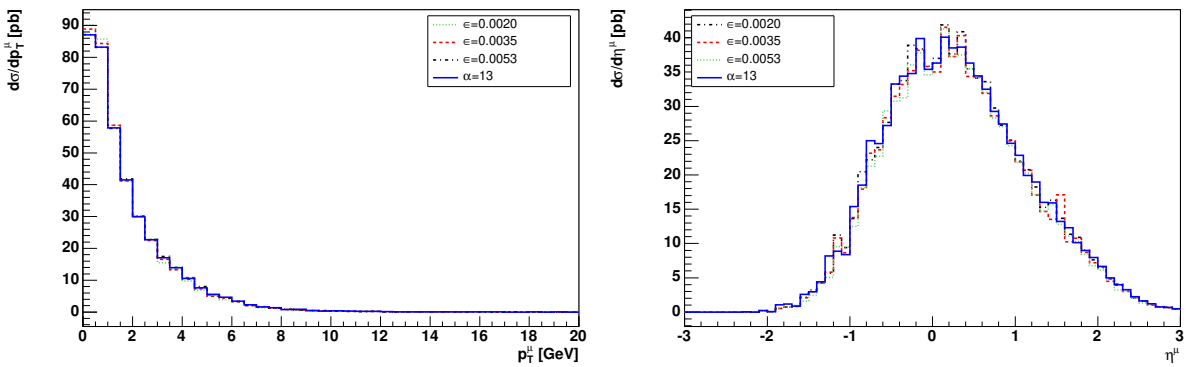

Figure 2.16: Changes in the differential NLO QCD cross section predictions from FMNR by changing the fragmentation. Shown are the differences in the cross sections differential in the transverse momentum of the muon p_T^μ (*left*) and the pseudo-rapidity of the muon η^μ (*right*).

As a last check, the influence on the chosen $\Lambda_{QCD}^{(5)}$ is investigated. The error of 0.0002 of the correspondingly used α_s value in the CTEQ5M proton PDF corresponds to a an error on $\Lambda_{QCD}^{(5)}$ of $^{+25}_{-23}$ MeV. Therefore $\Lambda_{QCD}^{(5)}$ is changed to:
[8]

-: $\Lambda_{QCD}^{(5)} = 0.200$ GeV

+: $\Lambda_{QCD}^{(5)} = 0.250$ GeV

The relative change of the total cross section is $^{+3.5\%}_{-4.0\%}$ yielding the relative change in the cross sections differential in p_T^μ and η^μ shown in Fig. 2.17.

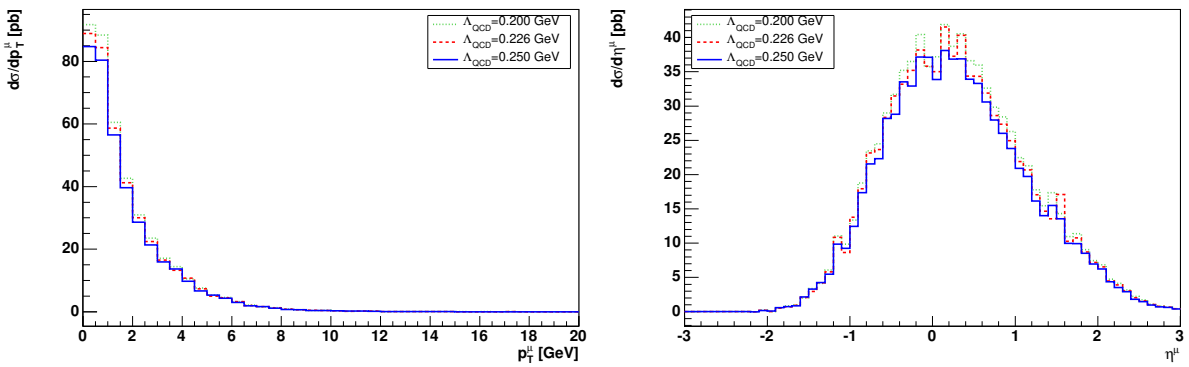

Figure 2.17: Changes in the differential NLO QCD cross section predictions from FMNR by changing Λ_{CQD}. Shown are the differences in the cross sections differential in the transverse momentum of the muon p_T^μ (*left*) and the pseudo-rapidity of the muon η^μ (*right*).

The influence of $\Lambda_{QCD}^{(5)}$ is small compared to the mass and scales influence.

The dominating systematic error on the NLO QCD dijet plus muon photoproduction beauty quark cross section prediction originates from the chosen hadronisation and renormalisation scales and the beauty quark mass. The influences from the proton PDF, fragmentation and $\Lambda_{QCD}^{(5)}$ are negligible when added in quadrature. The systematic error from the scales and beauty quark mass variation is taken as the systematic error of the NLO QCD predictions which will be used to compare to the measured cross sections of this thesis.

Chapter 3

Beauty Production in the Global Context

Since the discovery of the beauty quark more than 25 years ago [20], the analysis of its cross section posed a big challenge for particle physics and theory. The discovery itself in proton–nucleus collisions started a wealth of experiments dedicated to pin down the properties of the beauty quark. Although the *Standard Model* is well established, the beauty quark sector still shows some discrepancies in the description of all beauty quark cross section measurements.
This chapter presents a collection of beauty quark cross section measurements and summarises the current knowledge about beauty quark production in the *Standard Model*.

A short introduction of the beauty quark identification techniques used is given in the beginning. The subset of techniques relevant for this thesis is explained in detail in chapter 9.
The summary begins with a short overview of the development of the beauty quark cross section from fixed target experiments to collider experiments.
The selection of presented results is then restricted to beauty quark identification techniques closely related to this thesis. Results from UA1, CDF and D0 identifying beauty quarks by their semi-leptonic decays into muons present the current status in $p\bar{p}$ collisions. The results of UA1 are measured at a centre–of–mass energy comparable to HERA whereas the CDF and D0 results are measured at higher energies.
At last, the presentation of the corresponding results from ZEUS and H1 show the current status in ep collisions and provide the starting point for the beauty quark measurements in this thesis.

3.1 Beauty Quark Identification Techniques

Various methods for beauty quark identification are used for measurements of beauty quark cross sections. A detailed explanation of those techniques used in this thesis is given in chapter 9. In the following, brief introductions to the techniques used in the presented results are given.

1. Beauty quarks can be identified by their decay chain into muon pairs (dimuons) from J/ψ mesons: $(b \to J/\psi \to \mu^+\mu^-)$ (*J/ψ method*). The dimuon from the J/ψ is used to determine the secondary vertex by precision tracking. The secondary vertex is significantly displaced from the primary due to the long lifetime of the subsequent B meson. This displacement is used to identify the originating beauty quark.

2. Beauty quarks can be identified by their semi-leptonic decay into muons using the the transverse momentum of the muon relative to the associated hadron jet (p_T^{rel} *method*, see Sec. 9.1). For beauty quarks, the p_T^{rel} distribution is harder than for lighter flavours and charm quarks. Therefore, a fit of the lighter quark, charm quark and beauty quark p_T^{rel} distributions from simulation to the measured p_T^{rel} distribution yields the fraction of muons coming from beauty quark decays in the data.

3. Beauty quarks can be identified by their semi-leptonic decay into muons using the impact parameter of the muon (*impact parameter method*). The impact parameter of a muon coming from a beauty quark relative to the primary vertex or the beam spot is asymmetric with regard to an associated

jet axis. Due to the long lifetime, the impact parameter distribution for muons from beauty quarks is shifted to positive values. Similar to the p_T^{rel} method, a fit of the lighter quark, charm quark and beauty quark impact parameter distributions from simulation to the measured distribution yields the fraction of muons coming from beauty quark decays in the data.

4. The *jet–probability method* combines the identification of beauty quarks by their semi-leptonic decay into muons with the identification of the anti–beauty quark in the same event using the impact parameter information from all tracks belonging to the other high E_T jet . The combined impact parameter information can be transformed into a probability that the jet does not originate from a long-lived particle. As beauty quark have a long lifetime, a fit of lighter quarks, charm and beauty quark jet probability distributions to the data yields the fraction of anti–beauty quark jets in the data.

5. Beauty quarks can be identified in dimuon events using a simultaneous inclusive fit in distributions of the invariant mass and the angular difference of the two muons in $\Delta R = \sqrt{\Delta\eta^2 + \Delta\phi^2}$ and $\Delta\phi$. Simulated samples of all background contributions and the signal are fitted to the data distributions to extract the different contributions of the background and signal processes to the data. This technique is able to select a clean sample of *beauty quark chain decay* events where the dimuon pair results from the decay of the same beauty quark. For dimuon pairs resulting from decays of different beauty quarks, the p_T^{rel} method is used in addition to separate beauty and charm contributions.

The following chapters summarise beauty quark measurements which use one of the presented techniques.

3.2 From Fixed Target to Collider Experiments

The measurement of $b\bar{b}$ production cross sections is a longstanding and important project in the framework of the *Standard Model* carried out over decades. Started in 1977 by the discovery of the beauty quark pair bound state Υ in a fixed target experiment [20], the beauty quark cross section was measured at different centre–of–mass energies in fixed target experiments shifting the focus to open beauty production from B-mesons. The significantly increased centre–of–mass energy of collider experiments continued this program. A selection of beauty quark production measurements from fixed target and collider experiments [21] is shown in Tab. 3.1.

Exp./Publication	Target(s)	$b\bar{b}$ events	method	phase space coverage
$p-A$				
E789 [22]	Au	19 ± 5	J/ψ	$0 < x_F^{J/\psi} < 0.1$, $p_T^{J/\psi} < 2$ GeV
E771 [23]	Si	15	J/ψ	$x_F < -0.25$
HERA-B [24]	C,Ti	$10.5^{+13.1}_{-9.2}$	J/ψ	$-0.25 < x_F^{J/\psi} < 0.15$
$p\bar{p}$				
UA1 [25]	$p\bar{p}$	2859	p_T^{rel}	$\lvert y\rvert < 1.5$, $p_T^{\mu} > 6$ GeV
CDF [26]	$p\bar{p}$	387 ± 32	J/ψ	$\lvert y\rvert < 1.0$, $p_T^{\mu} > 6$ GeV

Table 3.1: Collection of $b\bar{b}$ production cross sections at fixed target experiments ($p-A$) and collider experiments ($p\bar{p}$). $x_F = p_{parton}/p_{nucleon}$ denotes the fractional momentum of the partons inside the nucleon.

The cross sections are compared to predictions from PYTHIA (see Sec. 2.4.1) using its default settings in pp collisions (see Fig. 3.1). The prediction is scaled by an empirical factor which is varied between $\kappa = 1$, $\kappa = 2$ and $\kappa = 3$. The production of $b\bar{b}$ pairs in $p\bar{p}$ collisions at the quoted centre–of–mass is dominated by gluon–gluon-fusion processes and the valence quark distributions are less important. Therefore, the beauty quark cross sections measured in $p\bar{p}$ collisions can be compared to the predictions from PYTHIA simulating pp collisions.

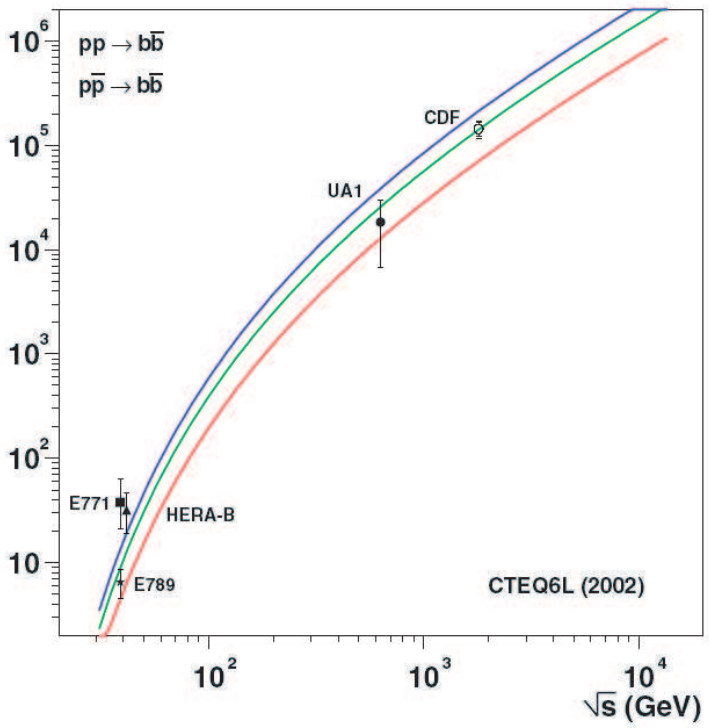

Figure 3.1: $b\bar{b}$ cross section measurement from fixed target and collision experiments (see Tab. 3.1) as a function of the centre–of–mass energy $\sqrt{s}$. The measurements are compared to predictions from PYTHIA for $pp \to b\bar{b}$ (see Sec. 2.4.1) with its default settings scaled up by an empirical factor of $\kappa = 1$, $\kappa = 2$ or $\kappa = 3$.

The presented production cross section measurements belong to the complete picture of the investigation of the beauty quark and show how they developed covering centre–of–mass energies from the fixed target regime up to $\sqrt{s} = 1.8$ TeV in $p\bar{p}$ collisions.

In the following, the focus is shifted to beauty quark cross section measurements from collider experiments. Following the approach in this thesis, the identification of beauty quarks is restricted to the detection of muons produced in semi-leptonic beauty quark decays.

3.3 Beauty Quark Production at the $Sp\bar{p}S$

The UA1 collaboration pioneered the measurement of beauty quark cross sections in single muon and dimuon events in $p\bar{p}$ collisions [27]. The UA1 detector was used to identify beauty quarks by their semi-leptonic decay into muons at the $Sp\bar{p}S$ collider at CERN at a centre–of–mass energy of $\sqrt{s} = 630$ GeV. Muons have been selected with a cut on the transverse momentum of the muon $p_T^\mu > 6$ GeV for single muons and $p_T^\mu > 3$ GeV for dimuons. The dimuon system was restricted to $m_{\mu\mu} < 35$ GeV^2. Beauty quarks have been identified using the p_T^{rel} method.
The measured inclusive single beauty quark cross section in an η range of $|\eta| < 1.5$ (Fig. 3.2) is compared to next–to–leading order QCD predictions [28] (these calculations are similar to the FMNR [17] calculations (see Sec. 2.4.2)) and found to be in good agreement.

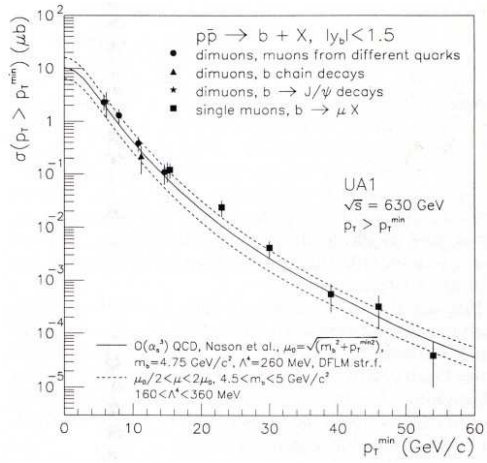

Figure 3.2: Inclusive single beauty quark cross section for $|\eta| < 1.5$ and $p_T > p_T^{min}$ from UA1. Presented are the cross section measurements extracted from single muon events and dimuon events originating from different beauty quarks and from beauty chain decays as well as measurements extracted from single muon events originating from J/ψ from beauty quarks and the comparison to a next–to–leading order calculation [28].

The cross sections extracted from single muon from beauty quark events as well as from dimuon events from subsequent J/ψ decays from beauty quarks [25] are also well described by the NLO calculation.

The importance of higher order contributions to the cross sections is confirmed by measurements of $b\bar{b}$ correlations in $\Delta R_{b\bar{b}} = \sqrt{\Delta\eta_{b\bar{b}}^2 + \Delta\phi_{b\bar{b}}^2}$ and $\Delta\phi_{b\bar{b}}$ in two different transverse momentum ranges of the beauty quark $p_{Tb}^{max} > 6(11)$ GeV (see Fig. 3.3).

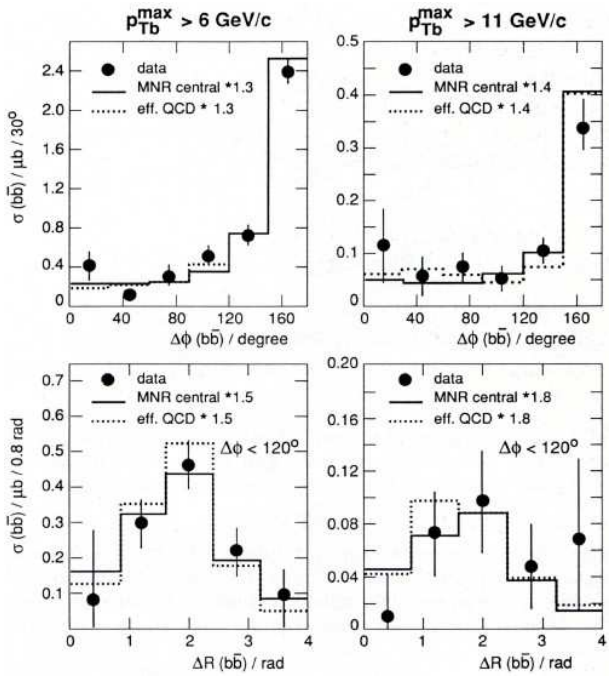

Figure 3.3: Beauty quark correlations from dimuon events in $\Delta R_{b\bar{b}}$ and $\Delta\phi_{b\bar{b}}$ in two different ranges of transverse momentum of the beauty quarks $p_{Tb}^{max} > 6(11)$ GeV compared to a NLO calculation.

The leading order contribution is expected to produce back–to–back configurations yielding a peak at $\Delta\phi_{b\bar{b}} = 180°$ whereas higher order contributions also produce configurations with lower $\Delta\phi$. The good

description of the measurement by the NLO QCD calculation especially at lower values of $\Delta\phi$ confirms the importance of higher order contributions in the QCD calculation.

3.4 Beauty Quark Production at the Tevatron

The Tevatron at the Fermi National Accelerator Laboratory (Fermilab) provides the experiments D0 and CDF with $p\bar{p}$ collision at centre–of–mass energies summarized in Tab. 3.2.

period	time	centre–of–mass energy
Run Ia	1992-1993	$\sqrt{s} = 1.8$ TeV
Run Ib	1993-1995	$\sqrt{s} = 1.8$ TeV
Run IIa	since 2001	$\sqrt{s} = 1.96$ TeV

Table 3.2: Tevatron running periods

This enables the experiments to continue the measurements of the UA1 collaboration (see Sec. 3.3) at significantly higher centre–of–mass energies.
The CDF [29] and D0 [30] experiments published early measurements of beauty quark cross sections (Fig. 3.4) using data from Run Ia.

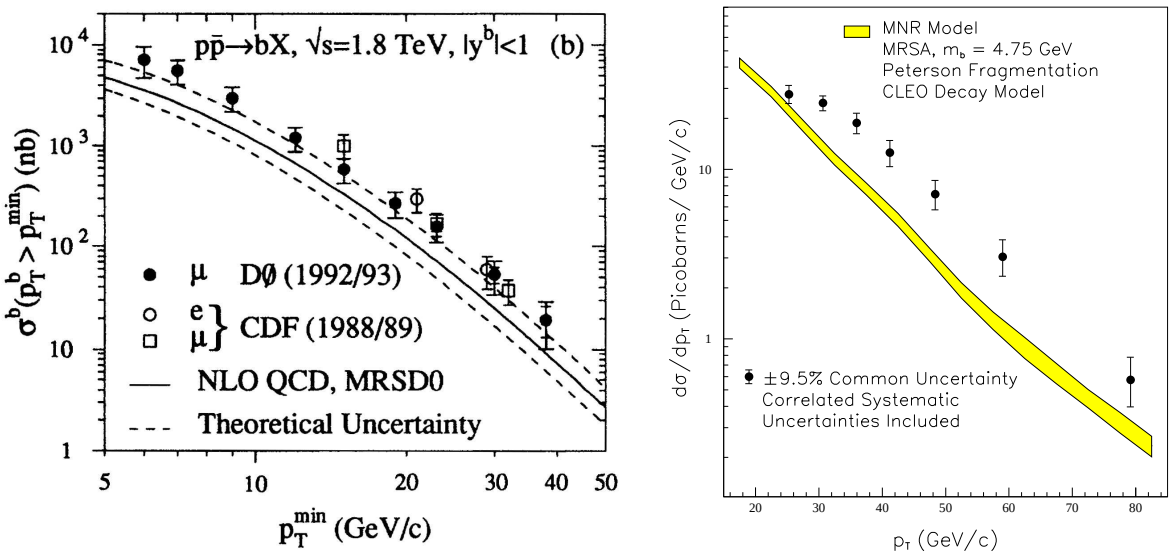

Figure 3.4: *Left:* Beauty quark cross section from D0 as a function of p_T^b using the p_T^{rel} method for $|y_b| < 1.0$ compared to a NLO QCD calculation. *Right:* Differential beauty quark cross section from CDF as a function of p_T^b using the jet–probability method. The shape of the cross section for $p_T^\mu > 9$ GeV, $|\eta^\mu| < 0.6$ and $|\eta^b| < 1.5$ is compared to a NLO QCD calculation.

Whereas the D0 collaboration reported compatibility of the measured cross section with NLO calculations within statistical and systematic errors, CDF showed that the shape of the cross section is reproduced by NLO but that the normalisation differs from the prediction by a factor ~ 2.

Further measurements of the D0 collaboration [31] showed the same behaviour like the CDF results. Although improvements of the inputs to the used Monte Carlo generator and NLO QCD calculation have been used compared to the first results and the shape of the measured cross section is still reproduced by the NLO calculation, the normalisation is different by a factor ~ 3 (see *left* in Fig. 3.5).

In contrast, the differential beauty quark correlation cross section as a function of $\Delta\phi^{\mu\mu}$ of the identified dimuon (see *right* in Fig. 3.5) is reasonably described by NLO predictions using HVQJET.

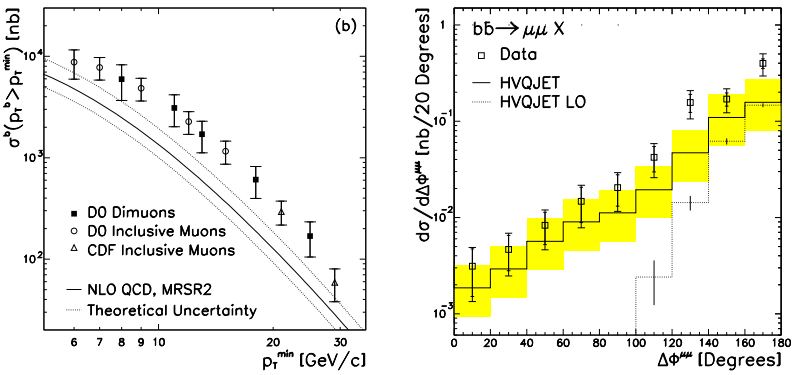

Figure 3.5: Beauty quark cross section from D0 as a function of p_T^b (*left*) and as a function of $\Delta\phi^{\mu\mu}$ (*right*) for $|y_b| < 1.0$ compared to NLO QCD calculations.

Recent developments in experiment and theory slowly converge towards a solution for the observed discrepancies. The NLO calculation can be refined by including resummations of logarithmic corrections for all perturbative orders and proper treatment of hadronisation/fragmentation [32]. Their predictions have been compared with previous measurements from CDF (see Fig. 3.6) including also latest preliminary measurements at a higher centre–of–mass energy ($\sqrt{s} = 1.96$ TeV) [33]). The normalisation difference seems to be solved by the improved calculations.

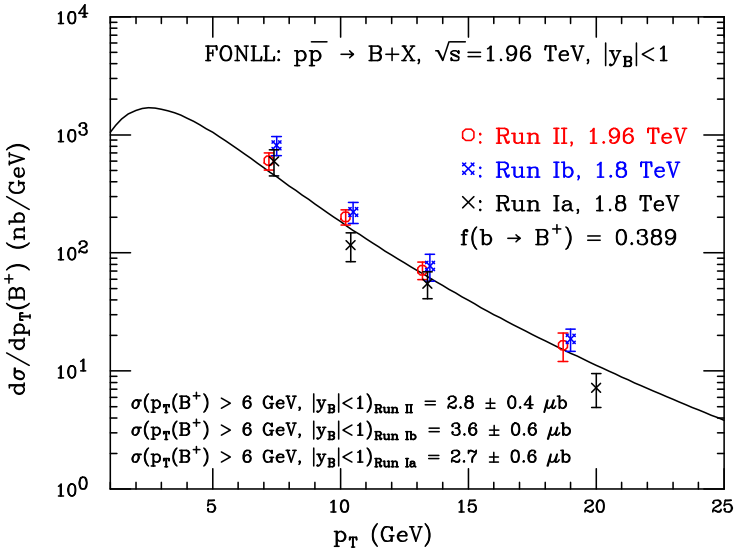

Figure 3.6: Development in time of CDF measurements for differential beauty quark cross sections as a function of $p_T^{B^+}$ using the J/ψ method from Run Ia [34], Run Ib [26] and Run IIa [35] compared to improved NLO QCD calculations.

Another approach supplementing the NLO calculation with the HERWIG Monte Carlo generator (*MC@NLO* [36]) results in a similar good description of the measured beauty quark cross sections.

The picture of beauty quark cross sections measured in $p\bar{p}$ collisions got complicated and not anymore consistent with NLO QCD predictions on the way from the UA1 measurements to higher centre–of–mass energies at the Tevatron. Although recent developments show a better description of the measured cross sections by improved calculations, *ep* collisions at HERA can significantly contribute to the solution of the *beauty puzzle*.

3.5 Beauty Quark Production at HERA

The nature of ep collisions compared to $p\bar{p}$ collisions should simplify the difficulties for theory to predict cross sections. Only one of the incoming particles is a proton with a partonic substructure and the other incoming particle is an electron which is very well known by theory. In practice, the theoretical treatment of ep collisions is as complicated as for $p\bar{p}$ collisions since photons can also exhibit a hadronlike structure.

In the following, a summary of the latest beauty quark cross section measurements of the ZEUS and H1 collaborations in the DIS and PHP regime are presented identifying beauty quarks by their semi-leptonic decays into muons.

In the DIS regime, the ZEUS collaboration identified beauty quarks using the p_T^{rel} method in ep events with at least one jet in the Breit frame[1] and a muon for photon virtualities $Q^2 > 2$ GeV^2 [37] (see *left* in Fig. 3.7). The H1 collaboration provides similar measurements supplementing the p_T^{rel} method with the impact parameter method for photon virtualities $2 < Q^2 < 100$ GeV^2 [38] (see *right* in Fig. 3.7)

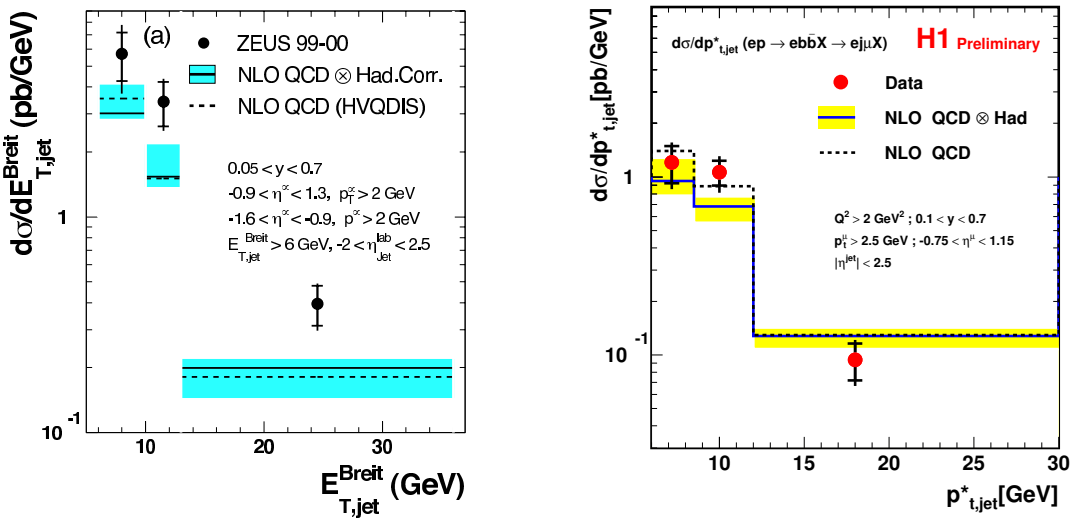

Figure 3.7: Differential beauty quark jet cross sections in DIS ep collisions compared to NLO QCD predictions from HVQDIS [39]. *Left:* Measurement of the beauty quark cross section differential in $E_{T,jet}^{Breit}$ for photon virtualities of $Q^2 > 2$ GeV^2 from ZEUS [37] using the p_T^{rel} method. *Right:* Measurement of the beauty quark cross sections differential in $p_{T,jet}^*$ in the Breit frame for photon virtualities $2 < Q^2 < 100$ GeV^2 from H1 using the p_T^{rel} method supplemented by the impact parameter method.

Both differential cross sections in the transverse energy (momentum) of the jet in the Breit frame are reasonably well described by NLO QCD calculations from HVQDIS [39] although the prediction is below the data in the ZEUS measurement. Here, for highest $E_{T,jet}^{Breit}$ the difference between measurement and NLO QCD prediction is about two standard deviations.

[1] In the QPM picture, the Breit frame denotes the frame in which the photon bounces off a brick wall formed from the incoming and outgoing quark. Any particles with non–zero transverse momenta can only be produced by strong interactions.

Changing to the PHP regime, the beauty quark measurements of semi-leptonic beauty quark decays from the ZEUS and H1 collaborations use the p_T^{rel} and impact parameter methods in dijet plus muon events.

The H1 collaboration used both the p_T^{rel} method [40] and the impact parameter method [41] (see Fig. 3.8) for a cross section measurement.

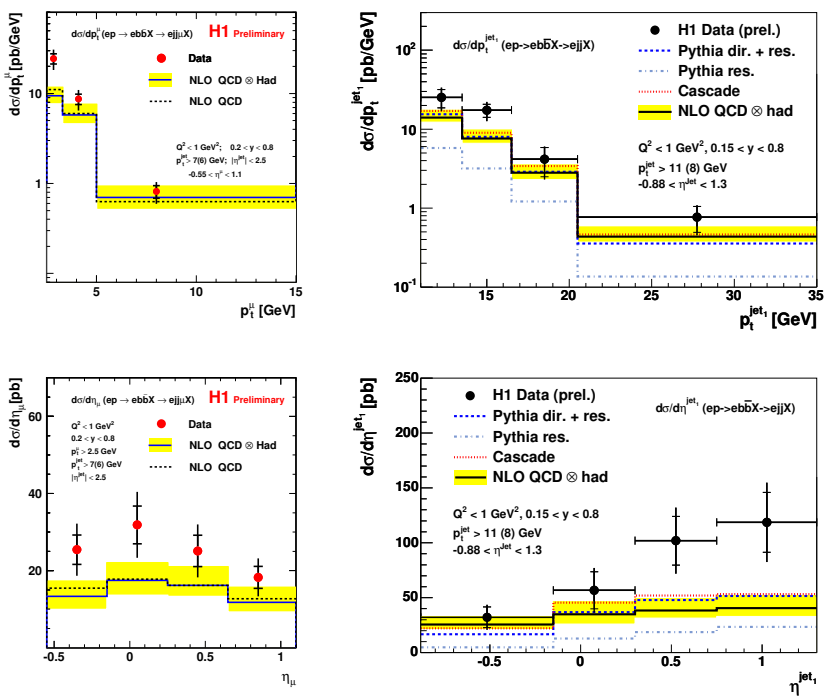

Figure 3.8: Differential beauty quark jet cross sections in PHP *ep* collisions by H1. *Left:* Measurements of beauty quark cross sections differential in p_T^{μ} and η^{μ} using the p_T^{rel} method. *Right:* Measurement of beauty quark cross sections differential in $p_T^{jet_1}$ and $\eta_T^{jet_1}$ using the impact parameter method. All cross sections are compared to NLO QCD predictions from FMNR [17].

Although the errors are large, the measurements are above the NLO QCD predictions from FMNR. The excess appears to decrease towards larger values of p_T^{μ} using the p_T^{rel} method and is mostly attributed to the region at positive η^{jet} using the impact parameter method.
The excess of the measurement over the FMNR [17] NLO QCD prediction is also visible in the corresponding cross sections differential in x_{γ}^{obs} (see Fig. 3.9). Here, the excess increases for lower x_{γ}^{obs}.

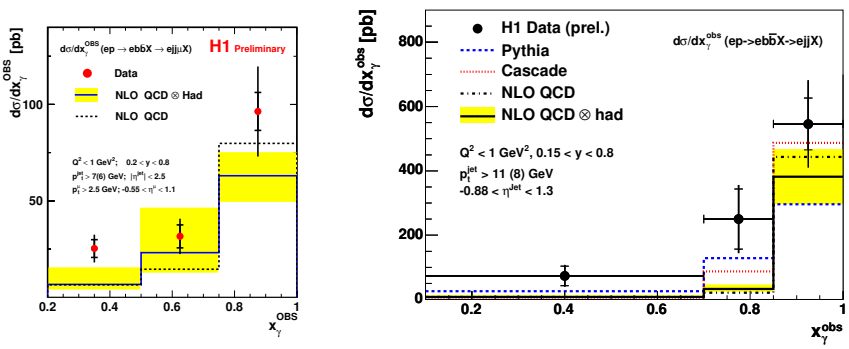

Figure 3.9: Differential beauty quark cross sections in x_{γ}^{obs} in PHP *ep* collisions by H1 using the p_T^{rel} method (*left*) and the impact parameter method (*right*). Both cross sections are compared to NLO QCD predictions from FMNR.

The ZEUS collaboration provides beauty quark measurements in the photoproduction regime in dijet plus muon events [42]. The differential cross sections in the muon transverse momentum and pseudo-rapidity (Fig. 3.10) are described by NLO QCD predictions from FMNR.

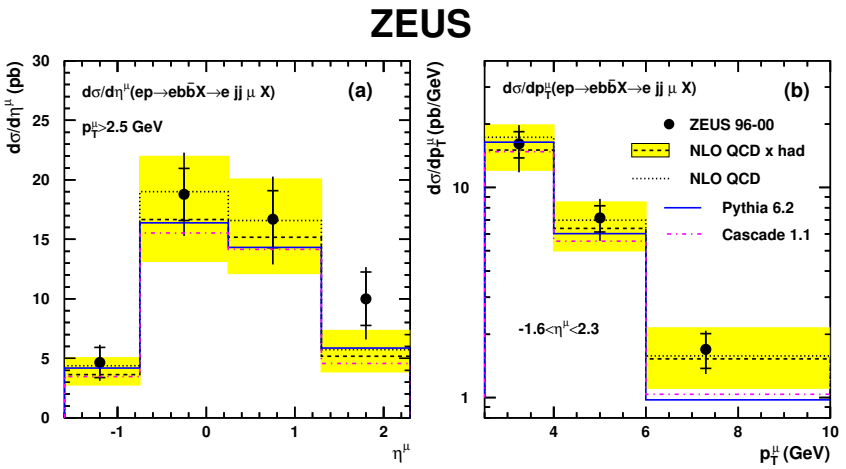

Figure 3.10: Differential beauty quark cross sections in PHP ep collisions by ZEUS as a function of p_T^μ *(a)* and η^μ *(b)* for $p_T^\mu > 2.5$ GeV and $-1.6 < \eta^\mu < 2.3$ using the p_T^{rel} method in ep events with at least two jets with $p_T^{jet_{1(2)}} > 7(6)$ GeV and $|\eta^{jet_{1(2)}}| < 2.5$ and requiring $0.2 < y < 0.8$ and $Q^2 < 1$ GeV^2. The cross sections are compared to NLO QCD predictions from FMNR.

The same behaviour can be seen in the beauty quark cross sections in muon regions (see Eq. 3.1) and differential in x_γ^{jets} (see Fig. 3.11).

$$\begin{array}{rl} rear & -1.6 < \eta^\mu < -0.9,\ p^\mu > 2.5 \text{ GeV}; \\ barrel & -0.9 < \eta^\mu < 1.3,\quad p_T^\mu > 2.5 \text{ GeV}; \\ forward & 1.48 < \eta^\mu < 2.3,\quad p^\mu > 4 \text{ GeV}, p_T^\mu > 1 \text{ GeV}; \end{array} \tag{3.1}$$

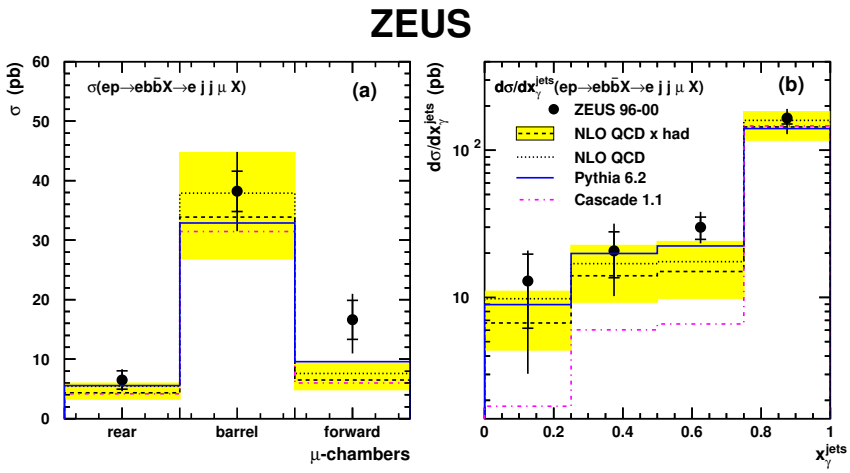

Figure 3.11: Beauty quark cross sections in muon regions (see Eq. 3.1) (*left*) and differential in x_γ^{jets} (*right*) in PHP ep collisions by ZEUS using the p_T^{rel} method in ep events with at least two jets with $p_T^{jet_{1(2)}} > 7(6)$ GeV and $|\eta^{jet_{1(2)}}| < 2.5$ and requiring $0.2 < y < 0.8$ and $Q^2 < 1$ GeV^2. Both cross sections are compared to NLO QCD predictions from FMNR.

In the context of beauty quark production measurements at fixed target experiments and in $p\bar{p}$ collisions,

the measurement of the cross section differential in the transverse momentum of the beauty quark shows a good description (see Fig. 3.12) by NLO QCD predictions from FMNR.

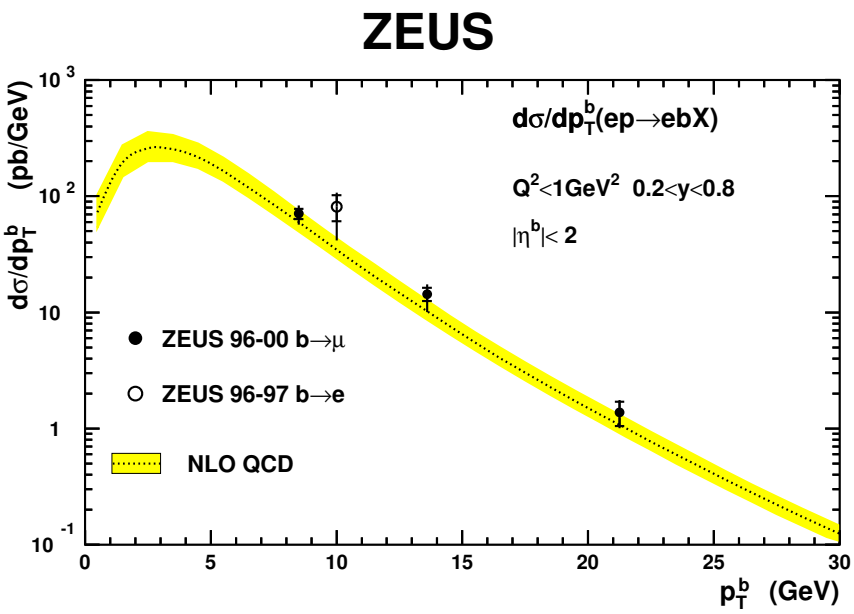

Figure 3.12: Differential beauty quark production cross section in ep collisions by ZEUS. The cross section differential in p_T^b is compared to NLO QCD predictions from FMNR.

Summarising the presented beauty quark cross section measurements, ep collisions provide an excellent testing ground and the results from the H1 and ZEUS collaborations show general agreement with NLO QCD predictions although some deviation of the predictions from the measurements can be seen.

The measurements in the DIS regime show this general agreement although for the ZEUS results the prediction is constantly below the measurement. This discrepancy increases for higher $E_{T,jet}^{Breit}$.

In the PHP regime, the general agreement in the ZEUS measurements could not be confirmed by H1. Here, the p_T^{rel} method resulted in discrepancies increasing for lower p_T^{μ} whereas the impact parameter method showed discrepancies attributed to the forward η_{jet} region. Also the description of the x_γ cross sections is below the H1 measurements for both methods whereas it is consistent for the ZEUS results.

The measurements presented in this thesis will contribute to the solution of the discrepancies in the photoproduction regime.

Chapter 4

Global Comparison of Beauty Quark Production with JetWeb

The *Standard Model* has to be simultaneously consistent with all available experimental facts to describe the microscopic structure of matter in all its manifestations. If one measurement is reproducibly not compatible with the *Standard Model* , the theory would have to be changed.
In practice, the verification of the consistency of a measurement with the *Standard Model* is complicated. As QCD makes predictions on the parton level but the observable particles are stable hadrons, an extrapolation between the two levels has to be performed for the comparison. This extrapolation, also called hadronisation/fragmentation, contains significant non-perturbatively calculable contributions which have to be modeled according to phenomenological approaches. A proper handling of these extrapolations is required for a reliable comparison between theory and experiment and also for the simultaneously consistency of different experiments with QCD.
A different way of comparing high energy particle measurements in the form of cross section measurements by the explicit and consistent usage of Monte Carlo simulations is described in the following. The comparison framework using the *HZTOOL* [43] package and the *JetWeb* [44] facility is introduced and the implementation and subsequent comparison of beauty quark measurements from UA1, D0 and ZEUS is presented.
With this comparison, the question can be answered if it is possible to describe all measurements with a single MC simulation used with the same set of parameters although some of the measurements are claimed to agree and others are claimed to disagree with theory predictions.

4.1 JetWeb and HZTOOL - a Monte Carlo Comparison Facility

The optimal Monte Carlo simulation would be the usage of NLO calculations interfaced to a hadronisation/fragmentation approach. Such a solution exists in the form of *MC@NLO* for $p\bar{p}$ collisions [36] but is currently not available for other colliders like for ep collisions. Therefore, the approach presented here to universally compare measurements from different experiments at different accelerators is based on leading order Monte Carlo simulations plus parton showers implemented in the PYTHIA MC generator (see Sec. 2.4.1).
The used *HZTOOL* package [43] consists of a general interface to Monte Carlo generators like PYTHIA and is described in the following.
HZTOOL can be used to simulate the hadronic final state on an event–by–event basis. It contains a large variety of parameters which can be used for tuning. It also provides the possibility to simulate final states from ep, ee and $p\bar{p}$ collisions with the same parameter set and therefore on the same basis of implementation of the *Standard Model*.
Each measurement, in form of differential cross sections in hadronic final state properties like particle momenta or jet quantities, has to be implemented individually into the HZTOOL package.
HZTOOL consists of three stages which take care of the initialisation of the MC generator and the implemented measurements, the generation of events and the finalization stage.

Initialisation:

- The MC generator is initialised with the selected collision mode (types of colliding particles and their energies) and the parameter configuration.
- The number of events which have to be generated in the second stage has to be determined. A coarse estimation of the cross sections of the processes corresponding to the initialised MC generator is the basis for the calculation of this number using the selected luminosity to be generated according to:

$$N = \mathcal{L}\sigma \tag{4.1}$$

- All histograms of the implemented differential cross sections are initialised.

Execution per generated event:

- The kinematic cuts of the different implemented cross sections are applied consecutively to the same generated event and the differential cross section histograms are filled with an entry per event if the event fulfilled the cuts.

Finalisation:

- All cross section histograms which up to now contain number of events fulfilling the respective kinematic cuts are transformed to cross sections using the luminosity corresponding to the number of generated events.

The *JetWeb* database [44] represents the superstructure of HZTOOL and stores the results for the individual cross section measurements in a database (details can be found in appendix A).

JetWeb also takes care of the absolute normalisation of the generated cross sections. Monte Carlo generators based on leading order calculations plus parton shower approaches can predict accurately the shapes of the kinematic distributions of the final state. Their absolute normalisation is not accurately calculated and has to be scaled to measurements.
JetWeb uses differential dijet photoproduction cross sections measured by the H1 [45] and ZEUS [46] collaborations to perform a χ^2 fit of the Monte Carlo simulation to these measurements to determine an overall normalisation factor.

As an example, two cross sections of the range of used differential dijet photoproduction cross sections and the outcome of the fit are shown in Fig. 4.1. The determined normalisation factor, called the *JetWeb-scale*, is 1.45 for the PYTHIA MC generator. This scale is then fixed for all subsequent cross section predictions.

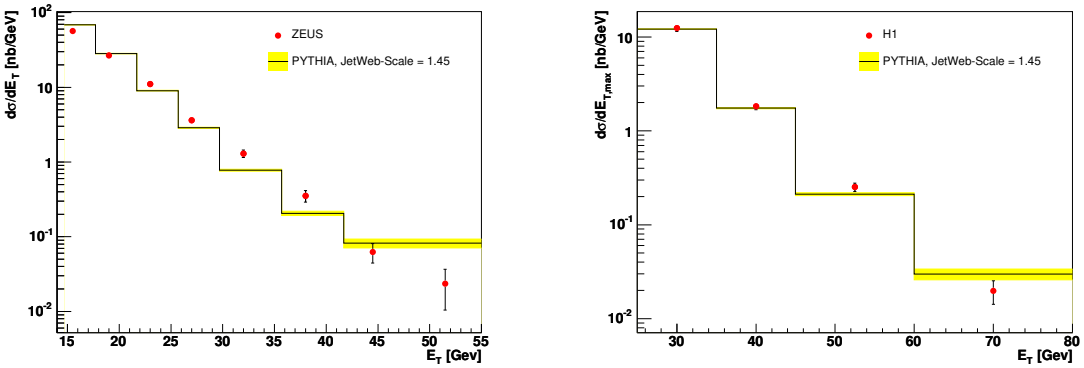

Figure 4.1: Two of the range of cross sections used for the JetWeb-scale determination: *Left:* dijet photoproduction cross sections differential in the transverse energy of the highest-E_T jet by the ZEUS collaboration [46] for $Q^2 < 1$ GeV^2, 134 GeV $< W_{\gamma p} <$ 277 GeV, $E_T^{jet_1} > 14$ GeV, $1 < \eta^{jet_1} < 2.4$, $E_T^{jet_2} > 11$ GeV, $0 < \eta^{jet_2} < 1$, $x_\gamma^{jets} < 0.75$. *Right:* dijet photoproduction cross section differential in the transverse energy of the highest-E_T jet by the H1 collaboration [45] for $p_T^{jet_1} > 25$ GeV, $0.05 < x < 0.6$, $0.1 < x_\gamma < 1$. Both cross sections are compared to the MC prediction by PYTHIA scaled by the JetWeb-scale of 1.45 determined by a χ^2 fit.

4.2 Comparison of Beauty Quark Cross Sections from UA1, D0 and ZEUS

The *JetWeb* facility is used to compare beauty quark results from UA1, D0 and ZEUS in a global comparison approach. The emphasis is placed on semi-leptonic beauty quark decays into muons related to this thesis.
A summary of the implemented cross sections is given in Tab. 4.1.

description	**variable**	**UA1**	**D0**	**ZEUS**
inclusive single beauty quark cross sections	$p_T^b > p_T^{min}$	$\sigma(p\bar{p} \to b\ X)$	$\sigma(p\bar{p} \to b\ X)$	
beauty angular correlation cross sections	$\Delta\phi_{b\bar{b}}$	$\sigma(p\bar{p} \to b\bar{b} \to X)$		
beauty angular correlation cross sections	$\Delta R_{b\bar{b}}$	$\sigma(p\bar{p} \to b\bar{b} \to X)$		
single muon dijet cross sections	μ-region (see eq. 3.1)			$\sigma(ep \to b\bar{b} \to e\ jj\ \mu\ X)$
	x_γ			$d\sigma/dx_\gamma(ep \to b\bar{b} \to e\ jj\ X)$
	η_μ			$d\sigma/d\eta^\mu(ep \to b\bar{b} \to e\ jj\ \mu\ X)$
	p_T^μ			$d\sigma/dp_T^\mu(ep \to b\bar{b} \to e\ jj\ \mu\ X)$
	$\eta^{j\mu}$			$d\sigma/d\eta^{j\mu}(ep \to b\bar{b} \to e\ jj_\mu\ X)$
	$p_T^{j\mu}$			$d\sigma/dp_T^{j\mu}(ep \to b\bar{b} \to e\ jj_\mu\ X)$
dijet beauty quark cross sections	η^{jb}			$d\sigma/d\eta^{jb}(ep \to b\bar{b} \to e\ jj_b\ X)$

Table 4.1: Summary of implemented beauty quark cross in HZTOOL for a global comparison. Shown are the implemented beauty quark cross sections by the UA1 collaboration [27], the D0 collaboration [31] and the ZEUS collaboration [42].

The cross sections have been chosen to give a reasonable summary of beauty quark measurements at $p\bar{p}$ and ep colliders with regard to this thesis. The results of UA1 [27] (see Sec. 3.3) have been chosen due to their confirmation of the importance of higher order contributions to the QCD calculation whereas the chosen results of D0 [31] (see Sec. 3.4) concluded in a normalization discrepancy of the NLO QCD calculation and the measurement. The ZEUS results [42] (see Sec. 3.5) have been chosen because they represent previous results with the same final state signature as the measurements of this thesis.

The used PYTHIA MC generator Version 6.2 [11] (see Sec. 2.4.1) provides a large variety of input parameters for MC tuning. For this comparison, the default parameter set which is supposed to reproduce most of the *Standard Model* physics is used. The proton and photon PDF's and the minimal transverse momentum of the hard subprocess are chosen according to following definitions:

Proton PDF: CTEQ5L

Photon PDF: GRV LO

min. transverse momentum: 3 GeV

The χ^2 fit to HERA jet data yields a JetWeb-scale of 1.45 applied as a global normalisation to all generated cross sections (exemplary jet cross sections used in the fit are shown in Fig. 4.1).

Beginning with the comparison of the ZEUS results to the generated cross sections by PYTHIA, the beauty quark cross sections from muon plus dijet events differential in the transverse momentum and the pseudo-rapidity of the muon are well reproduced by the Monte Carlo (see Fig. 4.2). The used JetWeb-scale determined from HERA jet cross sections shows the simultaneous compatibility with inclusive jet cross sections in ep collisions.

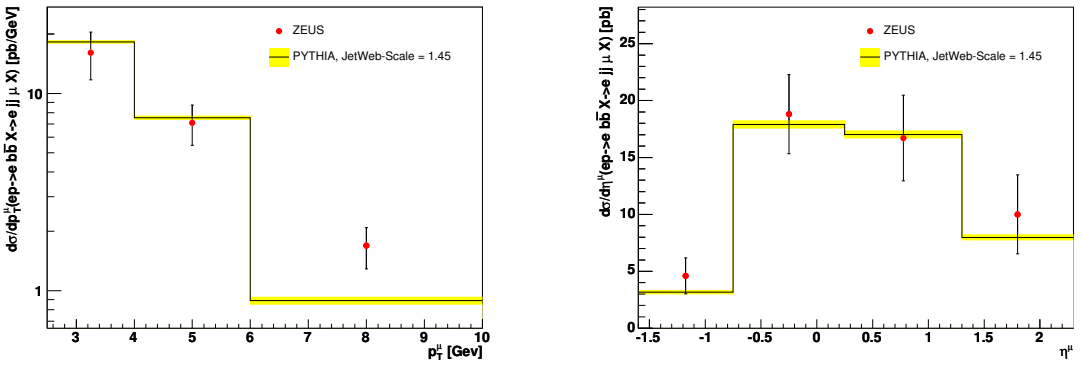

Figure 4.2: The beauty quark cross sections from ZEUS differential in the muon transverse momentum p_T^μ (*left*) and η^μ (*right*) compared to the PYTHIA MC prediction using the JetWeb-scale of 1.45. The statistical error of the MC cross section is shown as a yellow band.

The same behaviour can be seen in the differential jet cross sections. The measured cross sections differential in transverse momentum and pseudo-rapidity of the jet containing the muon (see *top* in Fig. 4.3) and containing the beauty quark (see *bottom* in Fig. 4.3) are well described by the PYTHIA MC.

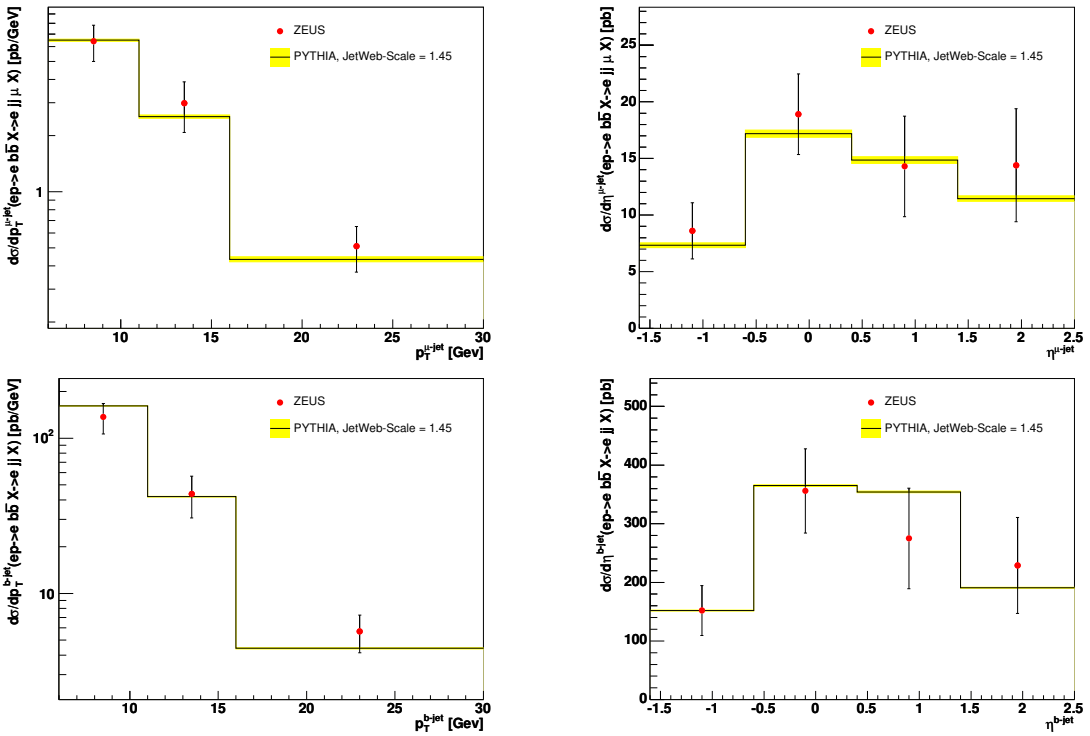

Figure 4.3: The beauty quark cross sections from ZEUS differential in $p_T^{\mu-jet}$ (*top left*), $\eta^{\mu-jet}$ (*top right*), p_T^{b-jet}(*bottom left*) and η^{b-jet} (*bottom right*) compared to the PYTHIA MC prediction using the JetWeb-scale of 1.45. The statistical error of the MC cross section is shown as a yellow band.

All differential cross sections measured in ep photoproduction collisions in dijet plus muon events are compatible with the scaled PYTHIA MC predictions. This is also shown by the good description of the cross section as a function of the muon region given by Eq. 3.1 and differential in x_γ (see Fig. 4.4).

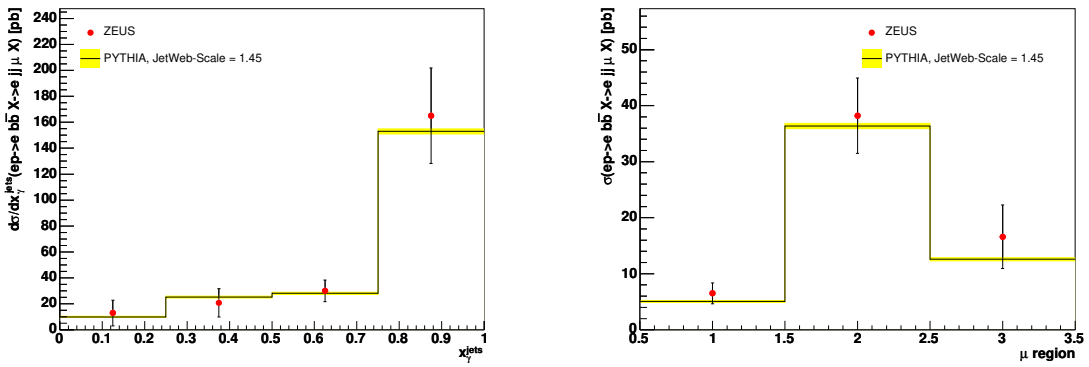

Figure 4.4: The beauty quark cross sections from ZEUS differential in x_γ (*left*) and muon region (see Eq. 3.1) (*right*) compared to the PYTHIA MC prediction using the JetWeb-scale of 1.45. The statistical error of the MC cross section is shown as a yellow band.

In the same context, the cross sections as a function of the transverse momentum of the b quark by the UA1 and D0 collaborations (see Fig. 4.5) are described as well by the PYTHIA Monte Carlo using the determined JetWeb-scale of 1.45. This shows the compatibility of ep and $p\bar{p}$ collision measurements of beauty quarks although the D0 collaboration concluded that the normalisation of the data is not described by NLO QCD predictions.

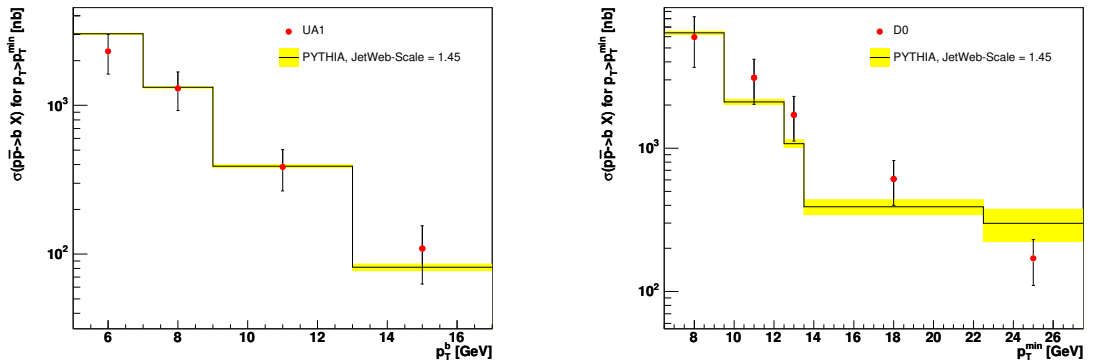

Figure 4.5: The beauty quark cross sections as a function of the beauty quark transverse momentum p_T^b of the UA1 (*left*) and D0 (*right*) collaboration for $p_T^b < p_T^{min}$ compared to the PYTHIA MC prediction using the JetWeb-scale of 1.45. The statistical error of the MC cross section is shown as a yellow band.

Investigations of beauty quark correlations by the UA1 collaboration (see Fig. 4.6) complete the picture of the universal description of ep and $p\bar{p}$ cross sections by the PYTHIA Monte Carlo. For transverse momenta of the beauty quark $p_T^b > 11$ GeV, the correlation cross sections in $\Delta R_{b\bar{b}}$ and $\Delta\phi_{b\bar{b}}$ are described by the PYTHIA Monte Carlo.

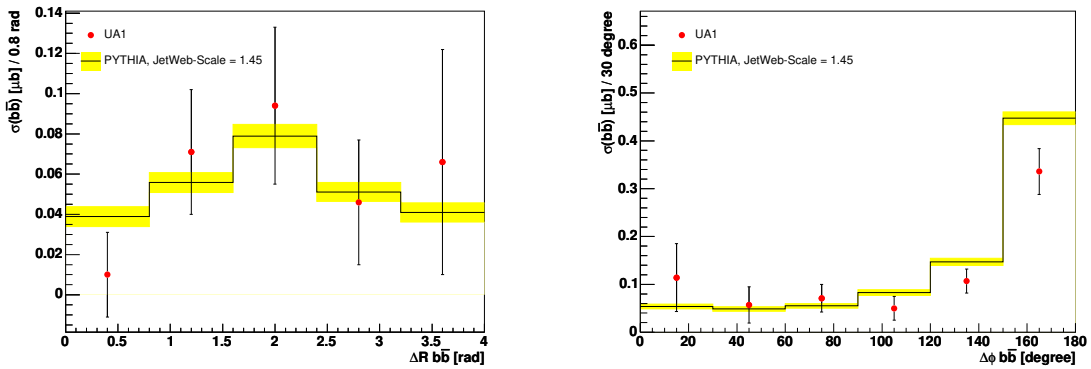

Figure 4.6: The beauty quark correlations cross sections differential in $\Delta R_{b\bar{b}}$ (*left*) and $\Delta\phi_{b\bar{b}}$ (*right*) of the UA1 collaboration for $p_T^b > 11$ GeV compared to PYTHIA MC predictions using the JetWeb-scale of 1.45. The statistical error of the MC cross section is shown as a yellow band.

Lowering the cut on the minimal transverse momentum of the highest-p_T beauty quark $p_T^b > 6$ GeV (see Fig. 4.7), the description of the cross sections differential in $\Delta R_{b\bar{b}}$ and $\Delta\phi_{b\bar{b}}$ by the PYTHIA Monte Carlo is worse. For all these comparisons, the PYTHIA MC uses the massless approach to calculate the cross section which could partially explain this discrepancy, since the second beauty quark can have relatively low p_T, a configuration for which the massless approach is not valid.

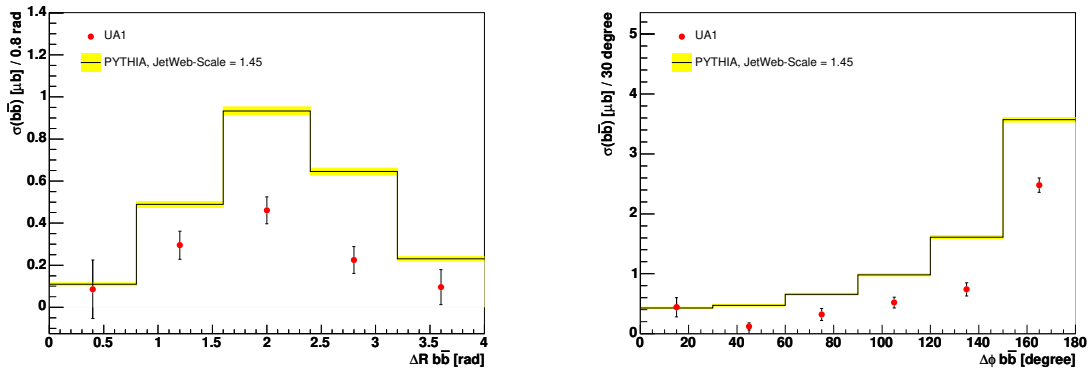

Figure 4.7: The beauty quark correlations cross sections differential in $\Delta R_{b\bar{b}}$ (*left*) and $\Delta\phi_{b\bar{b}}$ (*right*) of the UA1 collaboration for $p_T^b > 6$ GeV compared to the PYTHIA MC predictions using the JetWeb-scale of 1.45. The statistical error of the MC cross section is shown as a yellow band.

The presented comparison of beauty quark cross sections using the JetWeb facility shows a consistent and simultaneous description of the cross sections from ep and $p\bar{p}$ collisions with a single PYTHIA Monte Carlo generator. It is shown that, although the D0 collaboration reported the excess of their beauty quark cross section measurement over NLO QCD predictions, almost all cross sections are described by the PYTHIA Monte Carlo using the JetWeb-scale of 1.45 determined by a fit to differential jet cross sections.

In the future, this comparison can be extended to include more beauty quark cross section measurements also from the CDF collaboration. This would give a complete picture of the universality of beauty quark measurements in the *Standard Model* using the JetWeb facility.

Chapter 5

The ZEUS Detector at HERA

This chapter gives a brief introduction to the HERA collider and the ZEUS experiment. Detector components relevant for this analysis are described in more detail.

5.1 The HERA Collider

HERA (Hadron Electron Ring Anlage) [47] is the only high energy elementary particle accelerator in the world which collides electrons or positrons and protons. The HERA tunnel of 6.3 km circumference $15 - 30$ m below ground is situated at the *Deutsches Elektronen SYnchrotron* (DESY) in Hamburg, Germany, (Fig. 5.1) and contains two separate rings to store protons at a maximal energy of 920 GeV and electrons or positrons at a maximal energy of 27.5 GeV.

Figure 5.1: Airplane view of the DESY laboratory. The HERA collider and the pre-accelerator PETRA are marked by dashed lines.

Leptons are accelerated by normal and superconducting cavities to compensate for the energy loss due to synchrotron radiation. The acceleration system for protons is composed of normal conducting cavities only. The situation is reversed for the bending magnets in the arcs. Here, superconducting magnets providing a magnetic field of 5 T are used for deflecting the protons whereas normal conducting magnets of a field strength of 0.3 T bend the leptons [48]. The two particle beams are brought into collision at zero crossing angle at two interaction regions in the north and south experimental areas where the collider experiments H1 and ZEUS are located (Fig. 5.2). In addition, two areas in the east and west are equipped with experiments using only one of the two beams. In the east, the HERMES experiment uses

HERA design parameters

Running period	1993 - 1997		1998 - 2000		2003 - 2004	
Luminosity	$1.6 \cdot 10^{31}$ cm^{-1}s^{-1}		$1.6 \cdot 10^{31}$ cm^{-1}s^{-1}		$7.0 \cdot 10^{31}$ cm^{-1}s^{-1}	
Center-of-mass energy (actual)	300 GeV		318 GeV		318 GeV	
	Lepton	Proton	Lepton	Proton	Lepton	Proton
Energy (actual)	27.5 GeV	820 GeV	27.5 GeV	920 GeV	27.5 GeV	920 GeV
Max. number of bunches	210	210	210	210	180	180
Beam current	58	163	58	163	58	140
Particles per bunch	$3.65 \cdot 10^{10}$	10^{11}	$3.65 \cdot 10^{10}$	10^{11}	$4.18 \cdot 10^{10}$	10^{11}
Beam width (σ_x)	0.286 mm	0.280 mm	0.286 mm	0.280 mm	0.118 mm	0.118 mm
Beam height(σ_y)	0.060 mm	0.058 mm	0.060 mm	0.058 mm	0.032 mm	0.032 mm

Table 5.1: HERA design parameters [47, 51].

the lepton beam (which is longitudinally polarized in this area) to study the spin structure of the nucleon with an internal polarized gas target. The west area was used until 2003 by the HERA-B experiment. It was designed to measure $\mathcal{CP}$ violation in the $B^0\bar{B}^0$ system produced in collisions of the proton beam halo with a wire target.

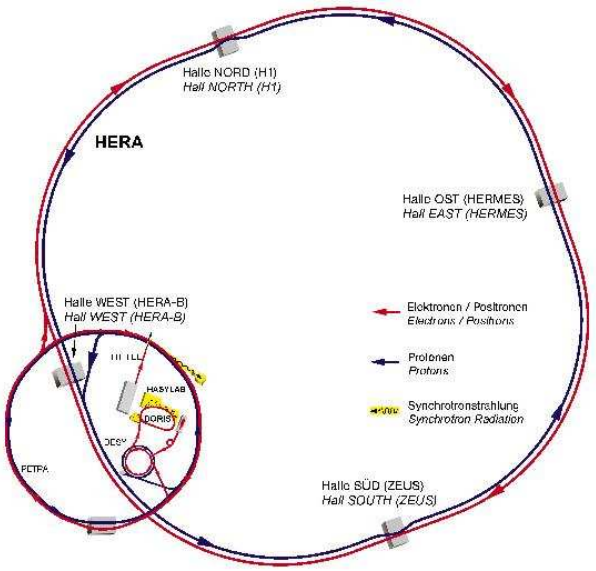

Figure 5.2: Schematic view of the HERA accelerator complex.

Built between 1984 and 1990, the HERA collider started operation in 1992 in the initial configuration with 820 GeV protons and 27.5 GeV positrons. From 1993 to 1997, HERA delivered a total luminosity of 73.09 pb^{-1} (Fig. 5.3). In 1998, the maximal proton energy was increased to 920 GeV and positrons were replaced with electrons. After that, HERA delivered a total luminosity of 25.2 pb^{-1} in electron–proton collisions till 1999. After the switch back to positron–proton collisions in 1999, the total delivered luminosity till 2000 was 94.95 pb^{-1}.

During the shutdown 2000/2001, the HERA collider was upgraded to achieve a five times higher specific luminosity in the collision points [49]. In addition, spin rotators have been included to rotate the spin of the leptons. The lepton beam is longitudinally polarized at all interaction regions. To solve severe background problems, a further longer shutdown was necessary in the middle of 2003 [50]. Since October 2003, HERA provided stable beam operations and delivered a total luminosity of 84.47 pb^{-1} .

A summary of HERA design parameters during the mentioned running periods 1993-1997 and 1998-2000 [47] and 2003-2004 [51] can be found in table 5.1.

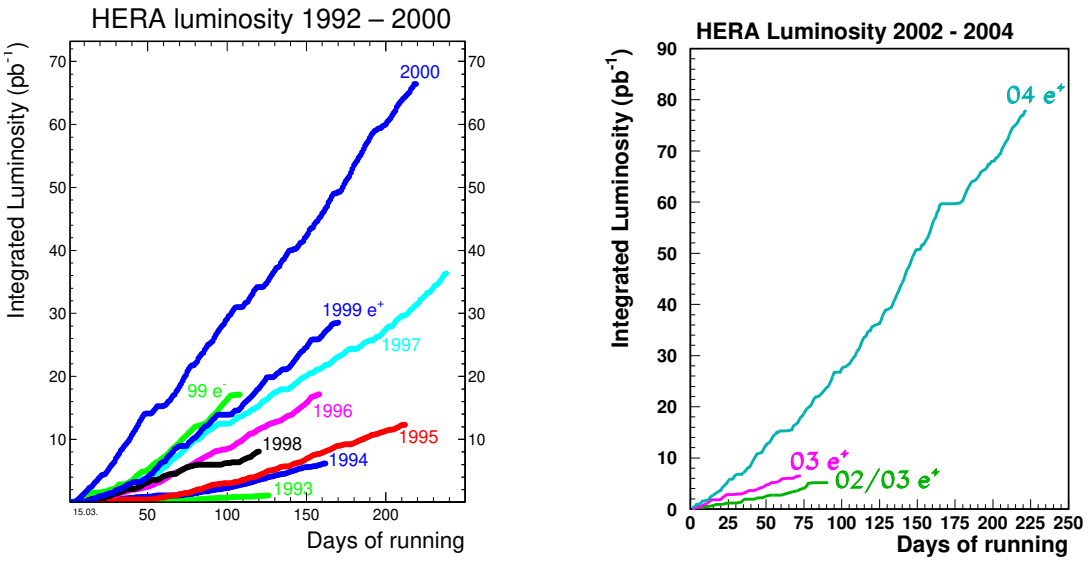

Figure 5.3: Integrated luminosity delivered by HERA for the running periods 1993-2000 (left) and 2003-2004 (right).

5.2 The ZEUS Detector

The ZEUS[1] detector [53] is a general purpose detector designed to study various aspects of lepton–proton scattering at HERA. It is a quasi hermetic detector since it covers most of the 4π solid angle with the exception of small regions around the beam pipe. Most of the final state particles are boosted to the forward direction because of the large momentum imbalance between the lepton and the proton beam. The layout of the detector was dictated by the topology of the processes to be studied at HERA. The detector can measure energies from few tens of MeV to hundreds of GeV in the forward region. For low momentum particles the tracking in the magnetic field is very precise (resolution: $\sigma(p_T)/p_T \sim p_T$), while high energy particles are well measured by the calorimetric system (resolution: $\sigma(E)/E \sim \sqrt{E}/E$). The ZEUS coordinate system is shown in Fig. 5.4. It is a right-handed, orthogonal system with the origin at the nominal interaction point (IP), the z axis pointing in the proton direction (also referred to as the *forward* direction), the x axis pointing toward the center of HERA and the y axis pointing upward. The polar angle θ and the azimuth angle ϕ are measured relative to the z and x axes respectively.

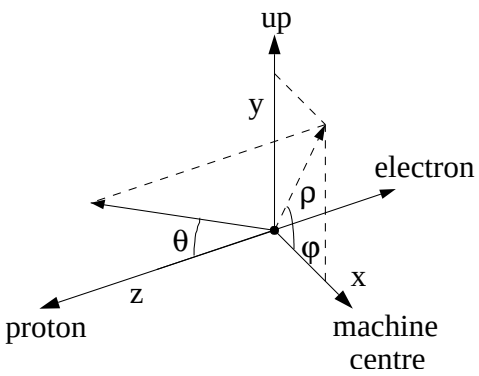

Figure 5.4: The ZEUS coordinate system.

The ZEUS sub-detectors are arranged coaxially but asymmetrically around the interaction point to accommodate the boost of the centre–of–mass system in the proton beam direction with respect to the

[1]The acronym ZEUS is derived from ancient greek: ΖΕΥΣ: Ζήτησις καθ' Εύρετής Ὑποκειμένης Συμμετρίας = Search to Elucidate Underlying Symmetry [52].

laboratory frame due to the large energy asymmetrie between the lepton and the proton beams. A cross section of the detector layout along the beam axis is shown in Fig. 5.5. The main detector is approximately 20 m long, 12 m wide and 11 m high and weighs around 3600 t.

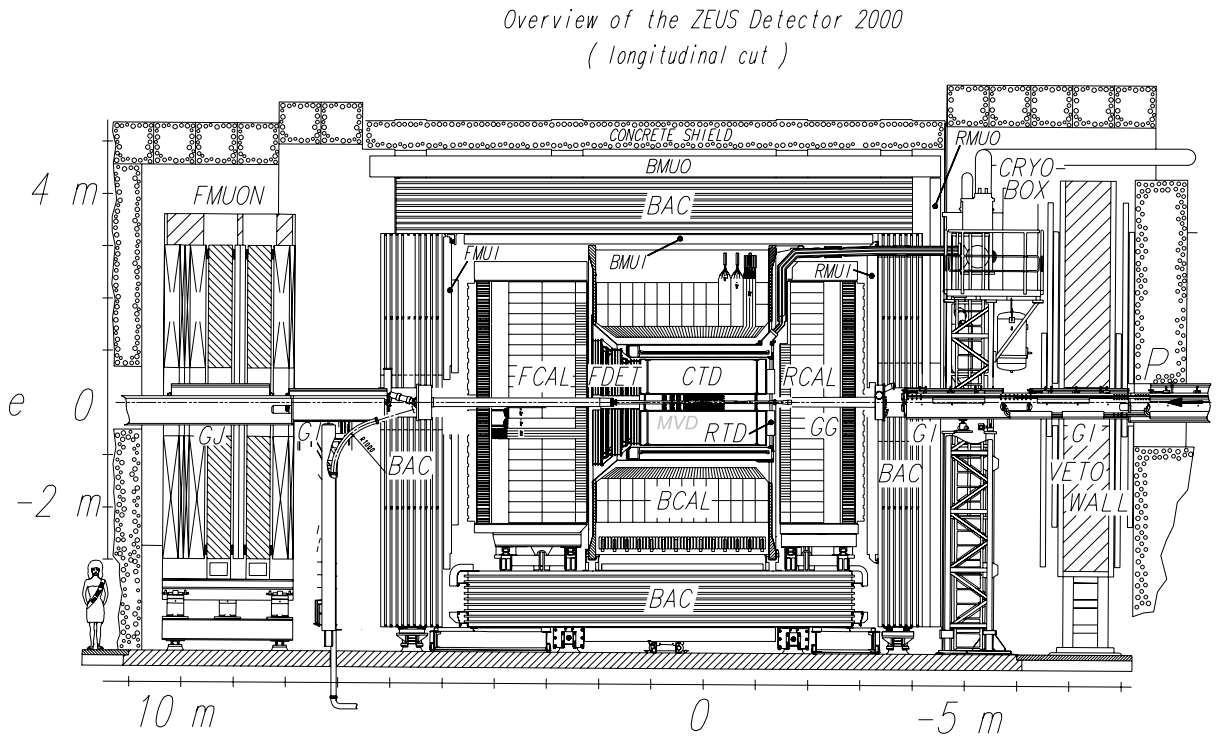

Figure 5.5: Cross section of the ZEUS detector along the beam axis after the upgrade in the year 2000/2001.

A short description of the main components of the detector is given in the following. The detector was commissioned and continuously upgraded during the years of data taking incorporating the technical understanding gained during previous running periods and taking into account the needs of the physics to be investigated. In the initial configuration, the innermost detector was the Vertex Detector (VXD) which was removed during the 1995-96 shutdown. In 2001, a silicon–strip micro vertex detector (MVD, see 5.2.2) was installed at the same place. During 1996-2000 data-taking the detector closest to the interaction point was the central tracking detector (CTD, see 5.2.1) which is a cylindrical drift chamber. It is enclosed by a superconducting solenoid providing a magnetic field of 1.43 T for the determination of charge and momentum of charged particles. The CTD is supplemented in the forward direction by three sets of planar drift chambers (FTD) with interleaved Transition Radiation Detectors (TRD) (labeled FDET in Fig. 5.5). The TRD system was replaced in 2001 by a Straw Tube Tracker (STT) consisting of two modules build of straw tube layers filling the gaps between the three FTD chambers. The commissioning of the STT is currently under way. The rear direction is supplemented by one planar drift chamber consisting of three layers (RTD).

The tracking system is surrounded by a compensating high resolution uranium–scintillator calorimeter (CAL, see 5.2.3) which is used as the main device for energy measurements. It is divided into forward, barrel and rear sections (respectively FCAL, BCAL and RCAL) with different thickness. The calorimeter is enclosed by an iron yoke that provides the return path for the solenoidal magnetic field flux, and serves as absorber for the backing calorimeter (BAC, see 5.2.5), which measures energy that escapes detection from the main calorimeter and acts as a tracking calorimeter for muon detection. Dedicated muon identification detectors (see 5.2.4) are located inside (FMUI, BMUI and RMUI) and outside (FMUO, BMUO and RMUO) the iron yoke.

Other detectors are located several meters away from the main detector along the beam pipe. The VETO wall is located in the rear direction at about $z = -7.5$ m from the interaction point. It consists of an iron wall supporting scintillator hodoscopes and is used to reject background from beam gas interactions. The LUMI detector (see 5.2.6) is made of a small lead–scintillator calorimeter at $z = -107$ m and detects photons from bremsstrahlung events for the luminosity measurement.

The luminosity recorded by the ZEUS detector in the running periods 1994-2000 and 2003-2004 which can be used for analysis purposes is shown in Fig. 5.6.

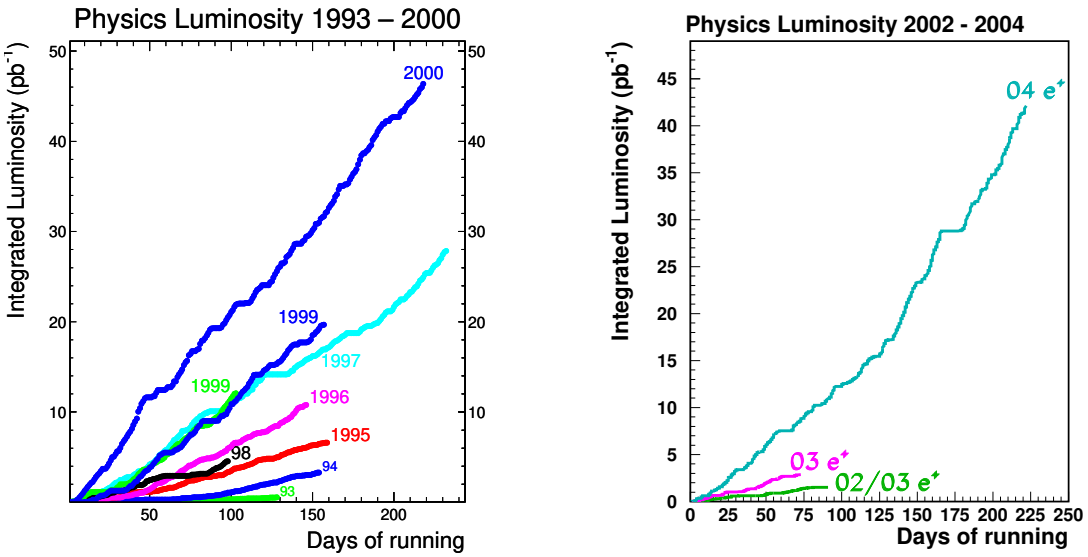

Figure 5.6: Integrated luminosity recorded by ZEUS for the running periods 1993-2000 (left) and 2003-2004 (right).

For the running period 1994-2000, the ratio of useful to delivered luminosity is $\sim 70\%$. Due to technical problems, this ratio is reduced for the running period 2003-2004 to $\sim 50\%$.

5.2.1 The Central Tracking Detector

The central tracking detector (CTD) [54] is a cylindrical wire drift chamber used to measure the direction and momentum of charged particles and to estimate the energy loss dE/dx of charged particles to provide information on particle identification. The inner radius of the chamber is 18.2 cm and the outer radius is 79.4 cm. Its active region covers the longitudinal interval from $z = -100$ cm to $z = 103$ cm resulting in a polar angle coverage of $15° < \theta < 164°$. The CTD is filled with a mixture of argon (Ar), carbon dioxide (CO_2) and ethane (C_2H_6) in the proportion 90:8:2. It consists of 72 radial layers divided into nine *superlayers* (SL) of eight sense wires respectively. A group of eight radial sense wires with associated field wires in one superlayer makes up a *cell*. The sense wires are 30 μm thick while the field wires have different diameters. A total of 4608 sense wires and 19584 field wires is contained in the CTD. The CTD is designed to operate in a magnetic field to improve the momentum measurement of charged particles. The Lorentz angle of the magnetic field is 45° measured relative to the radial direction. Therefore, the sense wires are tilted to compensate for the Lorentz angle. One octant of the CTD is shown in Fig. 5.7.
A charged particle crossing the CTD produces ionisation of the gas in the chamber. The electrons from the ionisation drift toward the sense wires (positive), whereas the positively charged ions drift toward the negative field wires. The drift velocity of the electrons is approximately constant and equal to 50μm/ns. An avalanche effect occurs close to the wire giving an amplification factor on the electrons of $\sim 10^4$ so that a measurable pulse is induced on the sense wires.
The superlayers are numbered so that number 1 is the innermost SL, whereas the outermost is number 9. Odd numbered SLs have wires parallel to the z direction (*axial superlayers*), while wires in even numbered SLs are at a small stereo angle of $\pm 5°$ (*stereo superlayers*) to achieve a better resolution in z. The achieved resolution is $\sim 100 - 120$ μm in the $r - \phi$ plane and ~ 1.4 mm in the z coordinate.
For trigger purposes, the three inner axial superlayers (SL1, SL3, SL5) are equipped with a system that determines the z positions using information on the arrival time of the particle (z–by–timing system). The resolution achieved on the z coordinate with this system is ~ 3 cm.
The resolution on the transverse momentum p_T [55] for tracks with $p_T > 150$ MeV fitted to the interaction vertex and passing at least three CTD superlayers is given by:

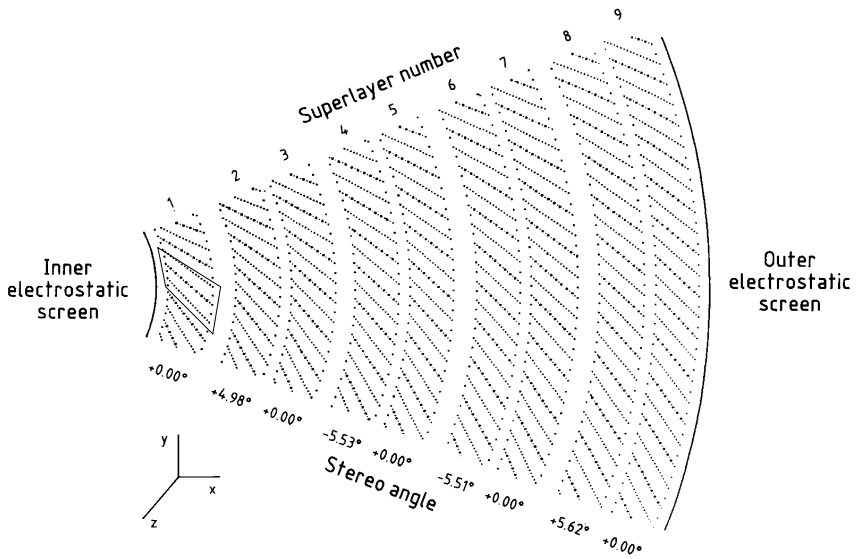

Figure 5.7: XY cross section of one octant of the CTD. The sense wires are indicated with dots.

$$\frac{\sigma(p_T)}{p_T} = 0.0058 \cdot p_T \oplus 0.0065 \oplus \frac{0.0014}{p_T} \tag{5.1}$$

where the symbol $\oplus$ indicates the quadratic sum. The first term is due to the hit position resolution, while the second and the third depend on the multiple scattering inside and before the volume of the chamber.
The situation for the resolution changed since the installation of the MVD in 2001. The influence of the new detector components on the resolution of the tracking system is still under investigation. It is expected that the influence from multiple scattering is larger (more material) but that the hit resolution is better compared to the above quoted resolution due to the inclusion of MVD hits [56]. Latest results integrating the MVD in the global track reconstruction parameterise the momentum resolution in a analogue way like the CTD–only resolution (see [57]):

$$\frac{\sigma(p_T)}{p_T} = 0.0026 \cdot p_T \oplus 0.0104 \oplus \frac{0.0019}{p_T} \tag{5.2}$$

(for further details see Sec. 7.1).

5.2.2 The Silicon–Strip Micro Vertex Detector

The silicon–strip micro vertex detector (MVD), installed in 2001 during the upgrade shutdown, is aimed at significantly improving tracking capabilities and increasing the acceptance for high-mass and high-Q^2 physics. It was constructed in particular to tag heavy flavour particles by their impact parameter with respect to the primary vertex and by secondary vertex reconstruction [58]. The physics requirements and the available space in the middle of the CTD lead to the following detector design characteristics:

- radial extension smaller than 32.4 cm (inner wall of the CTD);
- polar angular coverage between 10° and 150°;
- measurements of three points per track in two projections each;
- at least 20 μm hit resolution for normal incident tracks;
- two-tracks separation of 200 μm;
- hit efficiency better than 95%;
- noise occupancy better than 10^{-3}.

The resulting mechanical design of the MVD divides the detector into a *barrel region* (BMVD) and a *forward region* (FMVD) [59].
The barrel region length of 64 cm is constrained by the longitudinal interaction region distribution dominated by the proton bunch length (~ 20 cm). The BMVD consists of three double layers of silicon strip sensors arranged in concentric planes around the interaction point with a polar coverage between 30° and 150°. The inner layer of the BMVD is not complete due to the oval shaped beam pipe which is not centered around the interaction point (Fig. 5.8).

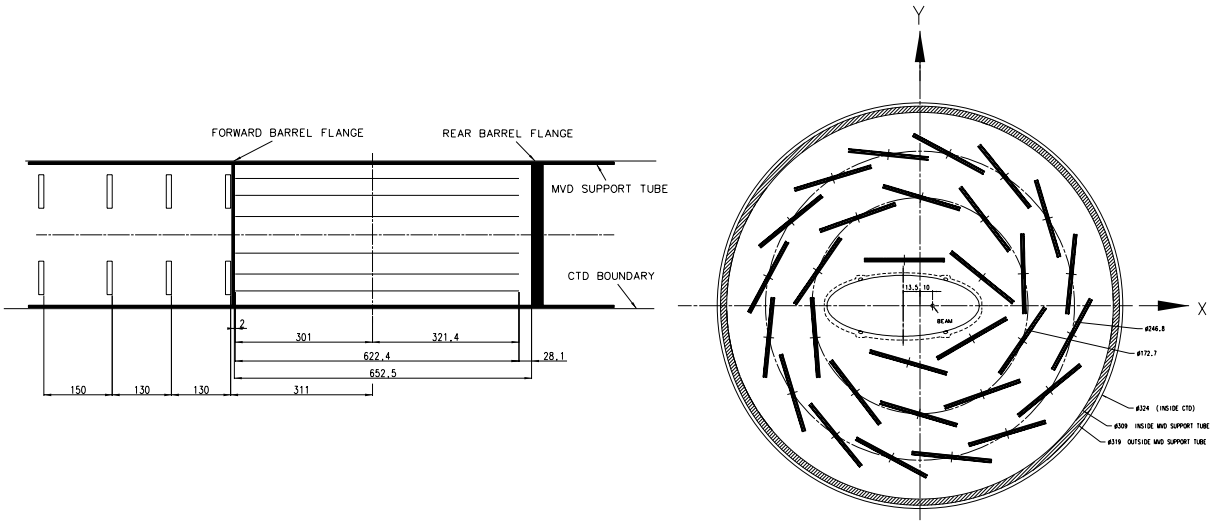

Figure 5.8: Schematic layout of the MVD along the beam direction (*left side*) and in the xy plane (*right side*) only showing the detector layers without support structures.

The BMVD single sided silicon sensors are square shaped (64.2×64.2 mm^2) and 320 μm thick. They are covered with 3082 strips with a pitch of 20 μm. Every sixth strip is read out resulting in 512 readout strips at a readout pitch of 120 μm. The position is determined through capacitive charge division between two readout strips. The single hit resolution determined in test beam measurements is 7.5 μm. Two sensors are glued together next to each other with perpendicular readout strips on the same side. They form a *half module* with 512 readout channels by connecting the readout strips of two neighbouring sensors. Two half modules are glued together back to back to form a module providing two coordinates for each particle traversing it. The ambiguity due to the connected sensors per half module is resolved at the reconstruction level.
The FMVD extends the coverage in pseudorapidity to $\eta = 2.6$ and provides additional forward tracking capabilities in a region which was not or only poorly covered before. It consists of four planes (wheels) perpendicular to the beam axis. Each wheel is made of two back to back layers of 14 wedge-shaped silicon sensors of the same type as in the barrel section. The number of readout strips per sensor is 480 for forward sensors tilted by 180°/14 to provide two coordinates for a particle traversing a wheel.

5.2.3 The Uranium–Scintillator Calorimeter

The ZEUS high resolution uranium–scintillator compensating calorimeter (CAL) [60] completely surrounds the tracking devices and the solenoid and covers 99.7% of the 4π solid angle. It consists of 3.3 mm thick depleted uranium plates (98.1% U^{238}, 1.7% Nb, 0.2% U^{235}) as absorber alternated with 2.6 mm thick organic scintillators (SCSN–38 polystyrene) as active material. The thickness of the absorber and of the active material have been chosen in order to have the same response for an electron or a hadron of the same energy ($e/h = 1.00 \pm 0.02$) passing through the detector (*compensation*). This allows a good resolution in the determination of both the electromagnetic and the hadronic energy. Under test beam conditions, the achieved electromagnetic resolution is

$$\frac{\sigma(E)}{E} = \frac{18\%}{\sqrt{E}} \oplus 2\%, \tag{5.3}$$

while the hadronic resolution is

$$\frac{\sigma(E)}{E} = \frac{35\%}{\sqrt{E}} \oplus 1\% \tag{5.4}$$

where E is the particle energy measured in GeV.
The CAL is divided into three regions: the forward (FCAL), barrel (BCAL) and rear (RCAL) calorimeter (see Figure 5.9).

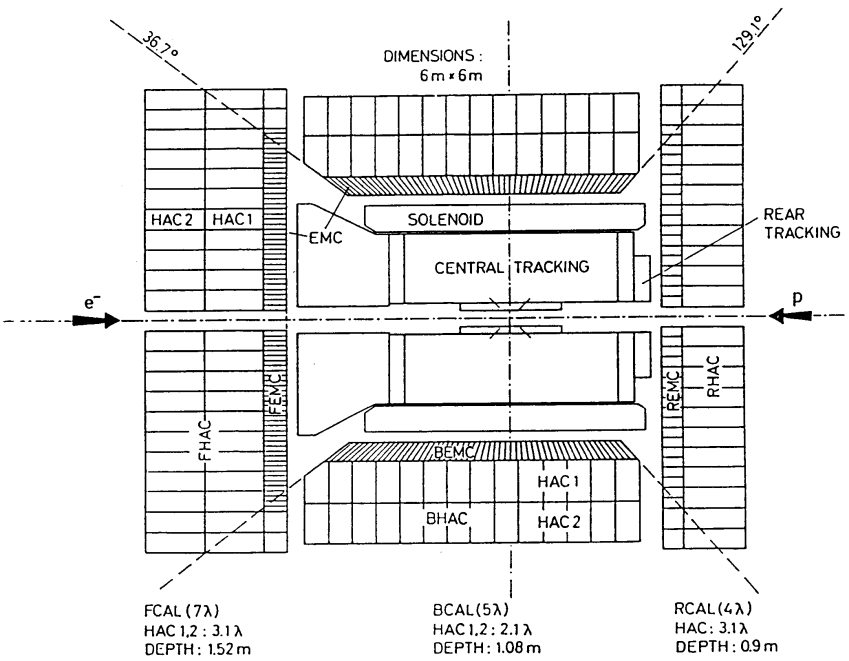

Figure 5.9: Schematic view of the CAL along the beam axis.

Since most of the final state particles in a lepton-proton interaction at HERA are boosted to the forward (proton) direction, the three parts are of different thickness, the thickest one being the FCAL ($\sim 7\ \lambda$), then the BCAL ($\sim 5\ \lambda$) and finally the RCAL ($\sim 4\ \lambda$), where λ is the interaction length.
Each region of the calorimeter is divided into *modules*. The 23 FCAL and 23 RCAL modules are rectangular, whereas the 32 BCAL modules which surround the cylindrical CTD are wedge-shaped covering 11.25^o in azimuth. An FCAL module is shown in Fig. 5.10.
Each module consists of so called *towers* of 20×20 cm which are subdivided longitudinally into one electromagnetic (EMC) and two (one in RCAL) hadronic (HAC) sections. The EMC sections are further transversely divided into four cells (only two in RCAL). The properties of the cells are summarized in Table 5.2.

CAL Part	Angular coverage	EMC	HAC
FCAL	$2.5^o - 39.9^o$	20×5 cm^2	20×20 cm^2
BCAL	$36.7^o - 129.2^o$	20×5 cm^2	20×20 cm^2
RCAL	$128.1^o - 178.4^o$	20×10 cm^2	20×20 cm^2

Table 5.2: Angular coverage of the CAL parts and dimensions of the cells.

The FCAL EMC section per tower consists of the first 25 uranium–scintillator layers and has a depth of 26 X^0, where X^0 is the radiation length. Each of the two HAC sections per FCAL tower is 3.1 λ deep and consists of the remaining 160 uranium-scintillator layers.
The BCAL EMC section per tower is made of the first 21 uranium–scintillator layers, the two HAC sections of the remaining 98 layers. The resulting depth is 21 X^0 for the electromagnetic section and 2.0 λ for each hadronic section.
The RCAL towers consist of one EMC and only one HAC section. Therefore its depth is 26 X^0 for the EMC part and 3.1 λ for the HAC part.

The light produced in the scintillators is read out by 2 mm thick wavelength shifter bars at both sides of the module and brought to one of the 11386 photomultiplier tubes (PMT) where it is converted into an electrical signal. The summed information per cell is used for energy and time measurements with a resolution of the order of 1 ns for particles releasing an energy deposit greater than 1 GeV. The excellent time resolution is used to reject non-*ep* background with characteristic timing patterns already at the trigger level. The comparison of the two signals per cell can be used to determine the horizontal position.

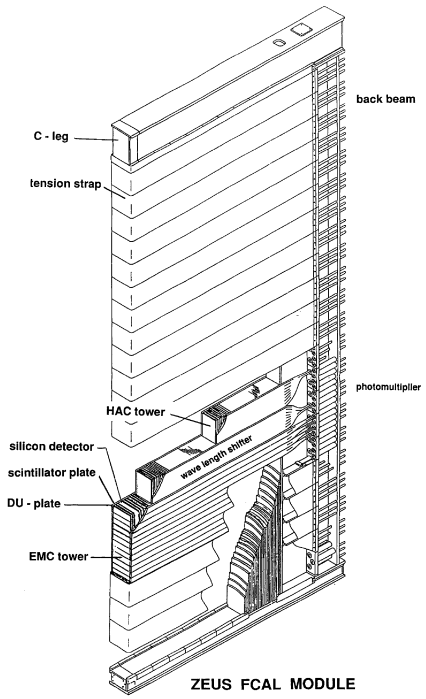

Figure 5.10: A module of the forward calorimeter.

The calibration of the PMTs and of the electronics is mainly performed using the natural radioactivity of the depleted uranium (wrapped in stainless steel foils in order not to interfere with the physical particles measurements) which produces a constant signal in the PMTs. The signal can be used to intercalibrate geometrically identical regions and to transport the absolute calibration scale determined in test beam measurements. In addition, laser, LED and test pulses are also used for the calibration. The achieved accuracy is better than 1%.

5.2.4 The Muon Detectors

Muons can traverse large amounts of material without being absorbed since they lose energy mainly by ionisation. The muon detectors have to measure tracks produced in the interaction region which cross the whole calorimeter thickness and the iron yoke.
The momenta of the muons can be very different depending on their polar angle due to the boosted system to the forward region. Muons with more than 10 GeV momentum are frequently produced in this region. In the barrel and rear regions the average momentum of the muons is expected to be much smaller. Therefore the muon detection system is split into two sub-detectors, the forward muon detector (FMUON, see 5.2.4.1) and the barrel and rear muon detector (BMUON and RMUON respectively, see 5.2.4.2).

5.2.4.1 The Forward Muon Detector

The forward muon detector [53] is divided into two regions (see Figure 5.11). The inner region is located between the FCAL and the BAC (FMUI), the other is positioned outside the BAC (FMUO). The FMUON detector consists of:

- a system of four planes of limited streamer tubes [61] trigger planes (LST1 - LST4) with digital ρ and ϕ readout;
- two coverage planes of limited streamer tubes with digital (ρ, ϕ) and analog (ρ) readout in the large polar angle region (LW1, LW2);
- four planes of drift chambers (DC1 - DC4);
- two large toroidal iron magnets providing a magnetic field of 1.7 T for the momentum separation and measurement in the angular region $5^\circ < \theta < 16^\circ$.

The first plane of LST and drift chambers make up the FMUI detector while the rest of the system is placed outside the iron yoke.

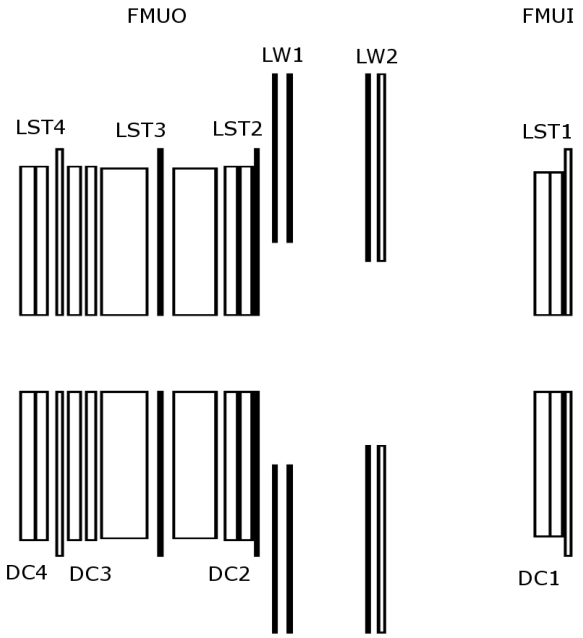

Figure 5.11: Schematic view of the forward muon detector along the beam axis.

The individual components of the FMUON detector are described in the following.

The limited streamer tube planes: The aim of the limited streamer tube (LST) planes is to trigger on muon candidates and to reconstruct their position in terms of the azimuthal and radial coordinates of the track. A trigger plane is made of four LST chambers grouped in two half-planes. A quadrant consists of two layers of LST positioned horizontally inside a plastic sheet. The tubes of the two planes are slightly displaced (0.5 cm) in order to achieve a complete geometrical acceptance. Each quadrant is contained in an aluminum air tight box. On the outer side, copper strips are glued in polar geometry. The LSTs induce a signal in the copper strips if a particle crosses the plane. The number of radial ρ strips is 132 while each strip is 1.9 cm wide. They are divided along the bisector of the quadrant so that the simplest unit of the trigger plane to be read out is the octant. The number of ϕ strips is 32 per octant. Each strip covers an interval of 1.4° in the azimuthal angle.

The drift chambers: The drift chambers are needed in order to obtain a good momentum resolution. Each plane consists of four chambers grouped two by two in two half planes fixed on a support panel. The basic element of the chamber is the *cell* made of four sense wires and of the layers needed to generate the appropriate electric field. The four sense wires measure the radial coordinate. The information gathered by the wires are sent to a TDC which converts them into a time interval related to the drift distance by a known relation.

The large angle coverage planes: The two large angle coverage planes (LW) are needed in order to achieve the desired geometrical acceptance also in the region left uncovered by the toroids ($16^\circ < \theta < 32^\circ$). Each plane consists of eight air tight aluminum wrappings that contain a LST layer. The LST signal is induced on copper strips with radial geometry spaced of 0.7° in the ϕ coordinate and of 1.8 cm in the ρ coordinate. The number of ϕ strips is 64 per octant while the ρ strips are 192 per octant. The achieved resolution in the ρ coordinate, using a center of gravity algorithm, is ~ 1 mm.

5.2.4.2 The Barrel and Rear Muon Detector

The barrel and rear muon detector [62] covers a very large area (~ 2000 m^2) and consist of LST *chambers* as the basic structure. The chambers covering the inner barrel part between the CAL and the iron yoke are called BMUI while the chambers situated outside the yoke are denoted as BMUO. The rear region is divided into RMUI and RMUO chambers in a similar way (see Fig. 5.12).

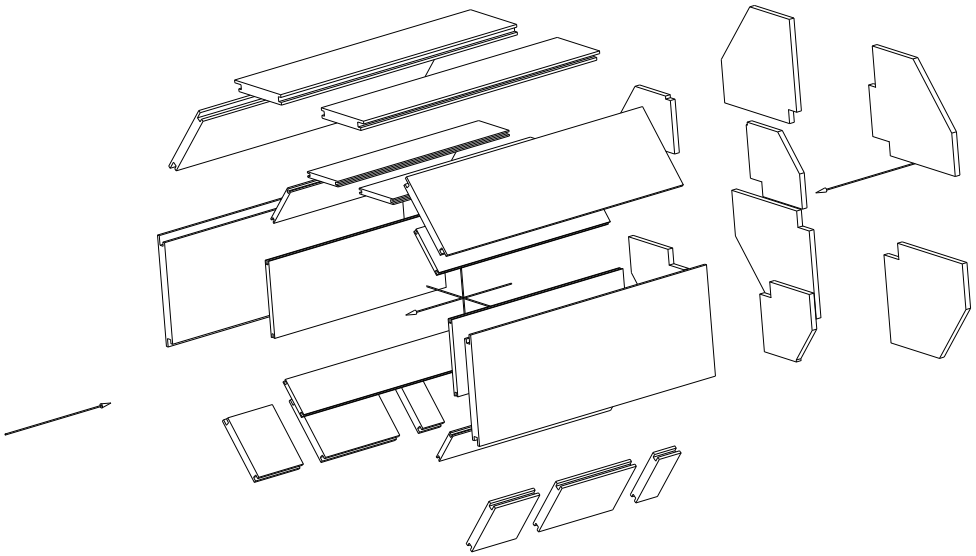

Figure 5.12: Layout of the barrel and rear muon detector.

The chambers have different shapes and dimensions depending on their location, but their internal structure is always the same. The supporting structure of each chamber is an aluminum honeycomb frame 20 cm thick in the rear chambers and 40 cm in the barrel ones. Two planes of LST are placed on both sides of the honeycomb. The two layers on the same side of the chamber are displaced by 8.3 mm in order to minimize dead areas for particles traversing at 90° with respect to the wire plane. Each LST is made of a plastic profile with eight cells. In each cell a copper-beryllium wire of 100 μm diameter is located. The distance between two sense wires is 1 cm.
Each LST plane is equipped on one side by 13 mm wide readout strips with 15 mm pitch that run orthogonal to the wires. In the BMUI and BMUO chambers the LSTs are parallel to the beam direction while in RMUI and RMUO they are horizontal (parallel to the ZEUS x direction). With the analog strip readout [63] the achievable spatial resolution on the coordinate orthogonal to the wires is 200 μm while it is 700 μm for the coordinate parallel to the wires.

5.2.5 The Backing Calorimeter

The backing calorimeter (BAC) [64] uses the return yoke as an absorber to build an additional tracking calorimeter from aluminum proportional tubes operated in a Ar-CO_2 atmosphere. The BAC vetoes showers leaking out of the CAL allowing the selection of event samples with a resolution corresponding to the intrinsic resolution of the CAL. It can distinguish between hadron and muon showers and provides muon identification and trigger capabilities in the bottom yoke and other areas where no muon chambers are present.
The BAC is built from modules inserted into the yoke (Fig. 5.5) consisting of $7-8$ tubes of a cross section of 11×15 mm and a length of $1.8-7.3$ m. The modules are equipped with 50 cm long aluminum

cathode pads in addition to the gold plated tungsten wires of 50 μm diameter. The wires are read out on one side and provide both analog and digital signals whereas the pads have only an analog read out. Energy is measured by summing up the analog signals from the wires grouped in addition into towers of a width of $25-50$ cm ($2-4$ modules) over the full depth of the BAC. The pads of $2-4$ neighbouring modules are added to pad towers with an area of 50×50 cm^2 (4 modules) similar to the wire towers. They provide a measurement of the location of the energy deposit along the wires. The signals from the wires provide also pattern of hit positions in the BAC to reconstruct muon trajectories.
A summary of the BAC modules is given in table 5.3.

	Barrel	Bottom	Forward	Rear
Area [m^2]	1902	296	460	322
Number of layers	9	9	10	7
Gas volume [m^3]	38.0	5.9	9.2	6.4
Number of 8-tube modules	2246	193	840	572
Number of 7-tube modules	658	120	280	112
Module length [m]	4.5 and 5.5	7.3	$1.8 \rightarrow 3.6$	$1.8 \rightarrow 3.6$
Number of wires	22574	2384	7980	5360
Wire towers	100	10	32	36
Pad towers	1100	150	222	230

Table 5.3: Summary of BAC modules.

The spatial resolution of the BAC is ~ 1 mm perpendicular to the wires, whereas the resolution parallel to the wires is defined mainly by the pad size. The energy resolution determined by test beam measurements is given in eq. 5.5 with E the particle energy in GeV.

$$\frac{\sigma_E}{E} \sim \frac{1.1}{\sqrt{E}} \tag{5.5}$$

5.2.6 The Luminosity Measurement

The luminosity measurement at ZEUS [65] is made using a particle reaction with a well known cross section σ_{proc} and the corresponding observed number of events corrected for acceptance and efficiency to calculate the luminosity by the following formula:

$$\mathcal{L} = \frac{N_{proc}}{\sigma_{proc}} \tag{5.6}$$

Lepton-proton bremsstrahlung $ep \rightarrow e'p\gamma$ where the lepton and the photon are scattered at very small angles is chosen for the luminosity measurement at ZEUS.

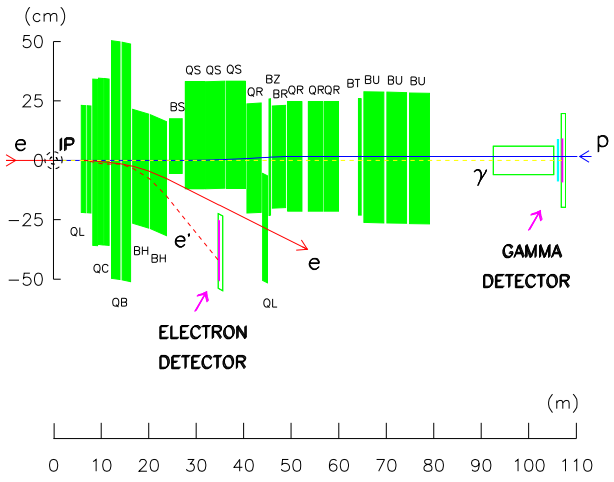

Figure 5.13: Schematic view of the lumi monitor system.

This process has a large cross section ($\sigma_{BH} \geq 20$ mb) yielding sufficient statistics and is well known by theory. The differential cross section as function of the photon energy of this process is described by the Bethe–Heitler formula [66] and is known with an accuracy of $\sim 0.5\%$:

$$\frac{d\sigma}{dk} = 4\alpha r_e^2 \frac{E'}{kE}\left(\frac{E}{E'} + \frac{E'}{E} - \frac{2}{3}\right)\left(\ln\frac{4E_pEE'}{m_em_pk} - \frac{1}{2}\right) \tag{5.7}$$

where α is the fine structure constant, r_e the classical electron radius, k, E and E' the energies of the photon, the incoming and outgoing electron, respectively.
Bremsstrahlung photons emitted at an angle $\theta_\gamma < 0.5$ mrad with respect to the beam axis leave the beampipe through a Cu-Be window of a thickness of 0.095 X^0 at $Z = -92.5$ m. They are detected by a lead/scintillator sampling calorimeter (LUMIG) at $z = -107$ m (Fig. 5.13).
The detector is shielded from synchrotron radiation by a graphite block with a thickness of 2 X^0 resulting in an energy resolution of $\sigma(E)/E = 23\%/\sqrt{E}$ (E measured in GeV). The impact position of the photons can be reconstructed with a resolution of 3 mm making use of the embedded layers of scintillator fingers. The bremsstrahlung event rate is determined by counting the number of photons above a fixed energy threshold. The luminosity is then calculated by dividing the evaluated rate by the bremsstrahlung cross section corrected for the detector acceptance.
The main contribution to the background is given by the bremsstrahlung of leptons on the residual gas in the beam pipe. This can be measured using *pilot* bunches, i.e. lepton bunches with no associated proton bunch, evaluating for these the rate of bremsstrahlung events. The statistical uncertainties are negligible due to the sufficiently large recorded Bethe-Heitler rates. The systematic uncertainty of the luminosity measurement originates mainly from the background subtraction, pile-up effects and the energy calibration, linearity and acceptance of the photon calorimeter. The achieved precision is of the order of $1.5 - 2\%$.

5.2.7 The ZEUS Trigger System

The HERA beam bunch structure leads to a beam crossing every 96 ns corresponding to a rate of potentially interesting events of 10.4 MHz. The rate of *ep* events ranges from less than 0.1 Hz for NC DIS events with $Q^2 > 100$ GeV^2 to 250 Hz for soft photoproduction (for an instantaneous luminosity of $2 \cdot 10^{31}$ cm^{-1}s^{-1}). The rate of background events, on the other hand, can exceed the rate of physics events by several orders of magnitude. It is coming mainly from interactions of electrons or protons with the residual gas nuclei or elements of the beamline (beam gas events). Beam gas events occur typically at a rate of 10 kHz. In addition, cosmic muons traversing the detector contribute to the background rate. The total data size per event is 150 kB and the writing speed is limited to ~ 1.5 MB/s. Hence a significant reduction of the data rate and size is required.
A three level trigger system [53, 67] with increasing complexity of the decision making algorithm and decreasing throughput rate is used to select events online as illustrated in Fig. 5.14:

- *first level trigger (FLT).* Each detector component is equipped with its own FLT implemented in hard-wired single-component logic circuits. Each FLT provides a fast trigger information based on such properties as energy sums, thresholds or timing information and passes it on to the global first level trigger (GFLT) which takes the trigger decision while the event data is stored in buffers. By combining 16 different trigger slots a decision is made by the GFLT after ~ 4.4 μs and the accepted events are passed to the next trigger stage. The GFLT output rate has to be below 1 kHz to avoid deadtimes.

- *second level trigger (SLT).* The SLT is implemented in a transputer network. The decision of the GFLT is analyzed further and the event quantities are recalculated to a higher degree of precision. Beam gas background is rejected on the basis of CAL timing information which is available at this stage. The decisions of several branches of the SLT are collected by the global second level trigger (GSLT) which provides a decision for up to 64 slots after 7 ms and reduces the event rate to $50 - 100$ Hz. In 2001, the global tracking trigger (GTT) [68] was implemented in hard- and software to combine the available information of the main tracking devices (CTD, MVD and STT) to benefit from the enhanced tracking capabilities. The combined trigger decision can be used to efficiently reduce rate on the second trigger level and is currently under commissioning.

- *third level trigger (TLT).* For accepted events the data of all components is combined in a single record of ADAMO [69] database tables by the event builder and passed on to the TLT. The TLT

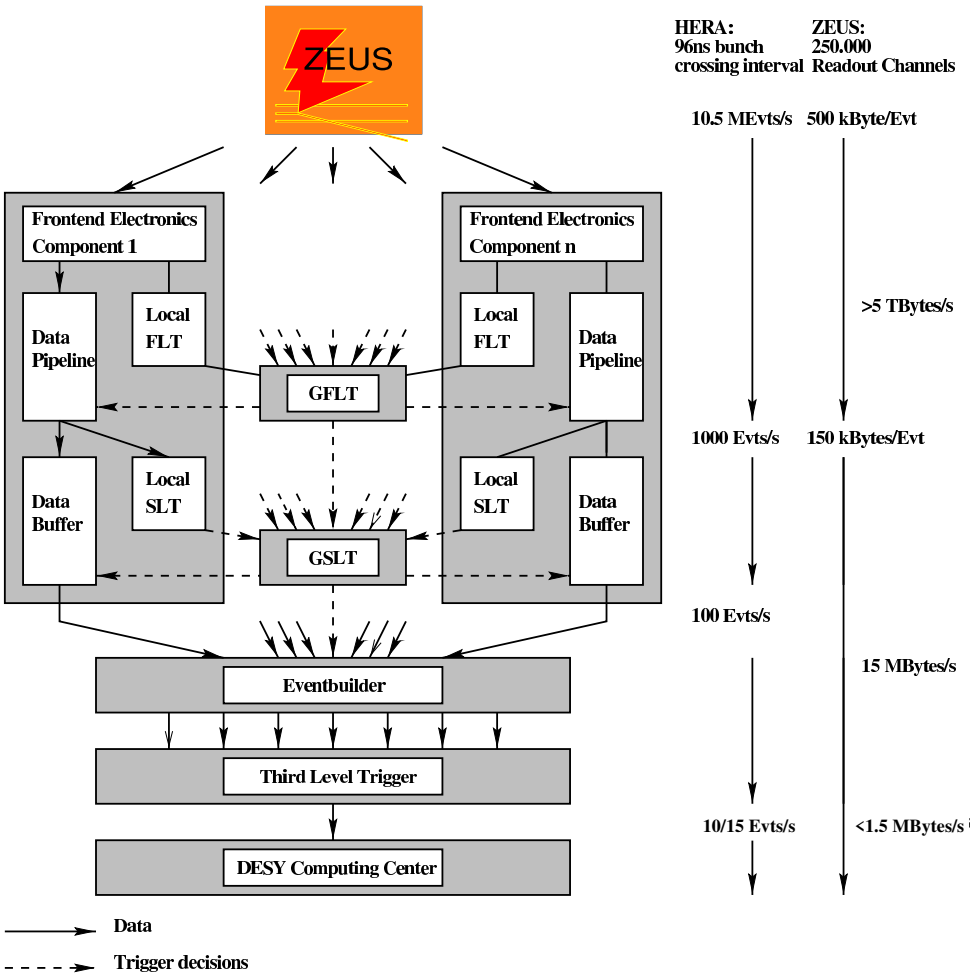

Figure 5.14: The ZEUS trigger and data acquisition system.

uses a computer farm for the analysis and classification of each event. Based on physical quantities of the fully reconstructed events, such as kinematical variables, output of the electron finding algorithms, topologies of hadronic final states etc., a decision is made split into 192 trigger slots and the accepted events are classified. Accepted events (with a size of approximately 150 kB) are written to tape at a rate of $5 - 10$ Hz and fully reconstructed offline by the ZEUS software.

5.3 ZEUS Detector Simulation

The events produced by the event generator PYTHIA (see Sec. 2.4.1) contain the four–vectors of the final state hadrons. To compare simulated events to detector measurements, the influence of the individual detector components on the simulated final state has to be taken into account. The *detector simulation* takes care of this influences by tracing the hadron through the detector. The detector geometry including the sizes and materials of the different detector components and the dead material is implemented in *MOZART*[2] using the *GEANT* package [70]. GEANT takes care of simulating the detector response taking into account processes like energy loss, multiple scattering and in–flight particle decays.
The simulated detector measurements are subject to a subsequent trigger logic simulation by the *CZAR* package[3].
In the end, the simulated event is passed to the event reconstruction *ZEPHYR*[4] which is the same for simulated and recorded events.

[2] **MO**nte Carlo for **Z**EUS **A**nalysis **R**econstruction and **T**racking
[3] **C**omplete **Z**GANA **A**nalysis **R**outine (*ZGANA*: **Z**EUS **G**EANT **ANA**lysis was the first ZEUS detector simulation and was further developed to exclusively simulate the trigger logic)
[4] **ZE**US **PHY**sics **R**econstruction

Chapter 6

Event Visualisation for the ZEUS Experiment

An indispensable tool for analysis of high energy particle interactions is the *event display* or *visualisation tool*.
The visualisation tool displays in a graphical way the detector geometry and the event information per recorded interaction where the event information consists of detector component signals as well as of reconstructed event objects.
The event display helps to diagnose the detector measurement during data taking and afterwards. It visualises event topologies and provides illustrations of the whole matter.
The technical task of this thesis consisted of the development of the new ZEUS event display incorporating the changes in the detector layout after the upgrade including the new micro–vertex–detector. The new solution provides event displays both for the pre– and post–upgrade running periods.
In the following, the development of the new ZEUS event display is presented in more detail.

6.1 ZeVis - the new ZEUS Event Display

The new detector components installed during the HERA upgrade 2000/2001, the MVD and the STT (see chapter 5), have a big impact on the capabilities of the ZEUS detector. They add a large number of individual detector signals and subsequent more and new reconstructed event objects like more precise tracks to the event information. These additions make a thorough revision of the event display necessary.

The requirements to the event display have been updated and are listed in the following:

1. The user has to be able to display all recorded events available in the ZEUS event store independent of the physical location of the user.
2. The latest detector geometry has to be available for display.
3. The complete detector component signals as well as event objects reconstructed by the latest analysis software have to be accessible.
4. The user should be provided with a graphical user interface (GUI) to display the information in three dimensional (3D) views as well as in two dimensional (2D) projections.

The location independent access to all recorded events using the latest analysis software is achieved by separating the extraction of the event information from the ZEUS event store from the user–interactive display of events. This *client–server structure* concentrates all location dependent tasks of the information extraction like storage access and analysis of the event on the *server side* with direct access to the DESY network domain and the ZEUS software and data store. The display of the event is taken care of by the *lightweight client* which uses the local computing resources of the users to display the event information and is independent of the DESY network domain and the ZEUS software and data store.

The client–server structure needs an easily maintainable and extendable software foundation. The implementation of new detector components and corresponding event information and newly emerging event

objects from analysis require a modular framework. *Object–oriented programming techniques* provide an excellent basis fulfilling these requirements.

In the following, the concept of the new event display *ZeVis* (short for **Z**eus **e**vent **Vis**ualisation) [71] is presented.

6.2 The Client–Server Event Display Concept

The concept of the client–server structure (see Fig. 6.1) separates the independent tasks to display an event from the tasks depending on the access to the ZEUS software and event store.

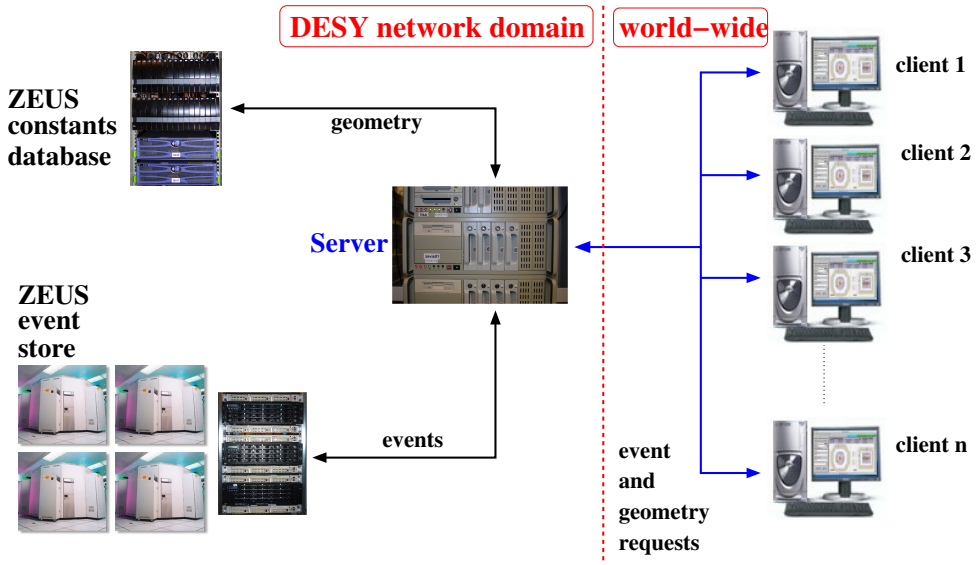

Figure 6.1: Client-Server structure of the new ZeVis event display.

The independent side is represented by the lightweight client. The client can be executed independent of the access to the DESY network domain. A direct access to the ZEUS event store and the usage of the ZEUS analysis software is not required. The client only has to have access to the event display server side to access the detector geometry and event information. These informations are exchanged between the server side and the client using an proprietary format.
The client provides the user with a GUI to:

- request the detector geometry from the server side once per session
- request the event information
- display the event and adjust the view options

The server side can provide informations concurrently for several clients. It is located in the DESY network domain and has full access to the ZEUS event store. The server side is able to

- provide the clients with the requested detector geometry
- lookup specific event information for the client event requests in the ZEUS data store
- retrieve the requested event information from the event store
- analyse the information using the latest ZEUS analysis software
- convert the information to the proprietary ZeVis format
- provide the clients with the requested converted event information

The choice for the underlying object–oriented framework which provides basic functionalities like

- displaying capabilities in 2D and 3D,
- GUI capabilities,
- input/output (I/O) capabilities including object persistency

is made after a thorough investigation process of the available library packages. The ROOT framework [72] is chosen which also defines the programming language to be C++, a commonly used language in the high energy physics community.
ROOT provides all requested functionalities including an advanced I/O component with object persistency as a basis for the proprietary ZeVis geometry and event information format. ROOT is widely available and well supported. It also provides the possibility to access data by the HTTP protocol. This easily enables the world-wide accessibility of event displays because the clients just have to communicate with the server side via HTTP which is widely spread through the internet network infrastructure. The protocol is also not limited by firewall restrictions because most firewalls accept HTTP traffic.

In the next chapters, the server and client sides of the ZeVis event display are introduced in more detail.

6.3 ZeVis - Server Side

The communication between the clients and the server side consists of the transfer of the detector geometry and event information. As the communication is carried out using HTTP-URL requests (*http://<server>/<file>.root*), the requested information has to be provided by the server side in the form of ROOT files containing detector and event information in proprietary formats.
The detector geometry ROOT file is generated offline using information from the ZEUS constants database and stored on the server side.
The event information files are converted using a standard ZEUS analysis job. The ZEUS analysis software provides a common analysis framework. Here, commonly used event objects and properties as well as calibrated detector signals are extracted from the ZEUS event store. The framework is implemented into a conversion program which converts the output of the analysis to the ZeVis format and stores it in a ROOT file.
The access to the event information in the ZEUS event store is handled by the *dCache* system [73] which takes care of the interplay of mass storage systems like tape robots and caching systems. The event information itself is stored in the *ADAMO* format [69] in files containing the information of multiple recorded events. The *RAW* detector signals are stored as well as the reconstructed event information in separate files. Summaries of the stored reconstructed event information are available in the form of mini-DST's (mini data summary tapes) which resolve the specific file name in the event store from the run and event numbers and preselect events suited for analysis.
The server side consists of several basic layers (see Fig. 6.2):

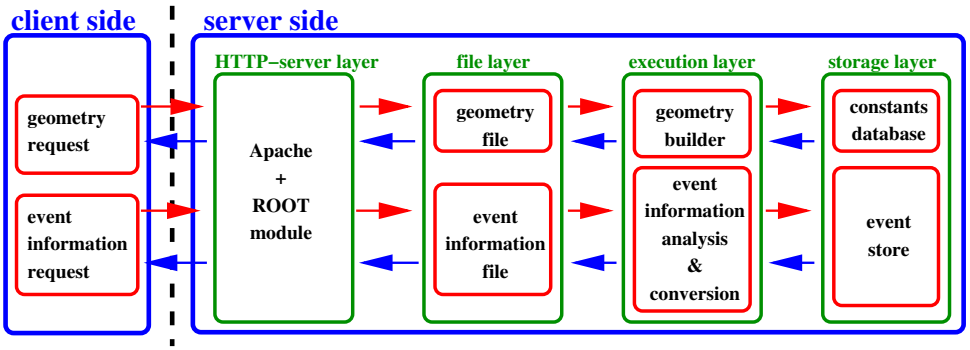

Figure 6.2: Layers of the server side.

HTTP-server layer: consists of a standard HTTP-server which is extended to handle ROOT file requests. The clients can open a ROOT file from the server like a local file;

File layer: consists of the pool of different ROOT files representing the detector geometry and event information which are served by the HTTP-server layer;

Execution layer: consists of the software for extraction of geometry and event information and conversion to the ZeVis format.

- The detector geometry is extracted offline and the resulting geometry file is stored on the file layer. A new extraction of the information is only necessary if the detector geometry changes.
- The event information is extracted by the modified analysis job and the converted event information is stored on the file layer.

Storage Layer: consists of the ZEUS constants database and the ZEUS event store which are used by the execution layer to extract information.

The detector geometry is requested once per session by the clients whereas the event information is requested repeatedly. The event requests are usually not in the same order as the events in the event files in the ZEUS store and usually not restricted to a single file. Therefore, the HTTP-server layer has to be extended to handle and process interactive event requests by the clients. The *single event request* accesses not a single ROOT file via the HTTP-server layer rather than an interactive server script, the *dispatcher* (see Fig. 6.3), which handles input parameters of the clients given in the URL (for example run and event number of the requested event).

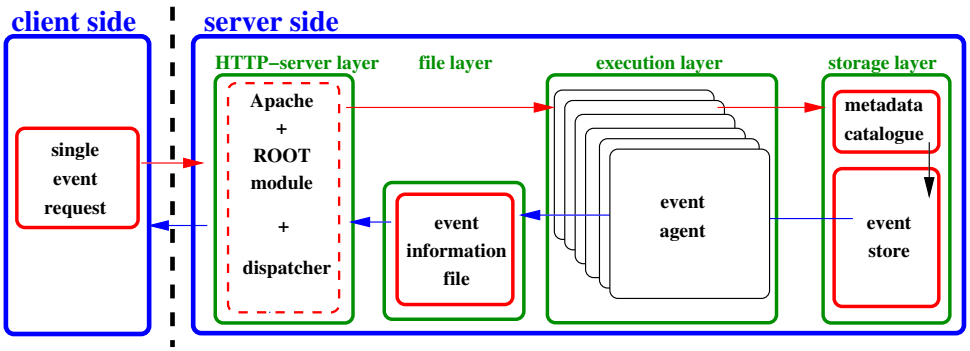

Figure 6.3: Single event request to the event agents using the metadata catalogue and the event store.

The dispatcher initiates the extraction and conversion of the event information by the execution of a corresponding analysis job. The ZEUS tag database is used to access the requested event information in the ZEUS event store. This metadata catalogue stores the location of events in a specific event file depending on the run and event number and event properties from the analysis framework. The metadata access to the event information not only speeds up the retrieval of the information but also enables event selection also by specific event properties for selection of subsamples with special physics content. For example, the metadata catalogue can select J/ψ samples by requiring only events with two muons.
The initialisation phase of the analysis job is rather long due to the initialisation of the memory structures of the ZEUS ADAMO data model and takes significantly longer than the extraction, analysis and conversion of the information of a single event. The time to convert a single event would consist almost completely of the initialisation. To solve this problem, the analysis job is modified to run in a deamonised state. The *event agent* waits pre-initialised for event requests from the dispatcher and converts only a single event which file is saved on the file layer. Several event agents run in parallel to provide event information for concurrent requests from different clients (for more details see App. B). In addition, the file layer provides a caching of already converted events. The dispatcher first checks for each request the file layer for an already existing corresponding file and only otherwise initiates the conversion by an event agent.
The single event request provides an easy, quick and random access to events for the clients and is the main access mode to event displays.

The server side also provides the clients with the possibility to request a consecutive sequence of events from a specific event file. The *download event file* request (see Fig. 6.4) is send to the dispatcher

containing parameters of the file in the event store, the number of events to convert and the number of events from the beginning of the file to start the conversion.

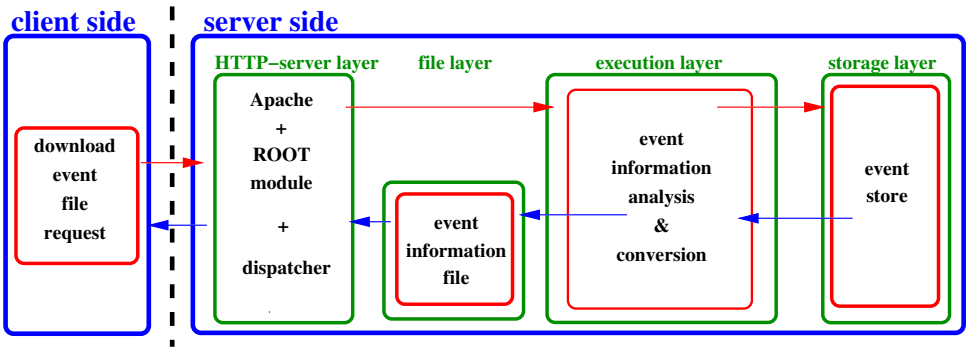

Figure 6.4: Download event file request to the analysis and conversion using the event store.

The corresponding analysis job is initiated by the dispatcher and the converted ROOT file is served to the client. The conversion of all available event file categories can be requested including the on–the–fly reconstruction of RAW files.

The possibility to immediately see the detector output during data taking is a very important diagnose tool. The correct operation of the DAQ chain and malfunctions of detector subcomponents can be spotted immediately by looking at recorded events online. Problematic is the time consumption of the reconstruction of the RAW data stream coming from the detector. The reconstruction is normally carried out offline on a farm of reconstruction machines. A pile up of unreconstructed events during data taking is avoided by the parallel reprocessing of the recorded events. For an *online event display* (see Fig. 6.5), the parallel reprocessing is not possible. To provide online reconstructed events, a substream of the recorded ZEUS RAW data at a reduced frequency of ~ 0.1 Hz is reconstructed online on a dedicated online reconstruction server and subsequently converted to the ZeVis format and the ROOT file is served by the HTTP-server layer.

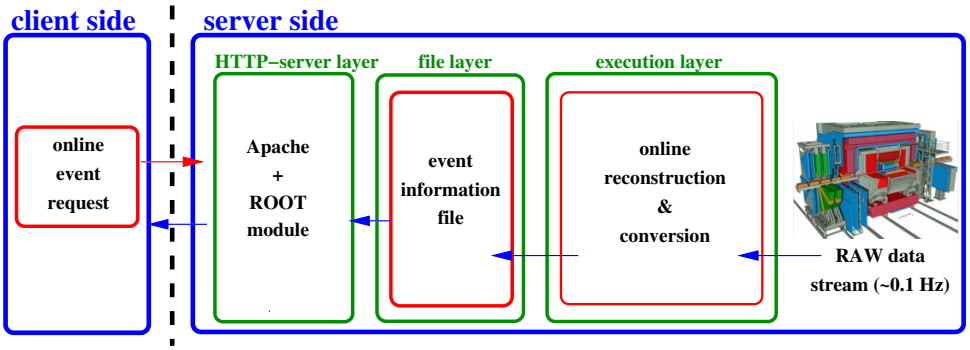

Figure 6.5: Online file request to the periodical reconstruction and conversion of the online data stream from the ZEUS detector.

The clients can request these events periodically and can see online recorded events with a short time delay. Due to the client–server structure, online events are available on every client independent of the location.

6.4 ZeVis - Client Side

The client side provides the user with a GUI to request and display events. Due to the client-server structure, the lightweight client is independent of the access to the ZEUS software and event store and only depends on the ROOT framework.

The GUI provides the user with the possibility to request the detector geometry and event information by the three server modes:

- single event request,
- download file request,
- online file request.

The user can specify all needed parameters for the different modes and browse the downloaded events. The GUI provides printing capabilities and the event pictures can be saved in various picture formats (for more details see App. B.2). The downloaded event files can be saved locally for later usage. If the geometry is downloaded as well, the client can display events without any connection to the server side in a standalone mode.

The GUI provides the user with two views of the detector geometry and the event information. Each view can be modified separately and adjusted to the user's needs.
The event can be shown in the following 3D and 2D view modes. The area of interest and the zoom level can be freely adjusted by the user.:

3D modes: The event information and the detector geometry can be displayed in a 3D view (see Fig. 6.6). If the event information is displayed together with the detector geometry, parts of the in-

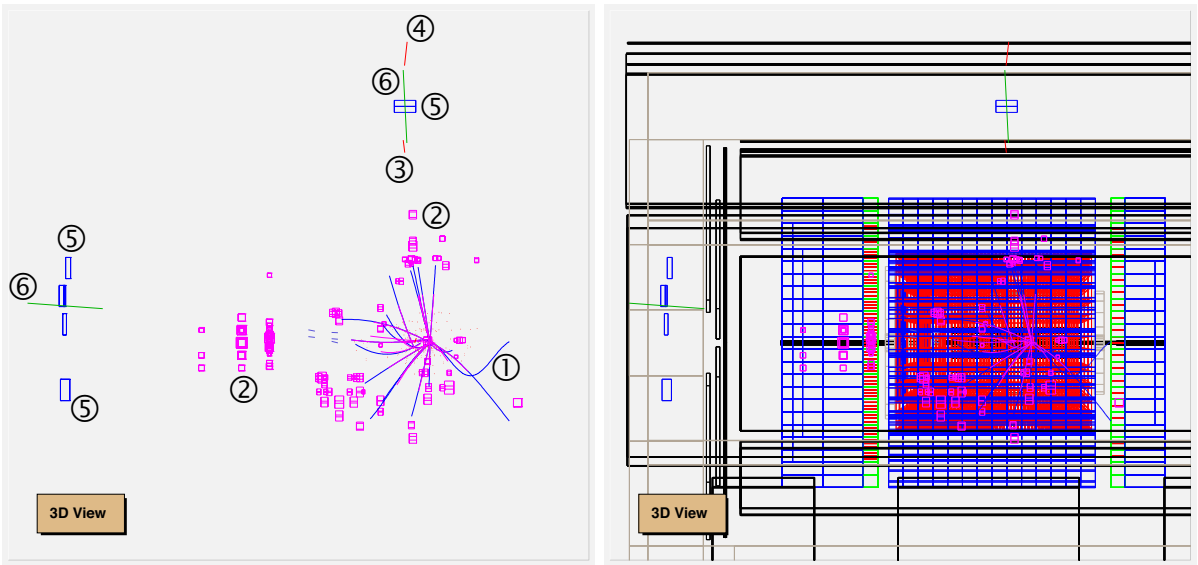

Figure 6.6: *Left:* 3D display of the event information: *1:* tracks, *2:* CAL cell energy measurements, *3:* inner muon chamber hit, *4:* outer muon chamber hit, *5:* BAC pad tower, *6:* BAC muon segment. *Right:* 3D display of the same event information partially obscured by the detector geometry.

formation is obscured by detector components obstructing their visibility. The orientation of the 3D view is freely adjustable. It can be used to display 2D projections in XY, XZ and YZ in the ZEUS reference frame (see Fig. 6.7) In addition, the client can display the event information and the detector geometry in external 3D viewers using hidden line and surface removal (see Fig. 6.8). Here, cross sections of the detector components can be displayed to reveal the event informations otherwise obscured by the detector geometry.

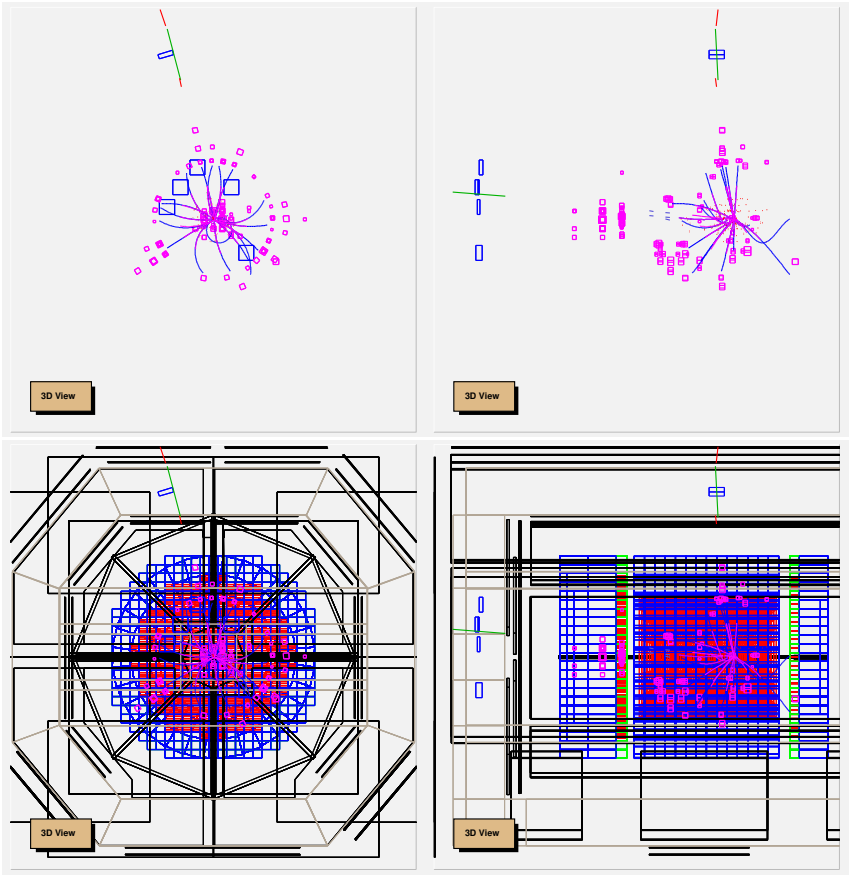

Figure 6.7: *Top:* 2D projections of the 3D display of the event information in XY (*left*) and ZY (*right*). *Bottom:* 2D projections of the same event information partially obscured by the detector geometry.

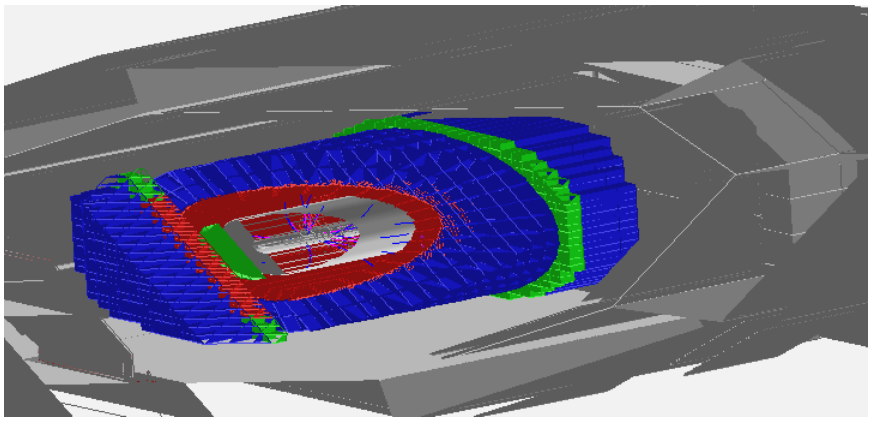

Figure 6.8: 3D displays of an event by the ZeVis event display in an external viewer. The viewer displays all information using hidden line and hidden surface removal. An adjustable cross section of the detector is shown cutting away parts of the muon chambers, the BAC and the CAL to uncover the tracks in the central tracking detectors.

2D layered projection modes: The 2D projections of the 3D view are not suited to give a simultaneous display of event information and detector geometry as the geometry partially obscures the event information. Special 2D layered projections have been implemented which display the event information on top of the detector geometry. The layered projections represent the standard view mode of the event display. Per default, two different projections are shown by the GUI (see Fig. 6.9). On the left side, the layered projection in XY is shown which correspond to the 2D projection

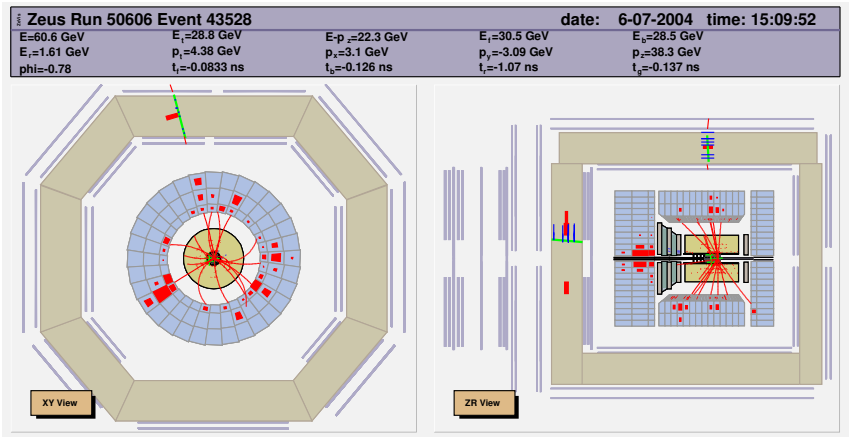

Figure 6.9: Default display of an event by the ZeVis event display. Shown on the top is the header with general event informations. Below, two representations of the detector including event information are shown in the **XY** and **ZR** layered projections.

in XY from the 3D display (see *left* in Fig. 6.7) removing the forward and rear parts of the detector including their event information. In addition, the event information for special components has to be adopted to the layered projection. For example, the energy contents of the CAL cells in the barrel region are summed up for cells at the same X and Y coordinates and only the sum is displayed in the layered projection.

On the right side, the layered projection in ZR presents the event information and the detector geometry in a transformed coordinate system. The transverse radius R is calculated from the coordinates X and Y by $R = \sqrt{X^2 + Y^2}$. The projections is separated in the upper half for positive radius and the lower half for negative radius where the radius is defined as positive if the azimuthal angle ϕ is between 0° and 180° in the ZEUS reference frame. The angular range can be adjusted by the user. The event information has to be transformed in a similar way as for the XY layered projection.

In the header, run and event number and recording date and time of the event are shown. In addition, general event quantities like calorimetric energies or properties of found electron candidates as well as trigger information from all three levels can be displayed (see Fig. 6.10).

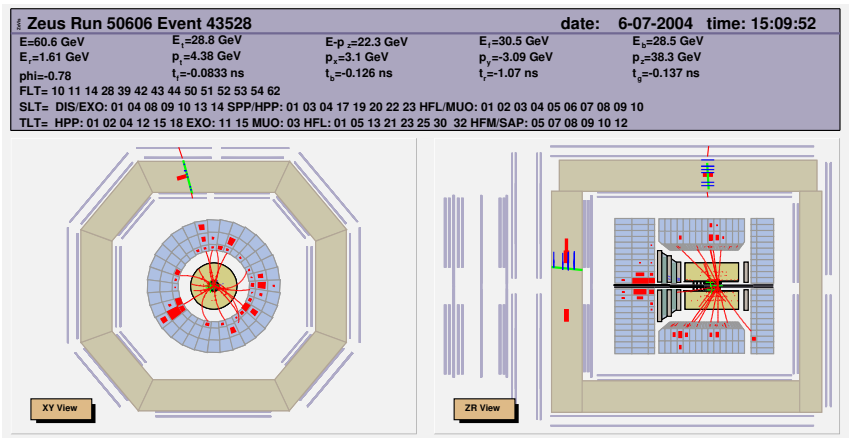

Figure 6.10: Display of the header information in the most verbose variant. Shown are general event information like run and event number and time and date of the data recording, calorimetric quantities and trigger information from all three levels.

The general event information contains amongst others:

- tracks in CTD and MVD, refitted to the primary and secondary vertices or prior to the vertex fit (see Fig. 6.11);

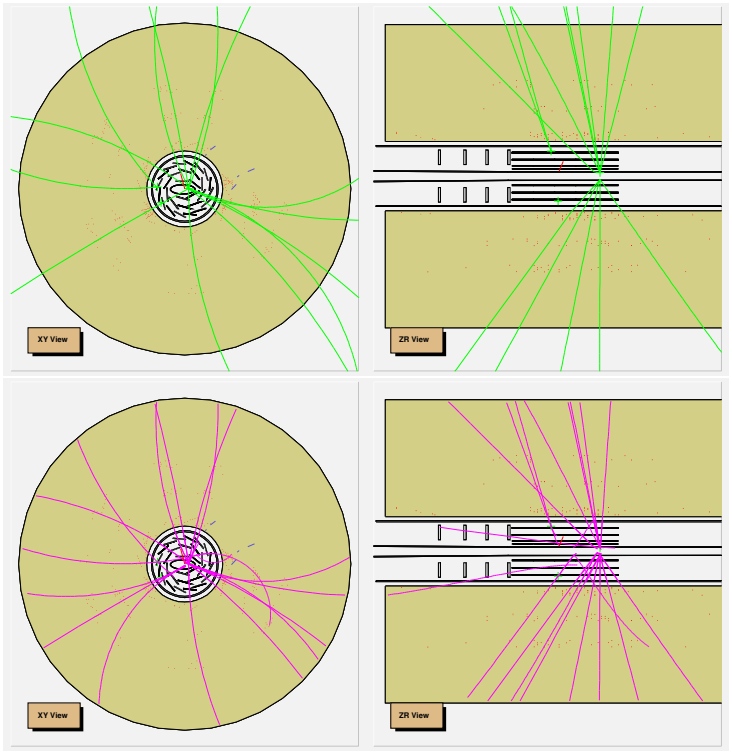

Figure 6.11: Detailed display of the tracking components MVD and CTD. *Top:* Display of vertex fitted tracks in MVD and CTD extrapolated to the inner ring of the CAL. *Bottom:* Display of non–vertex fitted tracks in the same event.

- energy cell contents in the CAL (see Fig. 6.12);

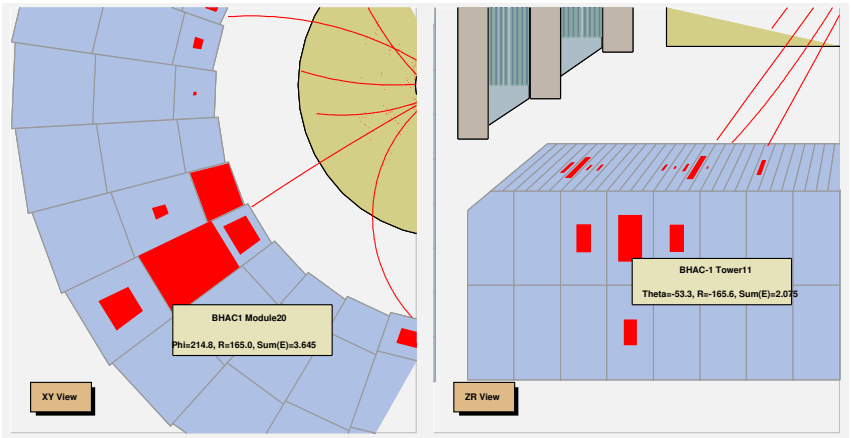

Figure 6.12: Display of CAL energy cell information. *Left:* Display of barrel CAL module energy contents in **XY**. *Right:* Display of barrel CAL tower energy contents in **ZR**. Detailed information of energy cell contents can be displayed using special text boxes.

- muon candidates in forward and barrel/rear muon chambers and the BAC (see Fig. 6.13);

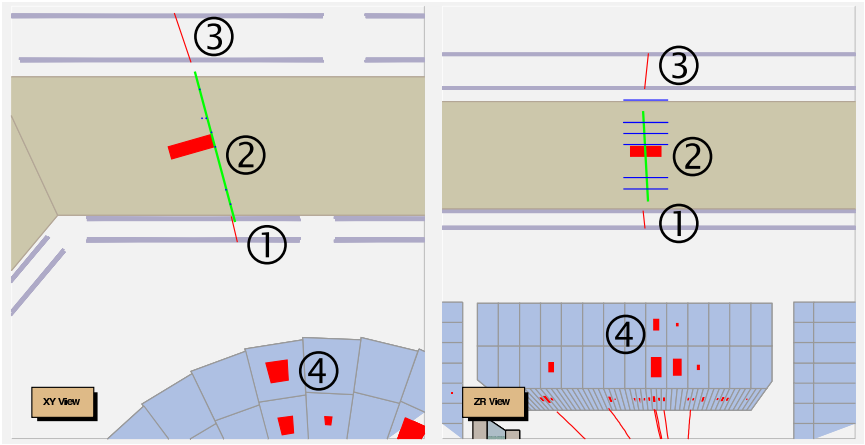

Figure 6.13: Display of a muon candidate in inner (1) and outer (2) muon chambers and the BAC (3) in **XY** (*left*) and **ZR** (*right*). The energy signature in the CAL (4) is also shown.

Also specific hit information can be displayed:

- hit information of the MVD and CTD (RAW hits in **XY** and z–by–timing hits in **ZR**, see Fig. 6.14);

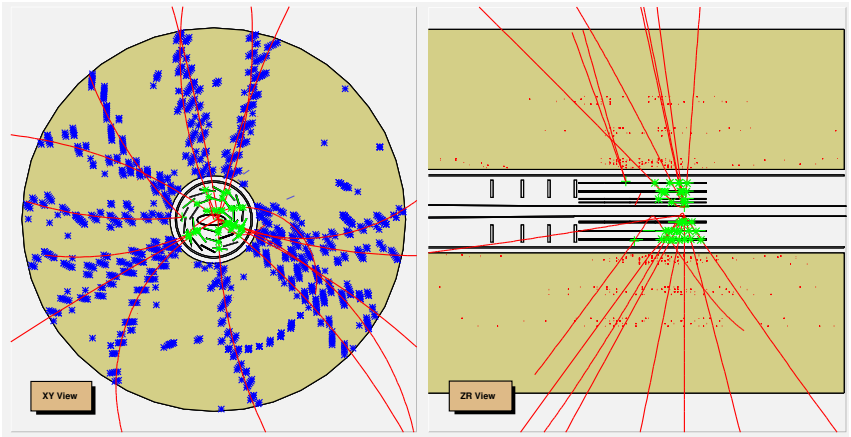

Figure 6.14: Detailed hit information display of MVD and CTD including corresponding vertex fitted tracks. *Left:* CTD hits in **XY** displaying the RAW hit information. *Right:* CTD hits in **ZR** display the RAW z–by–timing hit information.

The tracking information provided by the ZEUS experiment is very detailed and has a very high granularity while confined to a small space. In contrast, the information from the outer detector components has a lower detail level at a much lower granularity and a larger available space. The display of both regions at the same detail level poses a big challenge to the event display.
The *fish eye* transformation, which scales the tracking components differently than the outer calorimeter and muon detection components to provide a simultaneous presentation in sufficient detail for inner and outer detector parts, helps the user to display the event and detector information (see Fig. 6.15).

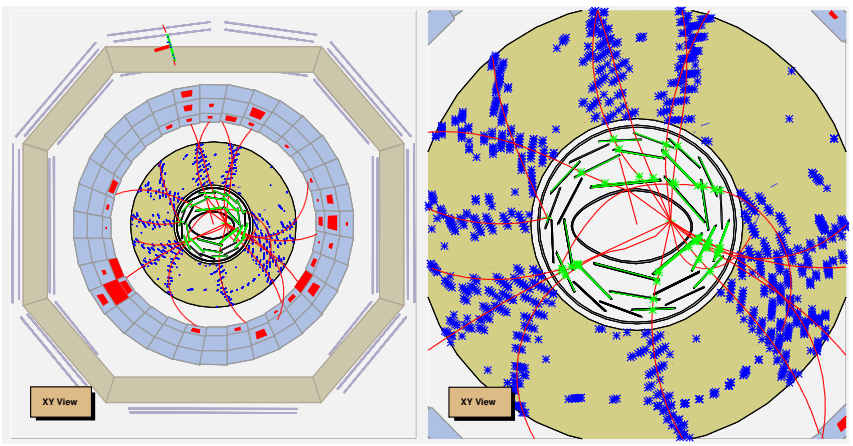

Figure 6.15: Detailed hit information display of MVD and CTD including corresponding vertex fitted tracks similar to Fig. 6.14 in fish eye mode. The inner tracking components are displayed using a larger scale than the outer components to improve the simultaneous visibility.

In summary, the new ZeVis event display provides a complete display solution for ZEUS events in a client–server structure decoupling the event conversion from the display part.

Chapter 7

Event Reconstruction

The reconstruction of the event properties to identify semi-leptonic decays of beauty quarks into muons consists of the identification of the hadronic system of the beauty quark decay and the associated muon by a general muon reconstruction.
The reconstruction of the hadronic system is based on tracking and energy information combined into energy flow objects (EFO's). They represent the input to the jet algorithm to reconstruct the hadronic shower from beauty quarks.

In the following, the different ingredients of the event reconstruction are presented.
The track reconstruction in the inner tracking detectors[1] is described pointing out the different tracking possibilities in the pre- and post-upgrade data taking periods. This is followed by a brief description of the calorimeter energy measurement.

The muon reconstruction possibilities of the ZEUS detector are introduced. The different reconstruction techniques mainly use event information from the forward (see Sec. 5.2.4.1) and barrel/rear (see Sec. 5.2.4.2) muon chamber measurements, the reconstructed track information and the information from CAL (see Sec. 5.2.3) and BAC (see Sec. 5.2.5). The different techniques are combined to a general muon reconstruction to benefit from redundancies.

In the end, the combination of the tracking information and the CAL energy measurements is described and the jet algorithm and its application are introduced.

7.1 Track Reconstruction in the Inner Tracking Detectors

The track reconstruction combines hit information from the inner tracking detectors to particle trajectories taking into account the errors on the hit measurements, the dead material distribution and corresponding multiple scattering influences and the magnetic field. The track reconstruction uses the CTD (see Sec. 5.2.1) and from 2001 on also the MVD (see Sec. 5.2.2). Therefore, the track reconstruction has to be described separately for the pre-upgrade and post-upgrade running periods.

Common to all running periods, tracks are given according to a five–parameter helix parametrisation [74] which is designed to describe particle tracks in a toroidal magnetic field parallel to the beam axis. Relative to the coordinate reference, the helix is given by five parameters. The first three parameters represent a circle in the XY plane and the latter two the location and pitch in Z:

1. ϕ_H: angle tangent to the helix in the XY plane
2. Q/R: Q is the charge and R the local radius
3. QD_H: D_H connects the helix to the reference point and is equal to the distance–of–closest–approach of the helix relative to the reference point
4. Z_H gives the Z coordinate of the reference point

[1] If not stated differently, the CTD is used in this chapter as a synonym for the inner tracking detectors.

5. $cot\theta = tan\lambda$: $\lambda = \pi/2 - \theta$ is the angle of dip with regard to the XY plane

and the covariance matrix of the parameter errors define a track in the ZEUS reference frame.
The helix for a positively charged track is shown in the XY plane in Fig. 7.1.

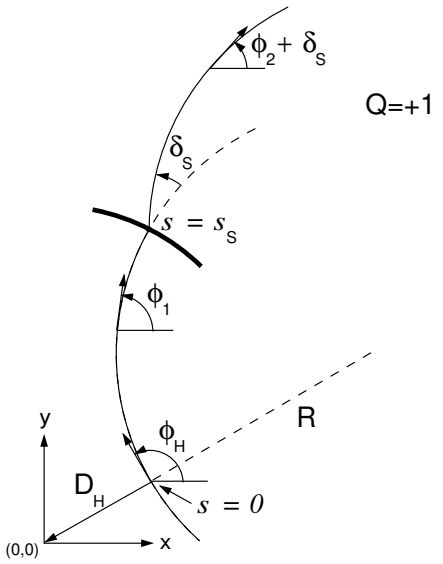

Figure 7.1: Helix in the XY view for a positively charged track.

In the following, the track reconstruction is described for the pre–upgrade running periods in the so called *CTD–only* mode followed by the description of the tracking for the post–upgrade running periods.

7.1.1 Track Reconstruction with the CTD

The *CTD–only* track reconstruction used in the running periods until the upgrade uses the CTD hits to reconstruct tracks by performing a helix-parameter fit [74].
The first step of the track reconstruction, the *pattern recognition*, assigns CTD segments to tracks starting from the most outer superlayer going inwards. In the XY plane, a CTD segment consists of all wire hits of a cell which can be up to 8 per cell. An additional ambiguity is introduced by the measurement principle of a wire drift chamber. A signal in a sense wire only measures the distance of the hit to the wire along the field lines, not on which side with respect to the wire it is measured. This ambiguity is broken by the pattern recognition and the following helix-parameter fit.
In a third step, a vertex fit is carried out using the reconstructed tracks. The tracks are refitted incorporating the vertex into the fit.

7.1.2 Track Reconstruction with the MVD and the CTD

The MVD supplements the CTD measurement along the track of a particle by high precision hit measurements between the vertex and the most inner CTD hits. From 2001 on, the tracking takes care of tracks using the following hit combinations:

1. *CTD–only* tracks only use CTD hits for the helix-parameter fit,
2. *CTD–MVD* tracks use both CTD and MVD hits,
3. *MVD–only* tracks are formed exclusively by MVD hits.

The pattern recognition described in the CTD–only pre-upgrade track reconstruction (see Sec. 7.1.1) is extended and consists of the following stages:

1. global pattern recognition which assigns CTD segments and MVD hit clusters to tracks
2. CTD pattern recognition for CTD–only tracks

3. MVD pattern recognition for MVD–only tracks

In the end, a vertex fit using all the track categories is performed and vertex refitted tracks are stored.

The tracks of the global reconstruction represent the most accurate tracks for the complete inner tracking system. The accuracy of the tracking near the vertex can be improved by using Kalman filter techniques [75]. The Kalman filter [57] uses CTD–MVD fitted tracks as a seed to improve the track parameter accuracy near the vertex taking into account multiple scattering influences in the dead material of the MVD. The Kalman-fitted tracks are input to a second vertex fit. In comparison to the global tracks and vertices, the Kalman-fitted information is predestinated for high-precision track information like secondary vertices of long-lived particles or impact parameter measurements.

7.1.3 Resolution

The MVD is expected to improve the resolution significantly due to the high precision hit measurements near the vertex. Fig. 7.2 shows the tracking resolution for the CTD–only and global reconstruction.

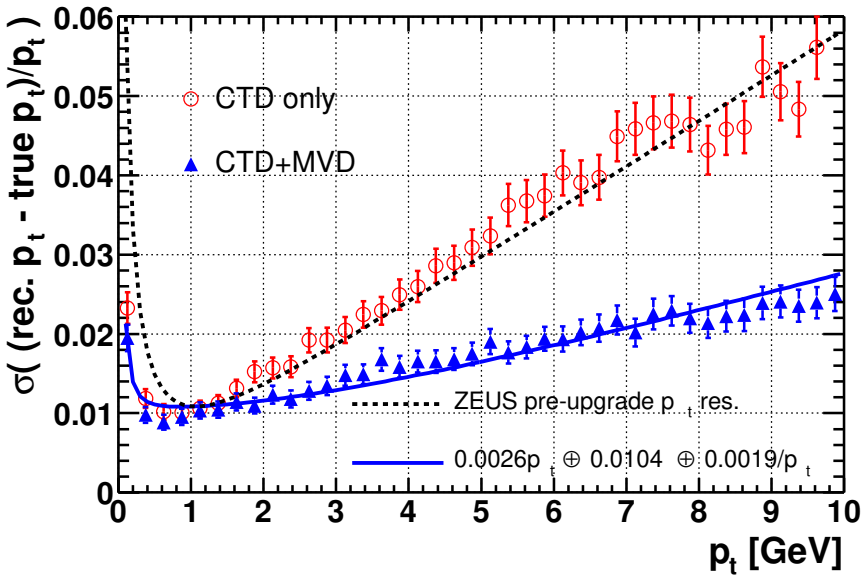

Figure 7.2: Resolution of the CTD–only and the CTD-MVD combined track reconstruction. The error on the comparison of true and reconstructed transverse momentum of a track is shown differential in $p_T^{\texttt{track}}$.

The transverse momenta of reconstructed tracks are compared to the corresponding true information using MC simulations [57]. The resolution of the Kalman filter track reconstruction (see. Eq. 5.2) is similar at lower transverse momenta and significantly better at higher transverse momenta compared to the pre-upgrade resolution (see. Eq. 5.1). Latest improvements in the internal alignment of the MVD and the alignment with respect to the CTD improves the resolution further.

For impact parameter studies, the accuracy of the reference point is an important ingredient and usually the primary vertex is chosen. Currently, the primary vertex is technically not stable. Therefore, the beamspot is taken as the reference. The beamspot is the averaged vertex distribution per run. Using Kalman-fitted tracks and the latest MVD alignment with a transverse momentum cut of $p_T^{\texttt{track}} > 0.5$ GeV and at least 4 used hits in the MVD, the primary vertex is determined by a vertex fit in all events of the run fulfilling above requirements. The distribution of primary vertices per run is fitted with a Gaussian where the sigma of the fitted Gaussian distributions gives the reconstruction width of the beamspot and therefore its resolution. Fig. 7.3 shows an exemplary beamspot fit for a single run yielding a beamspot resolution of ~ 150 μm in x and ~ 140 μm in y.

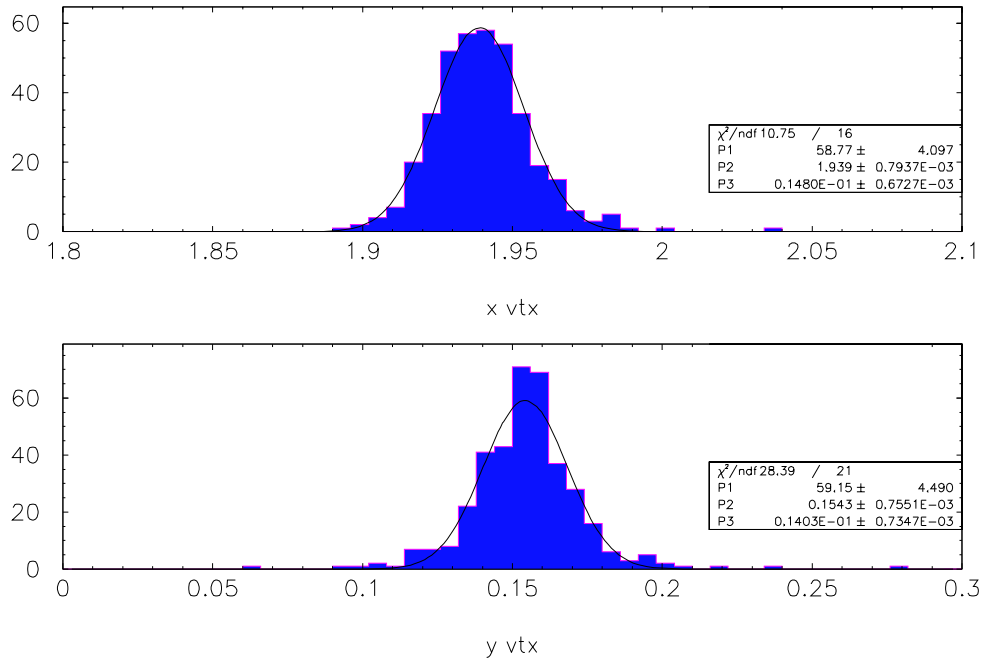

Figure 7.3: Resolution of the beamspot using Kalman-fitted tracks. The beamspot resolution is ~ 150 μm in x and ~ 140 μm in y.

7.2 Reconstruction of Calorimetric Variables

The energy measurements of the CAL (see Sec. 5.2.3) used for the reconstruction of calorimetric variables have to be corrected for several detector effects.

First, noisy cells have to be rejected and other noise related effects have to be suppressed from the energy cell measurements. Noisy cells usually arise from electronic malfunctioning and are excluded by calibration lists which have been generated offline individually per running year. Noise related effects are further suppressed by cuts on isolated cell contents. All isolated cells with an energy content in the electromagnetic part of less than 80 MeV and in the hadronic parts of less than 140 MeV are excluded. In addition, the imbalance between the two photo-multiplier measurements per cell is also used to suppress noise. Both noise sources are mostly related to sparks in the photomultipliers.

Studies comparing the calorimetric reconstruction in data and MC simulations resulted in a discrepancy which can be corrected by multiplying the energies measured in data events by a correction factor [76]. The corrections on the data are summarized in Tab. 7.1 separately for the electromagnetic and hadronic parts of the FCAL, BCAL and RCAL.

CAL section	cell type	energy correction 1996-1997	energy correction 1998-2004
FCAL	electromagnetic	+4.0%	+2.4%
	hadronic	-5.0%	-5.9%
BCAL	electromagnetic	+4.0%	+5.3%
	hadronic	+8.2%	+9.6%
RCAL	electromagnetic	+2.2%	+2.2%
	hadronic	+2.2%	+2.2%

Table 7.1: Energy correction factors for the electromagnetic and hadronic parts of the FCAL, BCAL and RCAL for the running period 1996-1997 and the running periods 1998-2004.

Dead material in front of the CAL and the presence of particles like muons which do not release all their energy in the CAL cause a systematic shift of the calorimetric reconstruction towards lower values and require additional corrections. They are applied directly to the energy flow objects (EFO's, see Sec. 7.4).

7.3 Muon Reconstruction

The muon reconstruction is especially important as it identifies the decay muon from the beauty quark.

From the reconstruction perspective, a muon is a minimally ionising particle (MIP) with a high penetration power. The energy loss of muons in uranium (see Eq. 7.1 [8])

$$\frac{dE}{dx} = 1.082 \frac{\text{MeV}}{\text{g/cm}^2} \tag{7.1}$$

does not fully describe the passage of a muon through the CAL. As the calorimeter consists of a sandwich of depleted uranium plates and scintillators, the response to a muon was determined in test beam measurements [60]. For the barrel CAL, the response was found to be 3.27 pC per muon traversing a tower of the electromagnetic section, 9.34 pC per muon traversing a tower of the first hadronic section and 9.41 pC per muon traversing a tower of the second hadronic section given in units of the charge collected by the photomultipliers.

A list of detector components suited for muon identification is given in the following:

tracking:

- central tracking: CTD
- forward tracking: FDET (not used in this thesis)
- since 2003 supplemented by MVD (used) and STT (not used in this thesis)
- forward muon chambers (FMUO)

calorimeter:

- CAL (forward, barrel and rear part)
- BAC (has also tracking capabilities)

muon chambers:

- forward muon chambers (FMUO)
- barrel and rear muon chambers (BRMUO)

The muon reconstruction is divided into a forward part and a barrel/rear part due to the different detector components used.
The forward muon reconstruction uses the forward tracking information from the CTD to reconstruct a muon track, the energy signature in the FCAL visible in the electromagnetic and both hadronic parts corresponding to a MIP, the muon hits in the forward muon chambers which give an own forward muon track reconstruction and also the BAC to reconstruct a muon.
The barrel/rear part uses the CTD to reconstruct a muon track and the CAL to measure the MIP signature of the muon. Only muons can reach the BAC and the outer barrel/rear muon chambers due to the amount of penetrated material.

The energy deposition of a muon corresponds to a MIP. But muons can be embedded in larger energy deposits for example if they are contained in a jet. The background to the muon reconstruction and identification are muonic K and π decays which mainly result in low momentum non-isolated muons. Also shower leakage and punchthrough's from the CAL can lead to a misidentification of hadrons as muons. These mainly non-isolated muons have often momentum and range inconsistencies. A last source of background can arise from reconstruction ambiguities.

In the following, the main muon reconstruction algorithms used in this thesis are introduced.

7.3.1 Muon Reconstruction Algorithms

The description of the used muon reconstructions starts with the most sophisticated algorithms. The *BREMAT* algorithm reconstructs muons in the barrel/rear region using the barrel/rear muon chambers while the *MPMATCH* algorithm carries out a similar reconstruction in the forward part using the forward muon chambers.
The muon reconstruction in the BAC is implemented in the *MUBAC* algorithm and all three are supplemented by the *MV* algorithm which uses the MIP signature in the CAL to reconstruct muons. An algorithm similar to the MPMATCH muon reconstruction is *MUFO*. In addition, the muon reconstruction algorithm for trigger purposes *GLOMU* is described in the end.

7.3.1.1 BREMAT - Barrel and Rear Extrapolation Matching

The BREMAT algorithm [77] reconstructs muons by extrapolating candidate tracks from the CTD to the inner barrel/rear muon chambers and a subsequent match with a reconstructed muon segment. It is suited for isolated as well as non-isolated muons coming for example from semi-leptonic beauty quark decays because it does not use the MIP signature of a muon in the CAL. Only muons above a momentum threshold of $\sim 1 - 1.5$ GeV are reconstructed by BREMAT because the muons have to penetrate the CAL to reach at least the inner muon chambers.

The extrapolation of a muon candidate track to a reference surface on the inner muon chambers has to take into account the characteristics of a muon traversing the ZEUS detector.
The momentum resolution is dominated by multiple scattering in the CAL. The magnetic field in the CAL does not have a strong influence on the track extrapolation. The field is small in the CAL compared to the inside of the solenoid. The GEANE package [78] is used for the extrapolation taking into account the measurement errors of the tracking and the muon chambers as well as the multiple scattering and energy loss. The tracks are extrapolated starting from the inner region going outward. This ensures the best treatment for low momentum muons as they deposit a significant portion of their energy until they reach the inner muon chambers. The following track preselection is applied to the muon candidate tracks:

- momentum $p > 1$ GeV
- azimuthal angle $\theta > 20^\circ$
- track starting from CTD superlayer 1 and extending at least to superlayer 3
- distance–of–closest–approach to the reference point $|D_H| < 10$ cm (see Sec. 7.1)
- z position of the distance–of–closest–approach to the reference point $|Z_H| < 75$ cm
- χ^2 per number of degrees of freedom $n.d.f.$ of the track fit $\chi^2_{n.d.f.} < 5$
- distance between a central point on a barrel/rear muon segment and the crossing point of a straight line obtained by continuing the track to the muon chambers $\Delta \leq 150$ cm

The track requirement ensures that the acceptance of the CTD is well under control. The cut on Δ has been safely set after a study of inclusive muon data samples to accept most of the low energy muons.

The extrapolation is terminated at the reference surface where the match with the muon segments is performed. A muon segment can either consist of hits in the inner muon chambers or, if the muon reached the outer muon chambers, it consists of inner chamber hits and the reconstructed momentum using inner and outer hits. The matching χ^2 is given by:

$$\chi^2 = \sum_{i,j} S^{-1}_{ij} \delta_i \delta_j = \delta S^{-1} \delta^T \tag{7.2}$$

where the summation starts at 1 and ends at 4 if the muon segment only consists of a hit in the inner chamber and 5 for segments consisting of hits in the inner and outer chambers. In the latter case, the momentum reconstruction is taken into account in the fit. $\delta = (\delta_1, ..., \delta_n)$ are the residuals $\delta_i = \xi_{M_i} - \xi_{P_i}$ of the measured ξ_{M_i} and predicted ξ_{P_i} track parameters at the reference surface. S^{-1} is the inverse of the covariance matrix of the residuals:

$$S_{ij} = \sum_{k,l} T_{ik}(\sigma^2_{track})_{kl} T^T_{lj} + (\sigma^2_{multi})_{ij} + (\sigma^2_{BRMU})_{ij} \tag{7.3}$$

where $k, l = 1, ..., n$. T is the so called transport matrix of the extrapolation, σ_{track} is the error matrix of the track from the inner tracking detectors, σ_{multi} is the error matrix due to multiple scattering and energy loss and σ_{BRMU} the error matrix of the barrel or rear muon chamber segments. The first two terms are calculated in steps using the detailed geometry and magnetic field information of the ZEUS detector.

7.3.1.2 MPMATCH - A Package to Match FMUON Tracks with Central Detectors

For forward muons, the equivalent algorithm to the BREMAT package is called MPMATCH [79]. It matches tracks in the forward muon chambers with tracks from the CTD while its angular coverage is limited mainly to the overlap between the forward muon chambers and the CTD.

A muon track reconstructed in the FMUON system is given in the ZEUS reference frame by five parameters: $(x, y, dx/dz, dy/dz, Q/p)$. The matching with a track from the CTD starts at a reconstructed FMUON track by opening a corridor in the polar angle θ and the azimuthal angle ϕ around the track. The inner tracking detectors are inspected for tracks located in this corridor. If at least one CTD track is found in the corridor, the FMUON track is extrapolated backwards to the z coordinate of the most outer hit of the CTD track using the GEANE package [78]. A fit between the two tracks is performed using a Kalman filter [75]. The resulting χ^2 is used to identify the best match in the case of more than one CTD track in the corridor.
For the best match, a vertex refit is done for the FMUON track and it is extrapolated backwards to the z coordinate of the vertex. In the end, a fit between the extrapolated FMUON track and the CTD track is carried out including the vertex position.

7.3.1.3 MUBAC - Reconstruction of Muon Candidates in the BAC

The backing calorimeter (BAC) provides a digital (hit) and an analogue (pad) readout which in combination reconstruct muon candidates. The position of the candidates is given in the ZEUS coordinate system taking into account the errors on the measurement. The BAC provides a clean muon signature with a larger geometrical coverage than for the barrel/rear and forward muon chambers especially in the bottom part of the detector and the gaps between the forward and barrel muon chambers. Due to the distance of the BAC from the interaction region and the amount of material on the path of the muon, the BAC imposes a momentum threshold on the reconstructed muon (Barrel: $p_T > 2$ GeV, Forward: $p > 2.8$ GeV, Rear: $p > 1.6$ GeV).

The reconstructed BAC muon candidate is matched with a vertex fitted track from the inner vertex detectors by a simple *distance–of–closest–approach* (DCA) algorithm. A match is required to have a DCA of less than 120 cm. For high quality reconstructed muons, the cut on the DCA is tightened to 50 cm.

7.3.1.4 MV - Reconstruction of Muons from CAL Cell Patterns

The MV algorithm uses the MIP signature of a muon in the CAL to reconstruct muons.
The reconstruction depends on the combination of CAL cell patterns to *clusters* of energy depositions. A two step procedure first forms islands starting from the most energetic CAL cell (seed). All neighbouring cells with non–zero cell content are associated to the island if the direct connection between the seed an the cells crosses only adjacent cells and consists only of cells with non-zero cell content. The associated cells of the island are marked and the island combination is repeated ignoring the marked cells. The centers of the resulting islands are calculated as the energy weighted sum of the corresponding cell centers after a correction using the imbalance of the two photomultiplier measurements per cell.
For the muon identification, the islands are clustered taking into account that muons originate from the interaction vertex. A cluster contains all island cells whose centers are inside a cone of 2α around the connection of the primary vertex and the island center. The clustering starts from the most energetic island and is repeated for all reconstructed islands. The angle α increases by the inclination of the vertex connection to the CAL surface to take into account the geometrical structure of the CAL. The clustering step also combines islands from different part of the CAL to one energy cluster.

The MV finder reconstructs muons from the CAL energy clusters using the *phase space probability function* (PSPF) method [80]. From the cluster reconstruction, eight input variables per cluster are chosen containing the polar θ and azimuthal ϕ angles of the cluster , the energy contents in the electromagnetic and hadronic sections of the CAL $E_{emc}, E_{hac1}, E_{hac2}$ and the number of associated cells in the sections $N_{emc}, N_{hac1}, N_{hac2}$. These variables form an eight–dimensional phase space which is divided into a grid of phase space regions equidistant in the eight variables. The reconstructed CAL clusters of separate MC samples for muons and hadrons are used to calculate probability density functions for each grid bin. The probability densities are later used to distinguish muon clusters from other clusters. The probability can also be used to qualify reconstructed muons.

The reconstructed muon is then matched using a distance–of–closest–approach method similar to the MUBAC matching algorithm.

MV has a good geometrical coverage and a low momentum threshold. The PSPF method results in an efficiency of 90% at a purity of 97.5% [80] but suffers from large hadronic background at low momenta. It is therefore suited for low momentum isolated muons and dimuons but also to supplement other reconstruction algorithms.

7.3.1.5 MUFO - Muon Reconstruction using FMUO and BAC

The *MUFO* reconstruction algorithm matches a track from the forward muon chambers to a track from the CTD similar to MPMATCH (see Sec. 7.3.1.2). It uses MUBAC (see Sec. 7.3.1.3) for additional background rejection and provides a momentum fit of the muon using the FMUO and CTD information. The advantages of the MUFO algorithm are the same as for the MPMATCH. It represents a sophisticated algorithm including a momentum fit using also the forward muon chambers. The MUFO algorithm is also suited for non-isolated muons. The disadvantages for both algorithms are the limited geometrical coverage due to the restriction to the FMUO–CTD overlap region and a high momentum threshold.
So the MPMATCH and MUFO algorithm are used in the following in combination. They are suited for high momentum non–isolated forward muons including muons from semi-leptonic beauty quark decays.
MUFO also provides a mode fitting a FMUON track directly to the vertex without a CTD track. This mode is not used for this thesis.

7.3.1.6 GLOMU - Inclusive Muon Reconstruction at the Third Trigger Level

The muon reconstruction algorithm *GLOMU* [81] at the third trigger level which is also available offline combines the muon track segment reconstruction in the inner barrel and rear muon chambers with the tracking in the CTD and the MIP signature in the CAL.

The following information from the three detector components are included in a χ^2 fit:

muon track segments in the inner barrel and rear muon chambers: muon track segments are reconstructed in the inner barrel and rear muon chambers to reconstruct track segments. For each track the point of entrance and the polar and azimuthal angle θ and ϕ with the associated errors are available.

good quality track in the CTD: a good quality track in the CTD satisfying:

- $\chi^2 \leq 20$,
- $D_H \leq 10$ cm,
- $|z| \leq 75$ cm,
- $\theta \geq 20°$,
- barrel region: $p_T \geq 1$ GeV,
- rear region: $p \geq 1$ GeV

is extrapolated outwards to a fiducial volume outside the CTD. Each extrapolated track provides position, the direction in polar and azimuthal angle θ and ϕ and the momentum and the errors at the fiducial volume.

MIP in the CAL: energy deposits corresponding to a MIP are reconstructed using a specialised MIP finder [82] giving the position in three coordinates and timing information for each MIP.

The matching is carried out separately in the polar and azimuthal angles θ and ϕ for all combinations of the following properties:

- $theta, \phi$ from the CTD track,
- $theta, \phi$ from the B/RMUI track,
- $theta, \phi$ given by the segment connecting the CTD-CAL points,
- $theta, \phi$ given by the segment connecting the B/RMUI-CAL points.

The total χ^2 is the sum of χ^2_θ and χ^2_ϕ. Matches are selected if the $\chi^2 \leq 20$. The GLOMU algorithm has a fairly low p/p_T threshold and reasonably low background. On the other hand, it is only suited for semi-isolated muons, has a reduced geometrical coverage due to the exclusive usage of the inner barrel and rear muon chambers and a moderate efficiency.

7.3.2 GMuon - A General Muon Reconstruction

The above described muon reconstruction algorithms are all suited for specific event topologies concerning for example muon isolation and have different thresholds and geometrical coverage. A general muon reconstruction benefits from redundancies by the combination of all algorithms. The *GMuon* package [83] collects the results of the reconstructions and combines their informations in a general list of reconstructed muon candidates. The qualities of the individual reconstructions are taken as a reference to categorize the muons by assigning a quality factor to each candidate. If a candidate is reconstructed by more than one algorithm, the quality factor is increased to benefit from the simultaneous identification. If the reconstruction of a single algorithm does not yield a sufficient accurate candidate on its own, the possible redundancy with other algorithms is used to recover this candidate.
The GMuon package assigns quality factors in the range of $0-6$ to the candidates from the general list. Quality 0 is the lowest quality whereas quality 6 describes the candidates with the highest reconstruction accuracy. The quality factor stages have been optimized on beauty and background MC samples to decrease the signal–to–background ratio by a factor of the order of 2 when increasing the quality by 1.

Muons with a quality of 4 and better are suited for beauty quark cross section measurements although further kinematic cuts have to be applied to increase the purity (see Cha. 8).
In detail, the different quality stages contain the following combinations of the individual muon reconstructions:

Quality 6**:** contains muon candidates reconstructed by

category 1: BREMAT requiring a muon reconstructed in the inner and outer muon chambers and a fit to a vertex track

category 2: MPMATCH or MUFO requiring a muon reconstructed with a probability of $p_{\texttt{MPMATCH}\vee\texttt{MUFO}} \geq 0.05$ and fitted to a vertex track

Quality 5**:** contains muon candidates reconstructed by

category 1: MPMATCH or MUFO requiring a muon reconstructed with a probability of $0.01 \leq p_{\texttt{MPMATCH}\vee\texttt{MUFO}} < 0.05$ and fitted to a vertex track

category 2: BREMAT requiring a muon reconstructed only in the inner muon chambers fitted to a vertex track supplemented by

- MUBAC reconstruction with a DCA < 120 cm **OR**
- MV reconstruction with a MIP probability of $p_{\text{MIP}} > 0.6$

category 3: all muons for $\theta_\mu > 122.5°$ or $\theta_\mu < 57.7°$ (not central) not found by MPMATCH, MUFO or BREMAT requiring:

- MUBAC reconstruction with a DCA < 120 cm **AND**
- MV reconstruction with a MIP probability of $p_{\text{MIP}} > 0.6$

Quality 4**:** contains muon candidates reconstructed by

category 1: BREMAT requiring a muon reconstructed only in the inner muon chambers fitted to a vertex fitted track

category 2: MUFO requiring

- $p_{\texttt{MUFO}} \geq 0.01$
- $p > 3$ GeV
- more than 2 used forward muon chamber planes

category 3: MUBAC requiring a DCA < 50 cm of the reconstructed muon to a vertex track

category 4: MUBAC requiring a DCA < 120 cm of the reconstructed muon to a vertex track supplemented by

- MV requiring a MIP probability of $p_{\text{MIP}} > 0.6$

7.3.2.1 Quality Correction for Forward Muons

MPMATCH or MUFO use the hits in the forward muon chambers to reconstruct muon tracks. As the forward muon chambers are very close to the beampipe, photons from lepton bremsstrahlung and secondary particles emitted by the proton can induce hits in the chambers. In addition, if the muon track does not start at the innermost detector plane, the quality of the track match with the CTD decreases. A modification of the muon quality is applied to reduce the quality of a muon reconstructed by MPMATCH or MUFO to take into account the above described effects. The reduction of spurious hits in the forward muon chamber is correlated with the number of used detector planes by the forward muon track fit. If more than 4 planes are used, no reduction is required, if 4 planes are used, the quality is reduced by 2 and if only 3 planes are used, the quality is reduced by 4. The minimal used number of planes for a forward muon track is 3. Therefore, correction for less than 3 used planes are not necessary.
The track match quality is correlated with the starting plane of the forward muon track. If the first used hit in the muon chambers is in the innermost plane, a modification of the quality of the muon is not necessary. If the first hit of the track is not in the first plane, the quality is decreased by 1.
The modified quality can be recovered by the redundancy with the MUBAC and MV algorithm. If the muon is reconstructed in addition to MPMATCH or MUFO by MUBAC, the quality is increased by 1, if it is reconstructed in addition by MV, increased by two. The increase in the quality is guaranteed not to exceed the initial muon quality before the complete quality correction.

If the forward muon ($\eta > 1.2$) is only found by MUBAC without using the forward muon chambers, the quality is reduced by 1 to correct for noise in the BAC.

7.3.2.2 Monte Carlo Efficiency Correction

The detector simulation is an important ingredient for the cross section measurement. MC generated event samples simulating the actual detector output are needed to determine the acceptance of the event reconstruction and selection. The implementation of the forward and barrel/rear muon chamber and BAC efficiencies in the detector simulation is not as perfect compared to other detector components. Therefore, their efficiency simulation has to be corrected by applying corrections to the MC samples on an event by event basis. These corrections are determined by the comparison of muon reconstruction efficiencies from MC simulated events with data events.

This section describes the determination and the application of the efficiency correction of the muon chamber and BAC detector components determined for the general muon reconstruction. The different detector components correspond to individual reconstruction algorithms. The MUBAC algorithm corresponds to the BAC, the BREMAT algorithm to the barrel/rear muon chambers and the MPMATCH and MUFO algorithms to the FMUON chambers. The correction of a simulated MC event depends on the combination of the algorithms which reconstructed the muon.

The correction has to be determined individually for all the algorithm combinations used in the above described quality stages. The two step implementation first determines muon reconstruction efficiencies separately for the three algorithms in reference to a fourth muon reconstruction for suited data and

MC samples. The second step uses these efficiencies to calculate the correction depending on the algorithm combination individually for each reconstructed muon. To unfold the kinematic dependencies, the efficiencies are determined differentially in the muon momentum p_T^μ and the muon pseudo-rapidity η^μ.

The decay $J/\psi \to \mu^+\mu^-$ is chosen as the source of muons due to its simple and easily selectable topology of two isolated muons. Due to this choice, the MV algorithm can be used as a reference because it is well suited for isolated muons and uses the CAL for the reconstruction which is an independent detector component with respect to the ones under investigation.
A clean J/ψ sample is selected using the following cuts:

- cut on the global event timing determined from the CAL relative to the bunch crossing: $|T_g| \leq 10$ ns
- cut on the vertex position:
  - $|z_{vertex}| \leq 50$ cm
  - non zero vertex in x and y: $x_{\texttt{vertex}} \neq 0$ cm, $y_{\texttt{vertex}} \neq 0$ cm
  - $\sqrt{x^2_{\texttt{vertex}} + y^2_{\texttt{vertex}}} \leq 3$ cm
- at least two muons reconstructed with GMuon of a quality of 1 or greater
- maximal number of vertex tracks: $n_{\texttt{vertex-track}} \leq 2$
- at least one dimuon system with
  - different charge of the two muons
  - invariant mass: 2 GeV $\leq m_{\mu^+\mu^-} \leq$ 4 GeV: the large mass window takes also muons from other usable processes (for example Bethe–Heitler processes) into account. The background is sufficiently suppressed by the complete selection.
  - angular distance between the two muons: $\Delta R = \sqrt{\Delta\eta^2 + \Delta\phi^2} > 0.5$
  - angular distance in θ between the two muons: $\Delta\theta = \sqrt{(\theta_{\mu_1} - (\pi - \theta_{\mu_2}))^2} > 0.0157$ to reject perfectly back–to–back muons for cosmics rejection
  - angular distance in ϕ between the two muons: $\Delta\phi = \sqrt{\left(\sqrt{(\phi_{\mu_1} - \phi_{\mu_2})^2} - \pi\right)^2} > 0.0157$ to reject perfectly back–to–back muons for cosmics rejection

The efficiency correction has to be determined separately for the pre–upgrade and post–upgrade running periods to consider changes in the detector layout and corresponding changes in the detector simulation. As systematic discrepancies in the shapes of the kinematic muon variables between data and MC simulation are not significant if the bins of the differentially determined efficiencies are sufficiently small, the data and MC samples only have to provide a sufficiently large amount of J/ψ events.

To avoid trigger biases, a special treatment of the muon handling dependent on the trigger is implemented. Therefore, the online muon reconstruction using the GLOMU algorithm is repeated offline to determine whether a reconstructed muon has triggered the event. Both muons from the dimuon pair can be used for the efficiency correction if the event is triggered by at least one non-muon trigger. If the event is triggered by a muon trigger which uses the muon chambers to reconstruct muons, the muon which triggered the event has to be excluded from the efficiency determination.
In the case of the J/ψ selection, if one of the muons of the dimuon pair triggered the event, only the other can be used for the efficiency determination. If both triggered the event, both can be used. Starting from the first muon which triggered the events, the second should be included in the event. But the second triggered also the event, resulting in the inclusion of the first. As both muons include the other in the correction, each of them is unbiased by the trigger and both can be included.

The used data samples are summarised in Tab. 7.2 and the used MC samples in Tab. 7.3
The available data and MC samples provide a sufficient amount of statistics for the pre–upgrade periods. The post–upgrade period corrections are currently still limited by the small available MC luminosity.

run period	luminosity [pb^{-1}]	selected events
96-97	38.62	16987
98-99	16.68	7429
99-00	65.88	26061
03-04	39.71	11992

Table 7.2: Data samples used for the efficiency correction determination of the muon reconstruction

run period	MC generator	characteristics	luminosity [pb^{-1}]	events
96-97	HERWIG [84]	inelastic $J/\psi \to \mu^+\mu^-$	38.18	4343
	DIPSI [85]	elastic $J/\psi \to \mu^+\mu^-$	6.75	17354
	DIPSI	elastic $J/\psi \to \mu^+\mu^-$	2.71	6972
	HERACLES [86]	elastic $J/\psi \to \mu^+\mu^-$	4.01	27761
	GRAPE [87]	elastic $J/\psi \to \mu^+\mu^-$	1135.32	38973
98-99	HERWIG	inelastic $J/\psi \to \mu^+\mu^-$	18.16	2257
	DIPSI	elastic $J/\psi \to \mu^+\mu^-$	55.18	82
	HERACLES	elastic $J/\psi \to \mu^+\mu^-$	75.49	32025
99-00	HERWIG	inelastic $J/\psi \to \mu^+\mu^-$	60.43	7307
	DIPSI	elastic $J/\psi \to \mu^+\mu^-$	7.23	27760
03-04	DIPSI	elastic $J/\psi \to \mu^+\mu^-$	13.19	43457

Table 7.3: MC samples available for the efficiency correction determination of the muon reconstruction

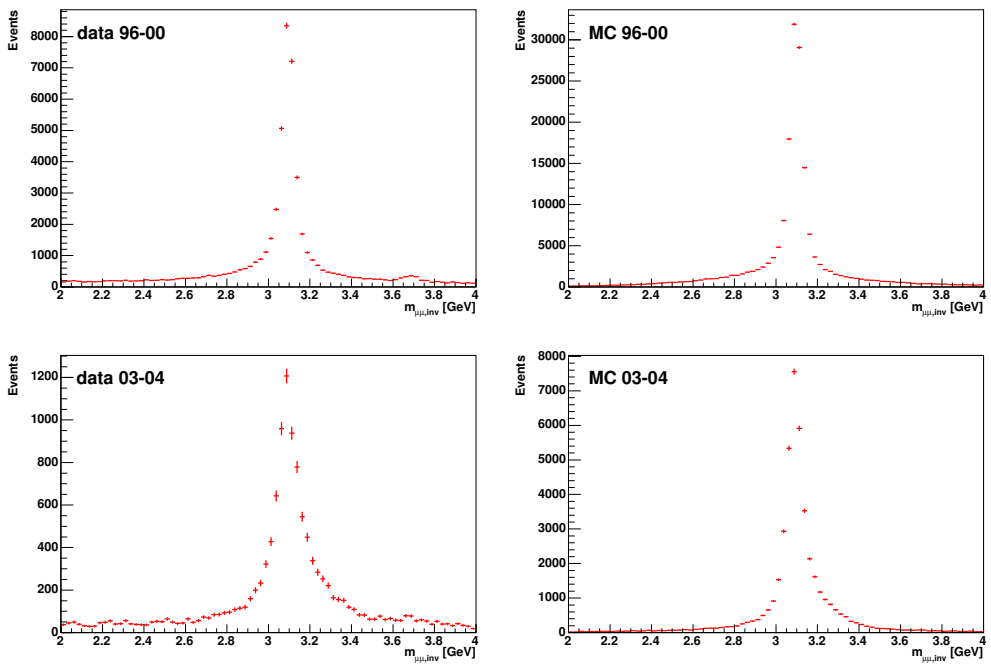

Figure 7.4: Dimuon invariant mass spectra for efficiency correction. *Top:* $m_{\mu\mu,inv}$ for data (*left*) and MC (*right*) samples from the run periods 96-00. *Bottom:* $m_{\mu\mu,inv}$ for data (*left*) and MC (*right*) samples from the run periods 03-04.

Fig. 7.4 shows the dimuon invariant mass spectrum from the data samples and from the MC samples for pre– and post–upgrade running periods.
The mass spectra show clear peaks at the J/ψ mass of 3.097 GeV [8] with a very low background contamination. Not all of the reconstructed dimuons with off-peak invariant masses contain background events. Also other processes with usable muon signatures like Bethe–Heitler processes are contained.

The selected J/ψ samples are used to calculate the data and MC efficiencies. The individual efficiencies ϵ are determined by the fraction of muons reconstructed by MV and BREMAT, MPMATCH, MUFO or

MUBAC and all muons reconstructed by MV (see Eq. 7.4):

$$\begin{aligned} \epsilon_{\texttt{FMUO}} &= \frac{N_{\texttt{MV}\wedge(\texttt{MPMATCH}\vee\texttt{MUFO})}}{N_{\texttt{MV}}} \\ \epsilon_{\texttt{BRMUO}} &= \frac{N_{\texttt{MV}\wedge\texttt{BREMAT}}}{N_{\texttt{MV}}} \\ \epsilon_{\texttt{BAC}} &= \frac{N_{\texttt{MV}\wedge\texttt{MUBAC}}}{N_{\texttt{MV}}} \end{aligned} \tag{7.4}$$

where N is the number of reconstructed muons from the J/ψ samples by the given muon reconstruction algorithm.

As an example for the result of the efficiency determination for the pre–upgrade running periods, the efficiencies for a transverse muon momentum range of 2.0 GeV $\leq p_T^\mu <$ 2.2 GeV for BREMAT and MUBAC and for $p_T^\mu \geq$ 2.0 GeV for MPMATCH are shown in Fig. 7.5 as a function of η^μ.

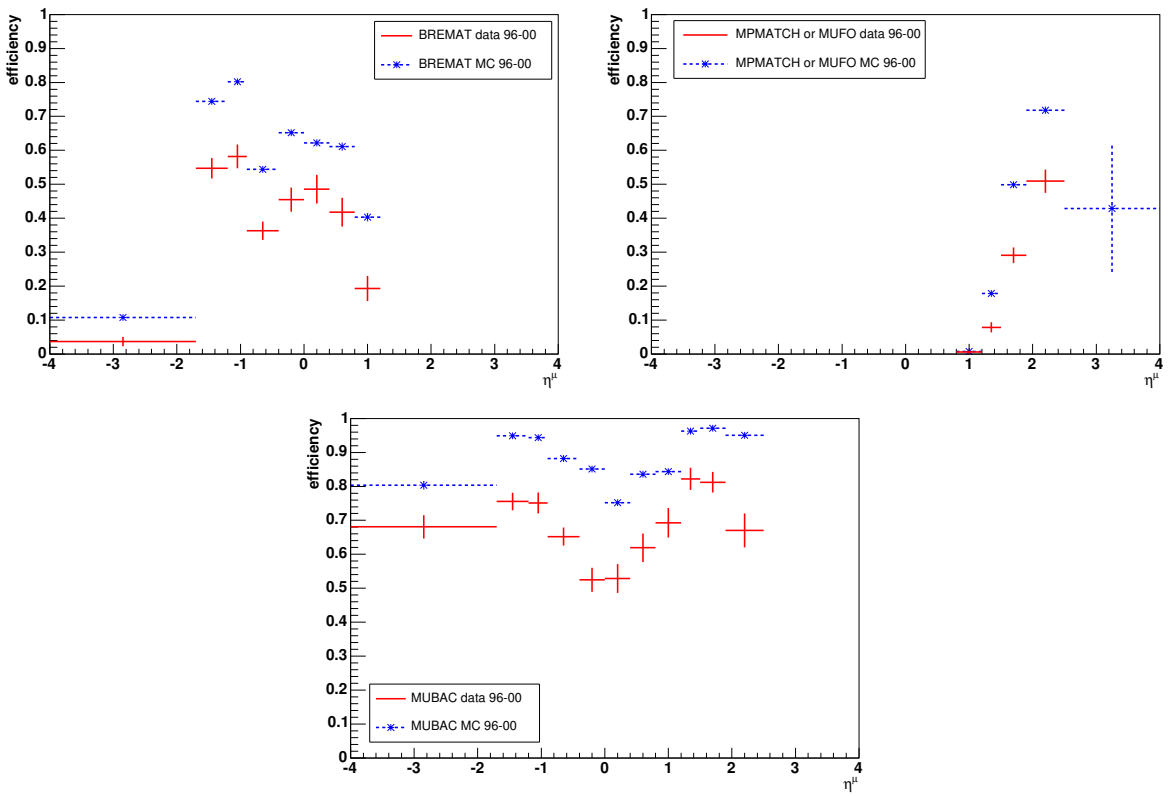

Figure 7.5: Exemplary muon reconstruction efficiencies from data and MC as a function of η^μ for 2.0 GeV $\leq p_T^\mu <$ 2.2 GeV for the barrel and rear muon chambers (BREMAT, *top left*) and the BAC (MUBAC, *bottom*) and for $p_T^\mu \geq$ 2.0 GeV for the forward muon chambers (MPMATCH, *top right*) in reference to the CAL muon reconstruction (MV) for pre–upgrade running periods.

The application of the efficiency correction to MC events

$$c = \frac{\epsilon^{\texttt{Data}}}{\epsilon^{\texttt{MC}}} \tag{7.5}$$

has to take into account the characteristics of each individual reconstructed muon. Depending on the combination of the algorithms which reconstructed the muon, the correction c is determined from the data and MC efficiencies ϵ_I^j where i is BREMAT, MPMATCH or MUBAC and j is data or MC corresponding to the transverse momentum p_T^μ and the pseudo-rapidity η of the reconstructed muon. The following cases have to be treated separately requiring a minimal quality of 4 of the reconstructed muon plus the forward muon quality modifications:

Muon reconstructed by BREMAT and by MUBAC:

$$c(p_T^\mu, \eta^\mu) = \frac{\epsilon^{\texttt{Data}}_{\texttt{BREMAT}}(p_T^\mu, \eta^\mu)}{\epsilon^{\texttt{MC}}_{\texttt{BREMAT}}(p_T^\mu, \eta^\mu)} \frac{\epsilon^{\texttt{Data}}_{\texttt{MUBAC}}(p_T^\mu, \eta^\mu)}{\epsilon^{\texttt{MC}}_{\texttt{MUBAC}}(p_T^\mu, \eta^\mu)} \tag{7.6}$$

Muon reconstructed by BREMAT and not by MUBAC:

$$c(p_T^\mu, \eta^\mu) = \frac{\epsilon^{\texttt{Data}}_{\texttt{BREMAT}}(p_T^\mu, \eta^\mu)}{\epsilon^{\texttt{MC}}_{\texttt{BREMAT}}(p_T^\mu, \eta^\mu)} \frac{1 - \epsilon^{\texttt{Data}}_{\texttt{MUBAC}}(p_T^\mu, \eta^\mu)}{1 - \epsilon^{\texttt{MC}}_{\texttt{MUBAC}}(p_T^\mu, \eta^\mu)} \tag{7.7}$$

Muon reconstructed by MUBAC and not by BREMAT:

$$c(p_T^\mu, \eta^\mu) = \frac{1 - \epsilon^{\texttt{Data}}_{\texttt{BREMAT}}(p_T^\mu, \eta^\mu)}{1 - \epsilon^{\texttt{MC}}_{\texttt{BREMAT}}(p_T^\mu, \eta^\mu)} \frac{\epsilon^{\texttt{Data}}_{\texttt{MUBAC}}(p_T^\mu, \eta^\mu)}{\epsilon^{\texttt{MC}}_{\texttt{MUBAC}}(p_T^\mu, \eta^\mu)} \tag{7.8}$$

Muon reconstructed by MPMATCH and by MUBAC:

$$c(p_T^\mu, \eta^\mu) = \frac{\epsilon^{\texttt{Data}}_{\texttt{MPMATCH}}(p_T^\mu, \eta^\mu)}{\epsilon^{\texttt{MC}}_{\texttt{MPMATCH}}(p_T^\mu, \eta^\mu)} \frac{\epsilon^{\texttt{Data}}_{\texttt{MUBAC}}(p_T^\mu, \eta^\mu)}{\epsilon^{\texttt{MC}}_{\texttt{MUBAC}}(p_T^\mu, \eta^\mu)} \tag{7.9}$$

Muon reconstructed by MPMATCH and not by MUBAC:

$$c(p_T^\mu, \eta^\mu) = \frac{\epsilon^{\texttt{Data}}_{\texttt{MPMATCH}}(p_T^\mu, \eta^\mu)}{\epsilon^{\texttt{MC}}_{\texttt{MPMATCH}}(p_T^\mu, \eta^\mu)} \frac{1 - \epsilon^{\texttt{Data}}_{\texttt{MUBAC}}(p_T^\mu, \eta^\mu)}{1 - \epsilon^{\texttt{MC}}_{\texttt{MUBAC}}(p_T^\mu, \eta^\mu)} \tag{7.10}$$

Muon reconstructed by MUBAC and not by MPMATCH:

$$c(p_T^\mu, \eta^\mu) = \frac{1 - \epsilon^{\texttt{Data}}_{\texttt{MPMATCH}}(p_T^\mu, \eta^\mu)}{1 - \epsilon^{\texttt{MC}}_{\texttt{MPMATCH}}(p_T^\mu, \eta^\mu)} \frac{\epsilon^{\texttt{Data}}_{\texttt{MUBAC}}(p_T^\mu, \eta^\mu)}{\epsilon^{\texttt{MC}}_{\texttt{MUBAC}}(p_T^\mu, \eta^\mu)} \tag{7.11}$$

The corrections applied to the MC is shown in Fig. 7.6 for all selected muons from the beauty quark selection (see Cha. 8) for pre– and post–upgrade running periods. The correction factor is set to maximal 4 to compensate run-away efficiencies in low–statistics regions. Also care is taken that a valid correction for a muon can be calculated. In particular the BAC efficiency in the MC is near perfect. If a muon is not found by the BAC but by another MUON finder under investigation because the muon barely reached the BAC, the denominator of the correction calculation can be zero. In the case of zero denominators in the calculation, no correction is applied and the correction factor is set to 1. It is taken care that less than 1% of all corrected muons in a sample show this characteristics.

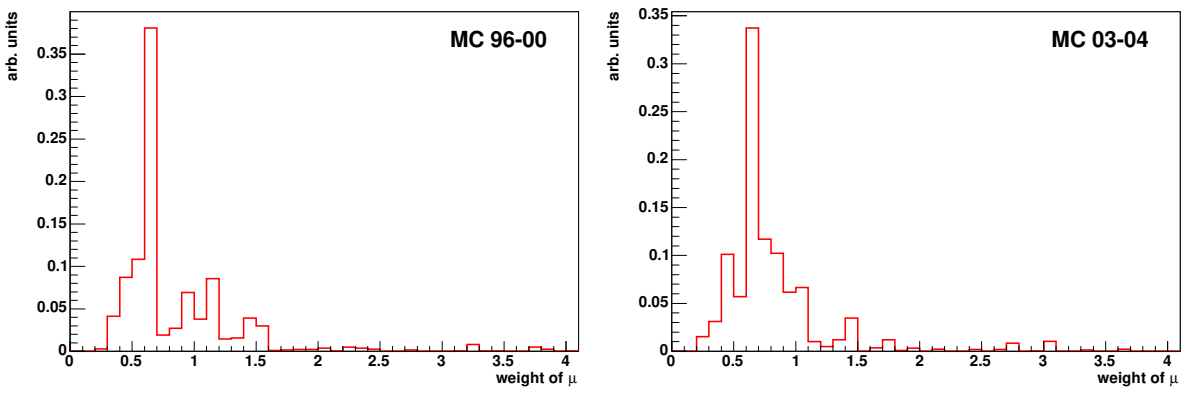

Figure 7.6: Pre– and post–upgrade muon efficiency correction factors for beauty and background MC for all selected muons by the beauty quark selection (see. Cha. 8).

For now, the fake muon contribution to the background MC samples is corrected in the same way as true muons. Future studies of the fake muon background description are in preparation and will investigate possible changes in the correction for these categories of reconstructed muons.

7.4 Reconstruction of the Hadronic System

The energy measurement of particles is an important ingredient to the reconstruction of the event properties. The energy resolution of the CAL (see Eqs. 5.3 and 5.4 in Sec. 5.2.3) is $\sigma(E)/E \sim 1/\sqrt{E}$ and decreases for higher particle energies whereas at lower particle energies, the resolution of the track reconstruction (see Eqs. 5.1 and 5.2 in Sec. 5.2.1) gives a better energy estimate [88] (see Fig. 7.7).

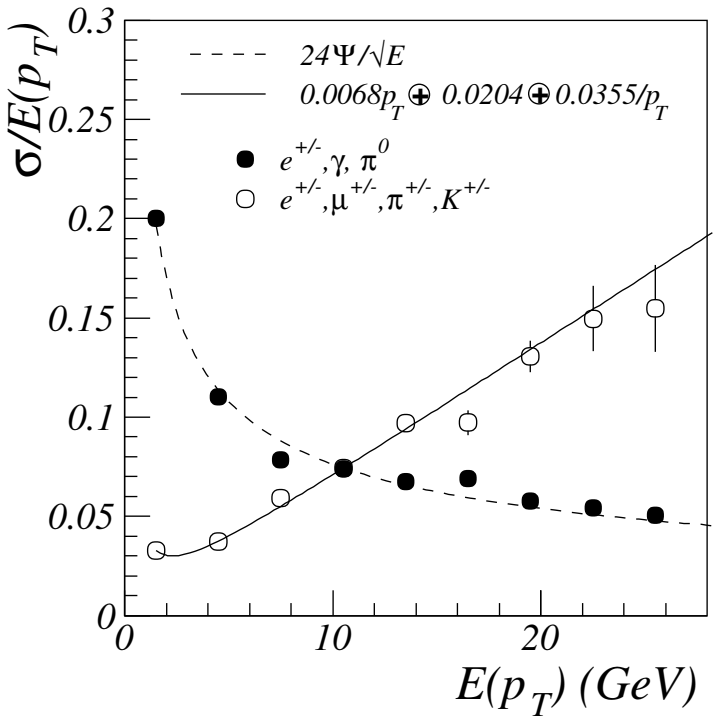

Figure 7.7: Resolutions from single particle MC simulations. The track transverse momentum resolution in the CTD (*open markers*) and the CAL energy resolution (*closed markers*) is shown.

To benefit from the most accurate energy determination in both energy ranges, the track reconstruction and the CAL energy measurement is combined to *energy flow objects* (EFO's). The track information is mainly used below $10 - 15$ GeV and the calorimetric energy measurement above to form four–vectors representing the oriented energy deposition of particles traversing the detector.

The combination process and corrections due to dead material influences and the presence of a muon are described in the following.

7.4.1 Reconstruction of Energy Flow Objects

The reconstruction procedure of EFO's [88] consists of two stages which take care of the geometrical separation of the different energy measurements in the CAL (see Sec. 5.2.3).

The first stage clusters energy cell measurements separately in the three sections of the CAL (FCAL, BCAL and RCAL) and the different cell layers (electromagnetic and hadronic cells). All cells are clustered to *islands* by starting from the highest energetic cell and associating all non–zero cell measurements with direct adjacent or indirect connections to the first. An indirect connection has to contain only non–zero cell measurements and is also not allowed to cross section and layer borders.
In the second stage, the islands belonging to a shower of a single particle or a jet of particles are grouped into *cone islands*. The matching starts from the most outward islands in the hadronic sections and proceeds inward by calculating the angular separation to neighbouring islands in polar and azimuthal angles θ, ϕ. The separation is transformed to a matching probability according to a single pion MC simulation [88]. Afterwards, all islands with a probability above a threshold are grouped into a cone island starting from the islands in the electromagnetic sections.

The cone island center is calculated as the energy weighted mean of the cell centers which have been corrected for the imbalance of the two photomultiplier measurements per cell. The energy weight is determined logarithmically rather than linearly to cope with the observed systematic bias due to the varying cell projectivity resulting from the CAL geometry.

For the track reconstruction (see Sec. 7.1), vertex fitted tracks with hits in at least 4 superlayers are selected in the transverse momentum range 0.1 GeV $< p_T^{\texttt{track}} <$ 20 GeV. If the track has hits in more than 7 superlayers, the upper transverse momentum cut is raised to $p_T^{\texttt{track}} <$ 25 GeV. The tracks are extrapolated to the inner CAL surface taking into account the magnetic field geometry and further into the CAL by a linear approximation using the track momentum vector at the CAL surface.
The matching of a track to a cone island uses the distance–of–closest–approach (DCA) method. A match is assigned between the extrapolated track and the cone island center (see Fig. 7.8)

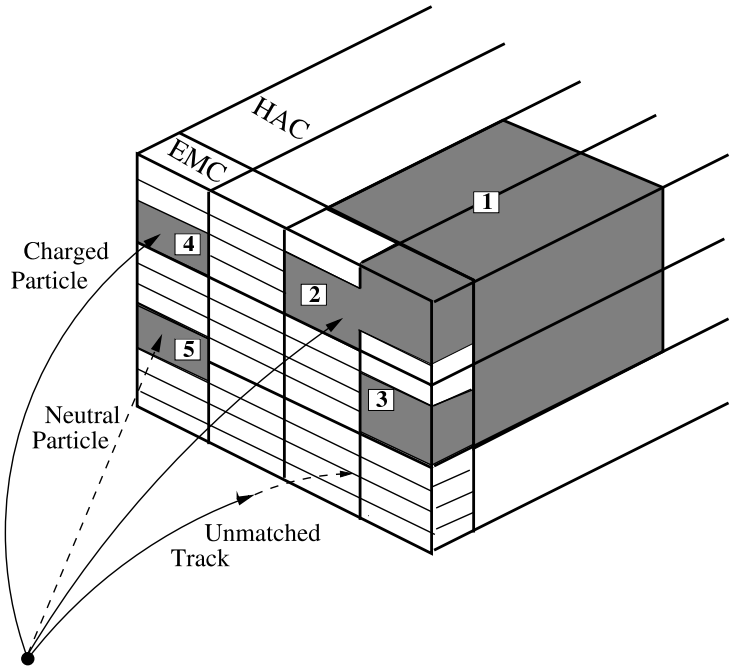

Figure 7.8: Reconstruction of EFO's by a match between CAL cells clustered into cone islands (HAC cell 1 and EMC cells 2 and 3 are joined to form a cone island) and tracks. The different match categories of a charged particle (track is matched to cone island 4), neutral particle (no track is matched to cone island 5) and unmatched track are shown.

if the distance is closer than the cone island radius or an minimal radius of $r_{\texttt{min}} = 20$ cm optimized using MC simulations to maximise the track–island matching efficiency for single particle CAL clusters:

$$\mathrm{DCA} \leq \max(\mathrm{r}_{\texttt{min}}, \mathrm{r}_{\texttt{island}}). \tag{7.12}$$

The track information is used instead of the CAL cone island measurement for the determination of the four–vector if:

- the relative uncertainty on the momentum determination is lower than the uncertainty on the energy measurement (see Fig. 7.7):
$$\sigma(p)/p < \sigma(E_{cal})/E_{cal} \tag{7.13}$$
where $\sigma(p)$ and $\sigma(E_{cal})$ are the resolutions of the momentum from the tracking and the energy in the CAL respectively;

- the track momentum exceeds the energy measurement in the CAL within the resolution on the measured ratio E_{cal}/p:
$$e_{cal}/p < 1.0 + 1.2 \cdot \sigma(E_{cal}/p) \tag{7.14}$$
where $\sigma(E_{cal}/p) = (E_{cal}/p^2)\sigma(p) \oplus (1/p)\sigma(E_{cal})$.

As muons are minimum ionising particles (MIP's) and lose their energy dominantly by ionisation, the measured energy in the CAL is not proportional to the momentum. Therefore, EFO's having the properties of a muon are treated differently and the tracking information is favoured over the energy measurement if:

- $E_{cal} < 5$ GeV;
- $E_{cal}/p < 0.25$;
- $p_T < 30$ GeV.

In addition to the described clean matches of one track to one cone island, the following categories of EFO's are treated similarly to determine the four–vector from the tracking information or the CAL energy measurement:

- tracks without an associated island are treated as charged particles and the CTD information is used under the assumption that the particle is a pion;
- cone islands not matched to a track are treated as neutral particles and the CAL energy measurement is used;
- cone islands with more than three associated tracks are treated as jets and the CAL information is used.

7.4.2 Correction of the Cone Islands

Comparisons between data and MC simulations have shown discrepancies in the reconstruction of EFO's using calorimetric islands [89]. The following corrections have been applied to the EFO's:

Energy loss in inactive material: Energy losses due to dead material are generally difficult to implement fully into the MC simulation. A detailed dead material map (see Fig. 7.9) is used to correct the contribution to the energy loss of mainly the beam pipe, the tracking detectors and the solenoid. The dead material contribution between the interaction point and the calorimeter varies with the

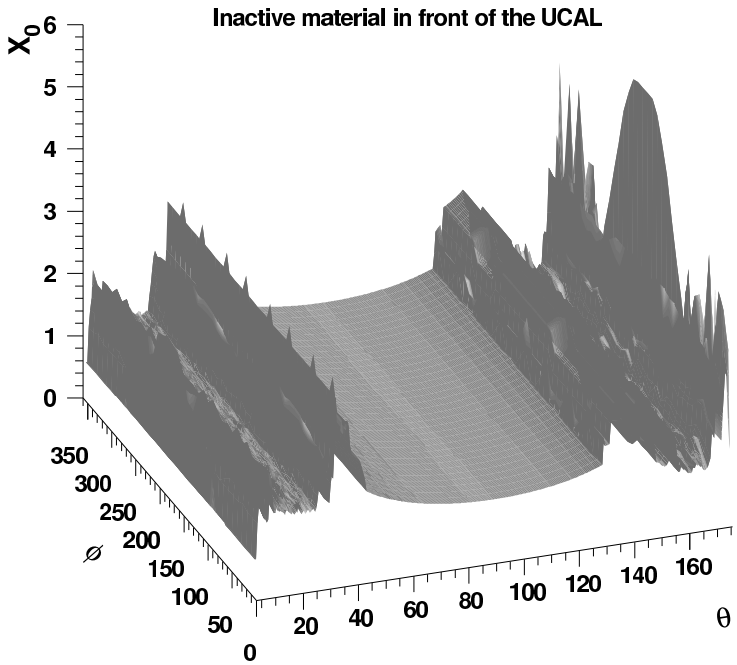

Figure 7.9: Map of the dead material distribution between the interaction region and the CAL as a function of θ and ϕ.

polar angle between 1 and 3 radiation lengths X^0 and is more significant for low energy particles. Corrections on the EFO's are introduced depending on the polar angle and the cone island energy.

Calorimeter geometry: The zones of the cracks between the calorimeter sectors are not well simulated and corrections are introduced.

Energy overestimation of low momentum hadrons: Protons and pions with momenta below $\sim$ 1 GeV lose energy mainly through ionisation without hadronic interactions. In this case, the CAL is not compensating anymore ($e/h \sim 0.6$). This effect causes an overestimation of the energy of low-momentum hadrons and is corrected.

7.4.3 Corrections for the Presence of a Muon

The reconstruction of the hadronic system of an event only from the CAL measurement would lead to an underestimation of the energy due to the presence of a muon. For a muon, a minimum ionising particle (MIP), the energy loss while traversing the CAL is dominated by ionisation and therefore the measured energy is not proportional to and usually less than the momentum.
If EFO's are used to reconstruct the hadronic system, this effect is compensated because EFO's have been optimised to correctly take the muonic energy signature in the CAL into account and favour the tracking information over the CAL measurement. This is only sufficient for semi-isolated muons. If the muon is contained in a hadron jet, like required for this analysis, and the corresponding EFO's represent more than one particle, further corrections have to be applied.

The energy release of a muon in the CAL is parametrised as a function of the polar angle θ using single muon MC simulations (see Fig. 7.10).

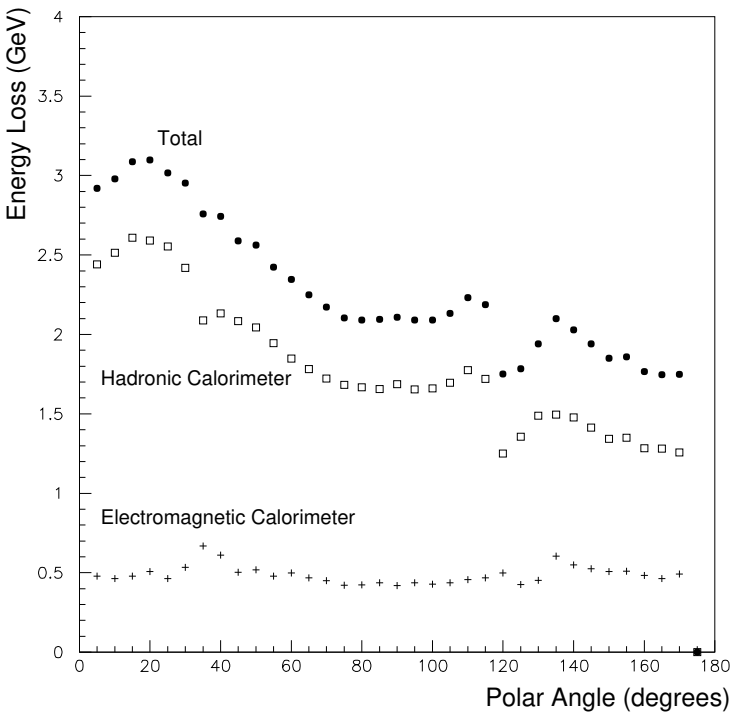

Figure 7.10: Energy loss of a muon in the CAL as a function of the polar angle θ (full circles) and the energy fractions in the electromagnetic (crosses) and hadronic (open squares) calorimeter sections.

A correction of the EFO corresponding to a muon is applied using the expected energy loss in the CAL. The correction is applied to EFO's consisting at least of a track. The muons are extracted from the general muon reconstruction (see Sec. 7.3) and are preselected by the following cuts to ensure a good quality muon:

- quality of the muon ≥ 4
- muon track is a vertex fitted track
- $p > 1$ GeV

The association of the muon to the EFO is carried out by the used track. The following corrections to the EFO's are applied per muon:

- If the EFO uses the track information for the energy determination, the EFO four–vector is determined from the reconstructed muon properties.
- If the EFO uses the CAL measurement for the four–vector determination and the energy of the EFO is between 50% and 150% of the predicted energy loss of a muon $0.5E_{\texttt{MIP}} \leq E_{\texttt{EFO}} \leq 1.5E_{\texttt{MIP}}$, the EFO four–vector is determined from the reconstructed muon properties.
- If the EFO uses the CAL measurement for the four–vector determination and the energy of the EFO is larger than 150% of the predicted energy loss of a muon $E_{\texttt{EFO}} > 1.5E_{\texttt{MIP}}$, a new EFO corresponding to the reconstructed muon is added and subtracted from the initial. Now, the muon contribution to the hadronic system is correctly reconstructed.
- If the EFO uses the CAL measurement for the four–vector determination and the energy of the EFO is less than 50% of the predicted energy loss of a muon $E_{\texttt{EFO}} < 0.5E_{\texttt{MIP}}$, the EFO four–vector is determined from the reconstructed muon properties.

7.5 Jet Reconstruction

The last step in the reconstruction of the event properties of semi-leptonic beauty quark decays into muons is the identification of the partons of the hard interaction. The properties of the partons are strongly correlated with the hadronic system originating from their hadronisation/fragmentation. This system is represented by a large amount of hadronic energy in a small angular region also called a jet of hadrons. In this analysis, the aim of the jet reconstruction is the unambigious identification of hadron jets from the EFO's (see Sec 7.4).
As jets are not uniquely defined in QCD and their definition relies on the implementation of the jet algorithm, early efforts started to define standards for jet algorithms to guarantee the universal applicability [90]. A jet finder especially suited for *ep* collisions has to fulfill the following requirements:

- simple application in experimental analyses and theoretical calculations;
- *collinear safety:* the resulting jets have to be independent of one parton splitting into two partons moving collinearly. Translated to the experimental point of view, the jet algorithm has to be independent of a particle releasing energy in two adjacent CAL cells;
- *infrared safety:* the resulting jets have to be independent of the emission of very low energy particles. Experimentally, this is related to the noise in the detector;
- correct treatment of beam remnants especially of the proton and if present of the photon;
- independence from longitudinal Lorentz transformations to accommodate for the usually boosted frame of interest.

In this analysis, a $k_\perp$*-type clustering algorithm* [91] is used to accommodate for these requirements. The clustering approach has the advantage of unambiguously assigning the EFO's to a jet whereas the resolution of the jets depends on the relative transverse momentum of the combined objects. This defines an effective radius depending on the hardness of the jet. The jet algorithm is implemented by the definition of:

- a test variable (energy-angle resolution) d_{kl} to specify whether two hadrons h_k and hl belong to the same cluster;
- a recombination procedure which defines the relation of the cluster resolution variables to the hadron variables;
- a hard scattering scale to separate hard and soft processes.

The used *KTCLUS* algorithm interactively clusters the EFO's into jets using the following prescription:

1. the resolution variables d_{kl} and d_k, d_l are calculated for all pairs of EFO's e_k and e_l and for the individual hadrons:

$$d_k = p_T^k \tag{7.15}$$
$$d_{kl} = \min(p_T^k, p_T^l)\Delta R_{kl}^2 \tag{7.16}$$

   where $\Delta R_{kl}^2 = \Delta\eta_{kl}^2 + \Delta\phi_{kl}^2$

2. The smallest resolution variable from the list of $\{d_k, d_{kl}\}$ is determined:

   - If d_{ij} is the smallest resolution variable, the two EFO's e_i and e_j are combined into a single *pseudoparticle* according to the *E recombination scheme* where the hadrons are treated as massive particles and their four–vectors are added: $p_{(ij)} = p_i + p_j$. The corresponding resolution variables are given by:

$$d_{(ij)} = (\vec{p}_{T,i} + \vec{p}_{T,j})^2 \tag{7.17}$$
$$d_{(ij)k} = \min((\vec{p}_{T,i} + \vec{p}_{T,j})^2, (\vec{p}_{T,k})^2)\Delta R_{(ij)k}^2 \tag{7.18}$$

     where $\Delta R_{(ij)k}^2 = (y_{(ij)} - \eta_k)^2 + \Delta\phi_{(ij)k}^2$ to guarantee the longitudinally boost invariance.
   - If d_k is the smallest resolution variable, e_k is included in the *remnant jets* and taken out of the list.

3. This procedure continues until all particles and pseudoparticles not included in the remnant jets have resolution variables larger than the hard scale $d_{\mathtt{cut}}$ where $\Lambda^2 \ll d_{\mathtt{cut}} \ll S$ with Λ the QCD scale and $\sqrt{s}$ the centre–of–mass energy.

This procedure results in *hard final state jets* and remnant jets. The E recombination scheme is favoured over other recombination schemes [91] because the massive approach describes the jets of heavy flavour beauty quarks with the smallest difference between the reconstruction of the detector measurement and the theoretical calculation [16].

The EFO's corresponding to reconstructed muons are marked during the correction for the presence of a muon (see Sec. 7.4.3). The EFO's are input to the jet clustering algorithm which tracks the individual EFO's through the clustering procedure and therefore assigns individual EFO's to jets. By the relation $\mu \rightarrow EFO \rightarrow jet$, the muon is unambiguously assigned to a jet which will be later used in the beauty quark identification method.

Chapter 8

Event Selection

For the analysis of semi-leptonic beauty decays into muons in the photoproduction regime, a dijet plus muon event selection is applied to data and MC events. The selection requires the presence of at least a muon and at least two high-p_T jets in the reconstructed final state.
After the introduction of the available data samples for the pre– and post–upgrade running periods, the MC samples for the signal and background are summarized. They are needed for the statistical methods to extract the beauty content from the data which is described in chapter 9. The adequate simulation of the shapes of final state kinematic variables is required for the applicability of the statistical extraction methods.
During the detailed presentation of the event selection, comparisons between data and MC distributions are shown to investigate the quality of the MC description.

8.1 Data and MC Samples

During the upgrade of the HERA accelerator and the ZEUS detector 2000/2001, significant changes have been made to the detector by the integration of new tracking detectors and to the collider by the increase of the possible delivered luminosity (see chapter 5). Therefore, the data and MC samples have been separated into the pre– and post–upgrade running periods.
The available data samples for the pre– and post–upgrade running periods are summarised in Tab. 8.1. The luminosities from the ZEUS luminosity measurement (see Sec. 5.2.6) and the colliding particles are given per running period. Special care has been taken for the correct operation of the forward and barrel/rear muon chambers during data taking. Runs with bad barrel/rear muon chamber running conditions have been identified by the barrel/rear data–quality-monitoring and have been removed from the list of available data samples. The FMUON operability has been investigated in the same way but only reconstructed forward muons have been removed in the questionable runs.

running period	hadron	lepton	luminosity [pb^{-1}]
1996-1997	p	e^+	37.55
1998-1999	p	e^-	15.89
1999-2000	p	e^+	60.17
2003-2004	p	e^+	39.71

Table 8.1: Available data samples from the pre– and post–upgrade running periods

Signal and background are simulated using the PYTHIA MC generator (see Sec. 2.4.1) also separated into the pre– and post–upgrade running periods. The statistical methods to extract the beauty quark content in the data (see chapter 9) require in addition a separate simulation of the signal and the background which is described in the following.

The signal has to be simulated separated into subsamples for direct, resolved and excitation in photon and proton processes due to the characteristics of the LO matrix element plus parton shower MC generator PYTHIA (see Sec. 2.4.1). The simulation of the beauty quark signal contains samples from all 4 process categories. The absolute cross section prediction of the PYTHIA generator is used to calculate the integrated luminosity of each sample of the 4 categories. The samples are then added weighted by

the respective integrated luminosity per sample.

The background to the signature of semi-leptonically decaying beauty quarks into muons is separated into two categories.
The first category of background is related to the misidentification of hadrons from the primary interaction as muons. Background to the muon selection can arise from the following conditions:

punchthrough: hadrons traversing the CAL and depositing energy can give rise to secondary particles which leave the CAL and induce signals in the muon chambers and the BAC;

sailthrough: hadrons rarely can traverse the whole detector without being stopped and induce signals in the muon chambers and the BAC;

in–flight decays: muons can be produced by secondary particle decays like $\pi^{\pm} \rightarrow \mu^{\pm}\nu_{\mu}(\bar{\nu}_{\mu})$ or $K^{\pm} \rightarrow \mu^{\pm}\nu_{\mu}(\bar{\nu}_{\mu})$

matching ambiguities: hadron tracks can be accidentally associated to BAC or muon chamber hits originating from another particle

MC samples for lighter flavours have been generated separated into direct and resolved processes to describe this background. They are treated by the same event selection like the data samples and the beauty MC samples.

The second category of background originates from semi-leptonic decays of charm quarks into muons where the charm quark does not originate from a beauty quark. They have a similar detector signature like the signal and are simulated by corresponding charm quark MC samples also separated into direct, resolved and excitations in the proton and the photon processes in the same way as the beauty signal is simulated.

The time consumed by the detector simulation (see Sec. 5.3) is not negligible. Therefore, care has to be taken to reduce the samples to manageable event numbers by preselection cuts on the generated hadronic final state.
The simulation of the beauty quark signal in an inclusive way without applying preselection cuts is possible because the cross sections for the different beauty quark processes are moderately low.
The charm subsamples have a considerably higher cross section which requires a sophisticated preselection. As the event selection is based on the reconstruction of two jets and a muon, a preselection based on a dijet plus muon requirement is applied which differs for the different running periods (see App. C). Due to the muon preselection, the hadronic background from charm events is not included in the charm MC simulation but could be selected from an inclusive MC sample. In this analysis, it is assumed to be indistinguishable from the lighter flavour background.
As the lighter flavour subsamples do not contain muons from heavy quark decays, a muon preselection requirement is not suited to reduce the number of generated events. For these samples, a dijet requirement is used supplemented for the pre–upgrade running periods by a single track requirement for selecting the fake muon background. The lighter flavour samples are simulated separately for direct and resolved processes.
The available MC samples for the pre–upgrade and post–upgrade running periods are given in Tab. 8.2 summarising the generated cross sections and available luminosities. The cross sections differ within the pre–upgrade running periods due to the different centre–of–mass energies and between the pre– and post–upgrade running periods due to changes in the minimum transverse momentum of the hard subprocess and the used proton PDF. A more detailed summary of the MC samples can be found in App. C.

	1996-1997		1998-1999		1999-2000		2003-2004	
process	σ(pb)	$\mathcal{L}$(pb^{-1})	σ(pb)	$\mathcal{L}$(pb^{-1})	σ(pb)	$\mathcal{L}$(pb^{-1})	σ(pb)	$\mathcal{L}$(pb^{-1})
b direct	4081	249.88	4393	75.10	4395	368.49	4119	39.37
b resolved	819	256.34	912	98.67	914	360.99	707	70.71
b excitation in photon	1499	240.11	1657	72.40	1657	361.96	1342	55.86
b excitation in proton	314	286.47	353	84.99	356	421.32	411	65.40
c direct	135200	252.91	143700	92.86	125500	324.96	149000	29.92
c resolved	12220	272.64	13420	127.98	12020	447.59	11780	96.48
c excitation in photon	96380	268.79	100440	97.46	87580	301.94	264000	26.44
c excitation in proton	9240	272.10	10170	83.28	10180	322.82	56010	27.07
lf direct	87420	157.49	93380	51.19	93360	176.88	225600	9.92
lf resolved	443100	162.17	492000	44.49	491900	127.72	1290000	10.06

Table 8.2: Generator cross section predictions and integrated luminosities of the available PYTHIA MC samples for signal (beauty quarks) and background (charm quarks and lighter flavours) for the pre– and post–upgrade running periods

The available MC samples for the post–upgrade running periods are currently very limited but are planned to be enlarged soon.

8.2 Trigger

The available data samples for the pre– and post–upgrade running periods have been taken by a three level trigger system (see Sec. 5.2.7) to record only physics interactions and reducing the fraction of recorded background events. A suitable trigger preselection is applied to the data samples for dijet plus muon final states to have a well-defined trigger efficiency. The detector simulation takes into account the simulation of the trigger system and therefore the same trigger preselection is also applied to the MC samples. The selection requires trigger slots on the third trigger level which are combinations of event quantities calculated on the third level and first and second level trigger slots.

The trigger slot definitions for the post–upgrade running periods differ from the definitions for the pre–upgrade running periods. The expected increase in luminosity has to be compensated by changes in the trigger slot configuration to restrict the output rate of the three–level trigger system to the maximum output rate the system is able to record. Therefore, the trigger selection is different for the two periods.

The third level trigger selection for the given running periods is summarised in Tab. 8.3.

running period	description	short summary of requirements
96-00	barrel/rear muon trigger (see Sec. E.1.1)	at least one barrel or rear muon reconstructed with the GLOMU algorithm (see Sec. 7.3.1.6)
96-99	low E_T dijet trigger (see Sec. E.1.2)	at least two jets with $E_T \geq 4$ GeV and $\|\eta\| < 2.5$
99-00	low E_T dijet trigger (see Sec. E.1.2)	at least two jets with $E_T \geq 4.5$ GeV and $\|\eta\| < 2.5$
96-00	semi-isolated muon trigger (see Sec. E.1.3)	at least one semi-isolated muon found in the barrel and rear muon chambers
99-00	muon plus dijet trigger (see Sec. E.1.4)	at least one muon found by GLOMU and two jets with $E_T > 3.5$ GeV and $\|\eta\| < 2.5$
03-04	inclusive dijets (see Sec. E.2.1)	at least two jets with $E_T > 4.5$ GeV and $\|\eta\| < 2.5$
03-04	inclusive semi-leptonic muon (see Sec. E.2.2)	at least one barrel/rear muon found by GLOMU
03-04	muon plus dijet trigger (see Sec. E.2.3)	at least one barrel/rear muon found by GLOMU and two jets with $E_T > 3.5$ GeV and $\|\eta\| < 2.5$

Table 8.3: Third level trigger selection for the running period 96-00 and 03-04.

As the third level trigger slots consist of cuts on event quantities calculated on the third level and require combinations of first and second level trigger slots, more details are given in App. E.

8.2.1 Trigger Corrections for Post–Upgrade Running Periods

The data taking of the post–upgrade running periods has been complicated by bad background conditions which caused high activity in the detector and therefore significantly higher data taking rates. To cope with the background situation, the trigger configuration definition was changed depending on the running conditions to enable data taking although the background condition would not allow to take data with the standard trigger configuration. Two main types of changes have been made to decrease the data taking rate for bad background conditions:

Track veto: On the first trigger level, a track veto is applied which is calculated by the ratio of vertex fitted tracks to all tracks. For bad running conditions, this veto is tightened.

Prescaling: To reduce the trigger rate of certain first level trigger slots, individual prescaling factors are applied to reduce the trigger rate. In practice, several slots are disabled by prescaling with a factor of 0.

This procedure enabled data taking for big fractions of the post–upgrade running periods but imposed problems for the trigger simulation for the MC. The used post–upgrade MC samples have been generated with the simulation of the standard post–upgrade trigger configuration and have to be corrected for the influences of the tighter track veto and prescaling.
The effect of the track veto is determined comparing suitable first level trigger slot efficiencies between data and MC. A correction is applied to the MC if the event is triggered by a slot which has always the tighter track veto.
In addition, the influence of prescaling of relevant first level trigger slots for the presented post–upgrade third level trigger selection is determined by averaging their efficiency over all taken data and correcting the MC for the average.
This correction procedure only represents a first step to adapt the MC simulation to the difficult data taking conditions. In the future, separate MC samples for the different trigger configuration will be simulated according to their fraction of the total data taken.
No systematic error is calculated for this correction so far due to the preliminary state of this correction.

8.3 Photoproduction Selection

The photoproduction regime is defined by photon virtualities $Q^2 < 1$ GeV^2 (see Sec. 2.4). Two techniques have been used to veto events from the DIS regime.

8.3.1 Veto on Reconstructed Electrons

To select only photoproduction events, events from the DIS regime have to be rejected. DIS events are characterised by an incoming electron scattered at a sizable angle in contrast to a photoproduction event where the scattered electron vanishes undetected in the beam pipe. Therefore, a veto on events including a reconstructed electron selects only photoproduction events unless an electron is not detected.

To reconstruct electrons, the *SINISTRA* electron finder is used [92]. SINISTRA analyses energy depositions in the electromagnetic and hadronic part of the CAL and distinguishes between electromagnetic and hadronic clusters. In the first part of the algorithm, a neural net gives the probability for a cluster to be electromagnetic whereas the second part selects the scattered electron from the list of electromagnetic clusters.
As the DIS cross section decreases rapidly with increasing Q^2, most of the DIS background to photoproduction is characterised by an electron scattered at very low angles. The usage of an electron finder which only uses the CAL and does not require the match with a track is best suited. Only the CAL provides a measurement at very low electron scattering angles due to the limited angular coverage of the CTD in this region.
SINISTRA gives as output the probability P, the energy of the scattered electron candidate determined by the CAL measurement E_{cand} and the inelasticity calculated following the *electron method*:

$$y_{el} = 1 - \frac{E_{cand}}{2E_e}\,(1 - cos(\theta_{cand})) \tag{8.1}$$

with E_e the energy of the incoming electron and θ_{cand} the polar scattering angle of the electron candidate.

The event is rejected if the candidate with the highest probability fulfills:

$$\begin{aligned} P &> 0.9 \\ E_{cand} &> 5 \text{ GeV} \\ y_{el} &< 0.9 \end{aligned} \tag{8.2}$$

The last two cuts prevent the electron veto from rejecting photoproduction events if another particle was misidentified as DIS electron. This can be the case for final state pions, electrons or photons and results in a large electron candidate inelasticity which is not the event inelasticity. Therefore, events with a considerable energy deposit in the electromagnetic CAL but a high inelasticity y_{el} are included in the event selection.

8.3.2 Veto on the Inelasticity with the Jacquet-Blondel Method

As identified DIS electrons are rejected for the selection and photoproduction events do not contain a reconstructed electron, the inelasticity has to be reconstructed using only the CAL and CTD measurements. The *Jacquet-Blondel* method [93] uses EFO's (see Sec. 7.4) to reconstruct the inelasticity by:

$$y_{jb} = \frac{\sum_i (E_i - p_{z,i})}{2E_e} \tag{8.3}$$

where E_i and $p_{z,i}$ are the energy and momentum parallel to the beam pipe of each reconstructed EFO respectively. E_e is the energy of the incoming electron.
The corrections on the reconstructed EFO's (see Sec. 7.4.2 and Sec. 7.4.3) improve the consistency between the reconstructed and true level significantly [94]. After the complete event selection, the comparison shows a remaining difference between true and reconstruction level (see Fig. 8.1) for the beauty quark samples for the pre– and post–upgrade running periods consistent with previous studies.

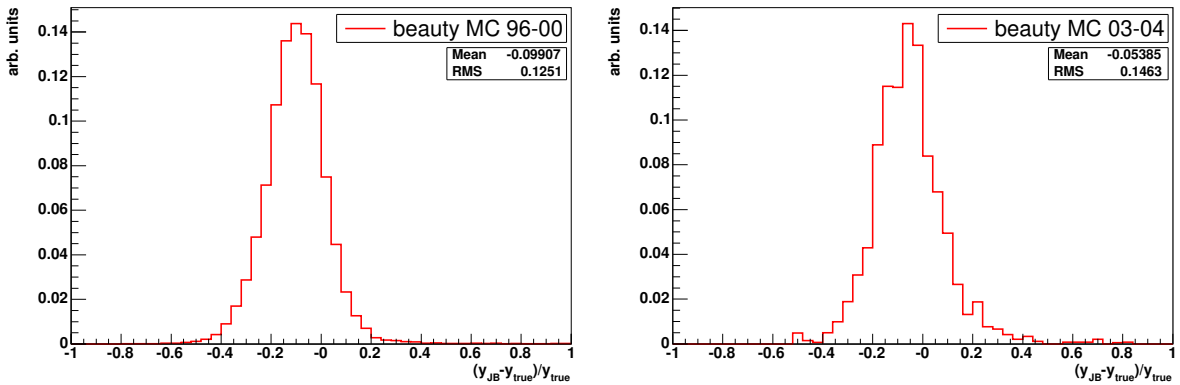

Figure 8.1: Comparison of true and reconstruction level for the inelasticity y_{jb} calculated with the Jacquet-Blondel method. Shown is the ratio $(y_{jb}^{\text{true}} - y_{jb}^{\text{rec}})/y_{jb}^{\text{true}}$ for the pre– (*left*) and post–upgrade (*right*) running periods.

In DIS events, the electron energy contributes to this measurement even if the electron is not identified yielding a fake y_{jb} of ~ 1. A cut on y_{jb} is therefore applied to reject background from residual DIS:

$$y_{jb} < 0.8 \tag{8.4}$$

In Fig. 8.2 and 8.3, the true (generator level) Q^2 distributions for the beauty charm and lighter flavour MC samples after all selection cuts are shown.
The residual contamination from the DIS regime ($Q^2 > 1$ GeV^2) is summarized in Tab. 8.4 and is about 1.2% (2.4%) for the beauty MC sample for the pre–upgrade (post–upgrade) running periods. The higher contamination from the DIS regime for the post–upgrade running periods is expected as the RCAL hole around the beampipe has been enlarged during the upgrade. Electrons which could have been identified

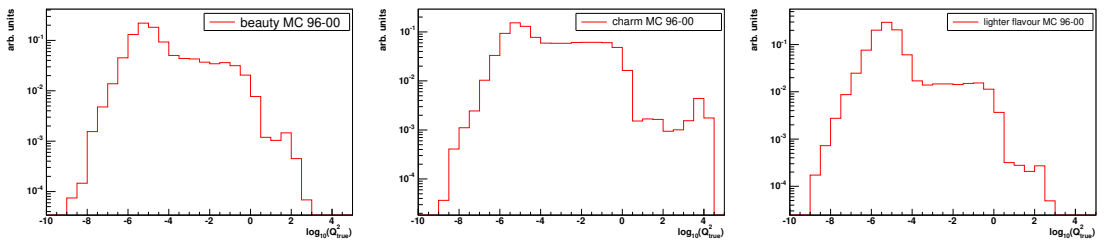

Figure 8.2: True (generator level) photon virtuality Q^2 after all selection cuts for the pre–upgrade running periods for the beauty (*left*), charm (*centre*) and lighter flavour (*right*) MC samples.

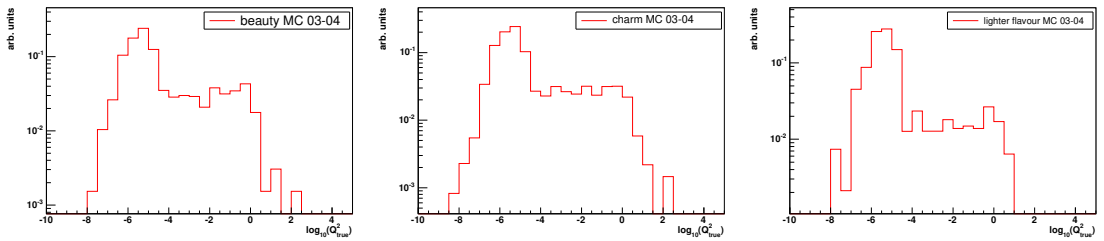

Figure 8.3: True (generator level) photon virtuality Q^2 after all selection cuts for the post–upgrade running periods for the beauty (*left*), charm (*centre*) and lighter flavour (*right*) MC samples.

MC sample	pre–upgrade DIS contamination [%]	post–upgrade DIS contamination [%]
beauty	1.2	2.4
charm	3.3	3.1
lighter flavours	0.4	2.3

Table 8.4: Residual DIS contamination of beauty, charm and lighter flavour MC photoproduction samples after the complete event selection.

in the pre–upgrade periods are not anymore detected in the post–upgrade periods due to the reduced angular coverage of the CAL and therefore not rejected.
The contamination of the charm MC samples is not higher for the post–upgrade running periods than for the pre–upgrade running periods mainly due to the differences in the simulation and the preselection.

8.4 Muon Selection

The general muon finder (see Sec. 7.5) is used to select good muons. The transverse momentum cut is optimised so that reconstructed muons reach at least the inner barrel and rear muon chambers and the BREMAT reconstruction using only the inner chambers is applicable. Good muons are selected from the general list of reconstructed muons with the following cuts:

$$\texttt{quality} \geq 4 \tag{8.5}$$
$$p_T^\mu \geq 1.5 \text{ GeV} \tag{8.6}$$
$$-2.0 < \eta^\mu < 2.5 \tag{8.7}$$

All muons are required to have a vertex–track association due to the implicit requirement on the EFO association (see Sec. 8.6). Due to the preselection cuts of the pre–upgrade charm MC simulation (see Sec. 8.1 and Sec. C.2), the cut on the transverse momentum of the muon has to be raised to $p_T^\mu \geq 2.0$ GeV for the pre–upgrade running periods. In the following, all pre–upgrade distributions are for $p_T^\mu \geq 2.0$ GeV and all post–upgrade distributions for $p_T^\mu \geq 1.5$ GeV if not stated differently.
The η ranges to define forward, barrel and rear muons follow the geometrical structure of the detector:

$$\begin{aligned} rear \quad & -2.0 < \eta^{\mu} < -0.9; \\ barrel \quad & -0.9 < \eta^{\mu} < 1.2; \\ forward \quad & 1.2 \leq \eta^{\mu} \leq 2.5; \end{aligned} \tag{8.8}$$

The distribution of the selected muons broken up into the 3 quality classes and the respective muon finder categories (see Sec. 7.3.2) is shown in Fig. 8.4 for the pre–upgrade running periods.

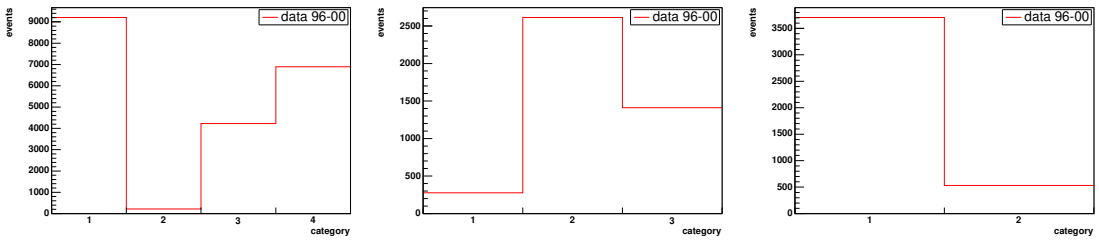

Figure 8.4: Selected muons for the pre–upgrade running periods broken up into muon finder categories. *Left:* muons found in quality class 4 by BREMAT (1), MUFO (2), MUBAC (3), MUBAC and MV (4). *Centre:* muons found in quality class 5 by MPMATCH or MUFO (1), BREMAT (2), MUBAC and MV. *Right* muons for quality class 6 found by BREMAT (1), MPMATCH or MUFO (2).

The fraction of muons found by the barrel and rear muon chambers dominates the selected muons and muons found by the BAC only represent a significant fraction of selected muons in the quality classes 4 and 5. A significant fraction of muons found by BREMAT, MPMATCH or MUFO are also found by MUBAC.
The muon efficiency in the MC is corrected by the correction procedure presented in Sec. 7.3.2.2 which is determined separately for pre– and post–upgrade periods. The description of the reconstructed muons in the data by the corrected MC simulation for the different finder combinations in the pre–upgrade running periods is shown in Fig. 8.5.

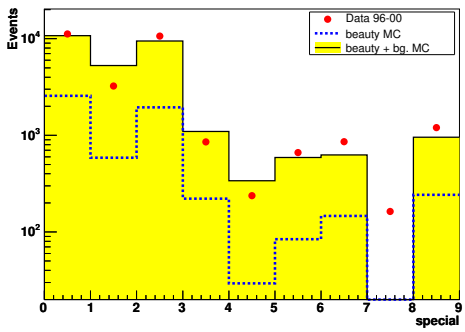

Figure 8.5: The distribution of muon finder categories is compared to the muon efficiency corrected MC samples for pre–upgrade running periods. The MC samples are scaled according to the pre–upgrade global p_T^{rel} fit presented in Sec. 9.1. The comparison is shown for barrel muons found by BREMAT and MUBAC (0), BREMAT and not by MUBAC (1), MUBAC and not by BREMAT (2); for rear muons found by BREMAT and MUBAC (3), BREMAT and not by MUBAC (4), MUBAC and not by BREMAT (5); and for forward muons found by MPMATCH or MUFO and MUBAC (6), MPMATCH or MUFO and not by MUBAC (7), MUBAC and not by MPMATCH or MUFO (8).

Fig. 8.5 shows that the efficiency correction is working reasonably with small problems for muons found only by one of the two finders. Since differences in the forward/barrel/rear muon ratios can be caused by physics as well as imperfect simulation of efficiencies, Fig. 8.6 shows the same distribution with the MC normalised separately to each region.

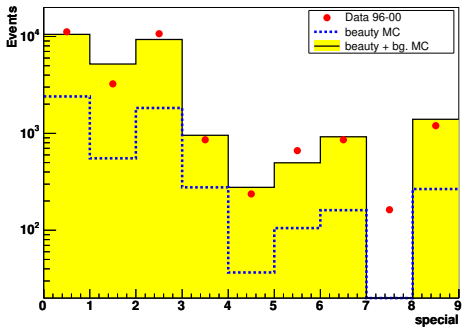

Figure 8.6: The distribution of muon finder categories is compared to the muon efficiency corrected MC samples for pre–upgrade running periods. The MC samples are scaled according to the pre–upgrade p_T^{rel} fits in the respective muon region (barrel, rear or forward). The comparison is shown for barrel muons found by BREMAT and MUBAC (0), BREMAT and not by MUBAC (1), MUBAC and not by BREMAT (2); for rear muons found by BREMAT and MUBAC (3), BREMAT and not by MUBAC (4), MUBAC and not by BREMAT (5); and for forward muons found by MPMATCH or MUFO and MUBAC (6), MPMATCH or MUFO and not by MUBAC (7), MUBAC and not by MPMATCH or MUFO (8).

The comparison shows a systematic underestimation of the BAC efficiency in the barrel and rear regions[1]. This might be due to the application of the BAC efficiency correction factor not only to the true muons, for which it has been determined, but also to the fake muon background. A more detailed correction of the BAC efficiency description will be implemented in the future.
The description of the kinematic distributions of the transverse momentum of the muon p_T^μ and the pseudo-rapidity of the muon η^μ is shown in Fig. 8.7.

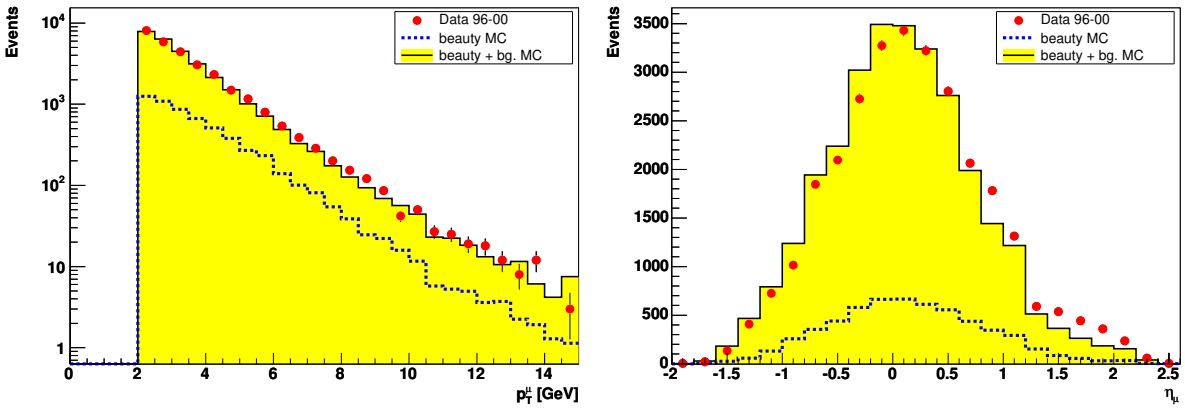

Figure 8.7: Comparison of the transverse muon momentum p_T^μ (*left*) and the muon pseudo-rapidity (*right*) to the MC simulation for pre–upgrade running periods. The signal and background contributions to the MC description are scaled according to the pre–upgrade global p_T^{rel} fit (see Sec. 9.1).

The difference in η^μ has also been observed in previous analyses and could be also a genuine physics effect. The differences due to the muon efficiency correction are also suspected to play a role.

[1] In addition, the J/ψ MC simulation used for the determination of the efficiencies for the correction (see Sec. 7.3.2.2) currently contains no muons reconstructed by the forward muon chambers and not by the BAC due to the 100% efficiency of the BAC in the MC. These combinations in the data can therefore currently not be simulated correctly but a suitable correction will be developed in the future. The effect is small and consistent with the total systematic error.

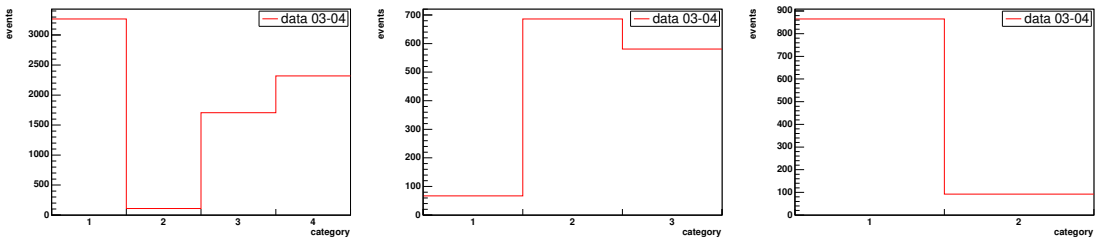

Figure 8.8: Selected muons for the post–upgrade running periods broken up into muon finder categories. *Left:* muons found in quality class 4 by BREMAT (1), MUFO (2), MUBAC (3), MUBAC and MV (4). *Centre:* muons found in quality class 5 by MPMATCH or MUFO (1), BREMAT (2), MUBAC and MV. *Right:* muons for quality class 6 found by BREMAT (1), MPMATCH or MUFO (2).

The post–upgrade muon finder category distribution for the three quality classes is shown in Fig. 8.8. As observed for the pre–upgrade running periods, muons are dominantly reconstructed using the barrel and rear muon chambers with a sizable contribution of muons reconstructed by the BAC in the lowest two quality classes.

Due to the limited available MC statistics for the muon efficiency correction, the description of the muons reconstructed in the post–upgrade data samples is not as good as for the pre–upgrade running periods (see Fig. 8.9) confirmed by the significantly larger systematic error (see Sec. 8.4.1) calculated for the later presented cross sections.

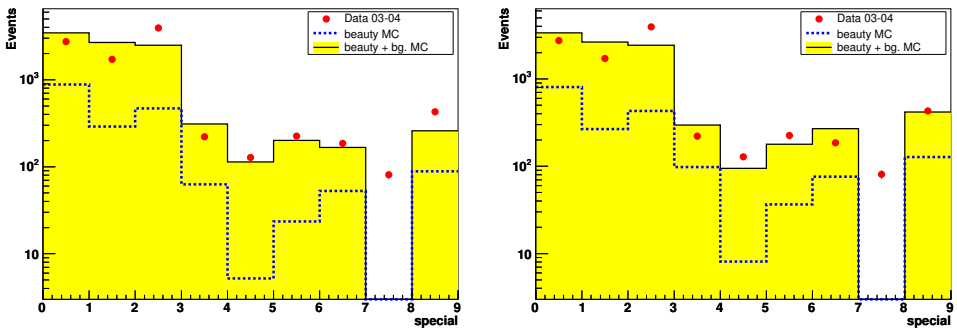

Figure 8.9: The distribution of muon finder categories is compared to the muon efficiency corrected MC samples for the post–upgrade running periods. The MC samples are scaled according to the global post–upgrade p_T^{rel} fit presented in Sec. 9.1 (*left*) and the corresponding fits in the three muon regions barrel, rear and forward. The comparison is shown for barrel muons found by BREMAT and MUBAC (0), BREMAT and not by MUBAC (1), MUBAC and not by BREMAT (2); for rear muons found by BREMAT and MUBAC (3), BREMAT and not by MUBAC (4), MUBAC and not by BREMAT (5); and for forward muons found by MPMATCH or MUFO and MUBAC (6), MPMATCH or MUFO and not by MUBAC (7), MUBAC and not by MPMATCH or MUFO (8).

The problems in the post-upgrade efficiency correction and the as well low available statistics for the signal and background MC samples have a significant influence on the comparison of the kinematic distributions of p_T^μ and η^μ with the MC simulation scaled by the post–upgrade global p_T^{rel} fit (see Fig. 8.10).

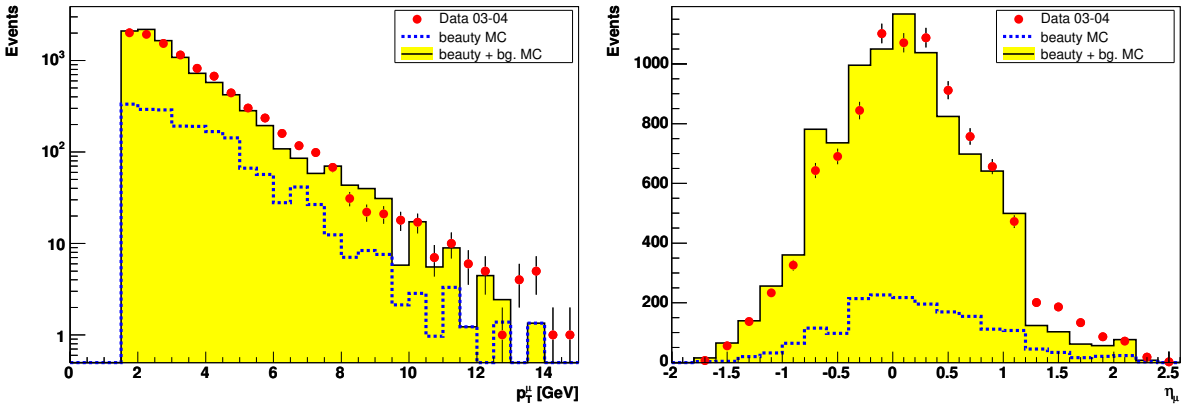

Figure 8.10: Comparison of the transverse muon momentum p_T^μ (*left*) and the muon pseudo-rapidity (*right*) to the MC simulation for post–upgrade running periods. The signal and background contributions to the MC description are scaled according to the global post–upgrade p_T^{rel} fit (see Sec. 9.1).

The difference in p_T^μ and η^μ between post–upgrade data and MC will be improved by enlarging the MC samples for signal and background as well as for the efficiency correction in the future.

The procedure to investigate the systematic influences of the muon efficiency correction due to the limited statistics, especially important for the post–upgrade running periods, is described in the following.

8.4.1 Muon Efficiency Correction Systematics

The muon efficiency correction (see Sec. 7.3.2.2) takes the efficiencies differential in p_T^μ and η^μ of the three different muon finder BREMAT, MPMATCH or MUFO and MUBAC as input to calculate the efficiency correction of a muon depending on the combination of which finder reconstructed the muon. As a weight is calculated by the correction procedure, the procedure does not take into account the statistical error of the individual finder efficiencies.

A systematic check is carried out varying the finder efficiencies differential in p_T^μ and η^μ randomly around the value of every double differential bin. A Gaussian distribution is taken for the variation with the square of the statistical error of the bin as the variance.

The random variation of the double differential efficiencies is repeated ten times. For the determination of the systematic effect of the muon efficiency correction on the cross sections calculated in the following (see chapter 10), the root–mean-squared of the variations of the cross sections from the nominal value by separate application of the 10 randomised efficiency corrections is taken as the systematic error.

This procedure takes into account the statistical fluctuations of the different muon finder efficiencies which is especially important for the post–upgrade running periods where the available MC statistics is very low and the description of the reconstructed data muons by the muon efficiency corrected MC simulation shows sizable deviations.

8.5 Jet Selection

Jets are reconstructed using the KTCLUS algorithm (see Sec. 7.5) in the longitudinal-boost-invariant mode with the E recombination scheme and are required to fulfill the following cuts:

$$p_T^{jet1} \geq 7 \text{ GeV} \tag{8.9}$$
$$p_T^{jet2} \geq 6 \text{ GeV} \tag{8.10}$$
$$|\eta^{jet1,2}| < 2.5 \tag{8.11}$$

to be consistent with previous jet selections [42] and with the trigger preselection. The corrected EFO's are used as an input to the jet finder.

True MC jets are formed using the MC true final states on the generator level by application of the KTCLUS algorithm in the same mode to the stable final state particles. For the MC true jets, B hadrons are defined as stable.

The difference between the reconstructed jets including the muons and true MC jets is shown in Fig. 8.11.

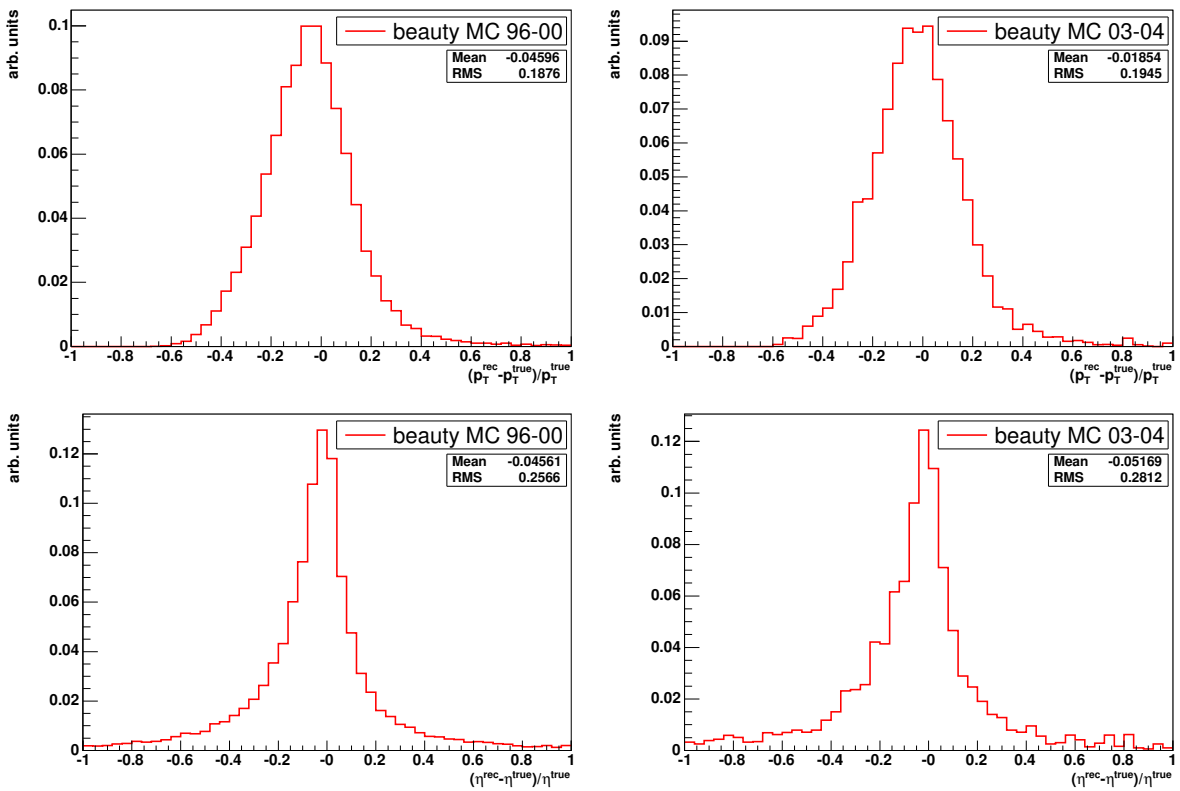

Figure 8.11: Comparison between true and reconstruction level for the transverse jet momentum p_T^{jet} (*top*) and the jet pseudo-rapidity (*bottom*) for the beauty dijet plus muon MC sample. The ratios $(p_T^{jet-\texttt{true}} - p_T^{jet-\texttt{rec}})/p_T^{jet-\texttt{true}}$ and $(\eta^{jet-\texttt{true}} - \eta^{jet-\texttt{rec}})/\eta^{jet-\texttt{true}}$ are shown for the pre– (*left*) and post–upgrade (*right*) running periods.

The correspondence shows a slight residual shift between true and reconstructed level as expected from previous studies [94]. One of the possible explanations is the absence of neutrinos in the reconstructed jets as they are formed from the corrected EFO's which depend on the tracking and energy reconstruction. Since true jets are build at B hadron level, these neutrinos are included in the true definition.

The comparison of the transverse momentum and the pseudorapidity of the jet associated to a selected muon determined from the pre– and post–upgrade data samples to the MC simulation is shown in Fig. 8.12. The signal and background contributions are scaled according to the respective global p_T^{rel} fit described in Sec. 9.1.

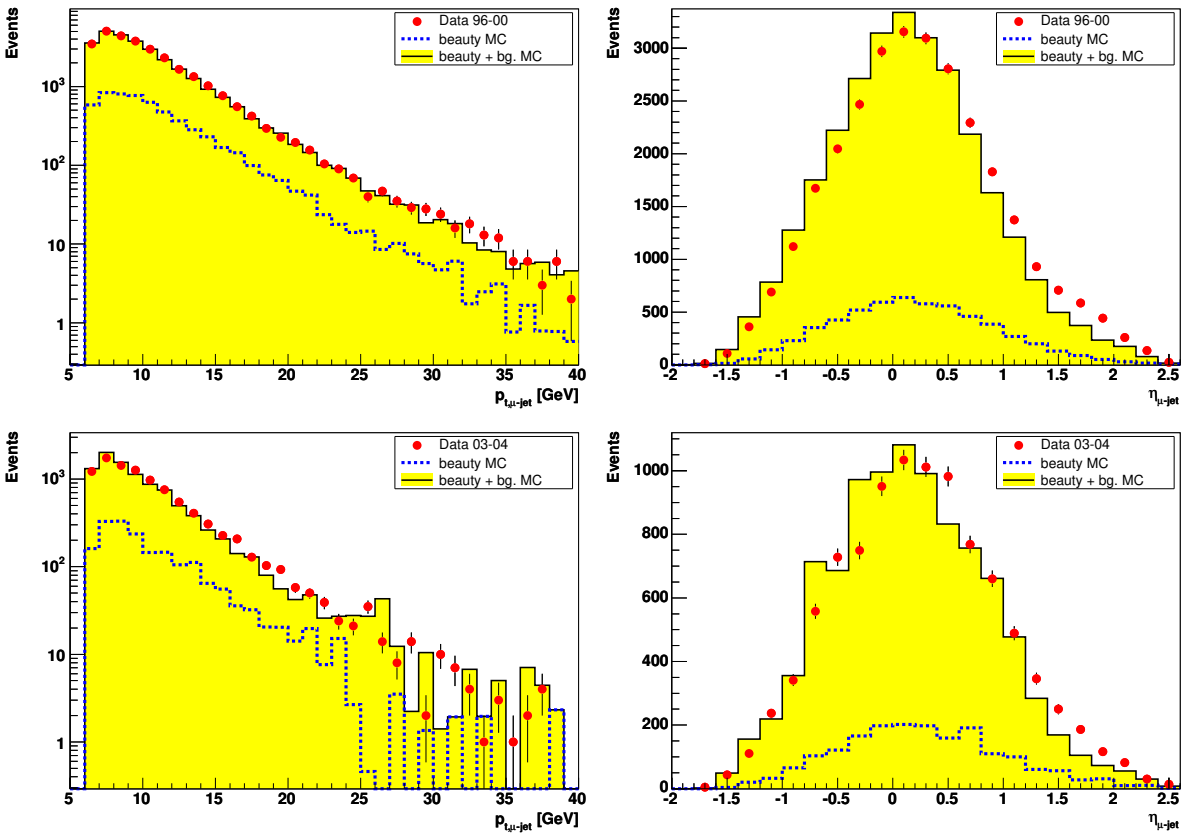

Figure 8.12: Comparison of the transverse jet momentum $p_T^{\mu-jet}$ (*left*) and the jet pseudo-rapidity $\eta^{\mu-jet}$ (*right*) to the MC simulation. The signal and background contributions to the MC description are scaled according to the respective global p_T^{rel} fit (see Sec. 9.1). The comparison is shown for the pre–upgrade (*top*) and post-upgrade (*bottom*) running periods.

The description of the p_T spectrum of the jet associated to a selected muon is very good for the pre–upgrade running periods but shows the influence of the insufficient available MC statistics for the post–upgrade running periods. The $\eta^{\mu-jet}$ comparison shows the same shift as the muon comparison. Since the shift is also observed in the barrel region where the acceptance is expected to be uniform or at least symmetric in η, it might reflect an actual physics effect.

Investigating the second half of the dijet selection, the comparison of the transverse momentum and the pseudorapidity of the *other jet* compared to the jet associated to a selected muon determined from the pre– and post–upgrade data samples to the MC simulation is shown in Fig. 8.13. The signal and background contributions are scaled according to the respective global p_T^{rel} fit described in Sec. 9.1.

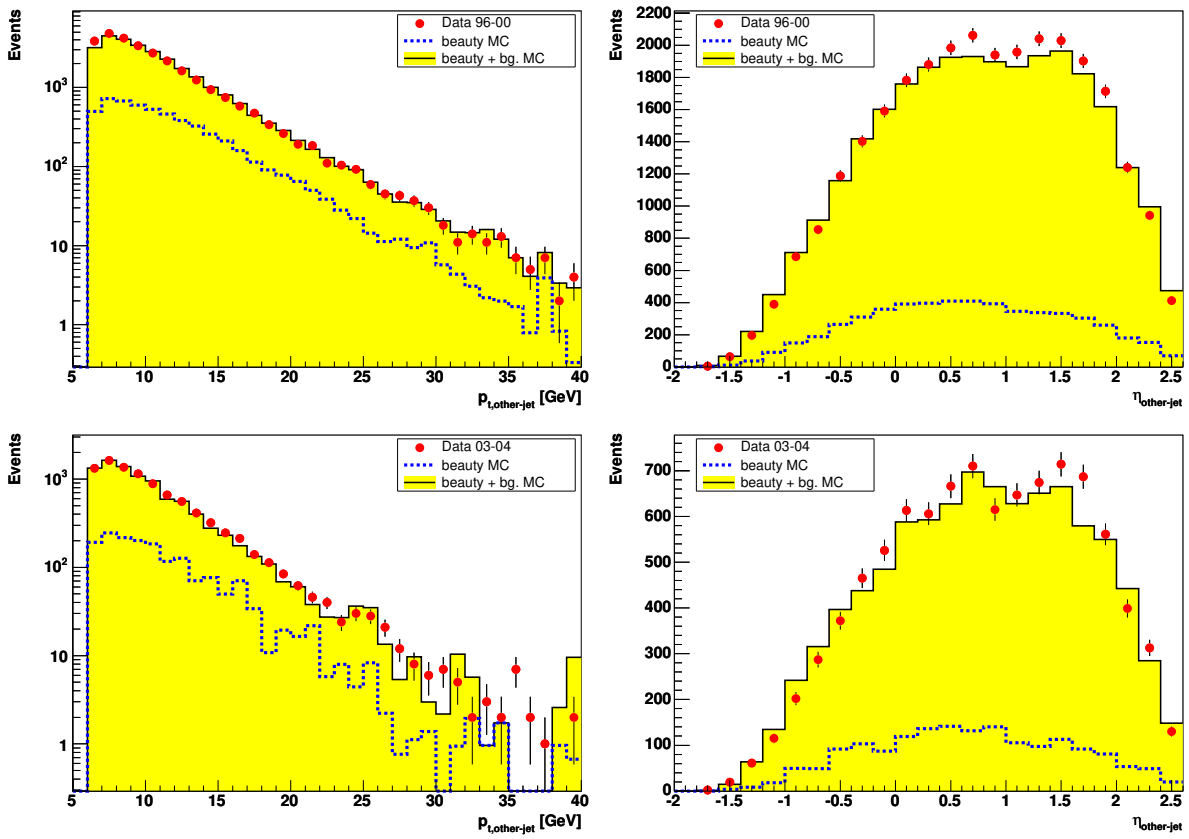

Figure 8.13: Comparison of the transverse jet momentum $p_T^{other-jet}$ (*left*) and the jet pseudo-rapidity $\eta^{other-jet}$ (*right*) with the MC simulation. The signal and background contributions to the MC description are scaled according to the respective global p_T^{rel} fit (see Sec. 9.1). The comparison is shown for the pre–upgrade (*top*) and post-upgrade (*bottom*) running periods.

The description of the p_T spectrum of the jet associated to a selected muon is very good for the pre–upgrade running periods but shows the influence of the insufficient available MC statistics for the post–upgrade running periods. In the lowest $p_T^{other-jet}$ bin is the description better for the post–upgrade periods. The difference to the pre–upgrade description is suspected to be a result of the jet–preselection in the lighter flavour MC samples for the pre–upgrade running periods which might be too hard. This can be solved in the future by lowering the lighter flavour jet–preselection. The $\eta^{other-jet}$ comparison shows a reasonable description in both running periods.

8.6 Jet-Muon Association

Only events with at least one valid jet–muon association of a jet fulfilling the jet cuts and a muon fulfilling the muon cuts are selected. As the dijet selection requires at least two jets fulfilling the requirements, also more than two jets can be reconstructed in an event. A jet is associated to a muon if it includes the muon EFO object identified by the EFO muon tagging (see Sec. 7.4.3). Only associations with a minimal transverse momentum are selected to retain a good jet reconstruction:

$$p_T^{jet} \geq 6 \text{ GeV} \tag{8.12}$$

A further non-negligible background to the selected dijet plus muon final state are cosmics events where a cosmic muon traverses the detector and the muon track is misidentified as two jets containing only a muon respectively. These events are rejected by requiring the transverse momentum of the jet minus the muon to be larger than

$$(p_T^{jet} - p_T^{\mu}) \geq 2 \text{ GeV} \tag{8.13}$$

This cut also yields events with a reasonable hadronic contribution to the jets for the later p_T^{rel} definition.

8.7 Additional Cuts

Beam gas events are rejected by requiring the following cuts on the primary event vertex:

$$|z_{\texttt{vertex}}| < 40 \text{ cm} \tag{8.14}$$

and on an inelasticity y_{jb} calculated by the *Jacquet-Blondel* method (misidentified beam gas events often have energy in the forward region only and hence very low y_{jb}):

$$y_{jb} > 0.2 \tag{8.15}$$

To reduce the contamination by cosmic muon events cuts on the ratio of the total transverse momentum and the total transverse energy p_T/E_T and the total transverse energy in the CAL minus the two inner rings around the beampipe in the FCAL $E_{T,rings}$ are applied using the corrected EFO's:

$$\begin{aligned} p_T/E_T &< 0.5 \\ E_{T,rings} &\geq 10 \text{ GeV} \end{aligned} \tag{8.16}$$

The cut on p_T/E_T reduces in addition the contamination from CC events and the requirement on $E_{T,rings}$ serves as a beauty quark preselection because $2m_b \approx 10$ GeV.
In addition, the reconstructed tracks are used to reject cosmics and beam gas. A minimum of three vertex–fitted tracks and a maximal ratio of total reconstructed track to vertex fitted tracks of 10.0 is required:

$$n_{\texttt{vertex}--\texttt{fittedtracks}} > 2 \tag{8.17}$$

$$\frac{n_{\texttt{tracks}}}{n_{\texttt{vertex}--\texttt{fittedtracks}}} \leq 10.0 \tag{8.18}$$

The remaining cosmics and beam gas contamination is negligible.

The presented selection is applied in addition to a CC MC sample to investigate the CC contamination and results in a significant number of selected events which are reduced by a cut on the total missing hadronic transverse momentum $p_{T,had}$ calculated from all reconstructed EFO's:

$$p_{T,had} \leq 10 \text{ GeV} \tag{8.19}$$

Applying the complete selection on isolated dimuon and Bethe-Heitler MC samples revealed surviving events with very high unphysical p_T^{rel} of the muon relative to the jet. As the p_T^{rel} method will be used to determine the fraction of events from beauty quarks in the sample, these events are rejected by a cut on the muon isolation calculated as the sum of the EFO's in a cone of $\Delta R = 1.0$ around the muon neglecting

the muon EFO itself. The event is rejected if this isolation for any selected muon iso_μ is smaller than the following cut:

$$iso_\mu < 0.5 \tag{8.20}$$

The isolation veto cut reduces the event sample by less than 0.2% in pre– and post–upgrade running periods.

8.8 Summary

Summarizing the complete selection, selected events of the data and signal and background MC samples are required to fulfill the following cuts apart from the trigger preselection (see Sec. 8.2):

Photoproduction selection:

- reject event if electron is reconstructed with:
  - $P_{el} > 0.9$
  - $E_{el} > 5$ GeV
  - $y_{el} < 0.9$
- cut on inelasticity using the Jacquet-Blondel method: $0.2 < y_{jb} < 0.8$

Muon selection: at least one muon is reconstructed by the general muon reconstruction fulfilling:

- $\texttt{quality} \geq 4$ (including forward quality corrections)
- $p_T^\mu \geq 1.5$ GeV
- $-2 \leq \eta^\mu \leq 2.5$
- vertex–track association

The pre–upgrade running periods are restricted to $p_T^\mu \geq 2.0$ GeV due to preselection cuts of the charm MC simulation.

Jet selection: at least two jets are reconstructed by the KTCLUS algorithm using corrected EFO's fulfilling:

- $p_T^{jet1} \geq 7$ GeV
- $p_T^{jet2} \geq 6$ GeV
- $|\eta^{jet1,2}| < 2.5$

Jet-Muon association: at least one muon is associated to a jet fulfilling:

- $p_T^{jet} \geq 6$ GeV
- $(p_T^{jet} - p_T^\mu) \geq 2$ GeV

Additional cuts: per event on:

vertex:

- $|z_{\texttt{vertex}}| < 40$ cm

corrected EFO's:

- $p_T/E_T < 0.5$
- $E_{T,rings} \geq 10$ GeV
- $p_T \leq 10$ GeV

Tracks:

- $n_{\texttt{vertex}--\texttt{fittedtracks}} > 2$
- $\frac{n_{\texttt{tracks}}}{n_{\texttt{vertex}--\texttt{fittedtracks}}} \leq 10.0$

Muons: reject event if at least one muon is reconstructed with muon isolation:

- $iso_\mu < 0.5$

Tab. 8.5 summarises the number of events selected in the different running periods. The number of selected events is smaller than the number of muons associated to a jet per event. More than one muon-jet combination can be reconstructed per event. In case of distributions from quantities from the muon-jet system, all reconstructed muon-jet objects (e.g. dimuons) are included. In case of general event properties, only one entry per event is taken into account.

running period	number of events	number of muon-jet associations
96-97	9241	9541
98-99	4294	4375
99-00	14871	15253
96-00	28406	29079
03-04	9435	9695

Table 8.5: Number of selected events and number of muon-jet associations in the different running periods

8.8.1 Control Distributions

Control distributions of the comparison of kinematic variables from pre– and post–upgrade running periods have already been presented for:

- the transverse momentum of the muon associated to a jet p_T^{μ} (see *left* in Fig. 8.7 and 8.10),
- the pseudo rapidity of the muon associated to the jet (see *right* in Fig. 8.7 and 8.10),
- the transverse momentum of the jet associated to a muon (see *left* in Fig. 8.12),
- the pseudo-rapidity of the jet associated to a muon (see *right* in Fig. 8.12).
- the pseudo-rapidity of the other jet (see *right* in Fig. 8.13).

In all cases, the signal and background MC samples after event selection, scaled using the corresponding p_T^{rel} fit (see Sec. 9.1), are compared to the distributions from the data samples. Good compatibility between data and MC simulation for the pre–upgrade running periods is observed in all given kinematic variables except for the pseudo-rapidity of the muon η^{μ}. The origin of the difference is suspected to be related to the muon efficiency correction but can also be a genuine physics effect. As the later described p_T^{rel} method (see Sec. 9.1) uses the well described p_T^{μ} spectrum to extract the beauty content of the data sample, no big impact is expected from this difference. The comparison shows the control of the signal and background shapes of the simulation needed for the statistical extraction of the beauty content described in chapter 9. The post–upgrade running periods suffer from low available MC sample statistics and show a worse description.

In the following, data distribution of additional kinematic variables are compared to the scaled MC prediction to demonstrate the good compatibility between data and MC simulation.
The jets are clustered from the corrected EFO's with the KTCLUS algorithm in the massive scheme taking into account the mass of particles forming a jet. The control distribution of the mass of the jet associated to a selected muon $mass_{\mu-jet}$ is presented in Fig. 8.14 and confirms the compatibility between data and simulation. The slightly higher jet mass for the beauty sample reflects the effect of the large beauty quark mass reduced by the non-identified neutrino.

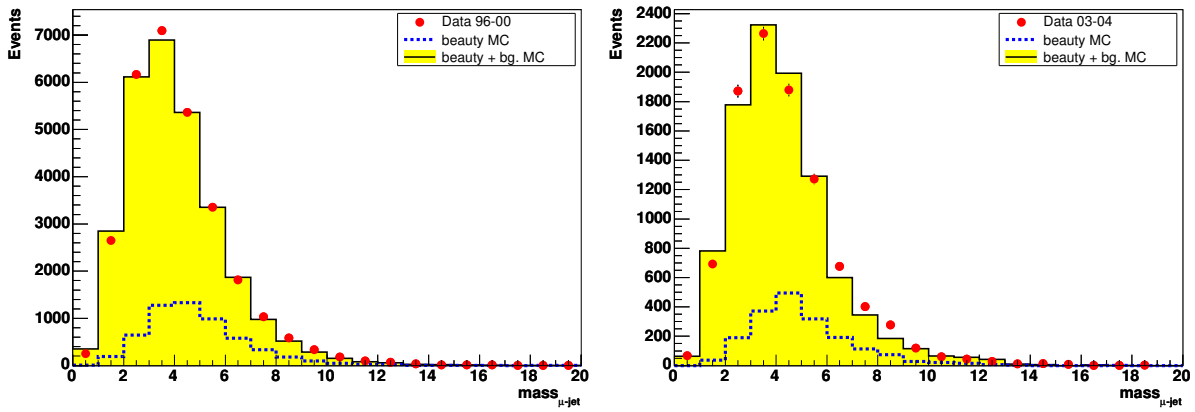

Figure 8.14: Comparison of the mass of the jet associated to a selected muon $mass_{\mu-jet}$ to the MC simulation. The signal and background contributions to the MC description are scaled according to the p_T^{rel} fit (see Sec. 9.1). The comparison is shown for the pre–upgrade (*left*) and post-upgrade (*right*) running periods.

The ratio of the muon transverse momentum to the jet transverse energy of a associated muon-jet object p_T^{μ}/E_T^{jet} represents the fraction of the transverse energy of the jet taken by the muon. The comparison of p_T^{μ}/E_T^{jet} between data and MC simulation shows also the description of the hadronic contribution to the jet in the data by the MC (see Fig. 8.15).

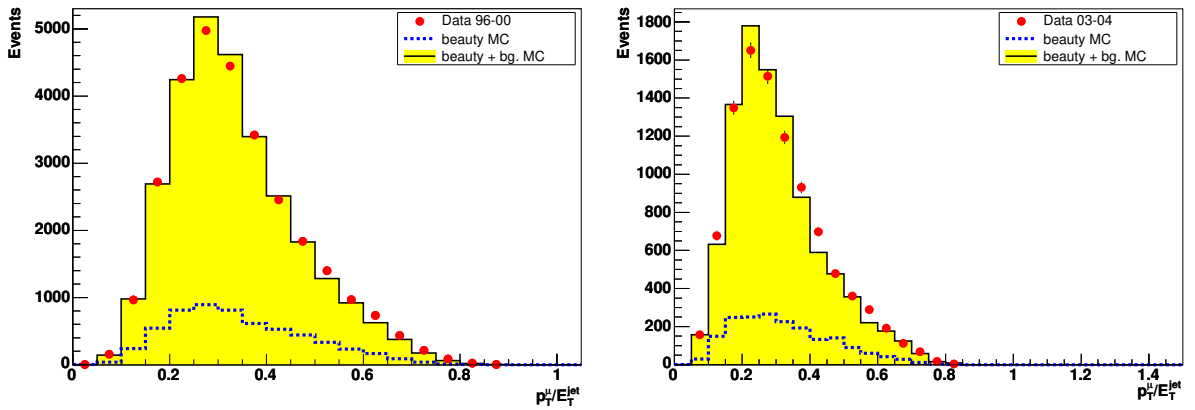

Figure 8.15: Comparison of the fraction of the muon transverse momentum with regard to the transverse energy of the jet p_T^{μ}/E_T^{jet} to the MC simulation. The signal and background contributions to the MC description are scaled according to the p_T^{rel} fit (see Sec. 9.1). The comparison is shown for the pre–upgrade (*left*) and post-upgrade (*right*) running periods.

The pre–upgrade comparison shows a good agreement between data and MC whereas the post–upgrade comparison suffers from the low available MC statistics. The difference in the mean value between pre– and post–upgrade running periods originates from the different kinematic cuts on the muon. In the pre–upgrade periods, the cut on the transverse momentum of the muon p_T^{μ} is raised to $p_T^{\mu} \geq 2.0$ GeV due to the preselection of the used charm MC simulation compared to the nominal cut of $p_T^{\mu} \geq 1.5$ GeV used in the post–upgrade periods.

The x_γ^{jets} distribution (see Eq. 2.28) is sensitive to the mixture of direct ($x_\gamma \gtrsim 0.75$) and resolved ($x_\gamma \lesssim 0.75$) contributions to the signal and background MC samples which is carried out according to their respective luminosities (see Sec. 2.4.1). If the data x_γ distribution is described simultaneously in the direct and resolved x_γ regions, no further corrections on the mixture of direct and resolved contributions have to be applied. Fig. 8.16 presents the x_γ comparison and shows a good description of the data by the scaled MC samples and confirms the validity of the addition of direct and resolved components using their relative luminosities. The small remaining difference at low x_γ^{jets} is still under investigation. The difference will be treated by a contribution to the systematic error by variation of the relative contributions of the direct and the resolved, excitation processes (see Sec. 10.1.3).

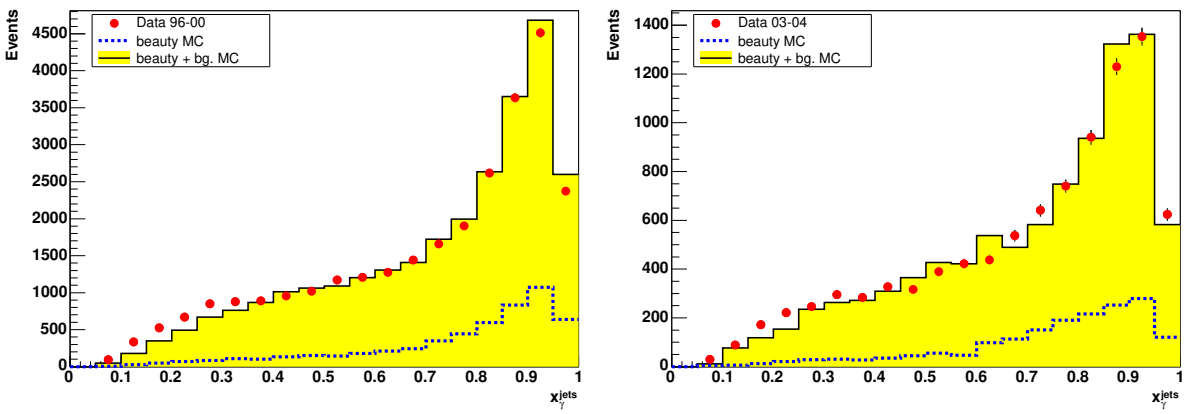

Figure 8.16: Comparison of the fraction of the x_γ distribution by the MC simulation. The signal and background contributions to the MC description are scaled according to the p_T^{rel} fit (see Sec. 9.1). The comparison is shown for the pre–upgrade (*left*) and post-upgrade (*right*) running periods.

The presented additional comparisons between data and MC kinematic distributions show a good compatibility between the data shapes and the simulated MC shapes. The measurement of beauty quark cross section can therefore be continued by the determination of the beauty quark content in the selected data sample by the statistical methods described in the next chapter.

Chapter 9

Beauty Quark Identification

The identification of beauty quarks in the selected dijet plus muon event sample (see chapter 8) is the last step after the reconstruction of the event properties (see chapter 7) on the way to the measurement of beauty quark cross sections.

This chapter describes two statistical methods to identify semi-leptonic beauty quark decays in the selected dijet plus muon data sample. In both methods MC samples are used to model the contribution of signal and background processes to the selected dijet plus muon data sample. The shape of a suitable signal sensitive observable extracted from the MC samples is fitted to the corresponding shape from the data to determine the fraction of signal contained in the data. In the following, the two methods exploiting the large mass of the beauty quark and its long lifetime are presented.

9.1 p_T^{rel} Method

Beauty quarks are significantly heavier than charm and lighter flavour quarks. This is reflected in their decay kinematics especially in the muon decay channel.
An observable which reflects the characteristics of the quark masses in semi-leptonic decays into muons is the transverse momentum of the muon relative to its parental quark. Due to the heavy beauty quark mass, the p_T^{rel} spectrum of muons originating from beauty quarks is harder than the p_T^{rel} spectrum from charm and lighter quarks.
As quarks are not experimentally observable, jets are reconstructed to represent the momentum of the quarks and define the reference for the calculation of the p_T^{rel} of the muon (see Fig. 9.1).

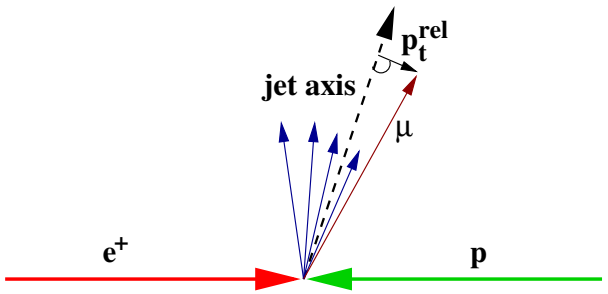

Figure 9.1: Definition of the transverse momentum of the muon relative to its associated jet p_T^{rel}.

Two definitions of p_T^{rel} are available which both are valid to exploit the heavy mass of the beauty quark to determine the fraction of beauty events in the selected event sample.
The first definition calculates the p_T^{rel} of the muon relative to its associated jet following Eq. 9.1.

$$p_T^{rel} = |\vec{p}_T^{\,\mu}| \cdot sin\left(acos\left(\frac{\vec{p}_T^{\,\mu} \cdot \vec{p}_T^{\,jet}}{|\vec{p}_T^{\,\mu}| \cdot |\vec{p}_T^{\,jet}|}\right)\right) \tag{9.1}$$

Fig. 9.2 shows the data p_T^{rel} shape and the p_T^{rel} shapes from beauty, charm and lighter flavour MC samples. The comparison of the MC p_T^{rel} shape shows the harder p_T^{rel} spectrum from beauty quarks whereas the p_T^{rel} shapes from charm and lighter flavour quarks show only a small difference in their shapes especially at larger values of p_T^{rel} where the spectrum from beauty quarks is much harder than those from charm and lighter flavour quarks.

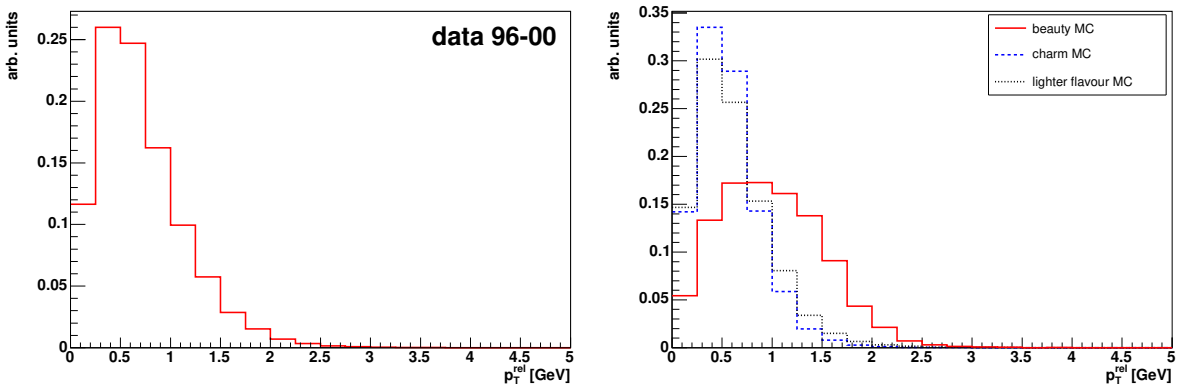

Figure 9.2: p_T^{rel} distributions from the data sample (*left*) and beauty, charm and lighter flavour MC samples (*right*) normalised to the lighter flavour MC samples.

The second definition subtracts the muon transverse momentum from the jet and calculates the transverse momentum of the muon relative to the new jet axis and calculates $p_T^{rel,jet-\mu}$ following Eq. 9.2.

$$p_T^{rel,jet-\mu} = |\vec{p}_T^{\,\mu}| \cdot sin\left(acos\left(\frac{\vec{p}_T^{\,\mu} \cdot (\vec{p}_T^{\,jet} - \vec{p}_T^{\,\mu})}{|\vec{p}_T^{\,\mu}| \cdot |(\vec{p}_T^{\,jet} - \vec{p}_T^{\,\mu})|}\right)\right) \tag{9.2}$$

By subtracting the muon transverse momentum from the jet to form the new reference axis, the calculated $p_T^{rel,jet-\mu}$ spectrum is shifted to larger values. The characteristics of the $p_T^{rel,jet-\mu}$ shape with respect to the originating quark flavour remains the same as for the first definition (see Fig. 9.3)

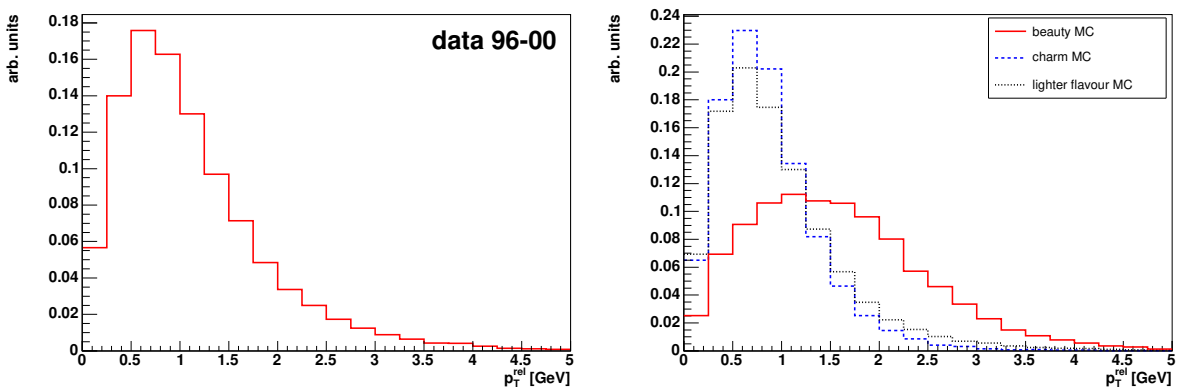

Figure 9.3: $p_T^{rel,jet-\mu}$ distributions from the data sample (*left*) and beauty, charm and lighter flavour MC samples (*right*).

The extraction of the relative contributions of the signal and background in the data sample is carried out by a χ^2 fit of the MC p_T^{rel} or $p_T^{rel,jet-\mu}$ spectra to the data. As the difference between the charm and lighter flavour p_T^{rel} or $p_T^{rel,jet-\mu}$ spectra is very small at larger values, the χ^2 fit is not sensitive to a separate determination of the charm and lighter flavour contribution in the data. Therefore, the charm and lighter flavour samples are added according to their respective absolute MC prediction.
The second definition of the transverse momentum relative to the jet is taken as the nominal definition following the approach of the previous results [42]. The other will be used as a contribution to the systematic error, as well as variations of the charm to light flavour ratio around the central value.

The fit function (see Eq. 9.3) to determine the contributions of the signal and background determines two scaling factors $\mathrm{P_{signal}}$ and $\mathrm{P_{background}}$ to fit the scaled fractions of the MC signal $\mathrm{N_{signal}}$ and the MC background $\mathrm{N_{background}}$ to the data $p_T^{rel,jet-\mu}$ distribution $\mathrm{N_{data}}$:

$$\mathrm{N_{data}} = \mathrm{P_{signal}} \cdot \mathrm{N_{signal}} + \mathrm{P_{background}} \cdot \mathrm{N_{background}} \tag{9.3}$$

The parameters are determined by the minimisation of the following test distribution:

$$\chi^2 = \sum_i \frac{\left(\mathrm{N^i_{data}} - \left(\mathrm{P_{signal}} \cdot \mathrm{N^i_{signal}} + \mathrm{P_{background}} \cdot \mathrm{N^i_{background}}\right)\right)^2}{\sigma^2_{\mathrm{i,data}} + \sigma^2_{\mathrm{i,signal}} + \sigma^2_{\mathrm{i,background}}} \tag{9.4}$$

where i is the sum over all bins in the $p_T^{rel,jet-\mu}$ distributions and $\sigma_{\mathrm{i,data}}$, $\sigma_{\mathrm{i,signal}}$ and $\sigma_{\mathrm{i,background}}$ are the statistical errors of the $p_T^{rel,jet-\mu}$ distributions per bin.
The fraction of beauty events in the data is calculated from the parameters using the total number of selected events in the signal and background MC samples $\mathrm{N^{total}_{signal}}$ and $\mathrm{N^{total}_{background}}$:

$$f_{\mathrm{beauty}} = \frac{\mathrm{N^{beauty}_{data}}}{\mathrm{N^{total}_{data}}} = \frac{\mathrm{P_{signal}} \cdot \mathrm{N^{total}_{signal}}}{\mathrm{P_{signal}} \cdot \mathrm{N^{total}_{signal}} + \mathrm{P_{background}} \cdot \mathrm{N^{total}_{background}}} \tag{9.5}$$

The errors on the parameters determined by the fit procedure using the ROOT [72] implementation of the Minuit package [95] are correlated. For the determination of beauty quark cross sections, only the number of beauty events in the data

$$\mathrm{N^{beauty}_{data}} = f_{beauty} \cdot \mathrm{N^{total}_{data}} \tag{9.6}$$

and the corresponding error

$$\sigma_{\mathrm{N^{beauty}_{data}}} = \sigma_{f_{beauty}} \cdot \mathrm{N^{total}_{data}} \tag{9.7}$$

is relevant.
The error on the beauty fraction is approximated using Eqs. 9.5 and 9.7:

$$\sigma_{fbeauty} = \frac{\sigma_{\mathrm{N^{beauty}_{data}}}}{\mathrm{N^{total}_{data}}} = \frac{\sigma_{\mathrm{P_{signal}}} \cdot \mathrm{N^{total}_{signal}}}{\mathrm{P_{signal}} \cdot \mathrm{N^{total}_{signal}} + \mathrm{P_{background}} \cdot \mathrm{N^{total}_{background}}} \tag{9.8}$$

Separately for the pre– and post–upgrade running periods, Fig. 9.4 shows the global $p_T^{rel,jet-\mu}$ fits for the selected data samples.

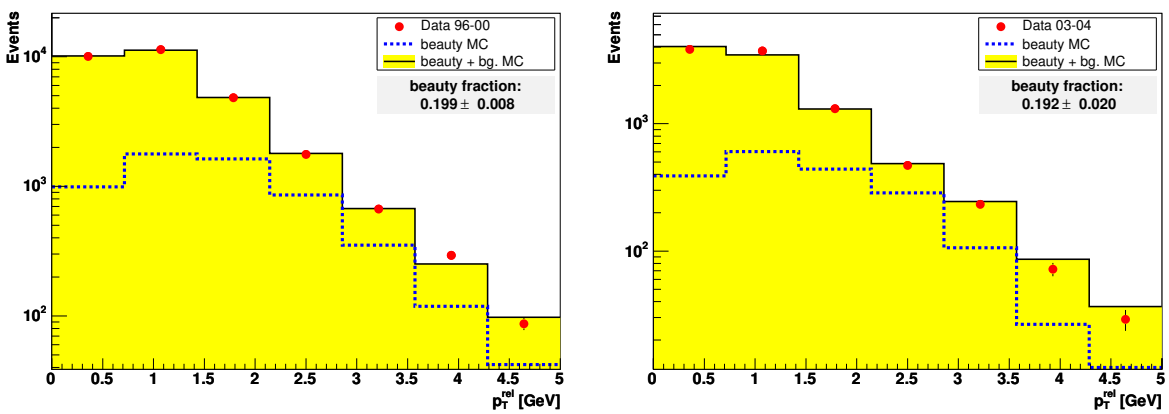

Figure 9.4: Global $p_T^{rel,jet-\mu}$ fits separately for the pre– (*left*) and post–upgrade (*right*) running periods.

The beauty fractions for the selected data samples for pre– and post–upgrade running periods are:

running period	beauty fraction $f_{\texttt{beauty}}$ from $p_T^{rel,jet-\mu}$	beauty quark MC scaling factor
96-00	$19.9 \pm 0.8\%$	2.06
03-04	$19.2 \pm 2.0\%$	2.77

Table 9.1: Beauty fraction determined from global $p_T^{rel,jet-\mu}$ fits separately for the pre– and post–upgrade running period and the corresponding scaling factor for the beauty quark MC samples.

As a systematic check, the same beauty fractions are determined using the first p_T^{rel} definition:

running period	beauty fraction $f_{\texttt{beauty}}$ from p_T^{rel}	beauty quark MC scaling factor
96-00	$18.9 \pm 0.8\%$	1.96
03-04	$19.1 \pm 2.2\%$	2.74

Table 9.2: Beauty fraction determined from global p_T^{rel} fits separately for the pre– and post–upgrade running period and the corresponding scaling factor for the beauty quark MC samples.

The difference in the scaling factors between the pre– and post–upgrade running periods can be partly explained by the different generator cross sections of the signal and background MC simulations due to differences in the chosen PYTHIA parameters. The muon and trigger efficiency corrections could play a role in explaining the remaining differences which are within the limits of the systematic errors.

The given beauty fractions are determined using the background $p_T^{rel,jet-\mu}$ shape correction which is described in the following.

9.1.1 Background $p_T^{rel,jet-\mu}$ and p_T^{rel} Shape Corrections

The $p_T^{rel,jet-\mu}$ and p_T^{rel} fit procedures depend on the good description of the background $p_T^{rel,jet-\mu}$ and p_T^{rel} shapes by the used MC simulation. For a comparison between data and MC of only the background $p_T^{rel,jet-\mu}$ and p_T^{rel} shapes, a data sample is selected by the same event selection as for the signal data sample (see chapter 8) but replacing the muon requirement by a single track requirement with the same kinematic cuts. The association of the selected tracks to jets is carried out using a cone around the jet axis. If the angular distance between jet and track fulfills

$$\Delta R = \sqrt{\Delta\eta^2 + \Delta\phi^2} < 1.0 \tag{9.9}$$

the track is associated with the jet and the transverse momentum of the track is calculated following definition one (see Eq. 9.1) and definition two (see Eq. 9.2) replacing the muon with the selected track. This selection is applied to the pre– and post–upgrade running periods separately assuming that this selection only selects background events.
The same modified selection is applied to the lighter flavour MC samples and the shape difference between data and MC is shown in Fig. 9.5 for $p_T^{rel,jet-\mu}$.
The comparison shows that the $p_T^{rel,jet-\mu}$ shape of the data is harder than the MC and influences the $p_T^{rel,jet-\mu}$ fit. Therefore, the determined beauty fraction would be larger if no correction is applied to the background MC samples.

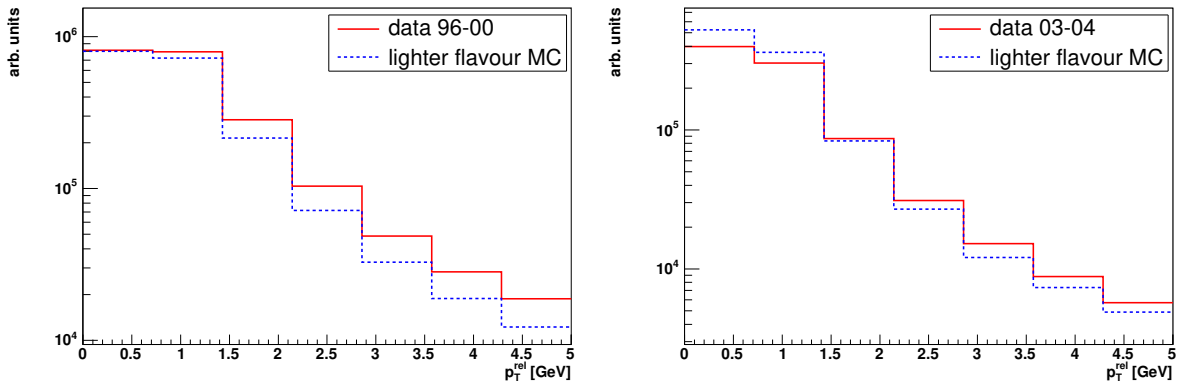

Figure 9.5: Comparison of background $p_T^{rel,jet-\mu}$ shapes between data and MC simulation for pre– (*left*) and post–upgrade (*right*) running periods.

The correction factor per bin is calculated by dividing the data background $p_T^{rel,jet-\mu}$ shape by the shape from the background MC bin by bin and is shown in Fig. 9.6.

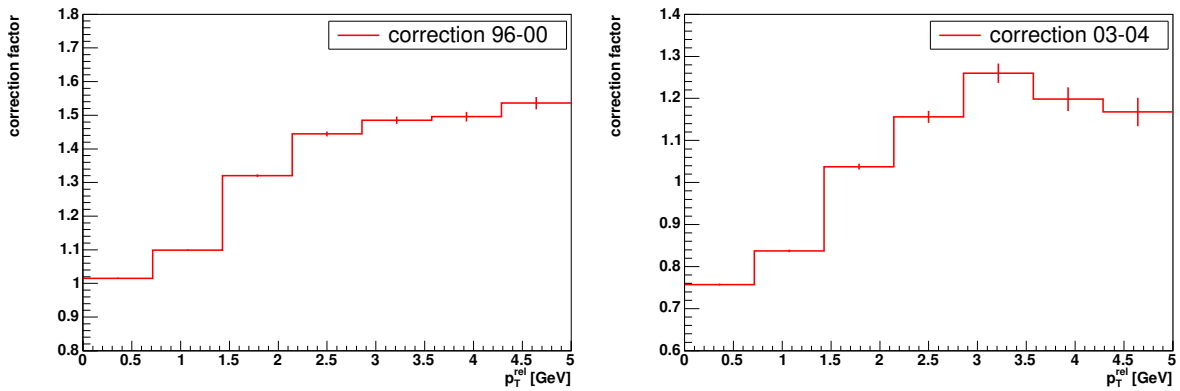

Figure 9.6: Correction factors for background $p_T^{rel,jet-\mu}$ shapes for pre– (*left*) and post–upgrade (*right*) running periods.

The correction factors are applied bin by bin to the $p_T^{rel,jet-\mu}$ distributions of the lighter flavour MC samples as the lighter flavour samples are assumed to only contain background from fake muons.
The treatment of the correction for the charm MC samples is more complicated. The charm samples contain events where the muon originates from a charm quark in addition to fake muon events and therefore do not only contain fake muon background for which the correction is calculated.
For now, the beauty quark MC samples are assumed to contain no fake muon contamination.
As an approximation, 50% of the correction is applied to the charm background MC samples. To determine the systematic influence, the determination of the beauty fraction is repeated applying 100% and 0% of the correction to the charm MC sample. The result of the systematic check for the above presented global $p_T^{rel,jet-\mu}$ fit is shown in Tab. 9.3.

applied correction fraction to charm samples	pre–upgrade beauty fraction from $p_T^{rel,jet-\mu}$ fit	post–upgrade beauty fraction from $p_T^{rel,jet-\mu}$ fit
100%	$18.9 \pm 0.8\%$	$18.0 \pm 2.1\%$
50%	$19.9 \pm 0.8\%$	$19.2 \pm 2.0\%$
0%	$21.0 \pm 0.8\%$	$20.2 \pm 2.0\%$

Table 9.3: Systematic influence of the charm $p_T^{rel,jet-\mu}$ background shape correction.

The systematic error on the later presented total beauty quark photoproduction cross section in dijet

plus muon events (see Sec. 10.1 and Sec. 10.2) using the beauty fractions from the global $p_T^{rel,jet-\mu}$ fit (see Tab. 9.3) related to the charm background $p_T^{rel,jet-\mu}$ shape correction is $^{+7.8}_{-7.1}\%$ for the pre–upgrade and $^{+5.2}_{-6.3}\%$ for the post–upgrade running periods.

9.2 Impact Parameter Method

The large decay length of beauty quarks arising from their long lifetime can also be used to define a beauty-sensitive observable.
The decay length l accessible by experiments is related to the *proper decay length* $c\tau$ where τ denotes the lifetime in the rest frame of the decaying particle taking into account the *hadron boost* $\beta\gamma \equiv |\vec{p}|/m$:

$$l = c\tau\beta\gamma \tag{9.10}$$

The probability P that a particle of characteristic decay length l traverses a distance L in the laboratory frame between production and decay is:

$$P(L) = exp\left(-\frac{L}{l}\right) \tag{9.11}$$

In this thesis, lifetime information is only extracted in a transverse plane perpendicular to the beam axis due to experimental reasons and therefore only the xy projection is relevant:

$$L_T = L \cdot sin(\theta) \tag{9.12}$$

where θ is the polar angle of the decaying particle.
The *impact parameter* δ of a particle originating from a hadron decay is the closest distance in the xy plane between the particle's trajectory and the production point of the decaying hadron:

$$\delta_{true} = L_T \cdot sin(\alpha) \tag{9.13}$$

where α is the angle in the xy plane between the hadron direction and the direction of the decay particle. The factor $sin(\alpha)$ approximately compensates the boost dependence of L_T.
The lifetime difference between charm and beauty quarks leads to significant differences in the impact parameter spectra resulting in a harder impact parameter spectrum of muons originating from beauty flavoured hadrons which is shown in the comparison of the true (generator level) impact parameter of muons originating from beauty and charm quarks in Fig. 9.7.

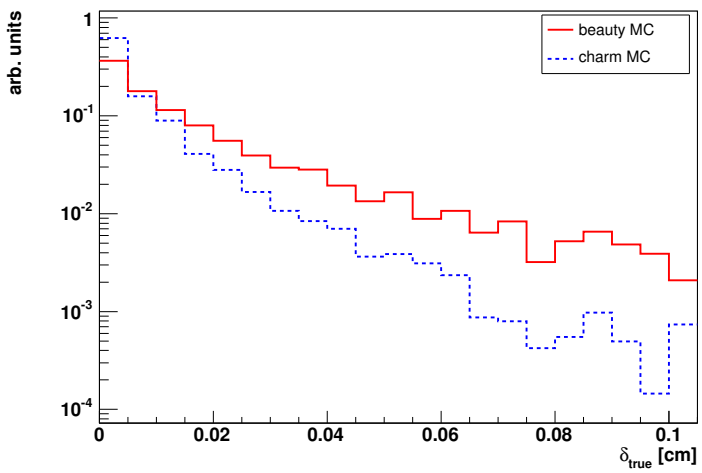

Figure 9.7: Comparison of true (generator level) impact parameter δ_{true} between muons originating from beauty and charm quarks.

Experimentally, the impact parameter (see Fig. 9.8) is defined as the distance of the muon track from the beamspot.

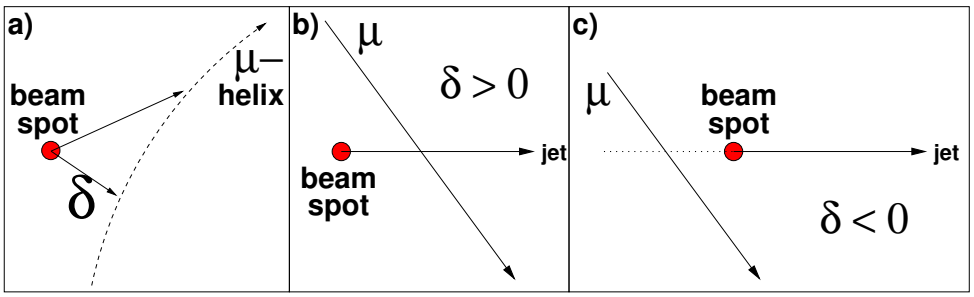

Figure 9.8: Definition of the impact parameter as the signed distance of the muon track helix to the beamspot.

As the impact parameter has to resolve lifetime differences of the beauty quarks and charm and lighter flavour background, only the MVD provides a sufficiently accurate single track resolution in the vicinity of the vertex and therefore restricts the application of the *impact parameter method* to the post–upgrade running periods.
The beamspot (see Sec. '7.1.3) is chosen as the reference of the interaction and not the primary vertex because the reconstruction of the primary vertex is currently technically not stable (see Sec. 7.1.3).
The muon track is given by the post–upgrade track reconstruction in the form of a helix (see Sec. 7.1) and the distance–of–closest–approach of the helix to the beamspot defines the magnitude of the beamspot (see a) in Fig. 9.8). Additional tracking specific cuts on the quality of the muon track are applied to guarantee a reliable acceptance:

- number of used superlayers of the CTD $n_{\texttt{superlayer}} \geq 3$
- reference point of the helix $|z_H| < 30$ cm
- number of used MVD hits $n_{\texttt{MVD-hits}} \geq 4$

The full luminosity for the post–upgrade running periods was not yet available for the impact parameter determination when this analysis was finished. Only 20 pb^{-1} have been included because only for this first half of the luminosity the final MVD alignment was available.
The sign of the impact parameter is introduced determined in reference to the jet associated to the muon which gives the reconstruction of the quark decay direction (see b) and c) in Fig. 9.8). Muons originating from the beamspot are expected to have a symmetric signed impact parameter distribution while muons originating from the decay of heavy flavour quarks have a clear bias to positive impact parameters.
The impact parameter distributions of data and signal and background MC samples can be used in analogy to the $p_T^{rel,jet-\mu}$ and p_T^{rel} methods to determine the fraction of beauty events in the data sample by a χ^2 fit (see Sec. 9.1).
Fig. 9.9 shows the impact parameter distributions determined from the reduced post–upgrade data sample and the beauty, charm and lighter flavour MC samples for the post–upgrade running periods (see Sec. 8.1).
The negative part is mirrored to the positive side to indicate the asymmetry of the impact parameter distribution which is significant for the beauty MC sample, smaller for the charm MC sample and the data and not existent for the lighter flavours samples as expected.

9.2.1 Background Impact Parameter Shape Corrections

Systematic errors of the impact parameter method arise mainly from the background description of the used MC samples. Although the available MC samples are small, a clear difference between the background impact parameter distributions in analogy to the $p_T^{rel,jet-\mu}$ and p_T^{rel} background shape differences (see Sec. 9.1.1) can be observed. Using the same procedure as in the case of the $p_T^{rel,jet-\mu}$ shape correction by replacing the muon requirement by a single track requirement, the difference between simulation and data is shown in Fig. 9.10.
A suitable correction for the discrepancy was not yet available when this analysis was finished. Therefore, the systematic error connected to this discrepancy was also not determined.

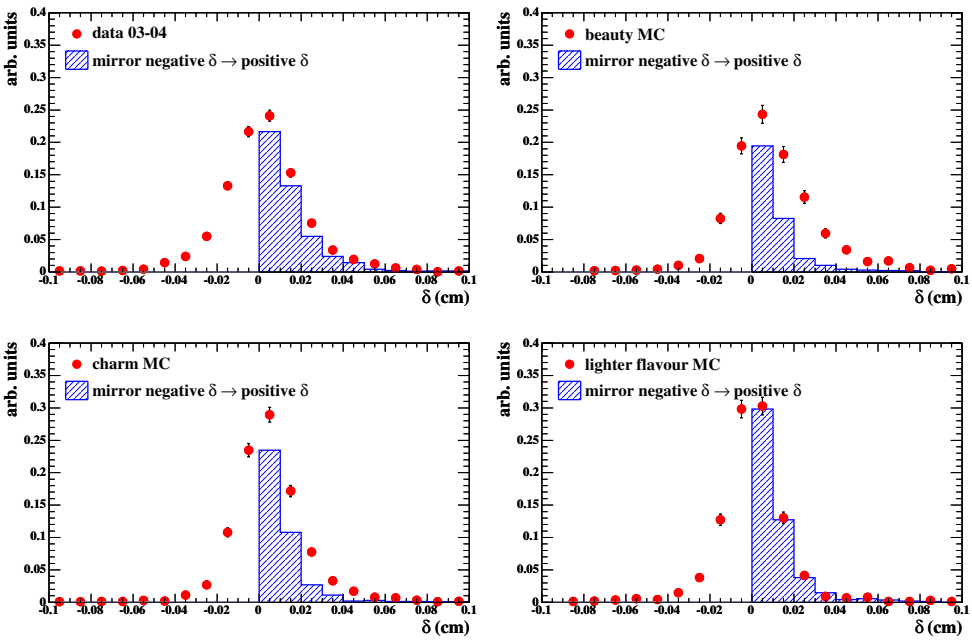

Figure 9.9: Impact parameter distributions showing also the negative part mirrored to the positive part to indicate the asymmetry for the reduced post–upgrade data sample (*top left*) and the post–upgrade beauty (*top right*), charm (*bottom left*) and lighter flavours (*bottom right*) MC samples.

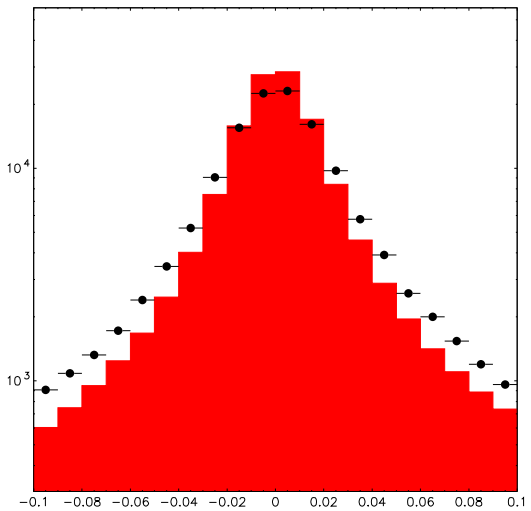

Figure 9.10: Comparison between impact parameter distributions from data (marker) and lighter flavours MC simulation (filled histogram).

In Sec. 10.3, the compatibility between the determined beauty fraction for the post–upgrade running periods with the impact parameter measurement is investigated as a first step to extract the beauty fraction from the selected dijet plus muon data sample by the impact parameter method.

Chapter 10

Measurement of Beauty Quark Cross Sections

One of the overall goals of the ZEUS post–upgrade beauty quark program is the measurement of beauty quark cross sections with a different beauty signal extraction method than the p_T^{rel} *method* (see Sec. 9.1). After the upgrade 2000/2001 and with the integration of the micro–vertex–detector MVD (see Sec. 5.2.2), the utilisation of the long lifetime of the beauty quarks became feasible with the improved track reconstruction accuracy of the MVD in the vicinity of the vertex (see Sec. 9.2). The goal of this thesis is to present first applicability studies of the impact parameter method in comparison to the well established p_T^{rel} method. Therefore, a suitable dijet plus muon event sample is selected separately from the pre– and post–upgrade running periods and the beauty contents are extracted by the p_T^{rel} method. These samples can be used afterwards for the method comparison as well as for new cross section measurements of for example jet–jet correlations.

The initial recorded luminosity of the post–upgrade running period was still relatively small but the impact parameter method eventually promises a higher background rejection than the p_T^{rel} method. Therefore, the first step in the preparation of a suitable dijet plus muon sample was the increase of the statistics of the selection with the *general muon finder* (see Sec. 7.3.2). The combination of different muon reconstruction algorithms including the lowering of the kinematic muon cuts allowed to increase the statistics by almost an order of magnitude compared to previous analyses accepting a slightly higher background fraction.

For the preparation of the post–upgrade dijet plus muon sample, the performance of the new event selection is investigated in the pre–upgrade running periods. With the previous results in the pre–upgrade periods [42], a good foundation exists to compare cross sections determined using the new event selection with previous measurements and to measure new cross sections.
The investigation of the pre–upgrade event selection is split into several stages. First, the description of the extracted beauty signal from the sample by leading order plus parton shower beauty quark MC simulations from PYTHIA (see Sec. 2.4.1) is checked to be accurate before cross sections are calculated. A good description of the inclusive dijet plus muon selection by the signal and background MC simulations was already shown in chapter 8.
An accurate signal description will confirm the correctness of the beauty content extraction by the p_T^{rel} method and is a prerequisite to calculate differential cross sections for muon, jet and event kinematic variables by the extraction of acceptances from the MC. The differential cross sections are then compared to PYTHIA to check the compatibility of the measured cross section with the leading order plus parton shower approach. In the end, the comparison of beauty quark cross sections to NLO QCD predictions from FMNR (see Sec. 2.4.2) will investigate the compatibility of the measured cross sections to the currently available most accurate theoretical calculations in next–to–leading order.

Having demonstrated the good performance of the new event selection in the pre–upgrade running periods, the emphasis is shifted to the post–upgrade running periods. Following the approach of the pre–upgrade running periods, the performance of the new event selection in combination with the p_T^{rel} method is investigated by comparisons of kinematic distributions of the extracted beauty signal in the data with the predictions of the PYTHIA MC. Cross sections are compared to the cross section predictions of the

leading order plus parton shower PYTHIA MC and a first comparison with NLO QCD predictions by FMNR is presented.
The key comparison between the differential cross sections from the pre– and post–upgrade periods, having demonstrated the correctness of the pre–upgrade cross sections before, demonstrates that the post-upgrade dijet plus muon sample can be used to extract beauty quark cross sections with the p_T^{rel} method and is suitable for the comparison to the impact parameter method.

In the end, the applicability of the impact parameter method is investigated and the current status and an outlook of future steps in the analysis are given.

10.1 Beauty Quark Cross Sections in Pre–Upgrade Running Periods with the p_T^{rel} Method

For the pre–upgrade running periods, previous beauty quark photoproduction cross section measurements using the p_T^{rel} method have been published [42]. The photoproduction and dijet selection is the same as the selection in this analysis. Only the muon selection in the previous analysis follows a more restrictive approach. As a cross check, the differential muon cross sections of the previous analysis are reproduced in their kinematic region and found to be consistent within the statistical errors (see App. F).

Following the approach of the previous analysis, muons, jets or dijets are counted rather than events in all shown distributions.

10.1.1 Beauty Quark Shape Comparison between Data and MC

As a prerequisite for the extraction of acceptances from the signal MC simulation, the accurate description of the extracted beauty quark signal from the data by the leading order plus parton shower prediction from PYTHIA has to be shown. In the following, the beauty quark signal in muon, jet and dijet kinematic observables is extracted from the selected pre–upgrade dijet plus muon sample using the p_T^{rel} method. The signal distributions are compared to the prediction of the beauty quark MC simulation by PYTHIA. As leading order plus parton shower MC generators only describe the shapes of kinematic variables of the selected final state and do not make an accurate prediction of the absolute normalisation, the MC prediction is scaled.

The kinematic observables most sensitive to the correct description of the dijet plus muon beauty quark selection are the transverse momentum and the pseudo-rapidity of the muon. As an example, the extraction of the beauty quark signal in the dijet plus muon data selection differential in the pseudo-rapidity η^μ is described in more detail.

Suitable bins in η^μ are selected with sufficiently high purity, the fraction of reconstructed muons which correspond to a true (generator level) muon:

$$purity = \frac{N^\mu_{\texttt{reconstructed}\wedge\texttt{true}}}{N^\mu_{\texttt{reconstructed}}} \tag{10.1}$$

where $N^\mu_{\texttt{reconstructed}\wedge\texttt{true}}$ is the number of true (generator level) muons which are reconstructed and $N^\mu_{\texttt{reconstructed}}$ the number of reconstructed muons. The beauty quark signal is defined in simulated beauty quark events fulfilling following cuts on the true (MC generator) level:

Photoproduction selection:

$$\begin{aligned} Q^2 &< 1\ \text{GeV}^2 \\ 0.2 &< y < 0.8 \end{aligned} \tag{10.2}$$

Dijet selection: at least two MC true jets:

$$\begin{aligned} p_T^{jet_{1(2)}} &\geq 7(6)\ \text{GeV} \\ |\eta_{jet_{1(2)}}| &< 2.5 \end{aligned} \tag{10.3}$$

Muon selection: at least one muon originating from a beauty quark:

$$\begin{aligned} p_T^{\mu} &\geq 2.0 \text{ GeV} \\ -2.0 &\leq \eta^{\mu} \leq 2.5 \end{aligned} \tag{10.4}$$

Four η^{μ} bins have been chosen in Tab. 10.1.

differential variable	binning
η^{μ}, the pseudo-rapidity of the muon	$-2.0 \leq \eta^{\mu} < -0.9$
	$-0.9 \leq \eta^{\mu} < 0.0$
	$0.0 \leq \eta^{\mu} < 1.2$
	$1.2 \leq \eta^{\mu} \leq 2.5$

Table 10.1: Binning in η^{μ}

Fig. 10.1 shows the purities in the chosen η^{μ} bins. Shown is the muon selection purity folded with the dijet and photoproduction selection purity which represents a significant contribution to the shown purity.

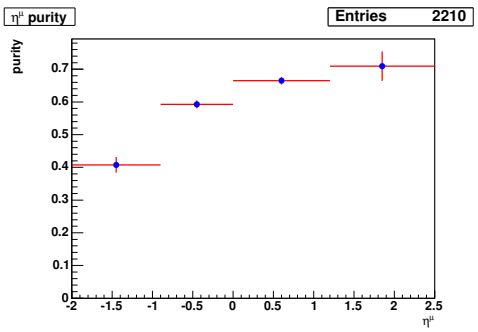

Figure 10.1: Purity of η^{μ} in the chosen binning for the pre–upgrade running periods. Shown is the muon selection purity folded with the dijet selection purity.

The purity is acceptable in the rear bin and good in the barrel and forward bins.

The fraction of muons from beauty quarks in the 4 η^{μ} bins is determined by 4 separate $p_T^{rel,jet-\mu}$ fits shown in Fig. 10.2.
The number of selected muons from beauty quarks differential in η^{μ} is calculated using the 4 beauty fractions in Tab. 10.2. In addition, the calculation of the differential cross sections using the acceptances in the individual bins is presented which will be shown in Sec. 10.1.2.

bin in η^{μ}	beauty fraction [%]	selected muons	muons from beauty quarks	acceptance [%]	differential cross section [pb/rad]
$-2.0 \leq \eta^{\mu} < -0.9$	24.1 ± 2.6	1756 ± 42	423.2 ± 46.8	46.3 ± 1.9	7.5 ± 0.9
$-0.9 \leq \eta^{\mu} < 0.0$	20.9 ± 1.3	10488 ± 102	2192.0 ± 138.0	57.1 ± 0.9	38.6 ± 2.6
$0.0 \leq \eta^{\mu} < 1.2$	18.2 ± 1.2	14609 ± 121	2658.8 ± 176.7	53.8 ± 0.7	37.2 ± 2.6
$1.2 \leq \eta^{\mu} \leq 2.5$	17.9 ± 2.8	2226 ± 47	398.5 ± 62.9	17.3 ± 0.7	16.1 ± 2.6

Table 10.2: Calculation of the number of muons coming from beauty quarks and the beauty quark cross section differential in η^{μ} with statistical errors only.

The acceptance, defined as the fraction of reconstructed muons over true (generator level) muons from the above described true (generator level) beauty quark selection:

$$\mathtt{acc} = \frac{N^{\mu}_{\mathtt{reconstructed}}}{N^{\mu}_{\mathtt{true}}} \tag{10.5}$$

is high for the barrel and rear η^{μ} bins while lower for the forward bin due to the hard cleaning cuts on the forward muon reconstruction (see Sec. 7.3.2.1).

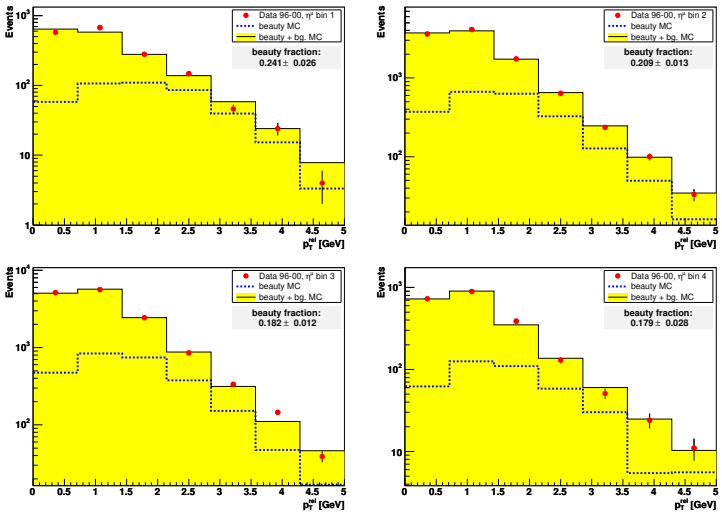

Figure 10.2: Separate determination of the beauty fractions for all 4 bins of the cross section η^{μ} distribution. Shown are the p_T^{rel} distributions from data, beauty MC and signal plus background MC scaled according to the $p_T^{rel,jet-\mu}$ fits and the respective beauty fractions.

For the shape comparison between the beauty quark signal and the beauty MC simulation, the MC is scaled by a factor 2.06 determined by the global pre–upgrade $p_T^{rel,jet-\mu}$ fit (see (*left*) in Fig. 9.4 and Tab. 9.2). The comparison is shown in Fig. 10.3.

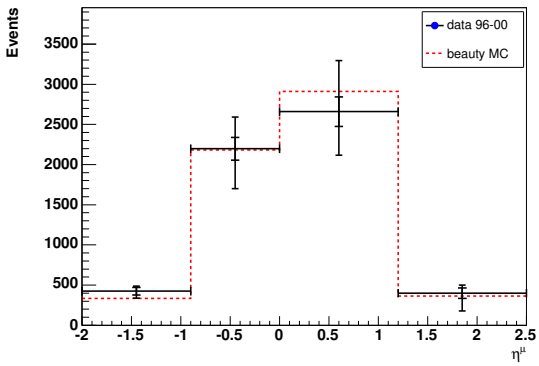

Figure 10.3: Shape comparison between the beauty signal from the pre–upgrade running periods and the beauty MC simulation differential in η^{μ}. Shown are the statistical error (inner error) and the quadratic sum of the statistical and systematic error (full error) for the data. The MC is scaled by a factor 2.06 determined by the global $p_T^{rel,jet-\mu}$ fit.

The systematic error calculation is described in more detail in Sec. 10.1.3. The following systematic effects on the nominal calculated cross section are added in quadrature:

- systematic effect on the $p_T^{rel,jet-\mu}$ shape correction (see Sec. 9.1.1);
- systematic effect of the muon efficiency correction (see Sec. 8.4.1);
- systematic effect of the charm normalisation;
- systematic effect of the resolved and excitation contributions.

The systematic error is determined as the deviation of the differential cross sections from the nominal value. For the calculation of the systematic error of the beauty signal, the determined fractional systematic error was applied to the measurement in the respective bin.

The description of the η^{μ} shape by the scaled signal MC prediction is compatible within statistical and systematic errors and permits the calculation of acceptances using the signal MC simulation.

Following the procedure described for muons from beauty quarks differential in η^{μ}, the description of the extracted beauty signal differential in the transverse momentum of the muon p_T^{μ} by the MC is investigated in Fig. 10.4.

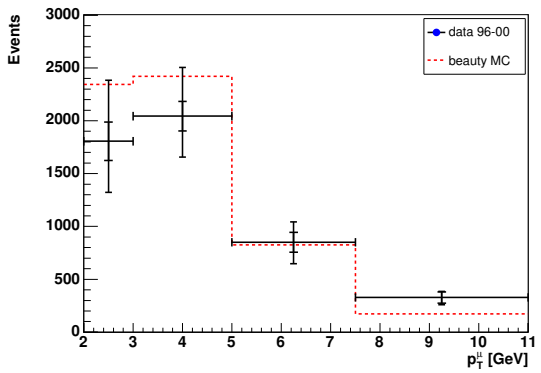

Figure 10.4: Shape comparison between the beauty signal from the pre–upgrade running periods and the beauty quark MC simulation differential p_T^{μ}. Shown are the statistical error (inner error) and the quadratic sum of the statistical and systematic error (full error) for the data. The MC is scaled by a factor 2.06 determined by the global $p_T^{rel,jet-\mu}$ fit.

Also the shape of muons from beauty quarks differential in p_T^{μ} is described within the statistical and systematic errors.
In summary, the selection of muons from beauty quarks in the dijet plus muon sample is described compatible by the beauty MC simulation.

The same picture can be drawn for observables of jets containing a selected muon which investigate the jet part of the dijet plus muon selection p_T^{rel} method.

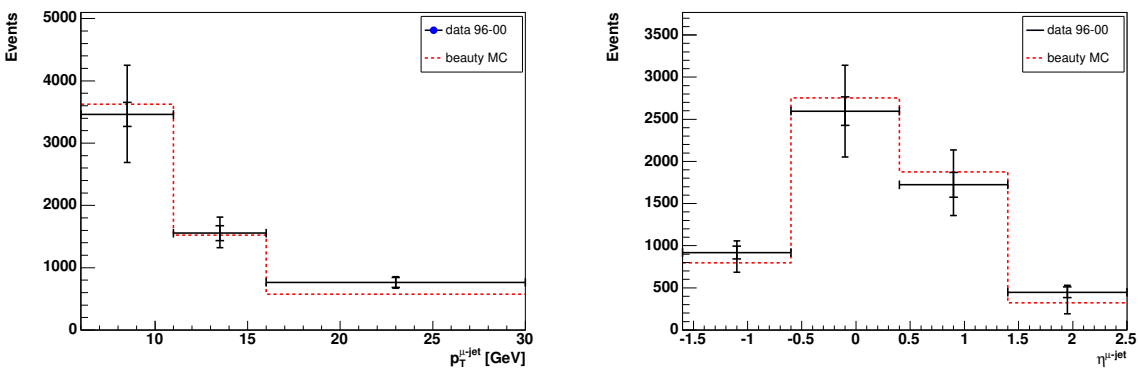

Figure 10.5: Shape comparison between the beauty signal from the pre–upgrade running periods and the beauty quark MC samples differential in $p_T^{\mu-jet}$ (*left*) and $\eta^{\mu-jet}$ (*right*). Shown are the statistical error (inner error) and the quadratic sum of the statistical and systematic error (full error). The MC is scaled by a factor 2.06 determined by the global p_T^{rel} fit.

The shape of the transverse momentum of the beauty quark jet containing the muon $p_T^{\mu-jet}$ and the pseudo-rapidity of the beauty quark jet containing the muon $\eta^{\mu-jet}$ are described within statistical and systematic errors by the beauty quark MC simulation (see Fig. 10.5). As well as for the muon spectra, the jet spectra are described by the beauty quark MC simulation which is therefore suited to extract

acceptances.

The shape comparisons are continued investigating jet–jet correlations of the selected dijet system. The shape of beauty quark events differential in x_γ^{jets} (see Eq. 2.28) is compared to the scaled MC prediction in Fig. 10.6.

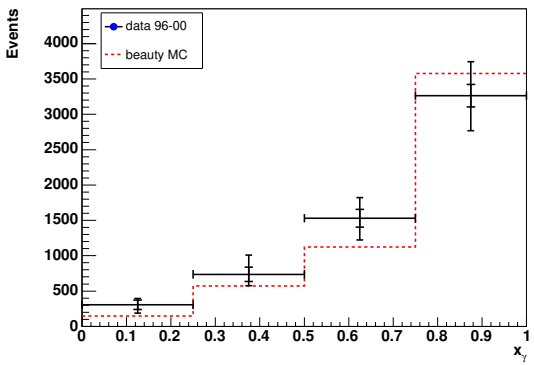

Figure 10.6: Shape comparison between the beauty signal from the pre–upgrade running periods and the beauty quark MC samples differential in x_γ^{jets}. Shown are the statistical error (inner error) and the quadratic sum of the statistical and systematic error (full error). The MC is scaled by a factor 2.06 determined by the global p_T^{rel} fit.

The simultaneous description of the high and low x_γ^{jets} regions by the beauty quark MC shows that the leading order separation into direct and resolved processes implemented in the PYTHIA MC simulation folded with the parton shower approach describes the beauty quark data within statistical and systematic errors. The low x_γ^{jets} part (dominated by the resolved and excitation contributions) might be slightly underestimated.

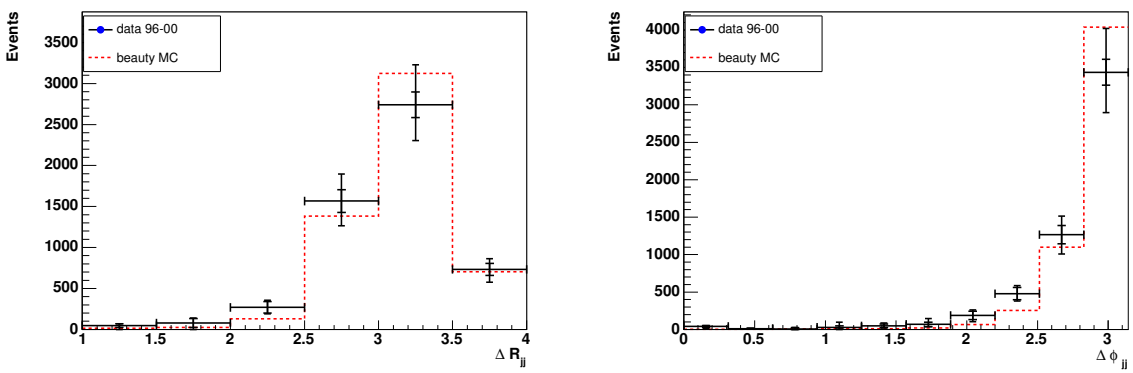

Figure 10.7: Shape comparison between the beauty signal from the pre–upgrade running periods and the beauty quark MC samples differential in ΔR_{jj} and $\Delta\phi_{jj}$. Shown are the statistical error (inner error) and the quadratic sum of the statistical and systematic error (full error). The MC is scaled by a factor 2.06 determined by the global p_T^{rel} fit.

The description of the shapes differential in $\Delta\phi_{jj}$ and ΔR_{jj} (see Fig 10.7) between the two highest-p_T jets in beauty quark dijet plus muon events is good and shows again that the higher order contributions and the parton–jet smearing are well described by the MC simulation. Leading order contributions are characterised by back–to–back configurations of the dijet system because only 2 partons are produced by the hard scatter in leading order. Higher order contributions involve more than two partons represented by more than two jets in the final state and the dijet system is not in a back–to–back configuration. Again, there is a slight tendency to underestimate the higher order contributions.

Overall, the shape comparisons to MC all show a good description of the measurement by the PYTHIA MC simulation. The MC samples are therefore suited to calculate the acceptances and the differential cross sections.

10.1.2 Differential Beauty Quark Cross Sections and Comparison to Leading Order plus Parton Shower MC

This section presents the calculation of beauty quark photoproduction cross sections from dijet plus muon events in the pre–upgrade running periods. The cross sections are compared to the prediction of the leading order plus parton shower MC predictions of the PYTHIA generator. This comparison will investigate the compatibility of the measurement with leading order theoretical calculations, supplemented by the parton shower approach to include also higher order topologies. As previously discussed (see Sec. 2.4.1), the leading order plus parton shower approach results in reliable predictions of the shapes of the kinematic distributions of the selected final state but shows differences in the absolute prediction. Therefore, the MC prediction is scaled by a factor of 2.06 to the data determined by the global pre–upgrade $p_T^{rel,jet-\mu}$ fit (see (*left*) in Fig. 9.4 and Tab. 9.2). The comparison only makes statements about the shape compatibility of differential cross sections. Therefore, only differential cross sections are presented in the following.

The shape comparison in Sec. 10.1.1 showed the compatibility between extracted beauty signal from the data and beauty quark MC simulation. Therefore, the beauty quark simulation can be used to calculate the acceptances for every bin of the cross sections following Eq. 10.5.
The cross sections are calculated in each bin by:

$$\sigma = \frac{N_{\texttt{data}} \cdot f_{beauty}}{\mathcal{L} \cdot \texttt{acc}} \tag{10.6}$$

where $N_{\texttt{data}}$ denotes the number of selected objects (muons, jets, dijets) in the dijet plus muon data sample, f_{beauty} is the beauty fraction determined by an individual $p_T^{rel,jet-\mu}$ fit in every bin of the cross sections, $\mathcal{L}$ is the luminosity corresponding to the dijet plus muon data sample and `acc` is the acceptance calculated from the beauty quark MC simulation. The statistical error on the cross section is determined by the error propagation of the statistical error of the selected dijet plus muon sample and the error on the beauty fraction (see Eq. 9.8).

The pre–upgrade running periods have different centre–of–mass energies and a correction is applied to quote all cross sections at the higher centre–of–mass energy of $\sqrt{s} = 318$ GeV. The effect on the cross sections was determined from NLO QCD predictions by the previous analysis [42] to be $\sim 2\%$ taking only the running periods 96-97 and 99-00 into account. A correction for the the cross sections presented here in the pre–upgrade running periods is calculated from the used beauty MC simulation. A correction of $\sim 3\%$ is determined from the respective beauty quark generator level cross sections and the data luminosities of the pre–upgrade running periods.

Starting with the beauty quark photoproduction cross sections differential in the transverse momentum of the muon p_T^{μ} and the pseudo-rapidity of the muon η^{μ}, the kinematic region for all of the following cross sections from dijet plus muon events at a centre–of–mass energy of $\sqrt{s} = 318$ GeV is defined by:

Photoproduction selection:

$$\begin{aligned} Q^2 &< 1 \text{ GeV}^2 \\ 0.2 &< y < 0.8 \end{aligned} \tag{10.7}$$

Dijet selection: at least two MC true jets:

$$\begin{aligned} p_T^{jet_{1(2)}} &\geq 7(6) \text{ GeV} \\ |\eta_{jet_{1(2)}}| &< 2.5 \end{aligned} \tag{10.8}$$

Muon selection: at least one muon originating from a beauty quark:

$$\begin{aligned} p_T^{\mu} &\geq 2.0 \text{ GeV} \\ -2.0 &\leq \eta^{\mu} \leq 2.5 \end{aligned} \tag{10.9}$$

In this kinematic region, the comparison of the differential muon cross sections

differential variable	cross section	binning
p_T^μ, the transverse momentum of the muon	$d\sigma/dp_T^\mu(ep \to ebbX \to e\mu jjX)$	$2.0\ \text{GeV} \le p_T^\mu < 3.0\ \text{GeV}$ $3.0\ \text{GeV} \le p_T^\mu < 5.0\ \text{GeV}$ $5.0\ \text{GeV} \le p_T^\mu < 7.5\ \text{GeV}$ $7.5\ \text{GeV} \le p_T^\mu \le 11.0\ \text{GeV}$
η^μ, the pseudo-rapidity of the muon	$d\sigma/d\eta^\mu(ep \to ebbX \to e\mu jjX)$	$-2.0 \le \eta^\mu < -0.9$ $-0.9 \le \eta^\mu < 0.0$ $0.0 \le \eta^\mu < 1.2$ $1.2 \le \eta^\mu \le 2.5$

Table 10.3: Definition of the beauty quark photoproduction cross sections differential in the transverse momentum of the muon p_T^μ and the pseudo-rapidity of the muon η^μ.

is shown in Fig. 10.8.

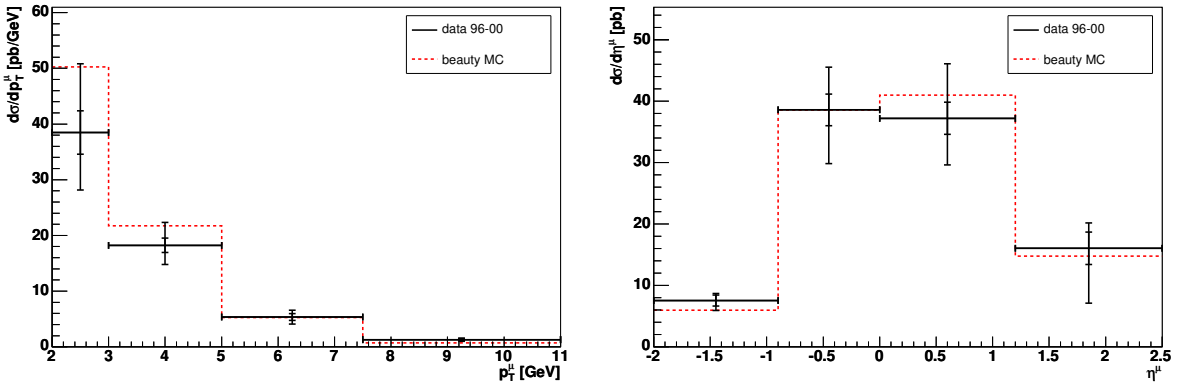

Figure 10.8: Comparison between cross sections differential in p_T^μ (*left*) and η^μ (*right*) from pre–upgrade data and beauty quark MC simulation. Shown are the statistical error (inner error) and the quadratic sum of the statistical and systematic error (full error). The MC is scaled by a factor 2.06 determined by the global p_T^{rel} fit.

The shape of the beauty quark cross sections differential in p_T^μ and η^μ are well described by the prediction of the PYTHIA beauty quark MC within the statistical and systematic errors. The differential cross section is therefore compatible to leading order plus parton shower calculations.

The same result yields the comparison of beauty quark cross sections differential in the transverse momentum of the jet containing a selected muon $p_T^{\mu-jet}$ and the pseudo-rapidity of the jet containing a selected muon $\eta^{\mu-jet}$

differential variable	cross section	binning
$p_T^{\mu-jet}$, the transverse momentum of the jet containing the muon	$d\sigma/dp_T^{\mu-jet}(ep \to eb\bar{b}X \to e\mu jjX)$	$6\ \text{GeV} \le p_T^{\mu-jet} < 11\ \text{GeV}$ $11\ \text{GeV} \le p_T^{\mu-jet} < 16\ \text{GeV}$ $16\ \text{GeV} \le p_T^{\mu-jet} \le 30\ \text{GeV}$
$\eta^{\mu-jet}$, the pseudo-rapidity of the jet containing the muon	$d\sigma/d\eta^{\mu-jet}(ep \to ebbX \to e\mu jjX)$	$-1.6 \le \eta^{\mu-jet} < -0.6$ $-0.6 \le \eta^{\mu-jet} < 0.4$ $0.4 \le \eta^{\mu-jet} < 1.4$ $1.4 \le \eta^{\mu-jet} \le 2.5$

Table 10.4: Definition of the beauty quark photoproduction cross sections differential in the transverse momentum of the jet containing a selected muon p_T^μ and the pseudo-rapidity of the jet containing a selected muon η^μ.

shown in Fig. 10.9.

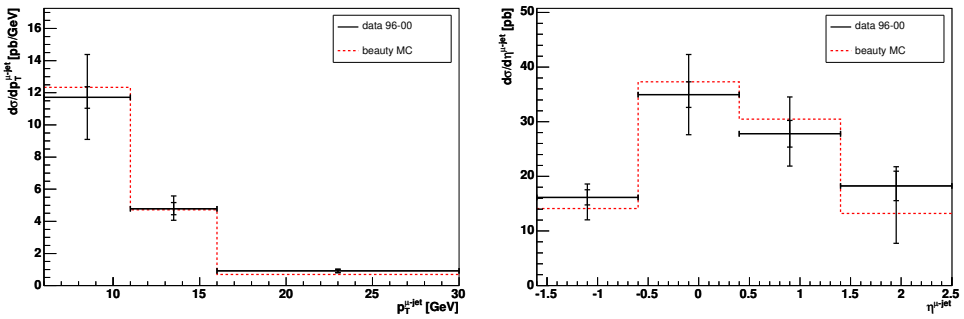

Figure 10.9: Comparison between cross sections differential in $p_T^{\mu-jet}$ (*left*) and $\eta^{\mu-jet}$ (*right*) from pre–upgrade data and beauty quark MC simulation. Shown are the statistical error (inner error) and the quadratic sum of the statistical and systematic error (full error). The MC is scaled by a factor 2.06 determined by the global p_T^{rel} fit.

The good description of the shape of the differential jet cross sections by the MC shows that the implementation of the parton to hadron level transformation implemented by the parton shower approach is compatible with the measurement.

The comparisons of jet–jet correlation cross sections to the leading order plus parton shower MC generator show the compatibility of the addition of higher order contributions to the leading order cross section calculation to the data.
The beauty quark cross section differential in x_γ^{jets}

differential variable	cross section	binning
x_γ^{jets}, the fraction of the momentum of the virtual photon transferred to the hard interaction (see Eq. 2.28)	$d\sigma/dx_\gamma^{jets}(ep \to ebbX \to e\mu jjX)$	$0.00 \leq x_\gamma^{jets} < 0.25$ $0.25 \leq x_\gamma^{jets} < 0.50$ $0.50 \leq x_\gamma^{jets} < 0.75$ $0.75 \leq x_\gamma^{jets} \leq 1.00$

Table 10.5: Definition of the beauty quark photoproduction cross section differential in x_γ^{jets}.

is sensitive to the ratio of separate simulated direct to resolved and excitation processes and compared to the scaled MC prediction in Fig. 10.10.

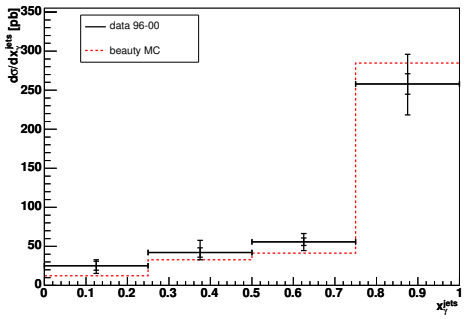

Figure 10.10: Comparison between the cross section differential in x_γ^{jets} from pre–upgrade data and beauty quark MC simulation. Shown are the statistical error (inner error) and the quadratic sum of the statistical and systematic error (full error). The MC is scaled by a factor 2.06 determined by the global p_T^{rel} fit.

The good simultaneous description of the low and high x_γ^{jets} regions of the differential x_γ^{jets} cross section shows the good compatibility of the measurement within statistical and systematic errors with the leading

order separation in direct and resolved processes taken from the PYTHIA MC simulation although some tendency to underestimate the low x_γ^{jets} region can be seen.

The MC comparison of the jet–jet correlation cross sections differential in $\Delta R_{jj} = \sqrt{\Delta\eta_{jj} + \Delta\phi_{jj}}$ and $\Delta\phi_{jj}$

differential variable	cross section	binning
ΔR_{jj}, ΔR between the two highest-p_T jets	$d\sigma/d\Delta R_{jj}(ep \to ebbX \to e\mu jjX)$	6 equidistant bins for $1.0 \leq \Delta R_{jj} \leq 4$
$\Delta\phi_{jj}$, $\Delta\phi$ between the two highest-p_T jets	$d\sigma/d\Delta\phi_{jj}(ep \to ebbX \to e\mu jjX)$	10 equidistant bins for $0 \leq \Delta\phi_{jj} \leq \pi$

Table 10.6: Definition of the beauty quark photoproduction cross sections differential in ΔR_{jj} and $\Delta\phi_{jj}$.

show the description of higher order contributions to the leading order cross section calculation implemented by the parton shower approach in the PYTHIA MC generator. As leading order contributions yield back–to–back configurations of the dijet system, higher order contributions would yield deviating configurations with more than two jets in the final state (see Fig 10.11).

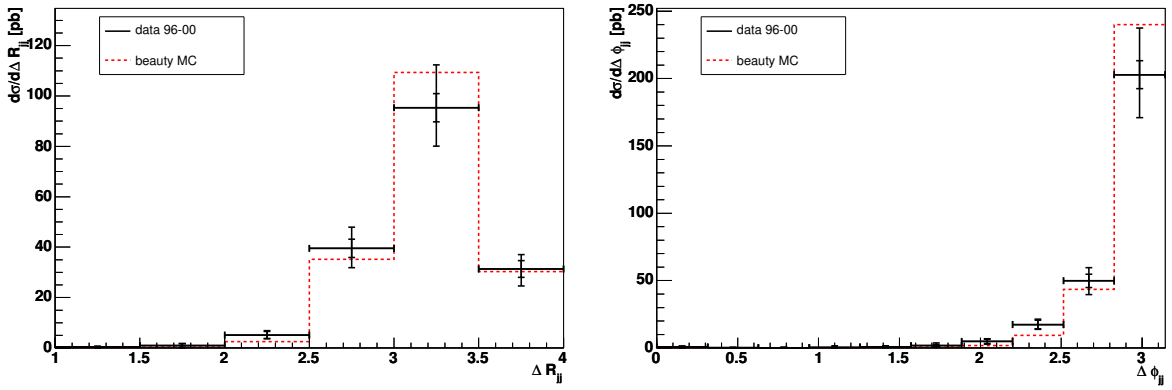

Figure 10.11: Comparison between cross sections differential in ΔR_{jj} (*left*) and $\Delta\phi_{jj}$ (*right*) from pre–upgrade data and beauty quark MC simulation. Shown are the statistical error (inner error) and the quadratic sum of the statistical and systematic error (full error). The MC is scaled by a factor 2.06 determined by the global p_T^{rel} fit.

The good description of the angular cross sections differential in $\Delta\phi_{jj}$ and ΔR_{jj} shows a good understanding of the higher order contributions to the cross section in the beauty quark MC simulation. Especially the reasonable description at $\Delta\phi_{jj}$ lower than π shows a compatible implementation of final states with more than two jets resulting from higher order contributions although an even stronger higher order contribution would further improve the agreement.

As a result, all comparisons of differential beauty quark photoproduction cross sections from dijet plus muon events show a good compatibility to the leading order plus parton shower MC prediction of the PYTHIA MC generator. The kinematics of muons and jets from beauty quarks, the separate simulation of direct, resolved, excitation in photon and proton contributions to the beauty quark cross section and the simulation of higher order contributions to the beauty quark cross section by the MC are all compatible to the presented cross section measurements.

10.1.3 Discussion of Systematic Errors

The systematic error arising from the event reconstruction and the beauty fraction extraction using the p_T^{rel} method are determined by varying the following procedures and corrections. The total systematic error is the quadratic sum of the individual changes in the total and differential cross sections.

p_T^{rel} **shape correction:** The correction for the difference in the shape of the lighter flavour MC samples and the data is also applied to the charm MC samples (see Sec. 9.1.1). For the correction of the

charm p_T^{rel} shape, 50% of the correction calculated using the lighter flavour samples are applied to the charm MC samples. As a systematic check, the p_T^{rel} correction is applied to 100% and not at all to the charm MC samples to investigate its systematic effect. The effect on the total beauty quark photoproduction cross section from dijet plus muon events is $^{+5.5}_{-5.1}$%.

Muon efficiency correction: The systematic effect of the muon efficiency correction is determined by varying the individual bins of the efficiency distributions used to calculate the efficiency correction randomly within their statistical errors. The random variation is carried out 10 times and the systematic effect is calculated as the root-mean-squared of the 10 measurements (see Sec. 8.4.1). The effect on the total beauty quark photoproduction cross section from dijet plus muon events is ±1.7% and reflects the statistics of the isolated dimuon sample used to calculate the corrections. Additional small corrections could arise from differences in the muon chamber and BAC response correction between true and fake muon candidates. These need additional systematic studies and are not yet accounted for.

Charm normalisation: The absolute charm normalisation with respect to the lighter flavour contributions is taken from the respective luminosities of the simulated MC samples. A systematic check is introduced by changing the fraction of the charm contribution by a factor ±2. The effect on the total beauty quark photoproduction cross section from dijet plus muon events is $^{+16.2}_{-13.4}$%.

Normalisation of resolved and excitation contributions: The resolved and excitation contributions to the MC simulation are taken from the respective generated luminosities. The corresponding systematic error is determined by varying the relative contribution of the resolved and excitation processes to the direct processes by a factor ±2 which embraces the differences measured in the x_γ^{jets}, $\Delta\phi_{jj}$ and ΔR_{jj} cross sections. The effect on the total beauty quark photoproduction cross section from dijet plus muon events is $^{+4.7}_{-4.3}$%.

p_T^{rel} **definition:** The beauty fraction is determined by p_T^{rel} fits using the $p_T^{rel,jet-\mu}$ definition (see Eq. 9.2). Changing the determination to use the p_T^{rel} definition (see Eq. 9.1) determines systematic errors in the definition of the hadronic part of the jets. The effect on the total beauty quark photoproduction cross section from dijet plus muon events is −4.8%.

All systematic checks have been determined for the total cross section and all bins of the differential cross sections, details can be found in App. G.
The dominant systematic error for the pre–upgrade cross section arises from the variation of the charm normalisation. The charm normalisation is checked by a comparison to charm cross section measurements with similar final state definitions like $ep \to D^* + dijet + X$ and found to be in agreement. In the future, the charm normalisation can be constrained to the experimentally determined value and its error and introduced as a constraint in a 3-component p_T^{rel} fit.

10.1.4 Differential Beauty Quark Cross Section Comparison to NLO QCD Predictions

NLO QCD predictions are intrinsically more accurate than the leading order plus parton shower implementation of MC generators. In comparison to the MC generator, the higher order contributions do not have to be implemented by phenomenological models because they are already included in the hard scattering matrix elements which are perturbatively calculated to next–to–leading order. In addition, the predictions from NLO QCD calculations not only describe the shape of kinematic distributions, they also predict the absolute normalisation of the cross section which makes a scaling of the prediction unnecessary.

This chapter compares the beauty quark cross sections differential in the transverse momentum of the muon p_T^μ and the pseudo-rapidity of the muon η^μ with NLO QCD predictions from FMNR (see Sec. 2.4.2). This completes the investigation of the pre–upgrade dijet plus muon selection.

The FMNR program produces photoproduction NLO QCD predictions by the generation of correlated sequences of partonic final states. For the direct comparison to the measured differential muon cross sections, the partonic final state has to be translated to a dijet plus muon final state. The jets are formed by the application of the KTCLUS algorithm directly on the partons while the beauty quark fragmentation is carried out according to the Peterson fragmentation function. The subsequent muon decay is taken from PYTHIA. The systematic error arising mainly from the choice of the beauty quark mass and the hadronisation and renormalisation scales are described in Sec. 2.4.2.

In the following, the differential muon cross sections are compared to the NLO QCD predictions. The cross section differential in the transverse momentum of the muon p_T^μ is described by the NLO prediction within the statistical and systematic errors (see Fig. 10.12).

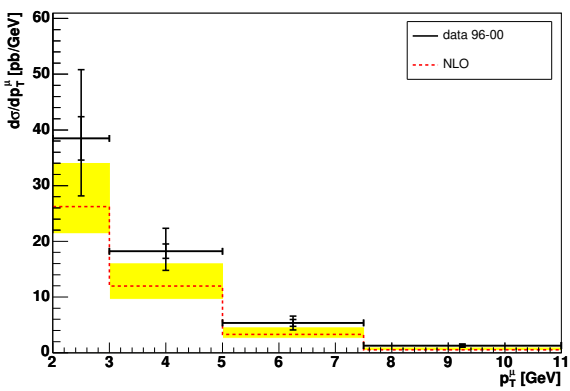

Figure 10.12: Comparison of the cross section differential in the transverse momentum of the muon p_T^μ to NLO QCD predictions from FMNR. Shown are the statistical and systematic errors added in quadrature and the statistical errors alone for the measurement. The error band around the NLO QCD prediction arises from the simultaneous variation of the beauty quark mass and the renormalisation and fragmentation scales.

The description of the p_T^μ spectrum by the NLO QCD prediction shows the same compatibility compared to the previous results (see *(a)* in Fig. 3.10) although they tend to higher values.

The same conclusion is drawn from the comparison of the cross section differential in η^μ with the NLO QCD prediction (see Fig. 10.13).

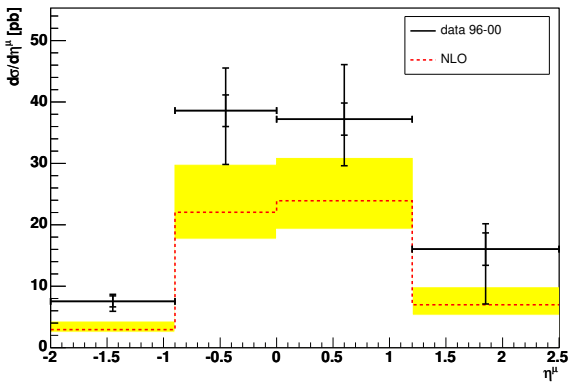

Figure 10.13: Comparison of the cross section differential in the pseudo-rapidity of the muon η^μ to NLO QCD predictions from FMNR. Shown are the statistical and systematic errors added in quadrature and the statistical errors alone for the measurement. The error band around the NLO QCD prediction arises from the simultaneous variation of the beauty quark mass and the renormalisation and fragmentation scales.

The differential cross sections are reasonably described by the NLO QCD predictions. In the following the total beauty quark photoproduction cross section from dijet plus muon events using the global $p_T^{rel,jet-\mu}$ fit is determined:

$$118 \pm 5(stat.)^{+21}_{-19}(syst.)\ pb \tag{10.10}$$

and can be compared to the sum of the differential cross sections in the different bins in p_T^μ (see Fig. 10.12): 93 pb and in η^μ (see Fig. 10.13): 109 pb. The differences of the total cross sections arise from the potential deviations from the predictions of the $p_T^{rel,jet-\mu}$ distributions in the different p_T^μ and η^μ bins. To take this systematics into account, the total cross section is taken as 109 pb. The statistical and systematic errors from the total cross section measurement are scaled to this value and the difference between this value and the other cross sections is taken as the additional systematic error and added in quadrature. The resulting total photoproduction beauty quark cross section in dijet plus muon events

$$109 \pm 5(stat.)^{+21}_{-23}(syst.)\ pb \tag{10.11}$$

can then be compared to the NLO QCD prediction from FMNR

$$61^{+20}_{-12}\ pb \tag{10.12}$$

The measurement is compatible within two standard deviations to the predictions.

Summarising the measurement of pre–upgrade beauty quark photoproduction cross sections from dijet plus muon events using the p_T^{rel} method, the extracted beauty cross sections are compatible to leading order plus parton shower MC predictions. The implementation of higher order contributions to the cross section and the separate simulation of direct, resolved and excitation processes in the PYTHIA MC generator is consistent with the measurement which is a non-trivial observation. In addition, the shapes of the differential muon and jet cross sections are correctly reproduced by the leading order plus parton shower MC. Increasing the accuracy of the theoretical calculation by also taking next–to–leading order matrix elements into account, the total as well as the differential muon cross sections are reasonably described by NLO QCD predictions compatible with previous results. Comparisons of other differential cross sections with NLO have not been carried out because their implementation in FMNR requires the association of the muon to a jet which is currently not implemented. This will be done in the future.

This section concludes that the described muon plus dijet selection results in consistent beauty quark cross sections.

10.2 Beauty Quark Cross Sections in Post–Upgrade Running Periods

After having established the presented dijet plus muon selection in the pre–upgrade running periods and having shown that the selection is suitable to measure beauty quark photoproduction cross sections, the selection is now applied to the post–upgrade running periods. The investigation of the applicability of the p_T^{rel} method by the measurement of beauty quark cross sections and the comparison of these results with the pre–upgrade running period will show if the post–upgrade selection and its signal and background simulation is sufficiently understood for a comparison to cross sections measured with the impact parameter method.

In the beginning, the same shape comparison between extracted beauty signal from the data and the leading order plus partons shower PYTHIA MC prediction is carried out in analogy to the pre–upgrade running period (see Sec. 10.1.1). This investigates the compatibility of the extracted beauty signal with the beauty quark MC simulation after having established the reasonable description of the inclusive dijet plus muon sample with the background plus signal simulation (see chapter 8) keeping in mind the insufficient statistics of the available MC samples. A direct data–data comparison is not carried out as the efficiencies are different for the two running periods.

Afterwards, cross sections are calculated following the pre–upgrade procedures and compared to the leading order plus parton shower simulation and NLO QCD predictions.

The pre–upgrade cross sections have been restricted to a smaller kinematic range for the muon selection ($p_T^\mu \geq 2$ GeV) due to the preselection of the used charm MC samples. This restriction does not exist for the post–upgrade charm samples. Therefore, the muon kinematic region is loosened to the nominal range of $p_T^\mu \geq 1.5$ GeV.

In the end, a direct comparison of the measured pre– and post–upgrade cross sections confirm the compatibility of the two running periods to establish the suitability of the selected sample for the comparison to beauty quark cross sections measured with the impact parameter method.

10.2.1 Beauty Quark Shape Comparison between Data and MC

For the shape comparison between the beauty quark signal and the beauty quark MC simulation, the MC is scaled by a factor 2.77 determined by the global post–upgrade $p_T^{rel,jet-\mu}$ fit (see (*right*) in Fig. 9.4 and Tab. 9.2).

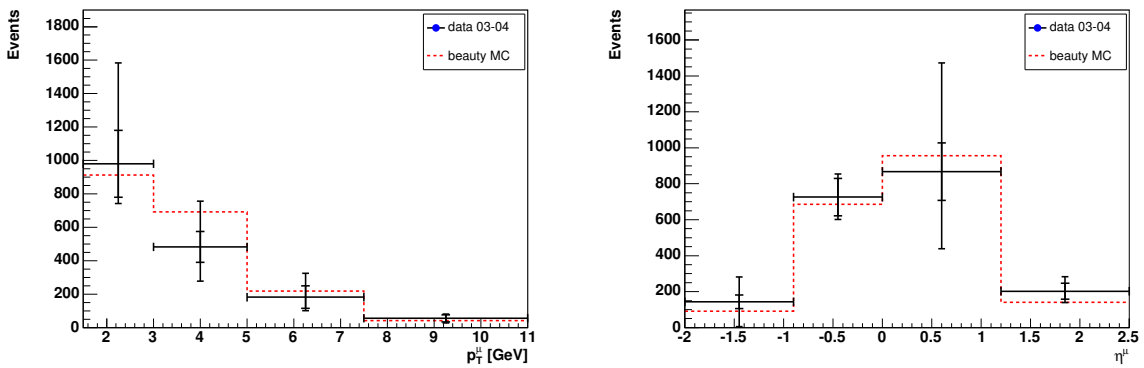

Figure 10.14: Shape comparison between the beauty signal from the post–upgrade running periods and the beauty quark MC samples differential in p_T^μ (*left*) and η^μ (*right*). Shown are the statistical error (inner error) and the quadratic sum of the statistical and systematic error (full error). The MC is scaled by a factor 2.77 determined by the global p_T^{rel} fit.

The shape of the transverse momentum of the muon p_T^μ and the pseudo-rapidity of the muon η^μ (see Fig. 10.14) is well described by the beauty quark MC simulation within statistical and systematic errors also

in the lowest p_T^μ bin which reaches down to smaller p_T^μ due to the vanished restriction in the charm MC simulation. The available MC statistics is small therefore the statistical and systematic errors determined in analogy to the pre–upgrade running periods (see Sec. 10.1.3) are large due to the small available MC statistics not only for the signal and background simulation but also for the muon efficiency correction (details can be found in App. G).
The difference of the pre– and post–upgrade scaling factors can partly be explained by the different generator cross sections due to the differently chosen parameters (see Sec. 8.1). Also the instable $p_T^{rel,jet-\mu}$ fit with very large error and the preliminary trigger correction procedure (see Sec. 8.2.1) are suspected to have an influence on the scaling factor but are still under investigation. The influence of the p_T^μ cut contributes to the difference but does not represent the main contribution. The scaling factors of the post–upgrade $p_T^{rel,jet-\mu}$ fit for $p_T^\mu \geq 1.5$ GeV and $p_T^\mu \geq 2.0$ GeV differ by $\sim 4\%$.
The MC statistics will be enlarged in the near future taking into account the different trigger configurations.

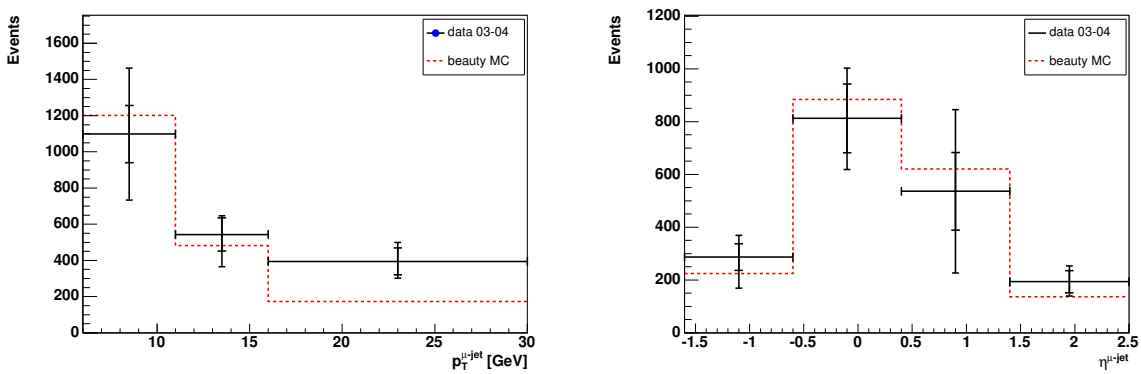

Figure 10.15: Shape comparison between the beauty signal from the post–upgrade running periods and the beauty quark MC samples differential in $p_T^{\mu-jet}$ (*left*) and $\eta^{\mu-jet}$ (*right*). Shown are the statistical error (inner error) and the quadratic sum of the statistical and systematic error (full error). The MC is scaled by a factor 2.77 determined by the global p_T^{rel} fit.

The same behaviour can be observed in the comparison of $p_T^{\mu-jet}$ and $\eta^{\mu-jet}$ (see Fig. 10.15) with the beauty quark MC simulation. Within the statistical and systematic errors, only the high-p_T region shows differences.

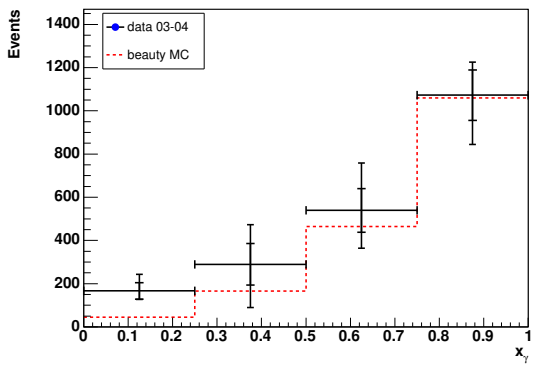

Figure 10.16: Shape comparison between the beauty signal from the post–upgrade running periods and the beauty quark MC samples differential in x_γ^{jets}. Shown are the statistical error (inner error) and the quadratic sum of the statistical and systematic error (full error). The MC is scaled by a factor 2.77 determined by the global p_T^{rel} fit.

The shape of x_γ^{jets} is approximately compatible within the large statistical and systematic errors with

the MC simulation (see Fig. 10.16) as an indication for the correctness of the simulation of the leading order direct and resolved components. More MC is needed to establish a conclusive picture.

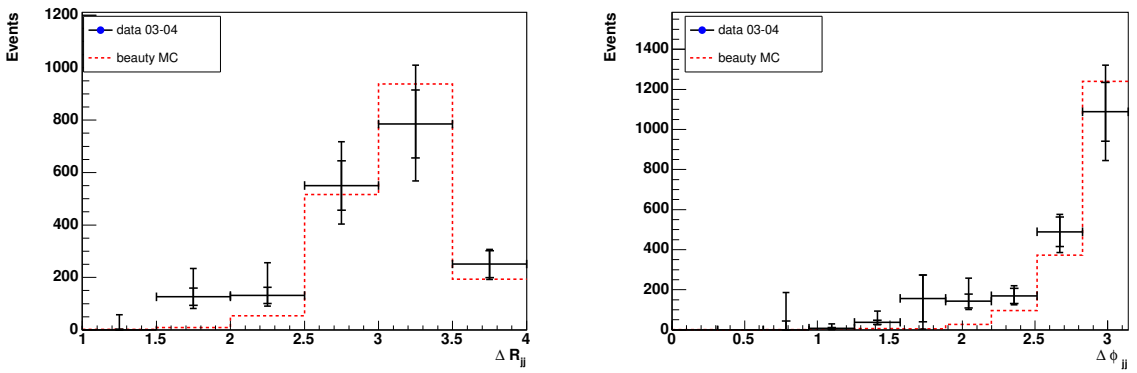

Figure 10.17: Shape comparison between the beauty signal from the post–upgrade running periods and the beauty quark MC samples differential in ΔR_{jj} and $\Delta\phi_{jj}$. Shown are the statistical error (inner error) and the quadratic sum of the statistical and systematic error (full error). The MC is scaled by a factor 2.77 determined by the global p_T^{rel} fit.

The angular shapes shown in Fig. 10.17 are also compatible with the beauty quark MC simulation within the large statistical and systematic errors.

Summarising, within the large statistical and systematic errors and taking into account the instability of the $p_T^{rel,jet-\mu}$ fit due to the small available MC statistics, the shape of the beauty signal is compatible with the prediction from the MC simulation. The calculation of the cross sections is continued in the next section taking into account the small available MC statistics.

10.2.2 Differential Beauty Quark Cross Sections in the Post–Upgrade Running Periods

After having shown that the extracted beauty signal is reasonably described by the post–upgrade beauty quark MC simulation (see Sec. 10.2.1), the acceptances are extracted and the cross sections are calculated in analogy to the pre–upgrade running periods (see Sec. 10.1.2).

The limitation of the preselection of the charm MC simulation that needed the kinematic muon region to be restricted to $p_T^{\mu} \geq 2$ GeV in the pre–upgrade running periods does not exists for the post–upgrade charm MC samples. Therefore, all cross sections are given for $p_T^{\mu} \geq 1.5$ GeV.

The differential post–upgrade cross sections measured at a centre–of–mass energy of $\sqrt{s} = 318$ GeV are compared in an analogue way like the pre–upgrade cross sections to the beauty quark MC simulation to confirm that the calculation of the acceptance can be carried out. The beauty quark MC cross section prediction from PYTHIA is scaled by a factor $f = 2.77$ determined by the global p_T^{rel} fit. In the following, the cross sections:

- differential in p_T^{μ} and η^{μ} (see Fig. 10.18),
- differential in $p_T^{\mu-jet}$ and $\eta^{\mu-jet}$ (see Fig. 10.19),
- differential in x_{γ}^{jets} (see Fig. 10.20),
- differential in ΔR_{jj} and $\Delta\phi_{jj}$ (see Fig. 10.21)

are compared to the scaled leading order MC prediction.

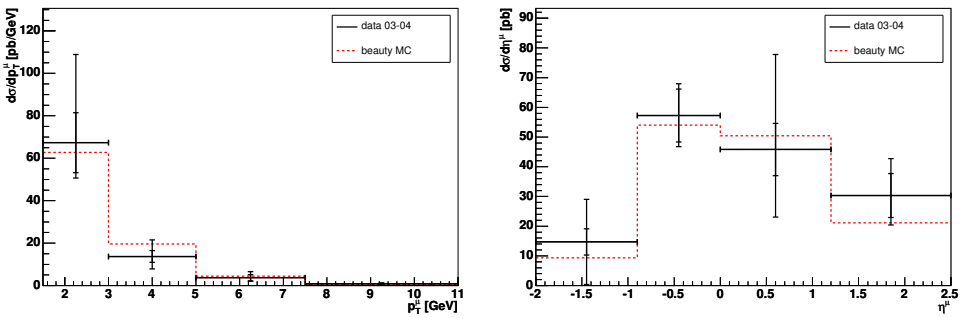

Figure 10.18: Comparison between cross sections differential in p_T^{μ} (*left*) and η^{μ} (*right*) from post–upgrade data and beauty quark MC simulation. Shown are the statistical error (inner error) and the quadratic sum of the statistical and systematic error (full error). The MC is scaled by a factor 2.77 determined by the global p_T^{rel} fit.

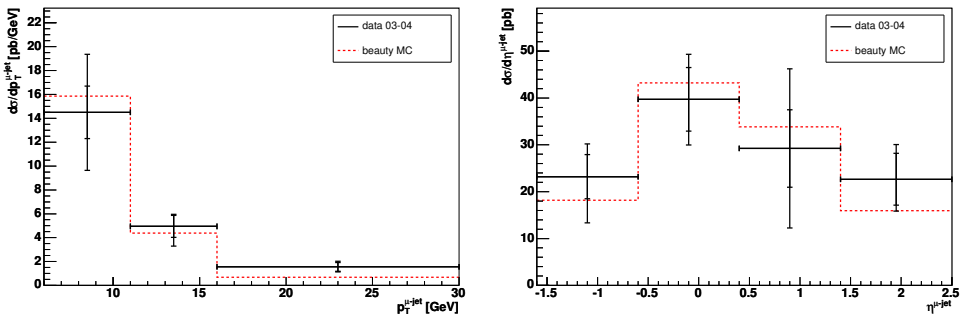

Figure 10.19: Comparison between cross sections differential in $p_T^{\mu-jet}$ (*left*) and $\eta^{\mu-jet}$ (*right*) from post–upgrade data and beauty quark MC simulation. Shown are the statistical error (inner error) and the quadratic sum of the statistical and systematic error (full error). The MC is scaled by a factor 2.77 determined by the global p_T^{rel} fit.

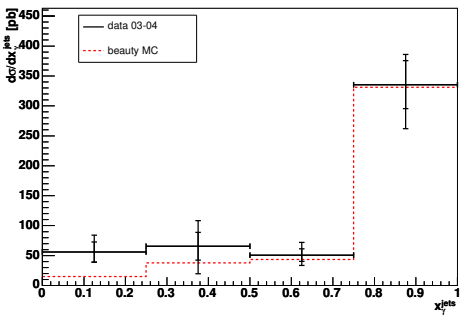

Figure 10.20: Comparison between the cross section differential in x_{γ}^{jets} from post–upgrade data and beauty quark MC simulation. Shown are the statistical error (inner error) and the quadratic sum of the statistical and systematic error (full error). The MC is scaled by a factor 2.77 determined by the global p_T^{rel} fit.

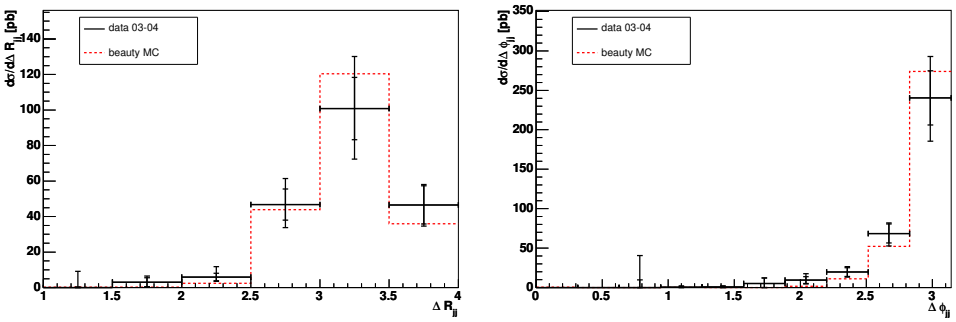

Figure 10.21: Comparison between cross sections differential in ΔR_{jj} (*left*) and $\Delta\phi_{jj}$ (*right*) from post–upgrade data and beauty quark MC simulation. Shown are the statistical error (inner error) and the quadratic sum of the statistical and systematic error (full error). The MC is scaled by a factor 2.77 determined by the global p_T^{rel} fit.

The comparison shows general compatibility with the MC prediction within the large statistical and systematic errors. As described in the shape comparison (see Sec. 10.2.1) the insufficient size of the available MC samples will be enlarged in the future to reduce the statistical and systematic errors.

The comparison to NLO QCD predictions also needs to take into account the small available MC statistics for the acceptance correction.

The cross sections differential in the transverse momentum of the muon p_T^μ and the pseudo-rapidity of the muon η^μ are reasonable described by the NLO prediction within the large statistical and systematic errors (see Fig. 10.22).

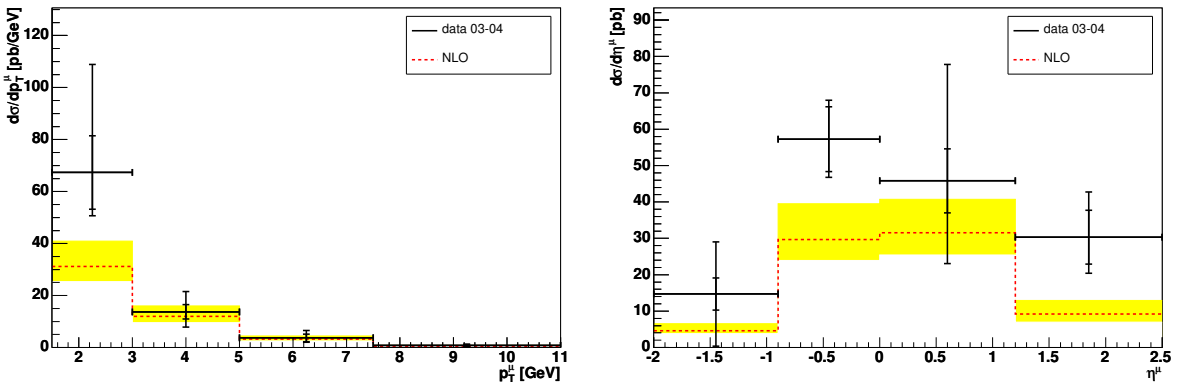

Figure 10.22: Comparison of the cross sections differential in the transverse momentum of the muon p_T^μ (*left*) and the pseudo-rapidity of the muon η^μ (*right*) to NLO QCD predictions from FMNR. Shown are the statistical and systematic errors added in quadrature and the statistical errors alone for the measurement. The error band around the NLO QCD prediction arises from the simultaneous variation of the beauty quark mass and the renormalisation and fragmentation scales.

The total post–upgrade cross section is determined using the global post–upgrade $p_T^{rel,jet-\mu}$ fit

$$169 \pm 19(stat.)^{+32}_{-32}(syst.)\ pb \tag{10.13}$$

and compared to the sum of the differential cross sections in the different bins in p_T^μ: 140 pb and in η^μ: 159 pb. In analogy to the pre–upgrade total cross section, the resulting total cross section taking into account the potential deviations from the predictions of the $p_T^{rel,jet-\mu}$ distributions in the different p_T^μ and η^μ bins

$$159 \pm 18(stat.)^{+32}_{-35}(syst.)\ pb \tag{10.14}$$

still differs from the NLO QCD prediction from FMNR

$$82^{+27}_{-16}\ pb \tag{10.15}$$

by more than two standard deviations. More systematic studies will be made as soon as the MC statistics has been enlarged significantly.

Summarising the comparison of the measured post–upgrade beauty quark photoproduction cross sections in dijet plus muon events, a reasonable compatibility to leading order plus parton shower and next–to–leading order predictions could be established despite the large statistical and systematic errors. The large errors mainly arise from the small available MC statistics which destabilise the $p_T^{rel,jet-\mu}$ fit and cause large systematic errors of the muon efficiency correction. The systematic errors are given in detail in App. G.

10.2.3 Differential Beauty Quark Cross Section Comparison between Pre– and Post–Upgrade Running Periods

The main test of the suitability of the post–upgrade dijet plus muon sample to compare the p_T^{rel} and impact parameter methods for the beauty quark signal extraction is the direct comparison of the measured beauty quark photoproduction cross sections with the p_T^{rel} method between pre– and post–upgrade running periods. As the pre–upgrade cross sections are restricted to $p_T^{\mu} \geq 2$ GeV due to the preselection of the pre–upgrade charm MC samples, the post–upgrade sample is now as well restricted to this region. All other aspects of the cross section determination remain the same.

The total cross sections from the pre–upgrade running periods

$$118 \pm 5(stat.)^{+21}_{-19}(syst.)\ pb \tag{10.16}$$

is compatible with the post–upgrade total cross section

$$115 \pm 14(stat.)^{+22}_{-22}(syst.)\ pb \tag{10.17}$$

within the statistical and systematical errors.

The comparison of the differential cross sections is shown in Fig. 10.23, Fig. 10.24, Fig. 10.25 and Fig. 10.26.

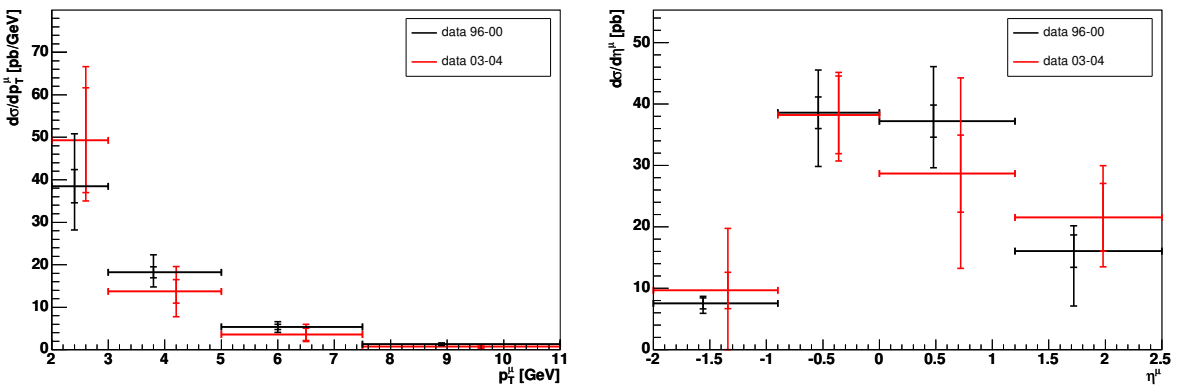

Figure 10.23: Comparison for $p_T^{\mu} \geq 2$ GeV differential in p_T^{μ} (*left*) and η^{μ} (*right*) from pre–upgrade and post–upgrade data. Shown are the statistical error (inner error) and the quadratic sum of the statistical and systematic error (full error).

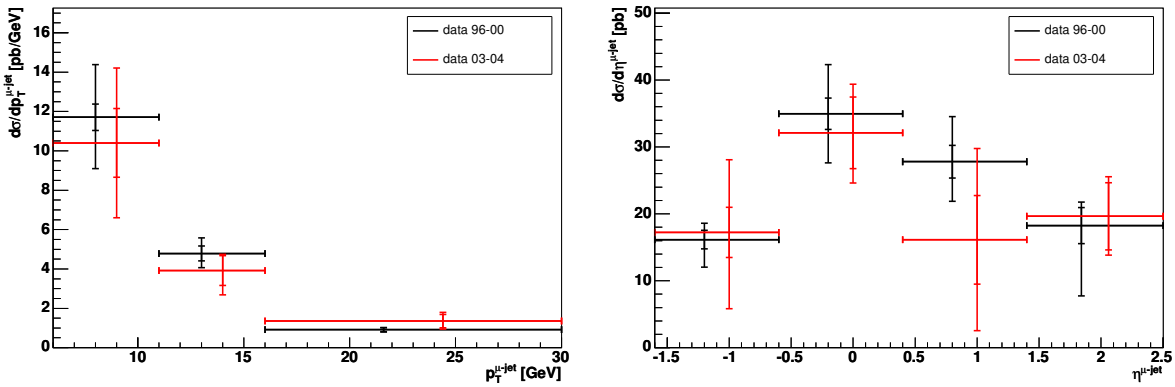

Figure 10.24: Comparison for $p_T^{\mu} \geq 2$ GeV differential in $p_T^{\mu-jet}$ (*left*) and $\eta^{\mu-jet}$ (*right*) from pre–upgrade and post–upgrade data. Shown are the statistical error (inner error) and the quadratic sum of the statistical and systematic error (full error).

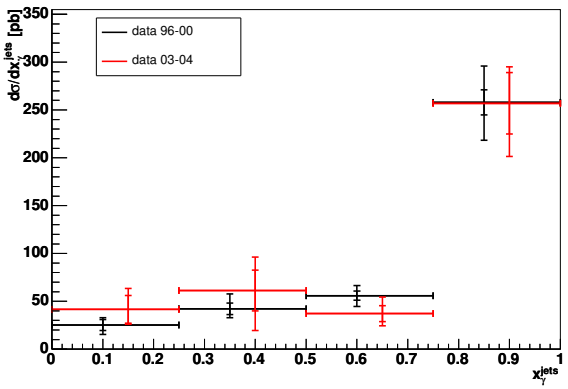

Figure 10.25: Comparison for $p_T^{\mu} \geq 2$ GeV differential in x_{γ}^{jets} from pre–upgrade and post–upgrade data. Shown are the statistical error (inner error) and the quadratic sum of the statistical and systematic error (full error).

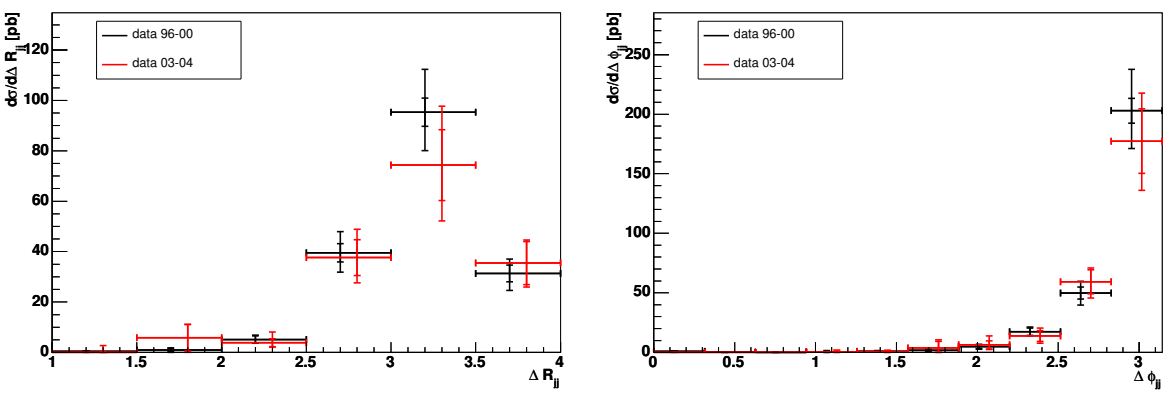

Figure 10.26: Comparison for $p_T^{\mu} \geq 2$ GeV differential in ΔR_{jj} (*left*) and $\Delta\phi_{jj}$ (*right*) from pre–upgrade and post–upgrade data. Shown are the statistical error (inner error) and the quadratic sum of the statistical and systematic error (full error).

As can be seen from the comparison, all differential cross sections are compatible within their systematic

and statistical errors which are large for the post–upgrade running periods.

This compatibility is non–trivial due to

- differences in geometry and trigger acceptances;
- differences in reconstruction efficiencies for the tracking and muon systems;
- differences in the MC samples used for the efficiency correction.

This comparison shows the compatibility between the two running periods although the systematic errors of the post–upgrade running periods have to be reduced by adding more MC statistics. The goal to select a suitable sample to compare the p_T^{rel} and impact parameter beauty quark signal extraction methods is fulfilled and the selection can be used in future for the comparison.

10.3 Impact Parameter Method in Post–Upgrade Running Periods

One of the overall goals of the beauty quark program in the post–upgrade running periods is the measurement of beauty quark cross sections with a different beauty quark signal extraction method than the p_T^{rel} method. All the different methods under investigation will depend on the precise track reconstruction in the vicinity of the vertex by the MVD to exploit the long lifetime of beauty quarks. The first approach is the impact parameter method (see Sec. 9.2) which measures the distance–of–closest–approach of the identified muon track to the beamspot. As the impact parameter distribution is harder for beauty quarks than for charm and lighter quarks, a χ^2 fit approach similar to the p_T^{rel} method can be applied to extract the beauty content in the data. For experimental reasons, the signed impact parameter to a reference axis is investigated. Here, beauty quarks show a significant asymmetry with a strong bias to positive impact parameter values.

As the dijet plus muon post–upgrade data sample is suitable for the comparison of the p_T^{rel} method to the impact parameter method, this selection will be used to extract the beauty signal with the impact parameter method.

The preliminary study carried out to extract the beauty signal with the impact parameter method from the dijet plus muon sample has limitations compared to the complete post–upgrade data selection.
Only half of the available post–upgrade luminosity was included because for only the first 20 pb^{-1}, the final MVD alignment was available. In addition, the muon efficiency correction was not available either at that time. The MC samples to describe the signal and background are, as for the complete selection, limited in statistics.

To perform a χ^2 fit of the signal and background impact parameter MC shapes to the data spectrum, a good description of the data by signal and background is required. The data impact parameter spectrum shows an asymmetry (see Fig.10.27) which is expected to originate also from the beauty content.
Using the post–upgrade beauty fraction of $19.2 \pm 2.0\%$ determined by the $p_T^{rel,jet-\mu}$ fit, the comparison of the data impact parameter spectrum to the scaled signal plus background MC simulation is shown in Fig. 10.28.
The asymmetry in the beauty content of the signal MC contribution is clearly visible but the complete simulation is not able to reproduce the data distribution. Especially in the negative part of the impact parameter distribution where no influences from heavy quarks are expected, the description is not accurate. Studies of the impact parameter distribution from lighter flavours in comparison to the MC description show deviations between simulation and data (see Fig. 9.10) which can explain the differences in the negative data description by the MC simulation. An impact parameter fit is therefore not directly possible because a correction for this effect is currently not available but under investigation.

Under the assumption that the lighter flavour background to the impact parameter distribution is totally symmetric, the compatibility of the data impact parameter distribution to the MC simulation can be checked. The negative part of the signed impact parameter distribution in data is subtracted from the positive side as the lighter flavour contributions cancel under the assumption of total symmetry. The

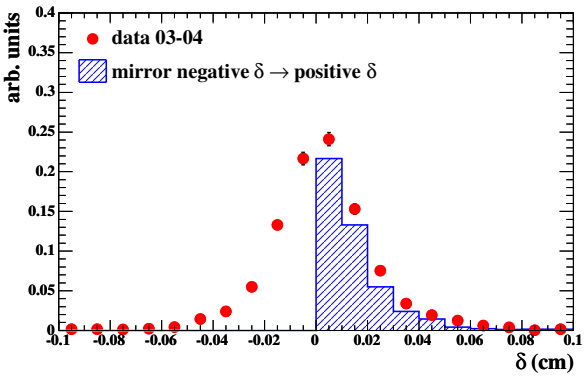

Figure 10.27: Impact parameter distributions showing also the negative part mirrored to the positive part to indicate the asymmetry for the reduced post–upgrade data sample.

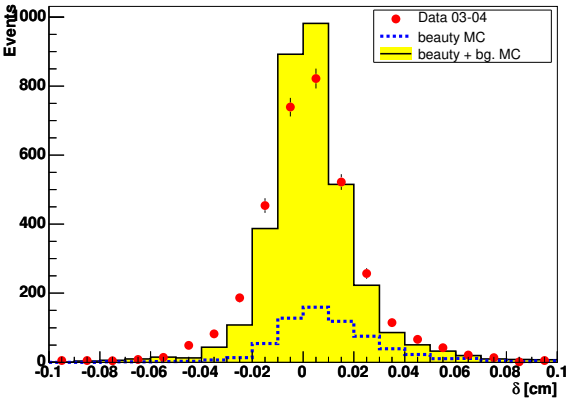

Figure 10.28: Impact parameter distribution of the reduced post–upgrade data sample compared to the signal plus background MC prediction scaled to the data using the post–upgrade beauty fraction of $19.2 \pm 2.0\%$.

mirrored-subtracted contributions from the charm and beauty quark MC simulations are compared to the *mirrored-subtracted* data distribution using the post–upgrade $p_T^{rel,jet-\mu}$ fit and the resulting beauty fraction of $f_{beauty} = 19.2 \pm 2.0$ (see Fig. 10.29).
The measured impact parameter distribution is reasonably compatible with the beauty and charm simulation and the measured beauty fraction determined by the p_T^{rel} method [96].

Further improvements for the impact parameter method are under preparation and will be available soon. The next section gives an outlook of the plans to exploit the long lifetime of the beauty quark in the post–upgrade running periods.

10.3.1 Outlook for the Post–Upgrade Beauty Quark Cross Section Measurements

This first very preliminary application of the impact parameter method in the post–upgrade running periods, which has already been presented at international conferences [96], will be improved in the future.
First of all the MC samples for beauty, charm and lighter flavour have to be enlarged taking into account a proper treatment of the different post–upgrade trigger configurations (see Sec. 8.2.1).
As a second step, the differences in the background MC simulation in the impact parameter distributions (see Sec. 9.2.1) have to be understood better and a suitable correction procedure in analogy to the p_T^{rel} shape correction has to be introduced until the data resolution is fully simulated.

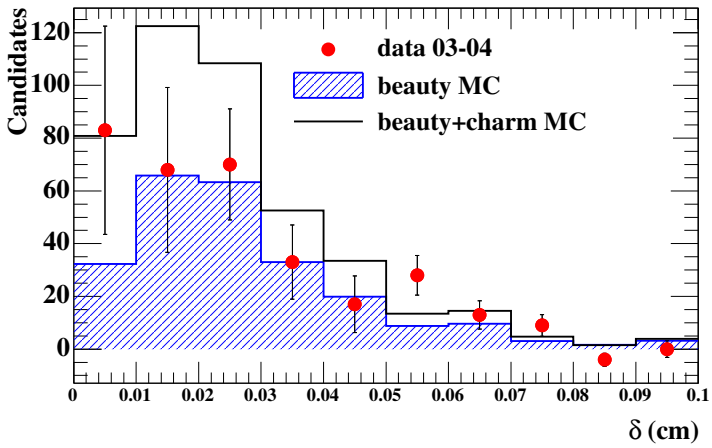

Figure 10.29: Comparison of the data mirrored-subtracted impact parameter distribution to the beauty and charm MC simulation. The MC samples have been scaled according to the beauty fraction determined by the post–upgrade $p_T^{rel,jet-\mu}$ fit. The charm contribution to the background is determined using the number of selected events in the charm and lighter flavours MC samples. Only statistical errors of the measurement are shown.

Taking into account the muon efficiency correction, a proper impact parameter fit can then be performed.

The procedure to exploit the long lifetime of the beauty quark to determine the beauty quark content in the data can be further improved.

First of all, the primary vertex will be used as the reference of the impact parameter calculation as soon as the vertex fit fully including the MVD information is technically stable.

Also the incorporation of the errors on the primary vertex fit and the muon track reconstruction have to be taken into account by measuring not the impact parameter but the impact parameter significance:

$$\delta_{sig} = \frac{\delta}{\sigma_\delta} \tag{10.18}$$

and performing the χ^2 fit for the impact parameter significance distributions of the data and the signal plus background MC simulation. For this step, a detailed understanding of the simulation of the errors of the impact parameter significance has to be reached. A good compatibility between measurement and simulation on the error level is a prerequisite for the applicability of the impact parameter significance method.

In the end, the full available lifetime information can be exploited using secondary vertices instead of the impact parameter significance.

Chapter 11

Conclusions and Outlook

In the study of the fundamental structure of matter, the goal of this thesis was to contribute to the solution of remaining discrepancies in the description of beauty quark production by the *Standard Model*. An important step towards the improvement of the beauty quark production measurements by ZEUS was made by investigating the impact parameter method in conjunction with the p_T^{rel} method to identify beauty quarks. As the impact parameter method exploiting the long lifetime of the beauty quarks is only applicable in the post–upgrade running periods after including the micro–vertex–detector in the ZEUS detector, the running periods have been investigated separately and compared directly.

The p_T^{rel} method was used to measure beauty quark photoproduction cross sections in ep collisions in the pre– and post–upgrade running periods. A comparison to leading order plus parton shower and NLO QCD predictions showed the compatibility of theoretical predictions of the *Standard Model* to the measurements. A further comparison of the measured cross sections between the pre– and post–upgrade running periods also showed the compatibility of the measurements amongst themselves and showed that the post–upgrade detector including its efficiencies is reasonably understood. The impact parameter method, a different method than the p_T^{rel} method to extract the beauty content, can now be applied to this well defined post–upgrade dijet plus muon sample and be compared to the p_T^{rel} method. A first applicability study showed the feasibility of this approach.

By the introduction of the new general muon reconstruction and the lowering of the kinematic muon cuts, the statistics of the dijet plus muon samples was increased by almost an order of magnitude compared to the previous analysis. The new muon reconstruction results in a higher background selection which will be compensated in the future by the application of the impact parameter method which promises a higher background rejection. This increase of the acceptance helped to make the first post–upgrade cross section measurements possible because the statistics in the first post–upgrade running periods was still small for beauty quark production analyses.

The general muon reconstruction was used first to select a high statistics dijet plus muon sample in the pre–upgrade running periods. Suitable muon efficiency corrections were implemented to correct the signal and background MC simulation. The consistency of the selection was confirmed by control distributions in several kinematic variables of the muon, the jet and the dijet system. The comparison of the beauty signal determined bin by bin by the p_T^{rel} method to the beauty quark MC simulation confirmed the compatibility of the extracted beauty quark signal with the leading order plus parton shower signal MC and was therefore used to calculate acceptances and calculate cross sections. The cross sections were compared to scaled leading order predictions from PYTHIA and found to be consistent. The new angular correlation cross sections of the dijet system showed a reasonable compatibility of the implementation of higher order contributions in the leading order plus parton shower MC to the data.
The comparison of the differential muon cross sections to NLO QCD predictions confirmed the *Standard Model* predictions implemented in the FMNR program within the statistical and systematic errors. However, they showed a tendency to slightly higher values. The investigation of the origin of the higher cross sections will be continued in the future.
The main differences between this and the previous analysis are the higher-statistics muon reconstruction and the larger kinematic range. The compatibility of the two event selections was first shown in a direct comparison in the kinematics of the previous results also using the lower-statistics muon reconstruction.

The presented compatibility to NLO QCD predictions then showed the compatibility of the two analyses. Globally, the presented measurements confirmed the beauty quark production description by the standard model within the large systematic errors. Due to these large errors, a strong statement within the global context of beauty production studies can not yet be made.

The JetWeb facility was used to compare beauty quark production measurements from different experiments to *Standard Model* predictions. The comparison proved the simultaneous compatibility between consistent and not consistent measurements. The experience from the pre–upgrade cross section measurements indicates that the treatment of systematic errors has a significant impact and might be the source of the disagreement of some of the measurements with theoretical predictions. In summary, the presented cross sections are compatible with the *Standard Model* within the large systematic errors and tend to disfavour found discrepancies by the Tevatron experiments.
In the following, an outlook on the pre–upgrade cross section measurements is given. The kinematic cut on the transverse momentum of the muon will be lowered to the nominal value of $p_T^{\mu} \geq 1.5$ GeV by using a new charm background MC sample without the preselection restriction. The charm contribution will be fixed from other measurements and taken as a constraint for the p_T^{rel} fit. This will reduce the dominant systematic error.
The comparison to NLO QCD predictions of the differential jet cross sections and especially of the angular correlation cross sections will be carried out as soon as these cross sections have been implemented in the FMNR program to calculate NLO QCD predictions.

In summary, the goal to establish a new high-statistics muon reconstruction and to measure new beauty quark photoproduction cross sections in dijet plus muon events using the p_T^{rel} method was reached.

The described selection was then applied to the post–upgrade data sample. Although the available MC statistics for signal and background description and muon efficiency correction is very small, the comparison of the pre– and post–upgrade differential cross sections showed that the selection is also understood in the post–upgrade running periods although efficiencies are different compared to the pre–upgrade running periods. The measured post–upgrade cross sections were reasonably described by leading order plus parton shower and NLO QCD predictions. The goal to select a suitable dijet plus muon sample with known beauty content determined by the p_T^{rel} method was reached. The sample was shown to be suited for the comparison of the two beauty quark signal extraction methods.

The first study of the impact parameter method using a reduced post–upgrade dijet plus muon sample showed a general applicability of the method although corrections for the background description are not yet available. In the future, the full potential of the method will be exploited once the background corrections have been implemented. Also the full available post–upgrade data statistics will be used and the muon efficiency correction will be applied. Then the impact parameter can be used to extract the beauty fraction and the result can be compared to the p_T^{rel} method.

The next step in the measurement of beauty quark cross sections using the precise track reconstruction of the MVD will be the usage of the impact parameter significance instead of the impact parameter. The advantage of the impact parameter significance method to also take into account the errors on the track reconstruction and the beamspot or primary vertex determination has to be prepared by the careful investigation of the MC description of the reconstruction errors. The final step to extract the beauty content from the measurement of secondary vertices will be addressed when all the described methods have been established and used and the detector and its simulation are well understood.

Appendix A

JetWeb - a WWW MC Comparison Database

The *JetWeb* facility [44] (see Sec. 4) provides global comparisons of cross section measurements using the *HZTOOL* package (see Sec. 4.1). In the following, a more detailed introduction of JetWeb is given.

A.1 An Introduction to JetWeb

Based on the HZTOOL package, JetWeb provides an "easy–to–use" facility to compare cross section measurements to Monte Carlo predictions. It is accessible via a web interface http://jetweb.hep.ucl.ac.uk and publicly available.
HZTOOL provides cross section predictions for differential cross sections from a selectable leading order Monte Carlo plus parton shower generator. The type of colliding particles and their energy can be varied according to the experimental conditions. Also the kinematic regions can be reproduced as defined by the differential cross sections. An HZTOOL job generates cross sections according to the selected luminosity which can be adapted to suit different available processing facilities.
JetWeb represents the superstructure for the HZTOOL package. It consists of a database to collect cross section predictions from HZTOOL which stores all generated differential cross sections bin–by–bin. It can initiate, execute and retrieve multiple HZTOOL processes to split the required luminosity into several instances for batch farm processing. The results are summed up according to their generated luminosity after retrieval and the JetWeb-scale (see 4.1) is determined by the described fit to HERA jet cross sections. In the end, the comparison result is presented graphically to the user by the web interface.
JetWeb is intended to help in the process of Monte Carlo tuning. A common Monte Carlo generator (available in JetWeb and HZTOOL right now: PYTHIA [11] and HERWIG [84]) provides numerous parameters to adapt the phenomenological part of the Monte Carlo generators to simulate the soft contribution of the cross section which are not covered by the leading order hard subprocess to specific experimental conditions and processes. JetWeb provides a possibility to investigate the influence of these parameters on the cross section prediction in a broader context. The Monte Carlo parameter configuration can be used to predict cross section measurements differential in final state quantities like transverse momentum of final and intermediate state particles or jet quantities in different kinematic regions and for different types and energies of initial colliding particles at the same time. With JetWeb, three main comparison procedures can be performed:

1. JetWeb can compare a single measurement to different parameter configurations of a Monte Carlo generator (see Fig. A.1).

2. JetWeb can compare a single measurement to different Monte Carlo generators (see Fig. A.2).

3. JetWeb can compare measurements differential in different variables from collider experiments with different initial particle types and energies to a single Monte Carlo generator (see Fig. A.3).

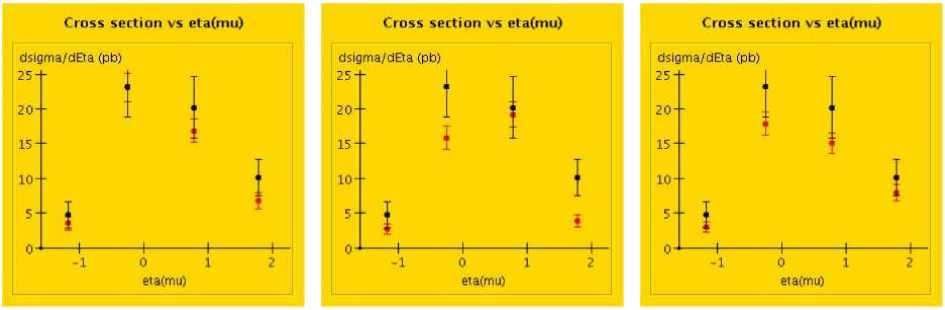

Figure A.1: JetWeb comparison of a generic differential cross section to different parameter configuration of the PYTHIA Monte Carlo generator. Exemplary, the comparison of the beauty quark cross section differential in the muon pseudo-rapidity of the ZEUS collaboration [42] is shown for different implementation of the simulation of the underlying event in PYTHIA (for details, see [11] and references within).

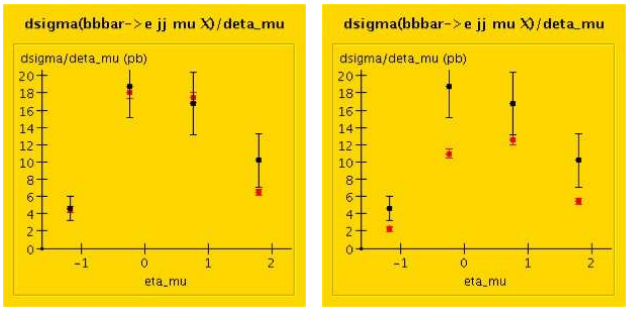

Figure A.2: JetWeb comparison of a generic differential cross section to different Monte Carlo generators. Exemplary, the comparison of the beauty quark cross section differential in the muon pseudo-rapidity of the ZEUS collaboration [42] to predictions from the PYTHIA MC generator (*left*) [11] and the HERWIG MC generator (*right*) [84] is shown.

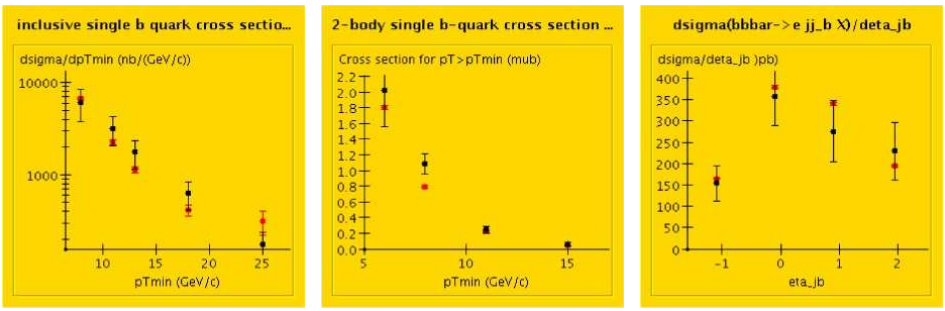

Figure A.3: JetWeb comparison of generic differential cross sections from different experiments the PYTHIA Monte Carlo generator. Exemplary, the comparison of beauty quarks cross sections differential in the beauty quark transverse momentum by the UA1 collaboration [31] and the D0 collaboration [27] and the cross section differential in the beauty quark jet pseudo-rapidity of the ZEUS collaboration [42] is shown for the PYTHIA MC generator [11].

Appendix B

ZeVis - a Technical Description

ZeVis - a Technical Description of the Object-Oriented Event Display for the ZEUS Experiment
This chapter introduces more technical details of the new ZEUS event display ZeVis and complements Cha. 6.

B.1 The Single Event Mode of the ZeVis Event Display

The *single event mode* represents the main access to ZEUS events with the ZeVis event display. It provides an easy–to–use and fast way to display in the simplest case an event of a selected run and event number.

The single event mode uses a pre-initialised deamonised version of the conversion application to overcome the disadvantage of the long initialisation (see Fig. 6.3 in Sec. 6.3). The *event agent* represents a conversion job which waits in a pre-initialised state for requests which are provided to the agent by the dispatcher. The dispatcher can address several agents in parallel to distribute the request load and to enable several concurrent requests at a time. By default, 10 event agents run in parallel on the server waiting for requests. In addition, the server caches requests and can immediately respond to requests which have been converted already and are available in the cache.

The server itself consists of a dual processor Intel XEON 2.2 GHz and a fast IDE Raid with 240 GB of storage capacity connected to the network by gigabit ethernet. The performance of the server has been measured by the response time of random requests (see Fig. B.1).
The response time to non-identical event requests with deactivated server cache is 2 sec in average. This includes the access to the tag database and the event store as well as the event analysis and conversion to ROOT format. The time of the network transfer of the event of an average size of 30 kB is negligible within the Intranet and is not included in the measurement.

In addition, an artificial stress test has been performed by measuring the response time for simultaneous requests (see Fig. B.2). The response time is below 4 sec for up to 9 simultaneous requests and up to 4 requests, no visible degradation of the response time could be observed. Therefore, the number of 10 agents running in parallel is safe to provide a stable and fast service. During normal operation, the concurrency of requests has hardly been observed and the server system is sufficiently dimensioned for further extensions of functionality and higher loads.

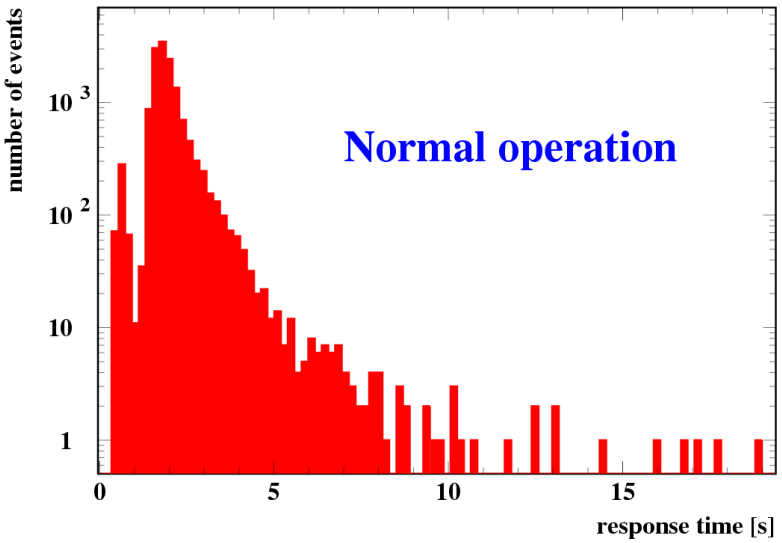

Figure B.1: Distribution of the response time to random single event requests.

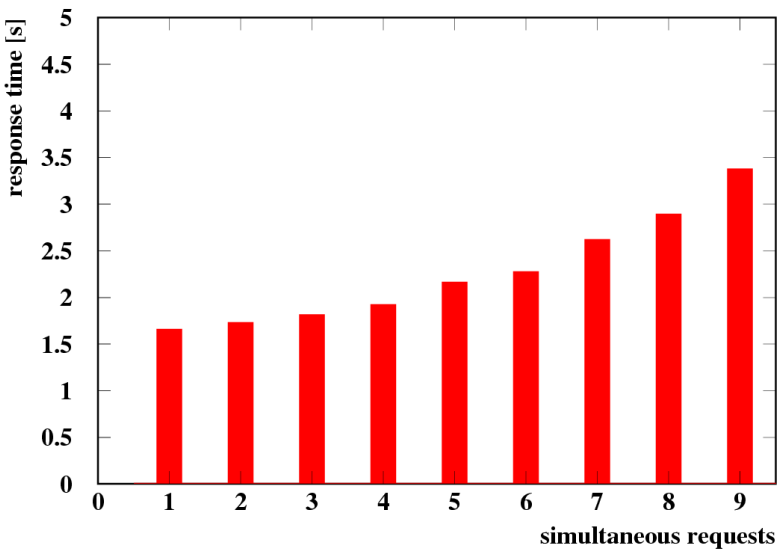

Figure B.2: Response time of concurrent single event requests of the ZeVis server.

B.2 The Graphical User Interface of the ZeVis Event Display

The graphical user interface (GUI) of the ZeVis event display provides the user with the display of the detector geometry in two separate views (pads) and the general event information in the header (see Fig. B.3).

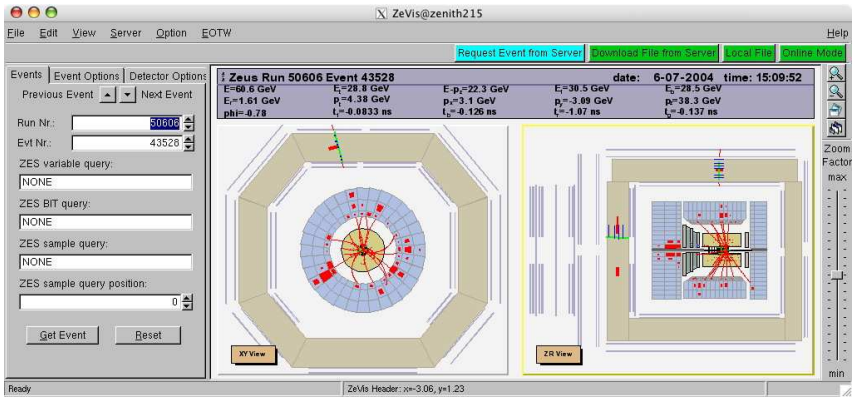

Figure B.3: The graphical user interface (GUI) of the ZeVis event display.

The GUI is separated vertically in 4 layers where the top layer is the menu bar followed by the mode button bar for the server mode selection.
The main layer consists of the tab bar on the left which contains the server mode steering and general event and detector option switches. The layout of the steering tab changes for the selected server mode. It is situated next to the main canvas where the event is displayed in two pads showing each a complete representation of the detector and the header. To the right of the canvas, the zooming and reset button bar including the zoom factor slider to adjust the zoom factor is located.
The status bar in the bottom layer presents information of the operating state of the client and information from objects below the mouse pointer.
In general, all displayed status informations are with respect to the currently active pad which is indicated by a yellow border. To change the active pad, the user has to select the pad by clicking the middle mouse button.
In general, the user can interact with the displayed information in the pad and the header in two ways. The *picking* of an object defined as pointing with the mouse pointer to an object displays related information in the status bar. The *clicking* of an object defined as clicking with the right mouse button on an object makes all related information and options available.
In the following, the different layers and components of the GUI are described in more detail:

Menu bar: The menu bar at the top of the ZeVis GUI window contains the following items:

File menu: The file menu (see *left* of Fig. B.4) provides to

- load the geometry from the server or define a local geometry ROOT file to be loaded;
- load a ROOT file with converted ZEUS events from a local file or by defining an URL for debugging purposes;
- save the currently loaded event or the currently loaded events into a local ROOT file for later usage;
- save a picture of the displayed event with the name

  `r<run number>e<event number>.<default picture type>`

  in the format defined by the default picture type in the *Options* menu or specify the name and type of the picture to save a picture of the currently displayed event;
- print the currently displayed event using the default printer defined in the *Options* menu or define the printer manually;
- save the current settings of the GUI in the ZeVis resource-file

  `.zevis.rsc`

  which will be loaded automatically the next time the GUI is started

Edit menu: This menu provides the *editor* mode to draw lines, boxes, etc. on the pads.

View menu: The view menu (see *center* of Fig. B.4) contains all available options to select and deselect the different available detector components and hit informations in the pads.

It also provides access to specialised 3D views in extra windows like *X3D* and *OpenGL*.

Server menu: The server menu provides access in extra windows to the two server event request modes, the single event request and the multiple event request.

Options menu: The options menu (see *right* of Fig. B.4) provides the user with the possibility to define the refresh time of the online mode, the default picture type and printer and the default event server. It also provides the change of the currently used style to generally select colour schemes and line widths.

EOTW menu: A specialised team of physicist scans periodically the recorded events for special criterias and publishes them in this menu.

Help menu: The help menu gives information about the version of the used software.

Figure B.4: The file (*left*), view (*center*) and options (*right*) menu of the ZeVis GUI.

Server mode steering bar: The steering bar provides four text buttons to switch between the different modes of ZeVis:

Request Event from Server: use ZeVis in the single event mode;

Download File from Server: use ZeVis in the multiple event mode;

Local File: display the events of a local file;

Online Mode: switch to online mode and start displaying the latest available event from the online reconstruction chain periodically.

The selection of the ZeVis running mode in the button bar directly influences the tab cards situated left to the main canvas. Three tabs are used to provide fast access to general event request and display options:

Events: The *events tab* changes according to the selected running mode and displays the server communication options for single and multiple event requests. In the single event mode (see *left* in Fig. B.5), the run and event number and the tag database selection of the request can be defined and it is possible to request the previous and next event following to the current request. In the multiple event mode (see *left center* in Fig. B.5), the filename for the multiple event request can be specified including the file format. A list of loaded and displayable events is presented after the request is processed by the server. In the local file mode (see *center right* in Fig. B.5), only a list of loaded events is shown. The online mode tab (see *right* in Fig. B.5) contains switches to start and stop the periodical display of online events as well as the possibility to change the refresh time.

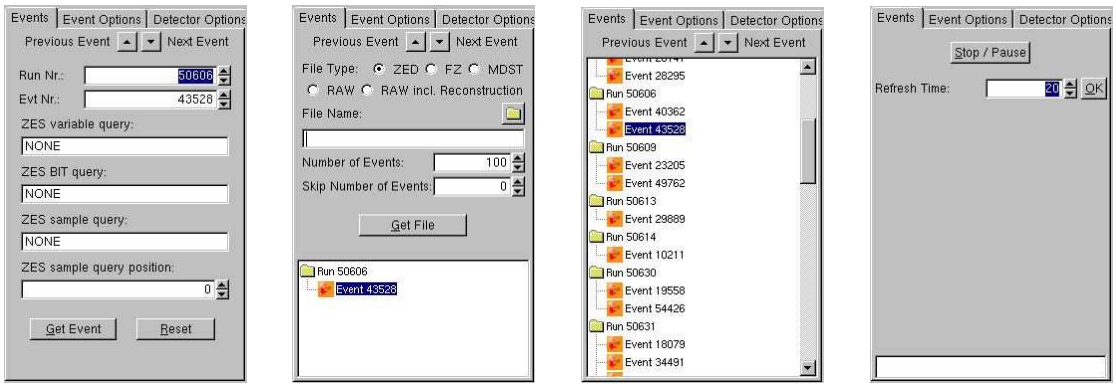

Figure B.5: The different server modes are represented by individual appearances of the events tab in the tab area: *Left:* single event server mode, *Left center:* multiple event server mode, *Right center:* local file mode, *Right:* online mode.

Event Options: This tab (see *left* in Fig. B.6) provides fast toggle switches to select and deselect groups of hit informations. As a rule of thumb, first activate the general switch in this tab before refining your selection in the *View* menu.

Detector Options: Similar to the event options tab, this tab (see *right* in Fig. B.6) provides fast toggle switches to select of deselect the display of complete detector components.

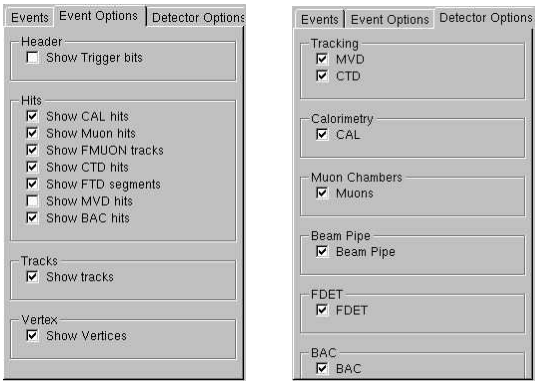

Figure B.6: Fast switches for event (*left*) and detector (*right*) display options can be accessed in the tab area.

To the right of the canvas, a vertical button bar provides zoom-in and zoom-out buttons as well as reset buttons for individual pads or the complete canvas. A vertical slides provides the possibility to increase or decrease the zoom factor for a more detailed zooming behaviour.
At the bottom, the message bar gives informations about the running condition of the client GUI as well as detailed informations of the objects the mouse is *picking* like the track momentum of a track while the mouse is pointing to it on a pad. If no detector of hit information object is beneath the mouse pointer, the ZEUS coordinates of the mouse pointer are displayed in the message bar.
The mouse can be used to move the currently displayed section of the detector in conjunction with the zooming functionalities to display a defined area of interest. This moving is initiated by pressing the left mouse button and letting it pressed while moving the mouse. As the mouse position on the pad is used to display special information of the detector of hit objects beneath the mouse pointer in the message bar, the moving functionality is only available when the mouse is not over a detector component or any hit information.
All displayed objects in the pad can be adjusted using the corresponding object menu by clicking while the mouse pointer is over the object. If no object is beneath the mouse pointer, the menu accessed by clicking (see Fig. B.7) steers the general display behaviour of the pad:

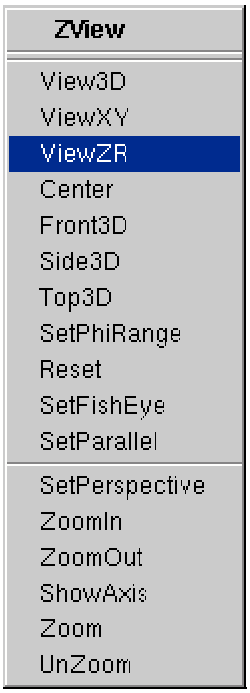

Figure B.7: Popup menu to steer the view mode and view options in the current pad.

- The display mode can be changed between the 3D display and the 2D layered projections in **XY** and **ZR**.
- The area of interest can be centered and special projections in the 3D display mode can be accessed.
- The ϕ range in **XY** which decides which objects are displayed with positive radius in the **ZR** mode can be selected for the pad.
- Also the *fish eye* mode with a non-linear scaling of inner and outer detector parts can be switched on and off.

In summary, the ZeVis GUI provides a large variety of possibilities to initiate and manipulate the display of ZEUS events.

B.3 Incorporating the MVD into the ZeVis Event Display

One of the major features of the new ZeVis event display is the display of the new MVD (see Sec. 5.2.2) amongst the tracking components.
In the following, the integration of the MVD is described in more detail as an example for the internal structure of ZeVis. As an introduction, the general structure of drawing the detector geometry with ROOT [72] is described first.

B.3.1 The ROOT Drawing Capabilities and the ZeVis Event Display

The 3D drawing capabilities of ROOT follow the principle of nested shapes. The drawing of a shape, for example a box, is separated into the shape itself with its dimensions and form and the position and rotation of this shape relative to a reference coordinate system (see Fig. B.8).

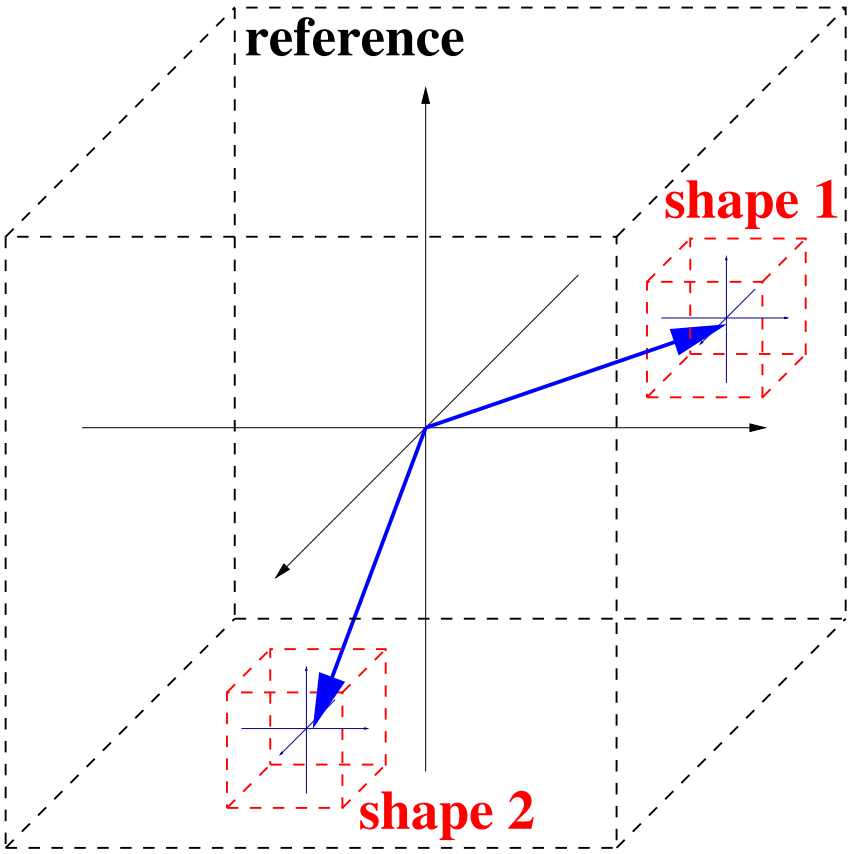

Figure B.8: The 3D drawing capabilities of ROOT represent 3D shapes as a nested shape hierarchy.

A hierarchy of 3D shapes forms the detector where the top shape of the ZEUS geometry (a box with the outer dimensions of the ZEUS detector) sets the global reference of the detector. Each component is represented by an individual shape hierarchy in reference to this top shape. In addition, each component shape contains separate lists of 2D shapes which form the 2D layered projections. Each available layered projection is represented by a separate list (see Fig. B.9).
Each shape, 2D or 3D, has a unique name and can be retrieved and accessed by this name from the top shape of the ZEUS detector. The hit information is mostly given in the notation of the corresponding component and does not contain any geometrical information (see Fig. B.10). For drawing, the spatial position of a hit has to be reconstructed from this information. As the detector geometry already contains all necessary spatial informations, the hit retrieves its corresponding 2D or 3D shape by the name of the shape and initiates its drawing in the reference of this shape.
By using the name lookup mechanism, the event information is completely defined without any geometry information. This reduces the amount of transferred data from the server to the client significantly. Also

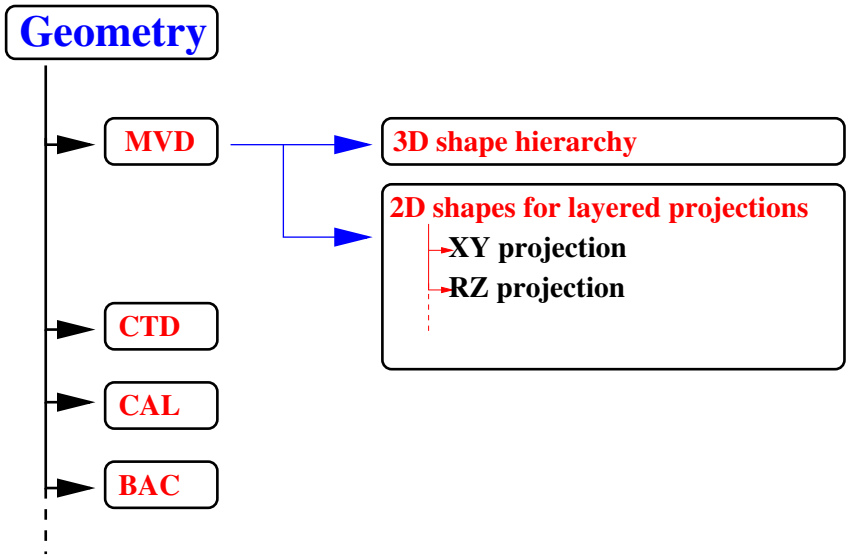

Figure B.9: ZeVis ROOT implementation of the ZEUS geometry containing 3D shape hierarchies and 2D shape lists for the representation of layered projections.

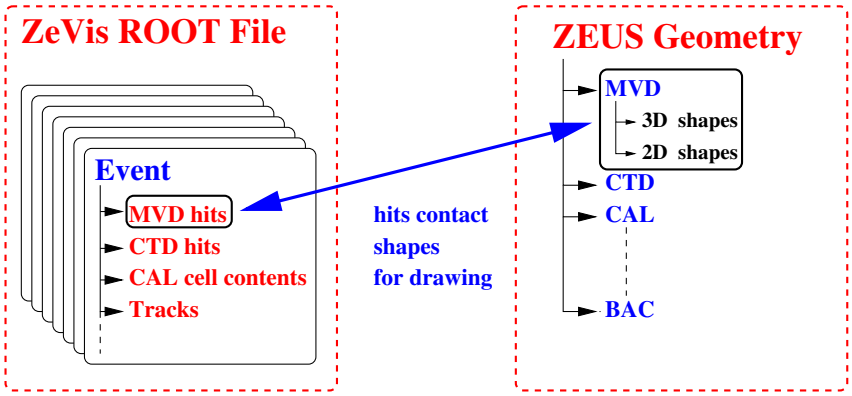

Figure B.10: Interplay of hit information from the ZeVis ROOT file and the geometry using the name lookup mechanism.

the processing time on the server to extract the information from the event store is reduced because no geometry dependencies have to be resolved on the server side.
In the following, the implementation of the MVD geometry and hit information is described in more detail as an example for the integration of a complex detector component.

B.3.2 The Implementation of the MVD Geometry

The dimensions of the following MVD shapes are extracted offline from the ZEUS constants database and follow closely the MVD design (5.2.2).
The hierarchy of 3D shapes is started with the top shape of the MVD which consists of a tube of an outer length of 210.25 cm and an outer radius of 15.95 cm. It is the reference for the MVD detector and subdivided into a forward, barrel and rear tubes (see Tab. B.1) which house the wheels, the ladders and cables respectively.
The forward tube contains four forward wheels (see Tab. B.2 and Fig. B.11) which hold the forward sectors arranged circularly around the beampipe.
Each wheel contains 14 sectors of trapezoidal shape. Two different sector sizes have been integrated (see Tab. B.3 and Fig. B.11) due to the elliptical shape of the beam pipe.
The forward sensors follow the shape of the sectors and contain 480 sense strips each.

Description	Outer radius [cm]	Extension in z [cm]		Length in z [cm]	Content
Forward	15.950	105.250	26.625	131.750	wheels
Barrel	15.950	23.225	-40.075	63.300	ladders
Rear	15.950	-43.125	-105.125	64.000	cables

Table B.1: Forward, barrel and rear tubes of the MVD. Positions in **z** are given with respect to the center of the top MVD tube.

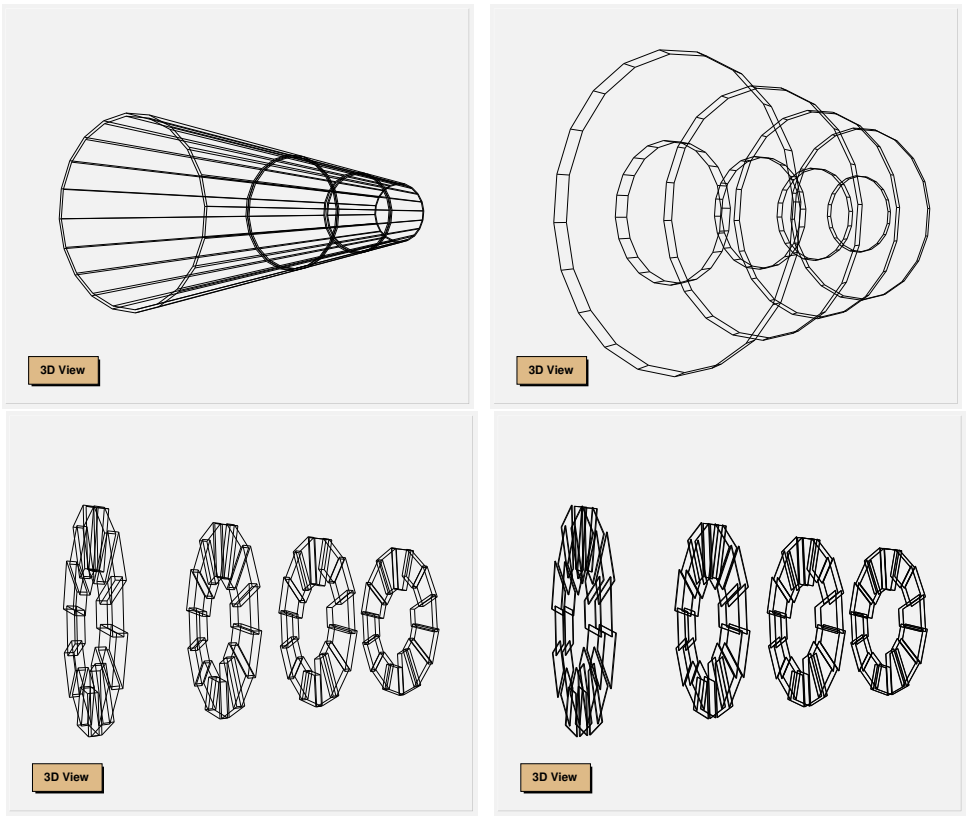

Figure B.11: The 3D shapes of the forward MVD in all stages of the 3D shapes hierarchy: *Top left:* tubes, *Top right:* wheels, *Bottom left:* sectors, *Bottom right:* forward sensors.

Description	Inner radius [cm]	Outer radius [cm]	Extension in z [cm]		Content
Wheel 0	5.998	13.535	-39.650	-38.450	14 sectors
Wheel 1	5.998	13.535	-26.650	-25.450	14 sectors
Wheel 2	5.998	13.535	-13.650	-12.450	14 sectors
Wheel 3	5.998	13.535	-1.350	-2.550	14 sectors

Table B.2: Four wheels of the forward MVD. Positions in **z** are given with respect to the center of the forward MVD tube.

Description	Smaller base length [cm]	Larger base length [cm]	Height [cm]
large sector	3.206	1.529	3.675
small sector	3.206	2.099	2.425

Table B.3: Two different sized trapezoidal shaped sectors.

The barrel tube consists of three cylinders arranged around the beampipe (see Tab. B.4 and Fig. B.12). Each cylinder holds ladders which represent the support structure to hold the barrel sensors.
The ladders are tilted with respect to an axis parallel to the beam axis through the center of a ladder. This results in overlaps between the different cylinders.
Each ladder has a length of 63.3 cm, a width of 6.424 cm and a height of 0.3 cm and contain 5 modules of

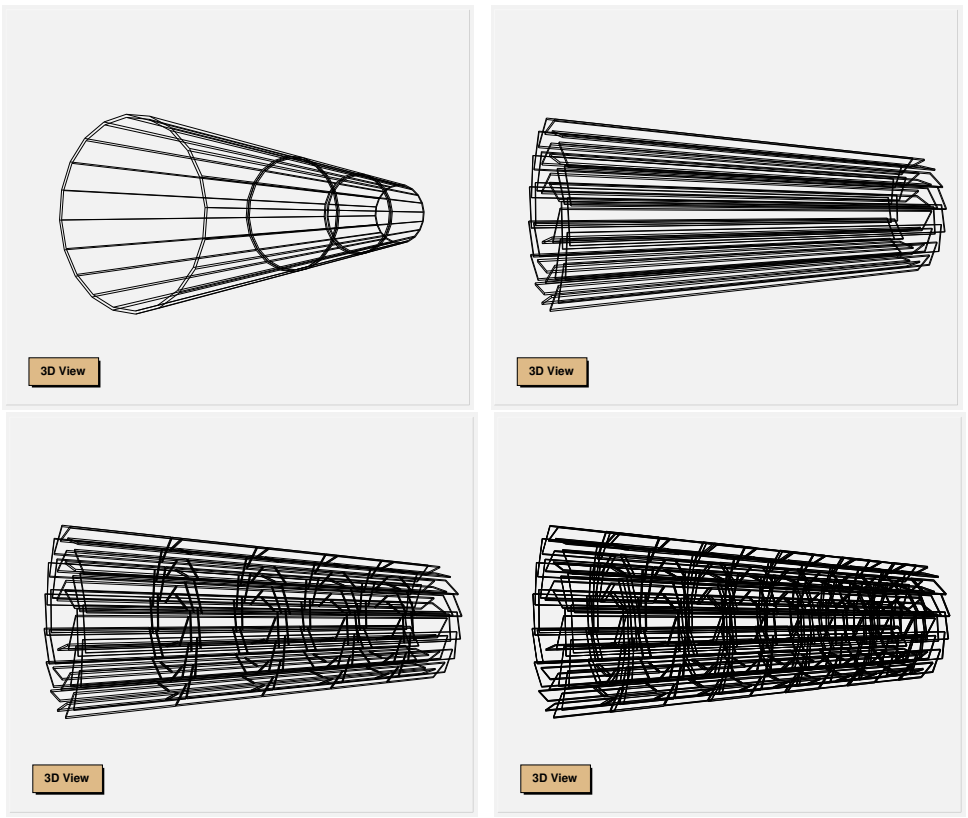

Figure B.12: The 3D shapes of the barrel MVD in all stages of the 3D shapes hierarchy: *Top left:* tubes, *Top right:* ladders, *Bottom left:* modules, *Bottom right:* sensors.

Description	Inner radius [cm]	Outer radius [cm]	number of ladders
cylinder 0	2.039	8.463	4
cylinder 1	5.995	12.419	10
cylinder 2	9.681	16.105	16

Table B.4: Three cylinders of the barrel MD. The cylinders overlap due to the tilt of the ladders with respect to the orthogonal to the radius vector.

size 12.368 cm $\times$ 6.424 cm $\times$ 0.27 cm. The modules contain 4 barrel sensors of an area of 6.424×6.424 cm^2 and a height of 0.03 cm arranged by two on each side of the module. The 512 sense strips on each sensor are orthogonal between the 4 sensors in a module.

The 2D representation of the barrel MVD corresponds to circles and rectangles in **XY** and only rectangles in **ZR** (see Fig. B.13). Due to the tilt of the ladders, the radial position of the ladders is calculated at the center of the ladder to give a clean representation of the ladders in **ZR**.

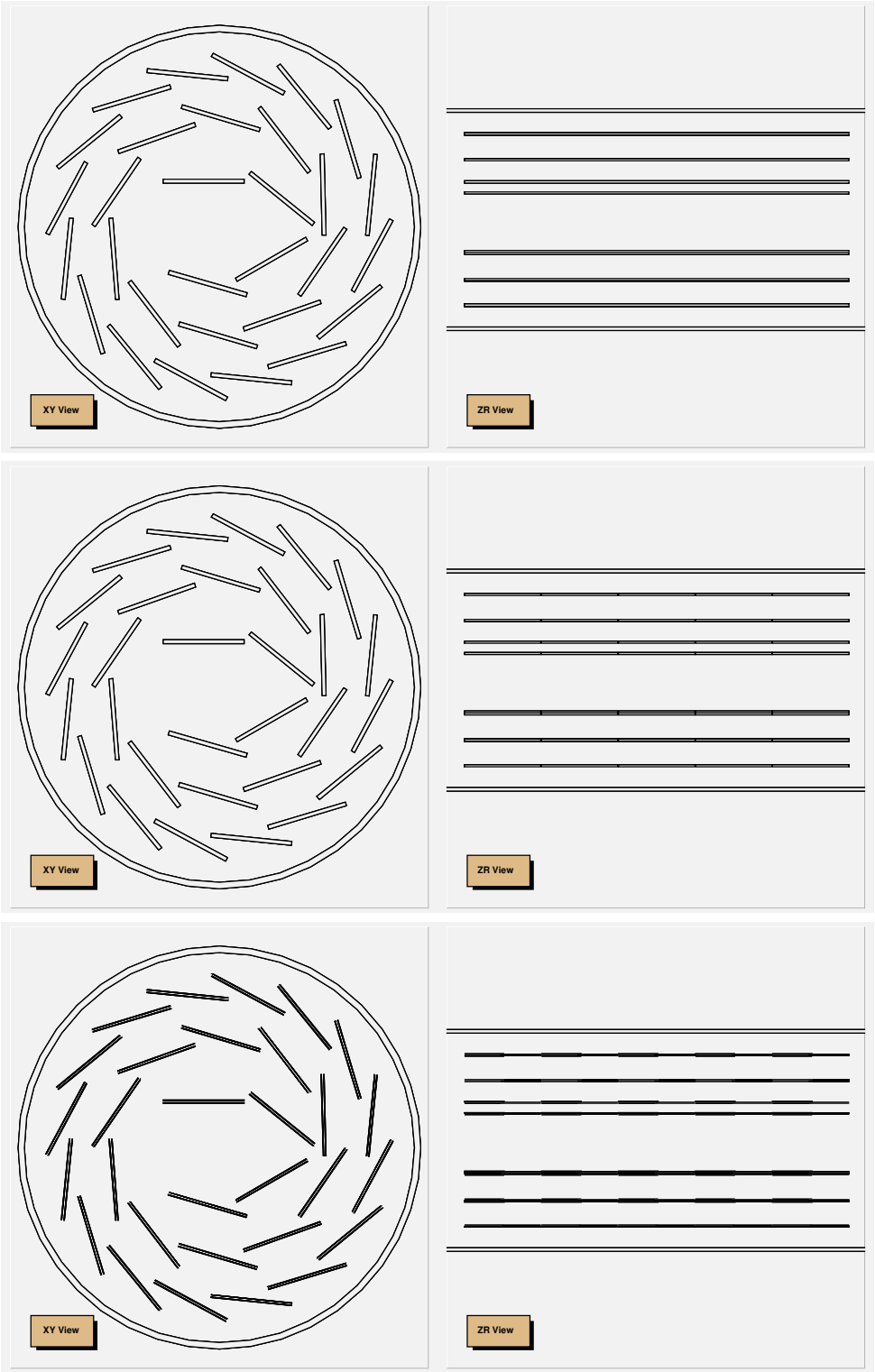

Figure B.13: The 2D shapes in the **XY** and **ZR** layered projection of the barrel MVD in different detail level: *Top:* ladders, *Center:* modules, *Bottom:* sensors.

The forward MVD is represented by trapezoidal shapes in **XY** and by rectangles in **ZR** (see Fig. B.14).

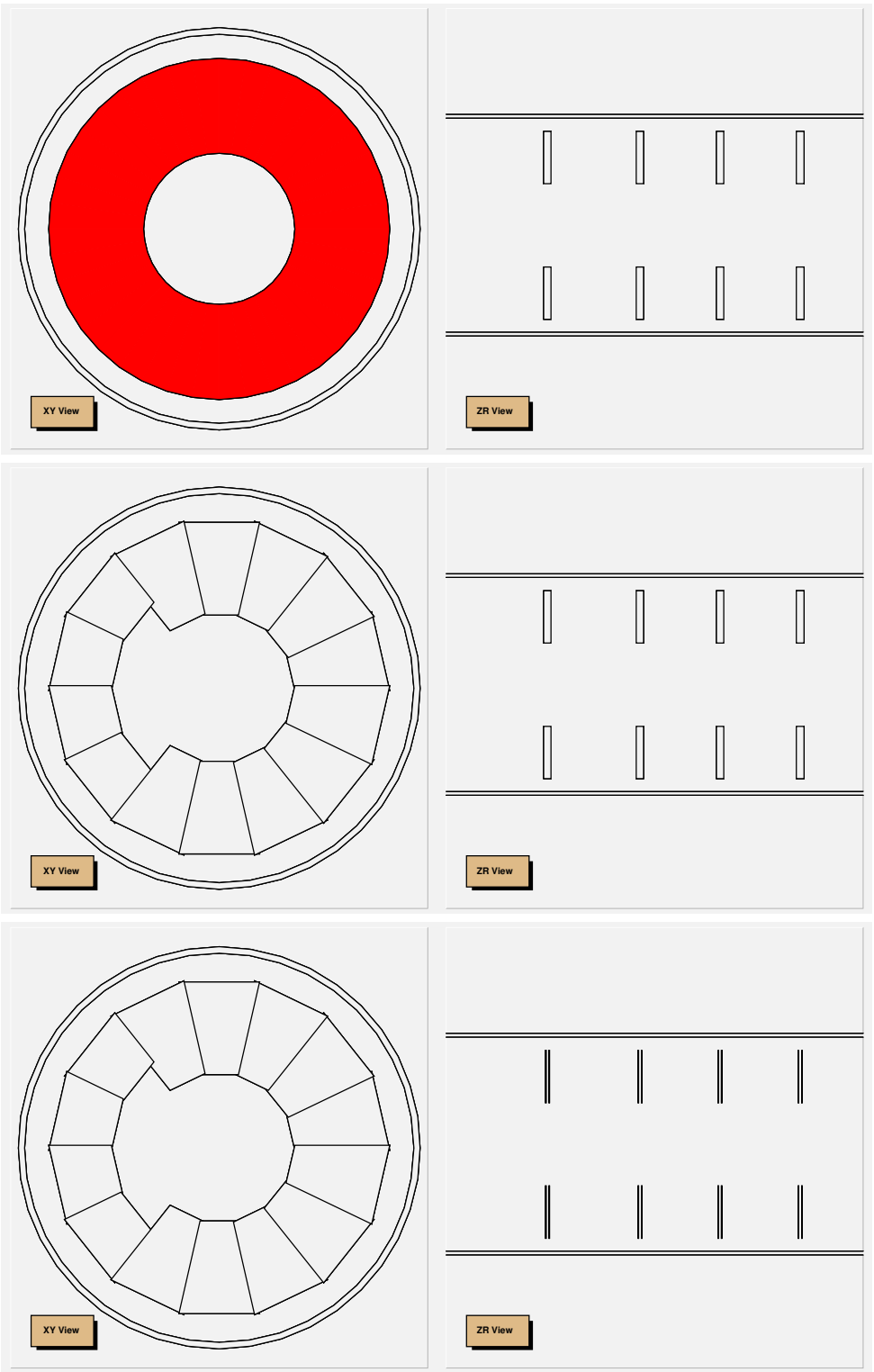

Figure B.14: The 2D shapes in the **XY** and **ZR** layered projection of the forward MVD in different detail level: *Top:* wheels, *Center:* sectors, *Bottom:* forward sensors.

The **XY** view was simplified by only displaying the shapes corresponding to the outermost wheel.

B.3.3 The Implementation of the MVD Hits

Raw hits in the MVD correspond to signals above a threshold in sense strips on the forward and barrel sensors. The data format for raw hits consists of the number of the corresponding cylinder, ladder, module, sensor and strip for barrel hits and wheel, sector, sensor and strip for a forward hit. Only this information is extracted from the ZEUS event store and sent to the client. The client constructs from the information the name of the corresponding sensor and initiates the drawing of the strip corresponding to the signal. This reduces the memory consumption and drawing time considerably. The hit display is also available in 3D (see Fig. B.15)

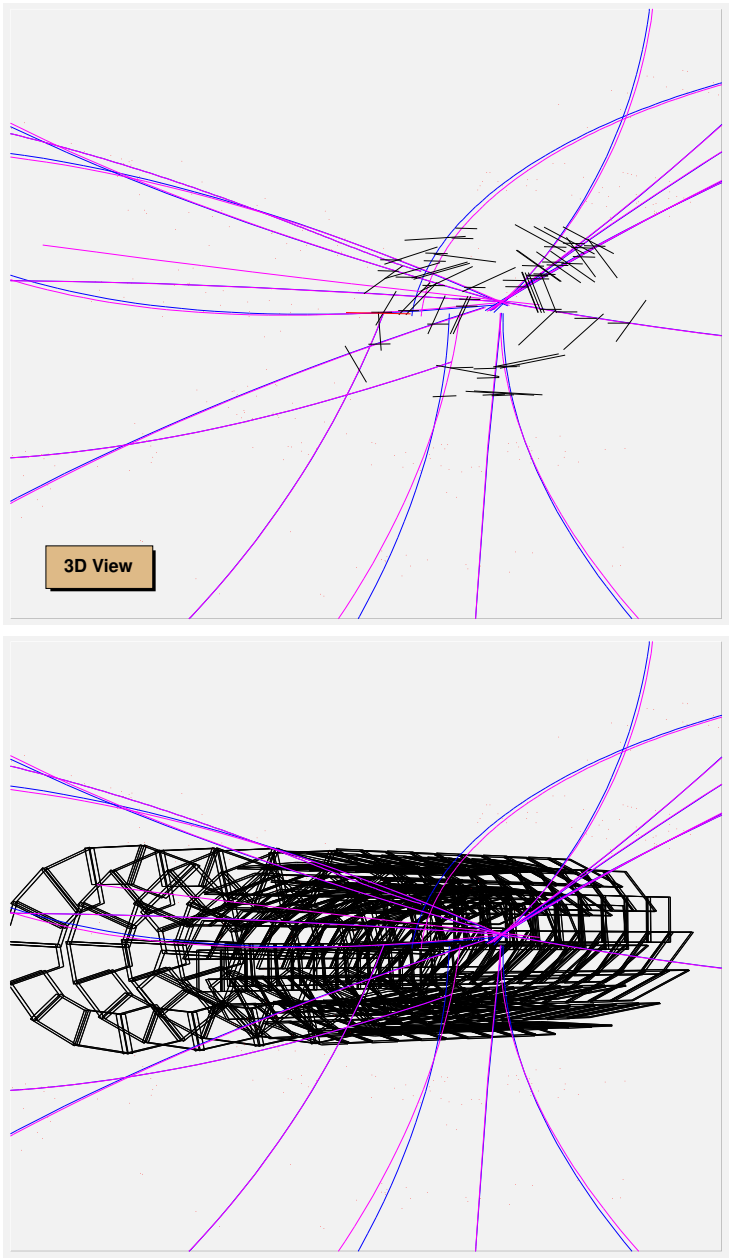

Figure B.15: 3D display of hits in the MVD without (*top*) and with (*bottom*) the geometry shown.

and in all 2D layered projections (see Fig. B.16).

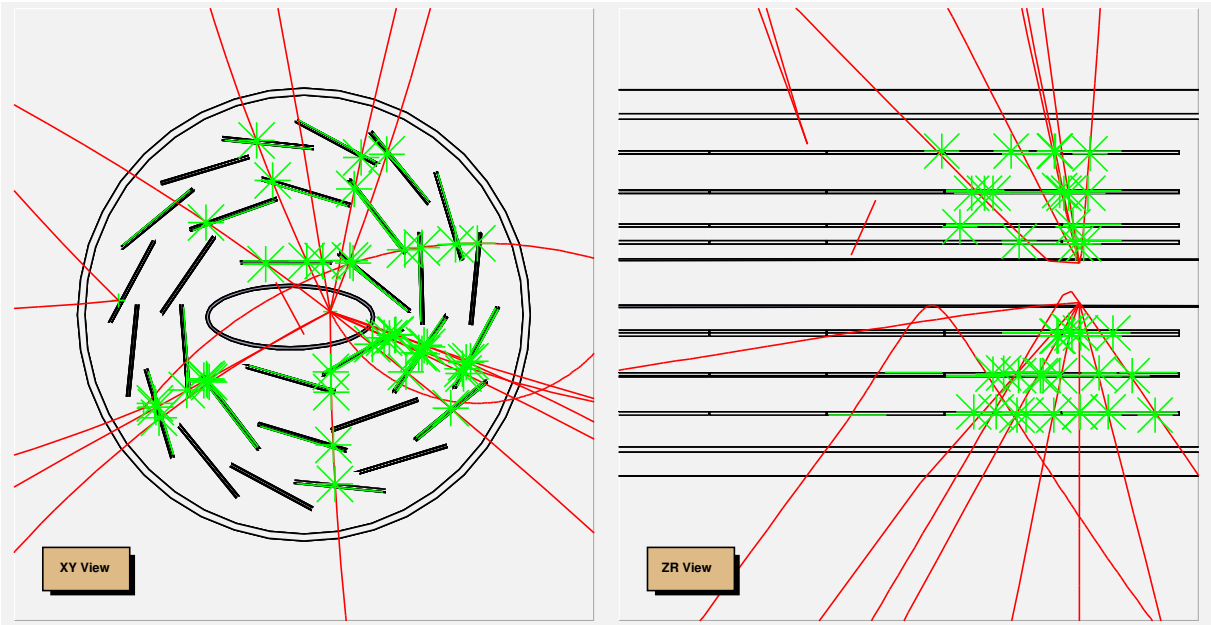

Figure B.16: 2D display of hits in the MVD in the **XY** and **ZR** layered projection.

Appendix C

Monte Carlo Samples

The PYTHIA MC generator Version 6.2 (see Sec. 2.4.1) is used to generate suited MC samples simulating the beauty quark signal and the background from charm quarks and lighter flavours (see Sec. 8.1). The detector simulation (see Sec. 5.3) is applied to all generated samples. The samples are generated separately for the pre– and post–upgrade running periods and the different process categories direct, resolved, excitations in photon and proton.

C.1 Beauty Quark MC Samples

The beauty quark samples are generated separately for the four process categories. In the following, the process categories and the corresponding leading order matrix elements are summarized:

beauty quarks from direct processes:

$$\gamma g \rightarrow b\bar{b};$$

beauty quarks from resolved processes:

$$\begin{aligned} q\bar{q} &\rightarrow b\bar{b}; \\ gg &\rightarrow b\bar{b}; \end{aligned}$$

beauty quarks from excitations in the proton:

$$\begin{aligned} b\gamma &\rightarrow bg; \\ bg &\rightarrow bg; \\ bq &\rightarrow bq; \\ b\bar{b} &\rightarrow b\bar{b}; \end{aligned}$$

beauty quarks from excitations in the photon:

$$\begin{aligned} bq &\rightarrow bq; \\ bg &\rightarrow bg; \end{aligned}$$

The beauty quark mass is set to $m_b = 4.75$ GeV and the PDF used for the proton is CTEQ4L [97] for pre–upgrade running periods and CTEQ5L [98] for post–upgrade running periods (see Tab. C.1). For all periods, the GRVG-LO [99] is chosen as photon PDF.
The minimal transverse momentum of the hard scatter p_T^{min} is chosen separately for pre– and post–upgrade running periods according to Tab. C.1.
No preselection is applied. Therefore, the fraction of events from beauty quarks decaying into muons is given by the branching ratio implemented in the PYTHIA MC generator.

sample	pre–upgrade			post–upgrade		
	beauty quark mass [GeV]	proton PDF	p_T^{min} [GeV]	beauty quark mass [GeV]	proton PDF	p_T^{min} [GeV]
direct	4.75	CTEQ4L	0	4.75	CTEQ5L	0
resolved	4.75	CTEQ4L	0	4.75	CTEQ5L	0
excitation in photon	4.75	CTEQ4L	4.5	4.75	CTEQ5L	0
excitation in proton	4.75	CTEQ4L	4.5	4.75	CTEQ5L	0

Table C.1: Beauty quark mass, proton PDF and minimal transverse momentum of the hard scatter for beauty quark MC samples.

C.2 Charm Quark MC Samples

The charm quark samples are generated with the same LO matrix elements for the four process categories like the beauty quark samples replacing the beauty quark with the charm quark. The same PDF's are used and the charm quark mass is set to $m_c = 1.35$ GeV (see Tab. C.2). The minimal transverse momentum of the hard scatter is set according to Tab. C.2.

sample	pre–upgrade			post–upgrade		
	charm quark mass [GeV]	proton PDF	p_T^{min} [GeV]	charm quark mass [GeV]	proton PDF	p_T^{min} [GeV]
direct	1.35	CTEQ4L	2	1.35	CTEQ5L	2
resolved	1.35	CTEQ4L	2	1.35	CTEQ5L	2
excitation in photon	1.35	CTEQ4L	3	1.35	CTEQ5L	2
excitation in proton	1.35	CTEQ4L	3.5	1.35	CTEQ5L	2

Table C.2: Charm quark mass, proton PDF and minimal transverse momentum of the hard scatter for charm quark MC samples.

A pre–selection is applied to reduce the number of events which have to be treated by the detector simulation. The generated charm quark events for the pre–upgrade running periods are required to satisfy the following cuts:

muons: at least one muon in the following kinematic region is required in the simulated final state:

- $p_T^{\mu} > 2$ GeV or $p_z^{\mu} > 3$ GeV or $p_z^{\mu} < -1.5$ GeV
- $10^{\circ} < \theta^{\mu} < 170^{\circ}$

jets: jets are reconstructed from the simulated final state using the KTCLUS algorithm (see Sec. 7.5) following the trigger cuts of the dijet trigger slot (see Sec. E.1.2):

1996-1997, 1998-1999: $E_T^{jet1,2} > 4$ GeV, $-3 < \eta^{jet1,2} < 3$

1999-2000: $E_T^{jet1} > 4.5$ GeV, $E_T^{jet2} > 3.5$ GeV, $-3 < \eta^{jet1,2} < 3$

For the post–upgrade running periods, the pre–selection cuts are slightly changed to:

muons: at least one muon in the following kinematic region is required in the simulated final state:

- $p_T^{\mu} > 0.5$ GeV

jets: jets are reconstructed from the simulated final state using the KTCLUS algorithm (see Sec. 7.5):

- $E_T^{jet1,2} > 4.0$ GeV, $-3 < \eta^{jet1,2} < 3$

C.3 Lighter Flavour MC Samples

The lighter flavour MC samples are generated for the following direct and resolved LO matrix elements where the lighter flavour quarks (u,d,s) are indicated by q:

lighter flavours from direct processes:

$$\begin{aligned} q\gamma &\rightarrow qg; \\ g\gamma &\rightarrow q\bar{q}; \end{aligned} \tag{C.1}$$

lighter flavours from resolved processes:

$$\begin{aligned} q\bar{q} &\rightarrow q\bar{q}(\mathrm{QCD}); \\ q\bar{q} &\rightarrow q'\bar{q}'; \\ q\bar{q} &\rightarrow gg; \\ qg &\rightarrow qg; \\ gg &\rightarrow q\bar{q}; \\ gg &\rightarrow gg; \end{aligned} \tag{C.2}$$

A pre–selection is applied similar to the charm selection to reduce the number of events which have to be treated by the detector simulation. As the lighter flavour samples are intended to describe the background from fake muon signals in the detector used to extract beauty quark events, a dijet selection is applied supplemented with a single track requirement for the pre–upgrade running periods:

single track: at least one track in the angular region $10^\circ < \theta^\mu < 170^\circ$ with the following kinematic cuts is required in the final state: $p_T > 1.35$ GeV or $p > 2.5$ GeV

jets: jets are reconstructed from the simulated final state using the KTCLUS algorithm (see Sec. 7.5) and required to fulfill the following cuts: $E_T^{jet1,2} > 5.25$ GeV, $-3 < \eta^{jet1,2} < 2.7$

The pre–selection is changed for the post–upgrade running periods to require only two jets in the final state:

jets: jets are reconstructed from the simulated final state using the KTCLUS algorithm (see Sec. 7.5):

- $E_T^{jet1,2} > 4.0$ GeV, $-3 < \eta^{jet1,2} < 3$

The proton PDF and the minimal transverse momentum of the hard scatter are set according to Tab. C.3. The photon PDF is set according to the other MC samples to GRVG-LO.

sample	pre–upgrade		post–upgrade	
	proton PDF	$p_T^{min}[GeV]$	proton PDF	$p_T^{min}[GeV]$
direct	CTEQ4L	4	CTEQ5L	3
resolved	CTEQ4L	4	CTEQ5L	3

Table C.3: Proton PDF and minimal transverse momentum of the hard scatter for lighter flavour quark MC samples.

Appendix D

Numbers of Selected Events

This chapter summarises the number of events remaining after the different groups of event selection cuts[1].

D.1 Pre–Upgrade Event Numbers

running period	96	97	98	99(e^i)	99(e^+)	00
total	17376000	27732000	6980000	14440000	18331000	44685000
trigger preselection and muon DQM	479521	1081495	139950	424867	545157	1239737
vertex selection	450031	1018732	131657	408464	513209	1184534
photoproduction selection	211872	506848	60599	200657	233208	546443
jet selection	38923	94366	11468	39283	53154	122253
muon selection	2912	7544	1080	3749	5278	11417
muon—jet selection	2572	6669	984	3310	4699	10172
complete selection	2572	6669	984	3310	4699	10172

Table D.1: Pre–upgrade data samples event numbers for $p_T^\mu \geq 2.0$ GeV

mc sample	beauty				charm				light flavour	
subprocess	direct	resolved	photon ex.	proton ex.	direct	resolved	photon ex.	proton ex.	direct	resolved
total	1019769	209945	359918	89952	99980	4995	79956	14992	1194665	5702167
trigger preselection	85781	8188	42434	12125	42029	1122	36842	5434	135094	537825
vertex selection	81954	7822	40660	11630	40296	1071	35339	5200	130088	518280
photoproduction selection	48236	5792	31621	8726	25347	829	27948	3753	83466	404572
jet selection	11671	1128	10786	3770	8448	261	8010	1480	51844	212243
muon selection	4031	308	2331	738	6009	130	5064	749	7863	23280
muon—jet selection	3724	274	2021	631	5867	122	4925	703	7340	21202
complete selection	3724	274	2021	631	5867	122	4925	703	6057	14487

Table D.2: Pre–upgrade 96-97 MC samples event numbers for $p_T^\mu \geq 2.0$ GeV

mc sample	beauty				charm				light flavour	
subprocess	direct	resolved	photon ex.	proton ex.	direct	resolved	photon ex.	proton ex.	direct	resolved
total	329894	89988	119966	30000	39868	2500	29980	5000	642445	1755143
trigger preselection	28157	3475	14204	4008	17065	606	14194	1808	64472	155143
vertex selection	27576	3405	13931	3939	16746	597	13958	1780	63373	152667
photoproduction selection	16597	2586	10852	3026	10669	475	11190	1322	40031	118496
jet selection	3864	473	3609	1322	3556	152	3060	514	23028	61792
muon selection	1349	134	808	267	2465	63	1887	252	4494	6797
muon—jet selection	1250	122	715	234	2410	61	1827	235	4160	6188
complete selection	1250	122	715	234	2410	61	1827	235	2088	4139

Table D.3: Pre–upgrade 98-99 MC samples event numbers for $p_T^\mu \geq 2.0$ GeV

[1]The difference between the last cut on the muon–jet association and the complete selection in the lighter flavour MC samples results from the exclusion of heavy flavour events in the inclusive MC samples.

mc sample	beauty				charm				light flavour	
subprocess	direct	resolved	photon ex.	proton ex.	direct	resolved	photon ex.	proton ex.	direct	resolved
total	1619522	329949	599773	149990	199913	10000	99787	19989	1696194	4934844
trigger preselection	130089	11810	64656	17161	137045	2515	54673	6482	192549	438010
vertex selection	126531	11492	63057	16817	133796	2451	53264	6344	188931	429952
photoproduction selection	76245	8530	49181	12600	39294	1468	32046	4628	121795	335313
jet selection	18138	1669	17331	6049	13578	507	9437	1982	76504	185180
muon selection	6286	447	3724	1155	9342	259	5950	1018	13033	20396
muon—jet selection	5810	405	3253	995	9116	239	5774	966	12214	18567
complete selection	5810	405	3253	995	9116	239	5774	966	7999	12500

Table D.4: Pre–upgrade 99-00 MC samples event numbers for $p_T^\mu \geq 2.0$ GeV

D.2 Post–Upgrade Event Numbers for $p_T^\mu \geq 1.5$ GeV

running period	03	04
total	3726492	47517488
trigger preselection and muon DQM	49486	957534
vertex selection	45822	900446
photoproduction selection	27593	536190
jet selection	6194	123580
muon selection	598	10883
muon—jet selection	528	9148
complete selection	528	9148

Table D.5: Post–upgrade data samples event numbers for $p_T^\mu \geq 1.5$ GeV

mc sample	beauty				charm				light flavour	
subprocess	direct	resolved	photon ex.	proton ex.	direct	resolved	photon ex.	proton ex.	direct	resolved
total	162165	49990	74967	26894	79990	19980	99977	19995	399847	1248180
trigger preselection	11932	1759	8517	2788	13179	994	9347	1257	28125	64067
vertex selection	11929	1758	8516	2787	13177	994	9344	1257	28119	64059
photoproduction selection	7265	1331	6503	2086	8290	787	7180	893	17382	49269
jet selection	1663	242	2297	819	2747	206	2260	353	7858	17688
muon selection	678	73	622	197	1265	70	900	106	1707	2465
muon—jet selection	618	61	482	164	1226	65	873	100	1598	2232
complete selection	618	61	482	164	1226	65	873	100	572	1093

Table D.6: Post–upgrade 03-04 MC samples event numbers for $p_T^\mu \geq 1.5$ GeV

D.3 Post–Upgrade Event Numbers for $p_T^\mu \geq 2.0$ GeV

running period	03	04
total	3726492	47517488
trigger preselection and muon DQM	49486	957534
vertex selection	45822	900446
photoproduction selection	27593	536190
jet selection	6194	123580
muon selection	466	8448
muon—jet selection	425	7316
complete selection	425	7316

Table D.7: Post–upgrade data samples event numbers for $p_T^\mu \geq 2.0$ GeV

mc sample	beauty				charm				light flavour	
subprocess	direct	resolved	photon ex.	proton ex.	direct	resolved	photon ex.	proton ex.	direct	resolved
total	162165	49990	74967	26894	79990	19980	99977	19995	399847	1248180
trigger preselection	11932	1759	8517	2788	13179	994	9347	1257	28125	64067
vertex selection	11929	1758	8516	2787	13177	994	9344	1257	28119	64059
photoproduction selection	7265	1331	6503	2086	8290	787	7180	893	17382	49269
jet selection	1663	242	2297	819	2747	206	2260	353	7858	17688
muon selection	557	60	472	148	971	53	677	83	1327	1768
muon—jet selection	513	52	399	131	945	49	657	79	1248	1626
complete selection	513	52	399	131	945	49	657	79	464	813

Table D.8: Post–upgrade 03-04 MC samples event numbers for $p_T^\mu \geq 2.0$ GeV

Appendix E

Trigger Selection

In the following, the complete trigger selection separated for the pre– and post–upgrade running periods is presented. The given third level triggers combine trigger selections on the second and first trigger level with additional requirements.

E.1 Pre–Upgrade Trigger Selection

The pre–upgrade trigger selection consists of at least of one of the following third level trigger slots.

E.1.1 Barrel/Rear Muon Trigger: TLT EXO 11/12

- one outer barrel/rear muon reconstructed by the GLOMU muon finder (see Sec. 7.3.1.6)
- cosmics rejection if:
  - $n_{\texttt{tracks-CTD}} \leq 3$ and
  - $E_{\texttt{FCAL}} < 1.0$ GeV and
  - the two tracks with highest p_T have $p_T > 0.5$ and $cos(\theta_{\texttt{tracks}}) < -0.9998$
- CAL timing cut compatible with physics event
- logical OR of first level trigger slots: FLT 14 (barrel muon), FLT 15 (rear muon)

E.1.2 Low E_T Dijet: TLT HPP 14

- 2 or more jets with $E_T \geq 4$ GeV and $|\eta| < 2.5$ for the running periods 96-99 or 2 or more jets with $E_T \geq 4.5$ GeV and $|\eta| < 2.5$ for the running periods 99-00
- CAL: $p_z/E < 1.0$,
- logical OR of second level trigger slots SLT HPP 1, 2, 3
- included logical OR of first level trigger slots: FLT 40, 41, 42, 43 required by SLT slots above

E.1.3 Semi-Isolated Muon with the Barrel/Rear Muon Chambers: TLT MUO 3

- good inner barrel/rear muon found on the second trigger level
- hit in barrel or rear inner muon chambers
- muon-like CAL-island
- $n_{\texttt{tracks-CTD}} \geq 1$
- track going into barrel or rear CAL with $p_T > 1$ GeV
- second level trigger slot: SLT MUO 1
- included logical OR of first level trigger slots FLT 8, 9, 10, 11 required by SLT slots above

E.1.4 Muon plus Dijets for Running Periods 1999-2000: TLT HFL 1

- only for running periods 1999-2000
- good muon found by barrel/rear muon chambers
- two jets with $E_T > 3.5$ GeV and $|\eta| < 2.5$
- CAL: $p_z/E < 1.0$ GeV
- CAL: $E - p_z < 100$ GeV
- logical OR of second level trigger slots: SLT HPP 1, 2, 3
- included logical OR of first level trigger slots: FLT 40, 41, 42, 43 required by SLT slots above

E.2 Post–Upgrade Trigger Selection

The post–upgrade trigger selection consists of at least of one of the following third level trigger slots.

E.2.1 Inclusive Dijets: TLT HFL 5

- two jets with $E_T > 4.5$ GeV and $|\eta| < 2.5$
- CAL: $p_z/E < 1.0$ GeV
- CAL: $E - p_z < 100$ GeV
- logical OR of second level trigger slots: SLT HFL 1, 2; SLT HPP 1, 2, 3, 7; SLT EXO 1, 2, 8, 11
- included logical OR of first level trigger slots: FLT 0, 1, 2, 3, 4, 5, 6, 14, 15, 28, 30, 31, 34, 35, 36, 37, 39, 40, 41, 42, 43, 44, 50, 51, 52, 53, 54, 62 required by SLT slots above

E.2.2 Inclusive Semi-Leptonic Muon: TLT HFL 13

- at least one forward or barrel/rear muon found on the SLT
- at least a barrel/rear muon
- muon reconstructed by hit in barrel/rear muon chambers with matching CTD track by GLOMU (see Sec. 7.3.1.6)
- CAL: $E_T > 9$ GeV
- logical OR of second level trigger slots: SLT HFL 7, 8, 18; SLT DIS 1, 4, 6, 7; SLT EXO 3, 10
- included logical OR of fist level trigger slots: 28, 30, 34, 35, 36, 37, 39, 40, 41, 42, 43, 44, 46, 47, 50, 51, 52, 53, 54, 62 required by SLT slots above

E.2.3 Muon plus Dijets: TLT HFL 25

- at least a forward or barrel/rear muon found on the SLT
- hit in barrel/rear muon chambers with matching CTD track by GLOMU (see Sec. 7.3.1.6)
- two jets with $E_T > 3.5$ GeV and $|\eta| < 2.5$
- CAL: $p_z/E < 1.0$ GeV
- CAL: $E - p_z < 100$ GeV
- logical OR of second level trigger slots: SLT HFL 3, 4, 5, 6, 9, 10, 11, 12, 13; SLT MUO 1, 2, 3, 4, 5, 6, 7; SLT EXO 8
- included logical OR of all first level trigger slots 0-63 required by SLT slots above

Appendix F

Comparison with Previous Results

The presented event selection (see Cha. 8) and beauty quark fraction determination using the p_T^{rel} method (see Cha. 9) are used to reproduce the previous results of beauty quark photoproduction cross section measurements in dijet and muon events [42]. As these measurements have been introduced in the summary of previous beauty quark results (see Cha. 3) and also have been used for the global comparison of beauty quark cross sections (see Cha. 4), only the differences in the selection are described in more detail.
The muon selection is changed with respect to the general muon reconstruction (see Sec. 7.3.2 and 8.4). In the forward part, the MPMATCH algorithm is used exclusively while in the barrel and rear part, the BREMAT algorithm requiring a muon segment in the inner and outer chambers matched to a track is used. The kinematic cuts on the muons are harder and different for the forward, barrel and rear muon regions (see Eq. 3.1).
The selection of the photoproduction regime and the dijet selection is the same for both analyses. Additional cuts (see Sec. 8.7) are taken over from this analysis.
The efficiency correction for the altered muon selection is taken over from the previous analysis but the correction of the charm and lighter flavour MC samples for the p_T^{rel} method is redone following the described procedure (see Sec. 9.1.1).

The number of events selected in the running periods 96-00 is 3799 which is about an order of magnitude smaller than the global muon reconstruction selection with relaxed kinematic muon cuts.
The global p_T^{rel} fit results in a beauty fraction of $0.238 \pm 0.016\%$ is shown in Fig. F.1.

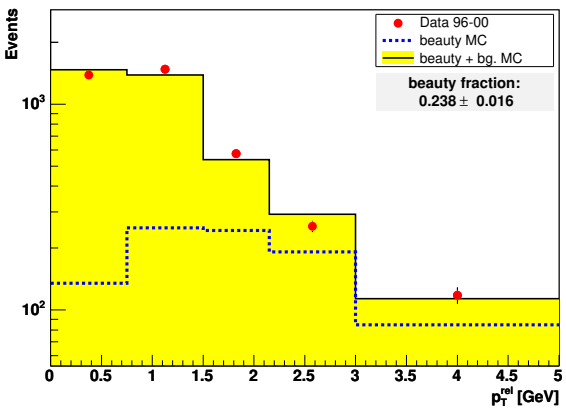

Figure F.1: p_T^{rel} fit for comparison to previous results.

It is used to scale the signal and background MC samples in the control distributions of the transverse momentum of the muon p_T^μ and the pseudo-rapidity of the muon η^μ (see Fig. F.2) .

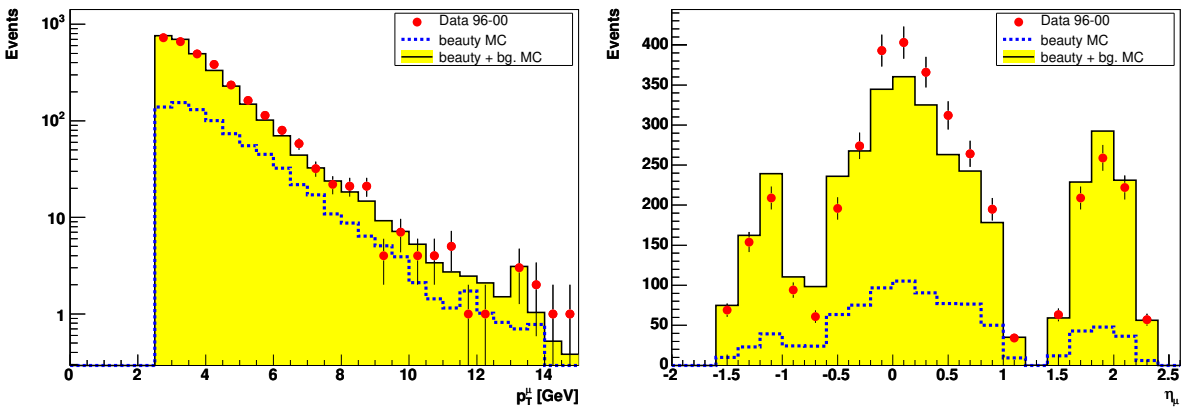

Figure F.2: Control distributions of the transverse momentum of the muon p_T^μ (*left*) and the pseudo-rapidity (*right*) for the comparison to the previous analysis.

The cross section differential in the transverse momentum of the muon:

$$d\sigma/dp_T^\mu(ep \to eb\bar{b}X \to e\mu jjX) \tag{F.1}$$

is measured by determination of the beauty fraction using the p_T^{rel} method separately for the three bins in p_T^μ:

$$\begin{aligned} 2.5 \leq p_T^\mu < 4.0 \text{ GeV} \\ 4.0 \leq p_T^\mu < 6.0 \text{ GeV} \\ 6.0 \leq p_T^\mu < 11.0 \text{ GeV} \end{aligned} \tag{F.2}$$

The differential cross section is well compatible with the previous results within the statistical errors (see Fig. F.3).

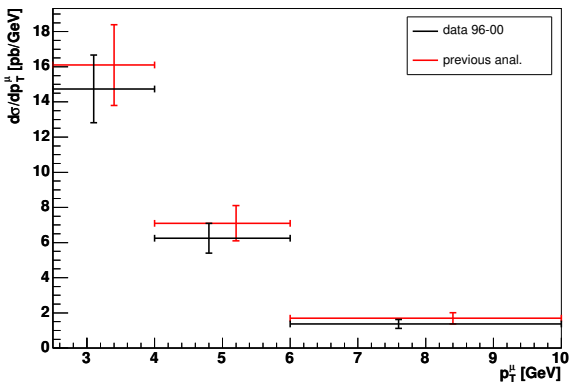

Figure F.3: Cross section differential in the transverse momentum of the muon $d\sigma/dp_T^\mu(ep \to eb\bar{b}X \to e\mu jjX$ compared to the result of the previous analysis. The cross sections are presented with statistical errors only.

The cross section differential in the pseudo-rapidity of the muon:

$$d\sigma/d\eta^\mu(ep \to eb\bar{b}X \to e\mu jjX) \tag{F.3}$$

is measured by determination of the beauty fraction using the p_T^{rel} method separately for the four bins in η^μ:

$$\begin{aligned} -1.60 \leq \eta^\mu < -0.75 \\ -0.75 \leq \eta^\mu < 0.25 \\ 0.25 \leq \eta^\mu < 1.30 \\ 1.30 \leq \eta^\mu < 2.30 \end{aligned} \tag{F.4}$$

The differential cross section is compatible with the previous results within the statistical errors (see Fig. F.4)

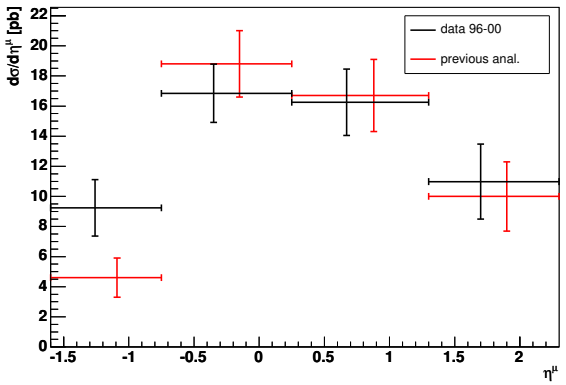

Figure F.4: Cross section differential in the pseudo-rapidity of the muon $d\sigma/d\eta^\mu(ep \to eb\bar{b}X \to e\mu jjX$ compared to the result of the previous analysis. The cross sections are presented with statistical errors only.

with slight problems in the most rear η bin.

In summary, the measured beauty quark cross sections in the reduced kinematic muon region are compatible with the previous results.

Appendix G

Systematic Errors for the Pre– and Post–Upgrade Running Periods

This chapter presents the systematic errors of the pre– and post–upgrade running periods for the total beauty quark photoproduction cross section from dijet plus muon events and for all bins of the differential beauty quark cross sections.

G.1 Systematic Errors for the Pre–Upgrade Running Periods

cross section	total	p_T^μ				η^μ			
bin		1	2	3	4	1	2	3	4
nominal	117.54	38.48	18.23	5.37	1.30	7.53	38.58	37.20	16.05
charm p_T^{rel} correction 100%	111.51	34.35	17.00	5.20	1.29	7.31	37.09	34.74	15.25
positive deviation from nominal	0.00	0.00	0.00	0.00	0.00	0.00	0.00	0.00	0.00
negative deviation from nominal	-6.03	-4.13	-1.22	-0.17	-0.01	-0.21	-1.50	-2.47	-0.81
charm p_T^{rel} correction 0%	123.99	42.96	19.49	5.54	1.30	7.71	40.08	39.95	16.96
positive deviation from nominal	6.44	4.49	1.26	0.17	0.01	0.19	1.50	2.75	0.91
negative deviation from nominal	0.00	0.00	0.00	0.00	0.00	0.00	0.00	0.00	0.00
randomised muon efficiency correction 1	114.63	38.94	17.43	5.33	1.29	6.73	37.99	35.35	16.71
randomised muon efficiency correction 2	116.08	37.97	18.21	5.23	1.27	7.28	38.13	36.66	16.09
randomised muon efficiency correction 3	120.41	39.22	18.47	5.58	1.33	7.68	40.66	37.19	15.19
randomised muon efficiency correction 4	119.81	38.53	18.68	5.39	1.20	8.12	41.24	38.10	13.67
randomised muon efficiency correction 5	118.95	38.97	18.49	5.55	1.33	7.70	40.53	36.43	16.62
randomised muon efficiency correction 6	120.45	39.32	18.50	5.54	1.32	7.40	40.55	38.05	17.06
randomised muon efficiency correction 7	121.15	38.42	18.36	5.41	1.34	7.00	39.65	41.00	15.33
randomised muon efficiency correction 8	117.44	39.35	18.14	5.28	1.29	7.40	38.00	38.92	14.70
randomised muon efficiency correction 9	118.77	39.10	18.39	5.42	1.29	7.69	39.80	38.15	15.10
randomised muon efficiency correction 10	120.69	38.98	18.59	5.59	1.34	7.83	39.81	39.34	14.91
RMS of randomised muon efficiency corrections	2.05	0.42	0.34	0.12	0.04	0.39	1.14	1.53	1.00
positive deviation from nominal	2.05	0.42	0.34	0.12	0.04	0.39	1.14	1.53	1.00
negative deviation from nominal	-2.05	-0.42	-0.34	-0.12	-0.04	-0.39	-1.14	-1.53	-1.00
charm normalisation changed by factor 2	101.84	31.10	15.84	4.67	1.25	7.16	34.02	31.04	14.06
positive deviation from nominal	0.00	0.00	0.00	0.00	0.00	0.00	0.00	0.00	0.00
negative deviation from nominal	-15.70	-7.38	-2.39	-0.70	-0.04	-0.36	-4.57	-6.16	-2.00
charm normalisation changed by factor 0.5	136.56	47.36	21.13	6.30	1.37	7.95	44.13	44.72	18.80
positive deviation from nominal	19.02	8.88	2.90	0.92	0.07	0.43	5.54	7.52	2.75
negative deviation from nominal	0.00	0.00	0.00	0.00	0.00	0.00	0.00	0.00	0.00
normalisation of resolved and ex. changed by factor 2	123.02	43.95	20.16	5.86	1.24	7.92	41.28	39.48	16.80
positive deviation from nominal	5.48	5.47	1.93	0.49	0.00	0.39	2.70	2.28	0.74
negative deviation from nominal	0.00	0.00	0.00	0.00	-0.05	0.00	0.00	0.00	0.00
normalisation of resolved and ex. changed by factor 0.5	112.48	34.05	16.49	4.90	1.34	7.06	35.86	35.11	15.47
positive deviation from nominal	0.00	0.00	0.00	0.00	0.04	0.00	0.00	0.00	0.00
negative deviation from nominal	-5.06	-4.43	-1.74	-0.47	0.00	-0.47	-2.72	-2.09	-0.59
p_T^{rel} definition 1	111.85	41.23	19.42	4.64	1.15	6.43	32.42	37.84	7.87
positive deviation from nominal	0.00	2.75	1.19	0.00	0.00	0.00	0.00	0.63	0.00
negative deviation from nominal	-5.70	0.00	0.00	-0.73	-0.15	-1.09	-6.16	0.00	-8.19
total positive deviation from nominal	20.91	11.70	3.91	1.07	0.09	0.72	6.45	8.49	3.15
total negative deviation from nominal	-18.58	-9.56	-3.22	-1.14	-0.17	-1.32	-8.35	-7.12	-8.55

Table G.1: Systematic errors for the pre–upgrade running period for $p_T^\mu \geq 2.0$ GeV for the total beauty quark photoproduction cross section and the cross sections differential in p_T^μ and η^μ

cross section	$p_T^{\mu-jet}$			$\eta^{\mu-jet}$			
bin	1	2	3	1	2	3	4
nominal	11.71	4.79	0.91	16.14	34.96	27.80	18.26
charm p_T^{rel} correction 100%	10.97	4.60	0.89	15.79	33.34	25.79	17.45
positive deviation from nominal	0.00	0.00	0.00	0.00	0.00	0.00	0.00
negative deviation from nominal	-0.73	-0.18	-0.02	-0.36	-1.62	-2.01	-0.81
charm p_T^{rel} correction 0%	12.50	4.97	0.94	16.47	36.64	30.07	19.18
positive deviation from nominal	0.80	0.19	0.02	0.33	1.67	2.27	0.92
negative deviation from nominal	0.00	0.00	0.00	0.00	0.00	0.00	0.00
randomised muon efficiency correction 1	11.41	4.82	0.87	15.18	33.85	26.84	17.71
randomised muon efficiency correction 2	11.63	4.60	0.94	16.19	34.71	27.38	17.63
randomised muon efficiency correction 3	12.02	4.84	0.91	16.83	36.44	28.05	16.69
randomised muon efficiency correction 4	12.29	4.79	0.93	17.34	37.11	28.20	15.91
randomised muon efficiency correction 5	11.96	4.80	0.92	16.70	36.48	26.60	18.54
randomised muon efficiency correction 6	12.21	4.87	0.93	16.21	36.52	28.75	18.96
randomised muon efficiency correction 7	12.39	4.95	0.96	15.84	35.97	31.20	18.33
randomised muon efficiency correction 8	11.88	4.72	0.94	15.80	35.02	29.02	17.31
randomised muon efficiency correction 9	12.13	4.78	0.93	16.45	35.85	28.68	17.46
randomised muon efficiency correction 10	12.22	4.96	0.92	16.36	36.51	29.13	17.84
RMS of randomised muon efficiency corrections	0.29	0.10	0.02	0.57	0.96	1.26	0.84
positive deviation from nominal	0.29	0.10	0.02	0.57	0.96	1.26	0.84
negative deviation from nominal	-0.29	-0.10	-0.02	-0.57	-0.96	-1.26	-0.84
charm normalisation changed by factor 2	9.79	4.27	0.89	14.92	30.12	23.08	17.01
positive deviation from nominal	0.00	0.00	0.00	0.00	0.00	0.00	0.00
negative deviation from nominal	-1.91	-0.52	-0.03	-1.22	-4.85	-4.71	-1.25
charm normalisation changed by factor 0.5	13.97	5.45	0.95	17.55	41.02	33.41	20.01
positive deviation from nominal	2.26	0.66	0.03	1.40	6.06	5.61	1.75
negative deviation from nominal	0.00	0.00	0.00	0.00	0.00	0.00	0.00
normalisation of resolved and ex. changed by factor 2	12.63	4.88	0.95	17.47	37.79	28.79	18.81
positive deviation from nominal	0.93	0.10	0.03	1.33	2.83	1.00	0.55
negative deviation from nominal	0.00	0.00	0.00	0.00	0.00	0.00	0.00
normalisation of resolved and ex. changed by factor 0.5	10.85	4.69	0.88	14.77	32.28	26.85	17.67
positive deviation from nominal	0.00	0.00	0.00	0.00	0.00	0.00	0.00
negative deviation from nominal	-0.86	-0.10	-0.03	-1.37	-2.68	-0.95	-0.59
p_T^{rel} definition 1	10.55	4.53	0.90	12.79	31.17	27.36	8.25
positive deviation from nominal	0.00	0.00	0.00	0.00	0.00	0.00	0.00
negative deviation from nominal	-1.15	-0.25	-0.01	-3.35	-3.79	-0.44	-10.01
total positive deviation from nominal	2.59	0.70	0.05	2.04	6.96	6.26	2.21
total negative deviation from nominal	-2.52	-0.62	-0.05	-3.88	-6.97	-5.38	-10.17

Table G.2: Systematic errors for the pre–upgrade running period for $p_T^{\mu} \geq 2.0$ GeV for the cross sections differential in $p_T^{\mu-jet}$ and $\eta^{\mu-jet}$

cross section	x_γ^{jets}				ΔR_{jj}					
bin	1	2	3	4	1	2	3	4	5	6
nominal	25.17	42.03	55.85	257.92	0.45	0.99	5.12	39.56	95.36	31.37
charm p_T^{rel} correction 100%	24.03	39.44	53.78	250.01	0.43	0.94	4.88	37.48	91.04	30.41
positive deviation from nominal	0.00	0.00	0.00	0.00	0.00	0.00	0.00	0.00	0.00	0.00
negative deviation from nominal	-1.14	-2.59	-2.07	-7.91	-0.01	-0.05	-0.24	-2.08	-4.32	-0.95
charm p_T^{rel} correction 0%	26.84	44.87	57.84	266.33	0.48	1.11	5.47	42.09	99.61	32.18
positive deviation from nominal	1.67	2.84	1.99	8.41	0.04	0.12	0.35	2.52	4.25	0.82
negative deviation from nominal	0.00	0.00	0.00	0.00	0.00	0.00	0.00	0.00	0.00	0.00
randomised muon efficiency correction 1	21.22	40.97	57.22	248.59	0.45	0.92	5.40	38.32	91.69	31.62
randomised muon efficiency correction 2	24.92	42.72	54.90	254.10	0.38	0.79	5.36	38.93	93.63	31.25
randomised muon efficiency correction 3	24.25	42.54	56.86	263.48	0.45	0.89	5.02	40.41	96.89	32.21
randomised muon efficiency correction 4	26.41	40.11	57.54	268.47	0.50	1.02	5.07	40.97	98.30	32.27
randomised muon efficiency correction 5	24.64	41.54	57.02	262.17	0.44	0.81	4.98	39.92	97.21	31.88
randomised muon efficiency correction 6	27.33	43.77	57.72	265.16	0.55	1.12	5.42	40.69	98.50	32.39
randomised muon efficiency correction 7	27.30	46.17	58.60	266.65	0.44	0.86	5.68	42.10	99.35	32.49
randomised muon efficiency correction 8	26.17	44.61	56.06	257.67	0.45	0.81	5.70	39.94	95.85	31.43
randomised muon efficiency correction 9	26.03	43.13	57.20	263.32	0.49	0.92	5.40	40.11	97.61	32.16
randomised muon efficiency correction 10	24.95	44.27	57.99	266.76	0.51	0.92	5.46	41.41	99.13	32.06
RMS of randomised muon efficiency corrections	1.71	1.73	0.98	6.00	0.05	0.10	0.24	1.06	2.34	0.40
positive deviation from nominal	1.71	1.73	0.98	6.00	0.05	0.10	0.24	1.06	2.34	0.40
negative deviation from nominal	-1.71	-1.73	-0.98	-6.00	-0.05	-0.10	-0.24	-1.06	-2.34	-0.40
charm normalisation changed by factor 2	22.32	36.34	50.59	229.38	0.46	0.88	4.61	34.39	83.04	28.22
positive deviation from nominal	0.00	0.00	0.00	0.00	0.01	0.00	0.00	0.00	0.00	0.00
negative deviation from nominal	-2.86	-5.69	-5.27	-28.53	0.00	-0.11	-0.51	-5.18	-12.32	-3.15
charm normalisation changed by factor 0.5	29.36	50.05	63.02	290.15	0.43	1.23	5.96	46.30	109.72	35.07
positive deviation from nominal	4.19	8.02	7.16	32.24	0.00	0.24	0.83	6.74	14.36	3.71
negative deviation from nominal	0.00	0.00	0.00	0.00	-0.02	0.00	0.00	0.00	0.00	0.00
normalisation of resolved and ex. changed by factor 2	24.97	38.99	48.44	269.07	0.47	0.79	5.35	41.56	100.49	33.90
positive deviation from nominal	0.00	0.00	0.00	11.15	0.02	0.00	0.22	2.00	5.13	2.53
negative deviation from nominal	-0.20	-3.04	-7.42	0.00	0.00	-0.20	0.00	0.00	0.00	0.00
normalisation of resolved and ex. changed by factor 0.5	25.17	43.96	61.81	243.86	0.46	1.16	4.95	37.65	90.41	28.98
positive deviation from nominal	0.00	1.93	5.95	0.00	0.01	0.17	0.00	0.00	0.00	0.00
negative deviation from nominal	-0.01	0.00	0.00	-14.06	0.00	0.00	-0.17	-1.91	-4.94	-2.38
p_T^{rel} definition 1	18.19	53.29	51.85	241.30	0.01	0.06	5.14	36.44	94.13	27.06
positive deviation from nominal	0.00	11.26	0.00	0.00	0.00	0.00	0.02	0.00	0.00	0.00
negative deviation from nominal	-6.99	0.00	-4.01	-16.62	-0.43	-0.93	0.00	-3.13	-1.22	-4.31
total positive deviation from nominal	4.82	14.34	9.57	35.64	0.07	0.33	0.96	7.54	16.00	4.58
total negative deviation from nominal	-7.83	-7.17	-10.20	-37.24	-0.44	-0.96	-0.64	-6.76	-14.21	-5.93

Table G.3: Systematic errors for the pre–upgrade running period for $p_T^{\mu} \geq 2.0$ GeV for the cross sections differential in x_γ^{jets} and ΔR_{jj}

cross section	$\Delta\phi_{jj}$									
bin	1	2	3	4	5	6	7	8	9	10
nominal	0.81	0.28	0.09	0.47	0.80	1.72	4.84	17.39	49.83	202.89
charm p_T^{rel} correction 100%	0.81	0.28	0.09	0.52	0.79	1.69	4.64	16.70	47.63	193.90
positive deviation from nominal	0.00	0.00	0.00	0.05	0.00	0.00	0.00	0.00	0.00	0.00
negative deviation from nominal	0.00	0.00	-0.01	0.00	-0.02	-0.03	-0.21	-0.69	-2.20	-8.99
charm p_T^{rel} correction 0%	0.81	0.29	0.12	0.33	0.85	1.77	5.12	18.19	52.33	211.66
positive deviation from nominal	0.00	0.01	0.02	0.00	0.04	0.05	0.28	0.80	2.50	8.77
negative deviation from nominal	0.00	0.00	0.00	-0.14	0.00	0.00	0.00	0.00	0.00	0.00
randomised muon efficiency correction 1	0.81	0.27	0.06	0.89	0.94	1.64	2.91	17.51	47.01	199.97
randomised muon efficiency correction 2	0.77	0.26	0.06	0.00	0.78	1.66	5.06	17.73	49.30	200.10
randomised muon efficiency correction 3	0.84	0.31	0.10	0.20	0.92	1.59	4.52	17.86	50.61	206.65
randomised muon efficiency correction 4	0.83	0.33	0.12	0.00	0.95	1.85	5.22	18.10	52.10	208.97
randomised muon efficiency correction 5	0.81	0.29	0.00	0.14	0.68	1.73	5.07	17.38	50.55	206.30
randomised muon efficiency correction 6	0.84	0.30	0.11	0.20	0.80	1.83	4.85	18.29	51.07	209.52
randomised muon efficiency correction 7	0.82	0.27	0.07	0.03	0.83	1.65	4.89	18.52	51.83	212.49
randomised muon efficiency correction 8	0.86	0.27	0.17	0.25	1.09	1.61	4.90	18.20	50.39	203.87
randomised muon efficiency correction 9	0.82	0.28	0.06	0.19	0.89	1.77	5.05	18.12	50.81	207.45
randomised muon efficiency correction 10	0.89	0.26	0.00	0.48	0.67	1.68	4.80	18.37	51.38	210.66
RMS of randomised muon efficiency corrections	0.03	0.02	0.05	0.26	0.12	0.09	0.63	0.36	1.38	4.00
positive deviation from nominal	0.03	0.02	0.05	0.26	0.12	0.09	0.63	0.36	1.38	4.00
negative deviation from nominal	-0.03	-0.02	-0.05	-0.26	-0.12	-0.09	-0.63	-0.36	-1.38	-4.00
charm normalisation changed by factor 2	0.81	0.29	0.06	0.20	0.80	1.61	4.59	15.96	43.91	177.07
positive deviation from nominal	0.00	0.01	0.00	0.00	0.00	0.00	0.00	0.00	0.00	0.00
negative deviation from nominal	0.00	0.00	-0.03	-0.27	0.00	-0.11	-0.26	-1.42	-5.92	-25.82
charm normalisation changed by factor 0.5	0.81	0.27	0.20	0.64	0.81	1.92	5.28	19.64	57.79	232.29
positive deviation from nominal	0.00	0.00	0.11	0.17	0.00	0.20	0.44	2.25	7.96	29.39
negative deviation from nominal	0.00	-0.01	0.00	0.00	0.00	0.00	0.00	0.00	0.00	0.00
normalisation of resolved and ex. changed by factor 2	0.83	0.24	0.14	1.53	1.27	1.56	3.73	18.07	50.03	214.59
positive deviation from nominal	0.01	0.00	0.05	1.05	0.47	0.00	0.00	0.69	0.21	11.70
negative deviation from nominal	0.00	-0.04	0.00	0.00	0.00	-0.15	-1.11	0.00	0.00	0.00
normalisation of resolved and ex. changed by factor 0.5	0.68	0.31	0.05	0.27	0.71	1.79	5.69	16.64	49.90	191.31
positive deviation from nominal	0.00	0.03	0.00	0.00	0.00	0.07	0.85	0.00	0.08	0.00
negative deviation from nominal	-0.13	0.00	-0.04	-0.20	-0.09	0.00	0.00	-0.75	0.00	-11.58
p_T^{rel} definition 1	0.23	0.35	0.30	0.07	0.80	3.55	4.09	16.93	43.77	200.66
positive deviation from nominal	0.00	0.07	0.21	0.00	0.00	1.83	0.00	0.00	0.00	0.00
negative deviation from nominal	-0.58	0.00	0.00	-0.40	0.00	0.00	-0.76	-0.46	-6.05	-2.24
total positive deviation from nominal	0.03	0.08	0.24	1.10	0.49	1.84	1.18	2.51	8.46	33.07
total negative deviation from nominal	-0.60	-0.05	-0.07	-0.60	-0.15	-0.21	-1.52	-1.84	-8.85	-30.05

Table G.4: Systematic errors for the pre–upgrade running period for $p_T^\mu \geq 2.0$ GeV for the cross section differential in $\Delta\phi_{jj}$

G.2 Systematic Errors for the Post–Upgrade Running Periods for $p_T^\mu \geq 1.5$ GeV

cross section	total	p_T^μ				η^μ			
bin		1	2	3	4	1	2	3	4
nominal	169.08	67.33	13.71	3.69	0.81	14.71	57.26	45.82	30.32
charm p_T^{rel} correction 100%	158.40	62.37	12.32	3.50	0.81	14.11	55.24	41.52	29.35
positive deviation from nominal	0.00	0.00	0.00	0.00	0.00	0.00	0.00	0.00	0.00
negative deviation from nominal	-10.68	-4.96	-1.39	-0.19	0.00	-0.60	-2.02	-4.30	-0.97
charm p_T^{rel} correction 0%	177.70	71.22	14.86	3.85	0.81	15.18	58.88	49.56	31.05
positive deviation from nominal	8.62	3.89	1.15	0.16	0.00	0.46	1.62	3.73	0.73
negative deviation from nominal	0.00	0.00	0.00	0.00	0.00	0.00	0.00	0.00	0.00
randomised muon efficiency correction 1	159.31	63.97	13.29	3.95	0.76	12.14	53.89	41.07	33.14
randomised muon efficiency correction 2	165.28	65.77	13.76	4.16	0.74	13.87	53.61	45.87	30.35
randomised muon efficiency correction 3	175.19	65.89	14.07	3.74	0.77	15.34	62.30	43.51	29.23
randomised muon efficiency correction 4	184.35	67.56	14.79	3.90	0.86	14.06	66.63	49.33	25.97
randomised muon efficiency correction 5	258.32	75.77	30.32	3.56	0.84	15.52	61.34	113.17	31.89
randomised muon efficiency correction 6	181.27	66.26	14.05	3.82	0.86	14.41	60.41	49.95	32.15
randomised muon efficiency correction 7	177.45	64.44	14.73	3.91	0.82	12.66	55.84	52.22	31.43
randomised muon efficiency correction 8	149.70	60.53	13.33	3.70	0.79	7.77	55.07	47.42	29.59
randomised muon efficiency correction 9	151.48	45.72	12.82	3.76	0.85	57.73	57.83	47.49	28.98
randomised muon efficiency correction 10	158.82	59.53	13.14	3.08	0.85	15.27	57.49	41.01	28.77
RMS of randomised muon efficiency corrections	29.76	7.26	5.00	0.27	0.04	13.46	3.97	20.33	1.99
positive deviation from nominal	29.76	7.26	5.00	0.27	0.04	13.46	3.97	20.33	1.99
negative deviation from nominal	-29.76	-7.26	-5.00	-0.27	-0.04	-13.46	-3.97	-20.33	-1.99
charm normalisation changed by factor 2	164.26	67.94	13.80	3.16	0.83	15.90	56.37	45.33	29.05
positive deviation from nominal	0.00	0.61	0.09	0.00	0.02	1.19	0.00	0.00	0.00
negative deviation from nominal	-4.83	0.00	0.00	-0.53	0.00	0.00	-0.89	-0.49	-1.27
charm normalisation changed by factor 0.5	176.71	66.73	13.76	4.49	0.79	14.05	58.78	47.12	32.34
positive deviation from nominal	7.63	0.00	0.05	0.80	0.00	0.00	1.52	1.29	2.02
negative deviation from nominal	0.00	-0.60	0.00	0.00	-0.02	-0.66	0.00	0.00	0.00
normalisation of resolved and ex. changed by factor 2	171.17	67.99	14.45	4.75	1.00	16.24	54.08	49.93	24.31
positive deviation from nominal	2.08	0.66	0.74	1.06	0.18	1.53	0.00	4.10	0.00
negative deviation from nominal	0.00	0.00	0.00	0.00	0.00	0.00	-3.18	0.00	-6.01
normalisation of resolved and ex. changed by factor 0.5	168.56	67.73	13.27	3.05	0.62	12.83	58.97	42.77	38.73
positive deviation from nominal	0.00	0.41	0.00	0.00	0.00	0.00	1.71	0.00	8.41
negative deviation from nominal	-0.52	0.00	-0.44	-0.64	-0.19	-1.89	0.00	-3.05	0.00
p_T^{rel} definition 1	168.25	105.49	18.87	5.82	0.62	13.82	60.52	68.16	34.92
positive deviation from nominal	0.00	38.16	5.16	2.13	0.00	0.00	3.26	22.33	4.60
negative deviation from nominal	-0.83	0.00	0.00	0.00	-0.19	-0.89	0.00	0.00	0.00
total positive deviation from nominal	31.98	39.05	7.32	2.53	0.19	13.61	5.85	30.73	10.03
total negative deviation from nominal	-32.00	-8.82	-5.21	-0.89	-0.27	-13.65	-5.55	-21.01	-6.53

Table G.5: Systematic errors for the post–upgrade running period for $p_T^\mu \geq 1.5$ GeV for the total beauty quark photoproduction cross section and the cross sections differential in p_T^μ and η^μ

cross section	$p_T^{\mu-jet}$			$\eta^{\mu-jet}$			
bin	1	2	3	1	2	3	4
nominal	14.50	4.95	1.55	23.20	39.72	29.23	22.65
charm p_T^{rel} correction 100%	13.41	4.77	1.54	22.76	37.24	25.23	22.27
positive deviation from nominal	0.00	0.00	0.00	0.00	0.00	0.00	0.00
negative deviation from nominal	-1.10	-0.17	-0.01	-0.44	-2.48	-4.00	-0.38
charm p_T^{rel} correction 0%	15.41	5.08	1.57	23.56	41.70	32.79	22.97
positive deviation from nominal	0.90	0.14	0.02	0.36	1.98	3.56	0.32
negative deviation from nominal	0.00	0.00	0.00	0.00	0.00	0.00	0.00
randomised muon efficiency correction 1	13.58	4.67	1.46	20.73	36.79	26.47	23.48
randomised muon efficiency correction 2	14.40	4.46	1.49	23.26	37.51	28.51	21.74
randomised muon efficiency correction 3	15.51	4.59	1.64	25.09	42.43	27.85	21.02
randomised muon efficiency correction 4	16.21	5.26	1.59	25.33	45.23	31.66	20.12
randomised muon efficiency correction 5	27.37	5.32	0.96	25.75	57.80	73.82	23.39
randomised muon efficiency correction 6	15.59	5.39	1.62	23.38	42.79	32.34	24.34
randomised muon efficiency correction 7	15.43	4.85	1.65	21.87	39.84	34.15	24.12
randomised muon efficiency correction 8	13.18	4.49	1.61	17.83	38.27	30.22	22.05
randomised muon efficiency correction 9	11.02	5.23	1.62	38.10	39.65	29.71	21.67
randomised muon efficiency correction 10	13.94	4.92	1.41	22.91	41.79	16.62	22.07
RMS of randomised muon efficiency corrections	4.17	0.34	0.20	5.08	5.76	14.30	1.31
positive deviation from nominal	4.17	0.34	0.20	5.08	5.76	14.30	1.31
negative deviation from nominal	-4.17	-0.34	-0.20	-5.08	-5.76	-14.30	-1.31
charm normalisation changed by factor 2	14.23	4.84	1.54	23.36	38.72	29.16	21.18
positive deviation from nominal	0.00	0.00	0.00	0.16	0.00	0.00	0.00
negative deviation from nominal	-0.28	-0.11	-0.01	0.00	-1.00	-0.07	-1.47
charm normalisation changed by factor 0.5	14.97	5.13	1.59	23.65	41.56	29.72	24.70
positive deviation from nominal	0.47	0.18	0.05	0.45	1.84	0.49	2.04
negative deviation from nominal	0.00	0.00	0.00	0.00	0.00	0.00	0.00
normalisation of resolved and ex. changed by factor 2	15.06	5.05	1.46	24.00	42.04	29.34	19.30
positive deviation from nominal	0.56	0.10	0.00	0.80	2.32	0.11	0.00
negative deviation from nominal	0.00	0.00	-0.09	0.00	0.00	0.00	-3.36
normalisation of resolved and ex. changed by factor 0.5	14.12	4.85	1.76	22.83	36.88	30.92	26.06
positive deviation from nominal	0.00	0.00	0.21	0.00	0.00	1.69	3.41
negative deviation from nominal	-0.39	-0.09	0.00	-0.37	-2.85	0.00	0.00
p_T^{rel} definition 1	14.51	3.62	1.50	16.25	38.94	29.29	25.19
positive deviation from nominal	0.00	0.00	0.00	0.00	0.00	0.06	2.53
negative deviation from nominal	0.00	-1.32	-0.05	-6.95	-0.78	0.00	0.00
total positive deviation from nominal	4.33	0.42	0.29	5.18	6.77	14.84	4.90
total negative deviation from nominal	-4.34	-1.38	-0.22	-8.63	-7.00	-14.85	-3.91

Table G.6: Systematic errors for the post–upgrade running period for $p_T^{\mu} \geq 1.5$ GeV for the cross sections differential in $p_T^{\mu-jet}$ and $\eta^{\mu-jet}$

cross section	x_γ^{jets}				ΔR_{jj}					
bin	1	2	3	4	1	2	3	4	5	6
nominal	56.12	65.72	50.75	335.45	0.00	2.98	5.94	46.78	100.78	46.56
charm p_T^{rel} correction 100%	55.17	61.35	48.92	318.36	0.00	2.96	5.88	44.92	93.93	44.52
positive deviation from nominal	0.00	0.00	0.00	0.00	0.00	0.00	0.00	0.00	0.00	0.00
negative deviation from nominal	-0.95	-4.37	-1.83	-17.09	0.00	-0.02	-0.06	-1.86	-6.85	-2.04
charm p_T^{rel} correction 0%	57.16	69.06	52.13	349.51	0.00	3.01	6.01	48.52	105.72	47.96
positive deviation from nominal	1.04	3.34	1.38	14.06	0.00	0.03	0.07	1.74	4.94	1.40
negative deviation from nominal	0.00	0.00	0.00	0.00	0.00	0.00	0.00	0.00	0.00	0.00
randomised muon efficiency correction 1	54.90	46.88	47.68	321.00	0.00	3.31	5.48	45.38	94.65	46.08
randomised muon efficiency correction 2	48.96	49.38	48.53	326.21	0.00	3.05	4.67	46.58	99.41	41.68
randomised muon efficiency correction 3	46.72	64.55	50.47	341.95	0.00	3.06	5.63	46.63	102.65	51.33
randomised muon efficiency correction 4	55.55	79.01	55.33	359.36	0.00	3.35	5.90	49.13	111.37	49.57
randomised muon efficiency correction 5	50.62	136.03	82.85	390.39	0.00	4.33	8.12	63.56	147.55	47.92
randomised muon efficiency correction 6	57.17	73.53	52.42	356.86	0.00	2.72	6.19	49.22	107.32	49.30
randomised muon efficiency correction 7	56.46	69.43	53.76	347.75	0.00	3.50	5.66	49.09	109.47	44.78
randomised muon efficiency correction 8	58.61	65.63	51.48	307.29	0.00	2.54	6.39	47.36	92.10	46.15
randomised muon efficiency correction 9	56.44	61.03	50.41	319.53	0.00	3.78	6.30	47.11	85.13	48.63
randomised muon efficiency correction 10	51.03	52.48	51.44	345.47	0.00	4.76	7.53	43.38	99.26	48.36
RMS of randomised muon efficiency corrections	3.79	24.19	9.71	23.04	0.00	0.65	0.95	5.23	16.17	2.63
positive deviation from nominal	3.79	24.19	9.71	23.04	0.00	0.65	0.95	5.23	16.17	2.63
negative deviation from nominal	-3.79	-24.19	-9.71	-23.04	0.00	-0.65	-0.95	-5.23	-16.17	-2.63
charm normalisation changed by factor 2	57.48	66.66	51.38	332.94	0.00	3.11	5.83	45.24	99.11	48.37
positive deviation from nominal	1.36	0.94	0.64	0.00	0.00	0.12	0.00	0.00	0.00	1.81
negative deviation from nominal	0.00	0.00	0.00	-2.51	0.00	0.00	-0.12	-1.54	-1.67	0.00
charm normalisation changed by factor 0.5	56.59	64.10	50.18	342.39	0.00	2.73	6.11	49.27	104.97	44.91
positive deviation from nominal	0.46	0.00	0.00	6.94	0.00	0.00	0.17	2.48	4.19	0.00
negative deviation from nominal	0.00	-1.62	-0.57	0.00	0.00	-0.25	0.00	0.00	0.00	-1.65
normalisation of resolved and ex. changed by factor 2	60.24	41.59	41.63	347.76	0.00	2.78	5.20	41.10	115.24	48.79
positive deviation from nominal	4.12	0.00	0.00	12.31	0.00	0.00	0.00	0.00	14.46	2.23
negative deviation from nominal	0.00	-24.13	-9.12	0.00	0.00	-0.20	-0.74	-5.69	0.00	0.00
normalisation of resolved and ex. changed by factor 0.5	56.59	91.74	59.00	318.61	0.00	3.04	6.79	56.83	87.05	43.11
positive deviation from nominal	0.47	26.02	8.25	0.00	0.00	0.06	0.85	10.05	0.00	0.00
negative deviation from nominal	0.00	0.00	0.00	-16.84	0.00	0.00	0.00	0.00	-13.73	-3.46
p_T^{rel} definition 1	77.77	45.82	63.80	283.94	9.19	5.31	11.28	41.59	107.13	45.11
positive deviation from nominal	21.65	0.00	13.05	0.00	9.19	2.33	5.34	0.00	6.35	0.00
negative deviation from nominal	0.00	-19.91	0.00	-51.51	0.00	0.00	0.00	-5.20	0.00	-1.45
total positive deviation from nominal	22.44	35.69	18.30	30.47	9.19	2.43	5.49	11.73	23.51	4.14
total negative deviation from nominal	-3.91	-39.82	-13.46	-61.36	0.00	-0.73	-1.21	-9.62	-22.35	-5.28

Table G.7: Systematic errors for the post–upgrade running period for $p_T^{\mu} \geq 1.5$ GeV for the cross sections differential in x_γ^{jets} and ΔR_{jj}

cross section	$\Delta\phi_{jj}$									
bin	1	2	3	4	5	6	7	8	9	10
nominal	0.00	0.00	0.00	0.57	0.77	5.28	9.40	19.66	68.52	240.37
charm p_T^{rel} correction 100%	0.00	0.00	0.00	0.55	0.77	5.27	9.37	19.33	67.11	223.58
positive deviation from nominal	0.00	0.00	0.00	0.00	0.00	0.00	0.00	0.00	0.00	0.00
negative deviation from nominal	0.00	0.00	0.00	-0.02	0.00	0.00	-0.03	-0.33	-1.41	-16.78
charm p_T^{rel} correction 0%	0.00	0.00	0.00	0.63	0.77	5.27	9.42	20.00	69.78	252.12
positive deviation from nominal	0.00	0.00	0.00	0.06	0.00	0.00	0.03	0.34	1.26	11.75
negative deviation from nominal	0.00	0.00	0.00	0.00	0.00	0.00	0.00	0.00	0.00	0.00
randomised muon efficiency correction 1	0.00	0.00	0.00	0.54	0.80	5.16	8.98	16.37	67.69	224.98
randomised muon efficiency correction 2	0.00	0.00	0.00	0.64	0.82	5.09	8.99	17.30	69.34	229.24
randomised muon efficiency correction 3	0.00	0.00	0.00	0.54	0.75	5.31	8.07	19.06	69.74	246.82
randomised muon efficiency correction 4	0.00	0.00	0.00	0.54	0.65	5.27	8.83	19.34	71.12	268.79
randomised muon efficiency correction 5	0.00	0.00	0.00	0.58	0.76	6.52	9.25	25.45	65.57	338.90
randomised muon efficiency correction 6	0.00	0.00	0.00	0.58	0.85	4.75	9.68	20.04	70.48	261.22
randomised muon efficiency correction 7	0.00	0.00	0.00	0.59	0.78	5.28	9.37	18.80	70.70	253.92
randomised muon efficiency correction 8	0.00	0.00	0.00	0.59	0.73	4.82	8.70	19.73	67.11	219.34
randomised muon efficiency correction 9	0.00	0.00	0.00	0.56	0.75	4.89	9.50	22.85	80.73	245.91
randomised muon efficiency correction 10	0.00	0.00	130.97	0.56	0.76	5.08	10.09	21.05	63.63	238.74
RMS of randomised muon efficiency corrections	0.00	0.00	39.29	0.03	0.05	0.47	0.54	2.49	4.36	32.36
positive deviation from nominal	0.00	0.00	39.29	0.03	0.05	0.47	0.54	2.49	4.36	32.36
negative deviation from nominal	0.00	0.00	-39.29	-0.03	-0.05	-0.47	-0.54	-2.49	-4.36	-32.36
charm normalisation changed by factor 2	0.00	0.00	0.00	0.70	0.76	5.31	9.30	19.26	67.63	238.71
positive deviation from nominal	0.00	0.00	0.00	0.13	0.00	0.04	0.00	0.00	0.00	0.00
negative deviation from nominal	0.00	0.00	0.00	0.00	-0.01	0.00	-0.10	-0.41	-0.89	-1.65
charm normalisation changed by factor 0.5	0.00	0.00	0.00	0.36	0.79	5.21	9.58	20.49	70.46	244.98
positive deviation from nominal	0.00	0.00	0.00	0.00	0.02	0.00	0.18	0.82	1.95	4.61
negative deviation from nominal	0.00	0.00	0.00	-0.21	0.00	-0.07	0.00	0.00	0.00	0.00
normalisation of resolved and ex. changed by factor 2	0.00	0.00	0.00	0.25	0.78	3.02	11.53	18.36	63.60	259.49
positive deviation from nominal	0.00	0.00	0.00	0.00	0.01	0.00	2.13	0.00	0.00	19.12
negative deviation from nominal	0.00	0.00	0.00	-0.32	0.00	-2.25	0.00	-1.30	-4.92	0.00
normalisation of resolved and ex. changed by factor 0.5	0.00	0.00	0.00	1.09	0.70	5.29	7.85	22.42	72.43	220.93
positive deviation from nominal	0.00	0.00	0.00	0.52	0.00	0.01	0.00	2.76	3.91	0.00
negative deviation from nominal	0.00	0.00	0.00	0.00	-0.07	0.00	-1.55	0.00	0.00	-19.44
p_T^{rel} definition 1	0.00	0.00	2.08	1.99	1.92	2.88	16.17	20.73	61.09	228.93
positive deviation from nominal	0.00	0.00	2.08	1.41	1.14	0.00	6.78	1.07	0.00	0.00
negative deviation from nominal	0.00	0.00	0.00	0.00	0.00	-2.40	0.00	0.00	-7.43	-11.44
total positive deviation from nominal	0.00	0.00	39.35	1.51	1.14	0.48	7.13	3.97	6.30	39.65
total negative deviation from nominal	0.00	0.00	-39.29	-0.39	-0.09	-3.32	-1.64	-2.86	-10.06	-42.90

Table G.8: Systematic errors for the post–upgrade running period for $p_T^\mu \geq 1.5$ GeV for the cross section differential in $\Delta\phi_{jj}$

G.3 Systematic Errors for the Post–Upgrade Running Periods for $p_T^\mu \geq 2.0$ GeV

cross section	total	p_T^μ				η^μ			
bin		1	2	3	4	1	2	3	4
nominal	114.47	49.30	13.72	3.61	0.77	9.66	38.24	28.67	21.54
charm p_T^{rel} correction 100%	106.90	46.00	12.33	3.41	0.77	9.49	36.83	25.52	20.96
positive deviation from nominal	0.00	0.00	0.00	0.00	0.00	0.00	0.00	0.00	0.00
negative deviation from nominal	-7.57	-3.30	-1.39	-0.20	0.00	-0.17	-1.41	-3.15	-0.59
charm p_T^{rel} correction 0%	120.51	51.88	14.87	3.77	0.77	9.80	39.36	31.34	21.97
positive deviation from nominal	6.04	2.58	1.15	0.16	0.00	0.14	1.12	2.67	0.43
negative deviation from nominal	0.00	0.00	0.00	0.00	0.00	0.00	0.00	0.00	0.00
randomised muon efficiency correction 1	108.09	45.91	13.29	3.87	0.73	8.00	35.72	25.87	23.35
randomised muon efficiency correction 2	113.21	47.47	13.76	4.10	0.70	8.93	35.32	30.22	21.02
randomised muon efficiency correction 3	119.84	49.84	14.09	3.68	0.74	9.99	41.84	27.59	21.14
randomised muon efficiency correction 4	125.02	50.10	14.80	3.80	0.81	9.53	43.11	31.89	18.70
randomised muon efficiency correction 5	170.93	55.93	30.33	3.46	0.80	10.27	39.97	71.92	23.10
randomised muon efficiency correction 6	123.07	49.99	14.06	3.73	0.81	9.68	40.20	31.94	22.85
randomised muon efficiency correction 7	118.77	44.47	14.73	3.82	0.78	7.96	36.71	32.62	21.97
randomised muon efficiency correction 8	96.65	41.15	13.35	3.64	0.75	5.59	36.45	29.57	20.38
randomised muon efficiency correction 9	103.32	33.06	12.83	3.67	0.80	40.60	39.07	30.40	20.61
randomised muon efficiency correction 10	103.01	39.32	13.15	2.98	0.81	9.81	37.80	24.06	20.48
RMS of randomised muon efficiency corrections	19.74	14.81	22.96	0.28	0.04	9.61	2.52	13.04	1.38
positive deviation from nominal	19.74	6.21	5.00	0.28	0.04	9.61	2.52	13.04	1.38
negative deviation from nominal	-19.74	-6.21	-5.00	-0.28	-0.04	-9.61	-2.52	-13.04	-1.38
charm normalisation changed by factor 2	112.03	50.30	13.81	3.11	0.79	10.19	37.96	28.08	20.54
positive deviation from nominal	0.00	1.00	0.09	0.00	0.02	0.53	0.00	0.00	0.00
negative deviation from nominal	-2.44	0.00	0.00	-0.50	0.00	0.00	-0.27	-0.59	-1.00
charm normalisation changed by factor 0.5	118.77	48.25	13.77	4.38	0.75	9.76	38.80	29.94	23.03
positive deviation from nominal	4.30	0.00	0.05	0.77	0.00	0.10	0.57	1.26	1.49
negative deviation from nominal	0.00	-1.05	0.00	0.00	-0.02	0.00	0.00	0.00	0.00
normalisation of resolved and ex. changed by factor 2	118.95	51.43	14.47	4.70	0.97	10.02	36.94	33.60	17.14
positive deviation from nominal	4.49	2.14	0.75	1.09	0.20	0.37	0.00	4.92	0.00
negative deviation from nominal	0.00	0.00	0.00	0.00	0.00	0.00	-1.30	0.00	-4.40
normalisation of resolved and ex. changed by factor 0.5	110.81	48.21	13.27	2.94	0.57	9.20	38.18	24.58	27.54
positive deviation from nominal	0.00	0.00	0.00	0.00	0.00	0.00	0.00	0.00	6.00
negative deviation from nominal	-3.66	-1.09	-0.45	-0.66	-0.20	-0.45	-0.06	-4.10	0.00
p_T^{rel} definition 1	116.02	59.16	12.69	4.88	0.65	7.76	35.75	27.26	18.15
positive deviation from nominal	1.56	9.86	0.00	1.27	0.00	0.00	0.00	0.00	0.00
negative deviation from nominal	0.00	0.00	-1.03	0.00	-0.12	-1.90	-2.48	-1.41	-3.39
total positive deviation from nominal	21.62	12.17	5.19	1.87	0.20	9.64	2.81	14.25	6.35
total negative deviation from nominal	-21.59	-7.19	-5.31	-0.90	-0.24	-9.81	-4.03	-14.11	-5.84

Table G.9: Systematic errors for the post–upgrade running period for $p_T^\mu \geq 2.0$ GeV for the total beauty quark photoproduction cross section and the cross sections differential in p_T^μ and η^μ

cross section	$p_T^{\mu-jet}$			$\eta^{\mu-jet}$			
bin	1	2	3	1	2	3	4
nominal	10.40	3.92	1.35	17.24	32.11	16.13	19.64
charm p_T^{rel} correction 100%	9.54	3.78	1.34	17.01	30.37	12.47	19.36
positive deviation from nominal	0.00	0.00	0.00	0.00	0.00	0.00	0.00
negative deviation from nominal	-0.86	-0.15	-0.01	-0.24	-1.74	-3.66	-0.28
charm p_T^{rel} correction 0%	11.09	4.04	1.37	17.43	33.50	19.32	19.84
positive deviation from nominal	0.69	0.12	0.01	0.19	1.39	3.19	0.21
negative deviation from nominal	0.00	0.00	0.00	0.00	0.00	0.00	0.00
randomised muon efficiency correction 1	9.69	3.68	1.27	15.53	29.71	13.86	20.62
randomised muon efficiency correction 2	10.36	3.56	1.31	17.10	30.25	17.43	18.90
randomised muon efficiency correction 3	11.33	3.69	1.42	18.71	34.33	16.50	18.37
randomised muon efficiency correction 4	11.70	4.13	1.37	18.88	35.51	19.28	17.46
randomised muon efficiency correction 5	20.15	4.17	0.74	19.03	45.36	51.48	20.53
randomised muon efficiency correction 6	11.24	4.29	1.42	17.13	34.33	19.22	21.16
randomised muon efficiency correction 7	10.88	3.83	1.44	16.04	31.43	19.78	20.47
randomised muon efficiency correction 8	8.97	3.53	1.40	12.69	30.88	16.94	18.54
randomised muon efficiency correction 9	7.52	4.17	1.43	50.21	32.74	17.17	19.19
randomised muon efficiency correction 10	9.54	3.84	1.20	16.82	33.15	6.19	19.08
RMS of randomised muon efficiency corrections	3.23	0.27	0.20	10.16	4.27	11.21	1.14
positive deviation from nominal	3.23	0.27	0.20	10.16	4.27	11.21	1.14
negative deviation from nominal	-3.23	-0.27	-0.20	-10.16	-4.27	-11.21	-1.14
charm normalisation changed by factor 2	10.36	3.85	1.33	17.42	32.00	14.75	18.13
positive deviation from nominal	0.00	0.00	0.00	0.17	0.00	0.00	0.00
negative deviation from nominal	-0.04	-0.07	-0.03	0.00	-0.11	-1.38	-1.51
charm normalisation changed by factor 0.5	10.58	4.05	1.42	17.73	32.66	18.15	21.65
positive deviation from nominal	0.18	0.13	0.06	0.48	0.55	2.03	2.01
negative deviation from nominal	0.00	0.00	0.00	0.00	0.00	0.00	0.00
normalisation of resolved and ex. changed by factor 2	10.99	3.91	1.29	17.17	34.04	17.48	17.47
positive deviation from nominal	0.59	0.00	0.00	0.00	1.93	1.35	0.00
negative deviation from nominal	0.00	-0.01	-0.06	-0.08	0.00	0.00	-2.17
normalisation of resolved and ex. changed by factor 0.5	9.93	3.93	1.54	17.88	29.71	16.80	21.63
positive deviation from nominal	0.00	0.01	0.19	0.64	0.00	0.68	1.99
negative deviation from nominal	-0.48	0.00	0.00	0.00	-2.40	0.00	0.00
p_T^{rel} definition 1	10.80	2.99	1.29	13.56	31.23	15.92	20.37
positive deviation from nominal	0.40	0.00	0.00	0.00	0.00	0.00	0.73
negative deviation from nominal	0.00	-0.93	-0.06	-3.68	-0.88	-0.21	0.00
total positive deviation from nominal	3.39	0.32	0.28	10.19	4.92	11.93	3.14
total negative deviation from nominal	-3.38	-0.98	-0.22	-10.81	-5.27	-11.87	-2.89

Table G.10: Systematic errors for the post–upgrade running period for $p_T^{\mu} \geq 2.0$ GeV for the cross sections differential in $p_T^{\mu-jet}$ and $\eta^{\mu-jet}$

cross section	x_γ^{jets}				ΔR_{jj}					
bin	1	2	3	4	1	2	3	4	5	6
nominal	41.50	61.24	37.08	256.95	0.00	5.83	3.88	37.66	74.33	35.44
charm p_T^{rel} correction 100%	40.37	57.45	35.78	244.15	0.00	5.82	3.84	36.20	68.84	33.94
positive deviation from nominal	0.00	0.00	0.00	0.00	0.00	0.00	0.00	0.00	0.00	0.00
negative deviation from nominal	-1.13	-3.79	-1.30	-12.80	0.00	-0.02	-0.04	-1.46	-5.49	-1.50
charm p_T^{rel} correction 0%	42.65	63.71	38.09	267.89	0.00	5.86	3.91	39.04	78.27	36.49
positive deviation from nominal	1.15	2.47	1.01	10.94	0.00	0.03	0.04	1.38	3.95	1.05
negative deviation from nominal	0.00	0.00	0.00	0.00	0.00	0.00	0.00	0.00	0.00	0.00
randomised muon efficiency correction 1	40.10	43.83	34.71	246.62	0.00	6.06	3.74	36.42	70.12	34.96
randomised muon efficiency correction 2	37.47	44.87	35.66	251.04	0.00	5.52	3.12	37.78	74.02	31.27
randomised muon efficiency correction 3	35.71	59.81	36.80	263.60	0.00	5.49	3.76	37.92	75.95	39.04
randomised muon efficiency correction 4	43.16	72.86	40.09	274.34	0.00	6.42	3.92	39.38	81.96	37.50
randomised muon efficiency correction 5	37.22	115.48	60.15	290.64	0.00	6.34	5.49	50.65	107.27	35.73
randomised muon efficiency correction 6	43.58	67.96	38.46	274.83	0.00	6.07	4.08	40.04	79.46	37.89
randomised muon efficiency correction 7	41.55	63.58	38.88	264.59	0.00	5.92	3.63	38.55	80.48	33.66
randomised muon efficiency correction 8	42.07	60.03	36.86	230.65	0.00	5.16	4.04	38.22	64.18	34.39
randomised muon efficiency correction 9	42.48	59.29	37.42	258.90	0.00	6.51	4.17	39.28	60.43	37.24
randomised muon efficiency correction 10	56.28	47.20	37.07	263.51	0.00	6.92	4.89	34.15	71.38	37.31
RMS of randomised muon efficiency corrections	5.43	19.63	7.00	15.80	0.00	0.51	0.64	4.12	12.18	2.23
positive deviation from nominal	5.43	19.63	7.00	15.80	0.00	0.51	0.64	4.12	12.18	2.23
negative deviation from nominal	-5.43	-19.63	-7.00	-15.80	0.00	-0.51	-0.64	-4.12	-12.18	-2.23
charm normalisation changed by factor 2	41.73	63.36	38.07	258.05	0.00	5.86	3.80	37.18	73.06	37.30
positive deviation from nominal	0.24	2.12	0.99	1.10	0.00	0.02	0.00	0.00	0.00	1.85
negative deviation from nominal	0.00	0.00	0.00	0.00	0.00	0.00	-0.08	-0.47	-1.26	0.00
charm normalisation changed by factor 0.5	43.94	58.06	36.03	259.04	0.00	5.80	4.00	38.79	77.61	33.48
positive deviation from nominal	2.45	0.00	0.00	2.09	0.00	0.00	0.12	1.13	3.28	0.00
negative deviation from nominal	0.00	-3.18	-1.05	0.00	0.00	-0.03	0.00	0.00	0.00	-1.96
normalisation of resolved and ex. changed by factor 2	43.43	43.81	30.79	264.03	0.00	4.04	3.33	33.91	85.36	36.63
positive deviation from nominal	1.93	0.00	0.00	7.09	0.00	0.00	0.00	0.00	11.04	1.19
negative deviation from nominal	0.00	-17.43	-6.29	0.00	0.00	-1.80	-0.54	-3.75	0.00	0.00
normalisation of resolved and ex. changed by factor 0.5	43.73	80.83	42.90	246.68	0.00	5.50	4.54	44.99	63.70	33.28
positive deviation from nominal	2.23	19.59	5.82	0.00	0.00	0.00	0.67	7.33	0.00	0.00
negative deviation from nominal	0.00	0.00	0.00	-10.27	0.00	-0.34	0.00	0.00	-10.63	-2.16
p_T^{rel} definition 1	56.65	37.10	49.03	217.88	2.66	0.00	7.74	33.41	81.55	34.64
positive deviation from nominal	15.16	0.00	11.95	0.00	2.66	0.00	3.86	0.00	7.23	0.00
negative deviation from nominal	0.00	-24.14	0.00	-39.07	0.00	-5.83	0.00	-4.24	0.00	-0.81
total positive deviation from nominal	16.59	27.92	15.09	20.62	2.66	0.51	3.97	8.60	18.68	3.31
total negative deviation from nominal	-5.55	-36.00	-9.56	-45.23	0.00	-6.14	-0.84	-7.17	-17.12	-4.05

Table G.11: Systematic errors for the post–upgrade running period for $p_T^{\mu} \geq 2.0$ GeV for the cross sections differential in x_γ^{jets} and ΔR_{jj}

cross section	$\Delta\phi_{jj}$									
bin	1	2	3	4	5	6	7	8	9	10
nominal	0.00	0.00	0.00	0.48	0.68	3.83	6.29	13.77	59.26	177.38
charm p_T^{rel} correction 100%	0.00	0.00	0.00	0.45	0.68	3.83	6.26	13.51	58.15	164.77
positive deviation from nominal	0.00	0.00	0.00	0.00	0.00	0.00	0.00	0.00	0.00	0.00
negative deviation from nominal	0.00	0.00	0.00	-0.03	0.00	0.00	-0.03	-0.26	-1.11	-12.61
charm p_T^{rel} correction 0%	0.00	0.00	0.00	0.54	0.68	3.82	6.32	14.04	60.23	186.43
positive deviation from nominal	0.00	0.00	0.00	0.07	0.00	0.00	0.02	0.27	0.97	9.05
negative deviation from nominal	0.00	0.00	0.00	0.00	0.00	0.00	0.00	0.00	0.00	0.00
randomised muon efficiency correction 1	0.00	0.00	0.00	0.43	0.70	3.34	5.83	11.57	58.19	166.76
randomised muon efficiency correction 2	0.00	0.00	0.00	0.55	0.74	3.85	5.57	12.07	60.06	170.31
randomised muon efficiency correction 3	0.00	0.00	0.00	0.48	0.66	4.16	5.33	13.44	61.03	182.91
randomised muon efficiency correction 4	0.00	0.00	0.00	0.49	0.58	3.84	6.01	13.63	60.88	197.82
randomised muon efficiency correction 5	0.00	0.00	0.00	0.50	0.67	16.27	6.49	19.18	56.79	249.77
randomised muon efficiency correction 6	0.00	0.00	0.00	0.51	0.75	4.15	6.87	14.09	60.98	193.94
randomised muon efficiency correction 7	0.00	0.00	0.00	0.48	0.68	4.42	6.08	12.95	60.40	185.57
randomised muon efficiency correction 8	0.00	0.00	0.00	0.46	0.64	3.74	5.50	13.42	58.79	152.74
randomised muon efficiency correction 9	0.00	0.00	0.00	0.49	0.66	3.70	6.37	24.63	75.55	183.80
randomised muon efficiency correction 10	0.00	0.00	0.00	0.51	0.64	4.05	6.89	14.62	54.55	171.57
RMS of randomised muon efficiency corrections	0.00	0.00	0.00	0.03	0.05	3.72	0.53	3.78	5.33	24.92
positive deviation from nominal	0.00	0.00	0.00	0.03	0.05	3.72	0.53	3.78	5.33	24.92
negative deviation from nominal	0.00	0.00	0.00	-0.03	-0.05	-3.72	-0.53	-3.78	-5.33	-24.92
charm normalisation changed by factor 2	0.00	0.00	0.00	0.64	0.67	3.87	6.24	13.34	59.41	177.38
positive deviation from nominal	0.00	0.00	0.00	0.16	0.00	0.04	0.00	0.00	0.16	0.00
negative deviation from nominal	0.00	0.00	0.00	0.00	-0.01	0.00	-0.05	-0.44	0.00	0.00
charm normalisation changed by factor 0.5	0.00	0.00	0.00	0.19	0.69	3.79	6.39	14.61	59.68	179.50
positive deviation from nominal	0.00	0.00	0.00	0.00	0.01	0.00	0.10	0.83	0.42	2.12
negative deviation from nominal	0.00	0.00	0.00	-0.29	0.00	-0.04	0.00	0.00	0.00	0.00
normalisation of resolved and ex. changed by factor 2	0.00	0.00	0.00	0.11	0.71	3.56	8.59	11.86	57.84	190.50
positive deviation from nominal	0.00	0.00	0.00	0.00	0.03	0.00	2.30	0.00	0.00	13.12
negative deviation from nominal	0.00	0.00	0.00	-0.36	0.00	-0.27	0.00	-1.91	-1.42	0.00
normalisation of resolved and ex. changed by factor 0.5	0.00	0.00	0.00	1.02	0.61	3.11	4.72	16.91	60.20	164.02
positive deviation from nominal	0.00	0.00	0.00	0.54	0.00	0.00	0.00	3.14	0.94	0.00
negative deviation from nominal	0.00	0.00	0.00	0.00	-0.07	-0.72	-1.57	0.00	0.00	-13.36
p_T^{rel} definition 1	0.00	0.00	0.00	1.72	1.59	5.33	12.53	14.31	52.23	174.07
positive deviation from nominal	0.00	0.00	0.00	1.24	0.91	1.51	6.24	0.54	0.00	0.00
negative deviation from nominal	0.00	0.00	0.00	0.00	0.00	0.00	0.00	0.00	-7.03	-3.31
total positive deviation from nominal	0.00	0.00	0.00	1.37	0.92	4.01	6.67	5.01	5.52	29.66
total negative deviation from nominal	0.00	0.00	0.00	-0.46	-0.09	-3.80	-1.65	-4.26	-9.01	-31.14

Table G.12: Systematic errors for the post–upgrade running period for $p_T^\mu \geq 2.0$ GeV for the cross section differential in $\Delta\phi_{jj}$

References

[1] Halzen, F. and Martin, A.D., *Quarks and Leptons: An Introduction Course in Modern Particle Physics*. John Wiley & Sons, 1984.

[2] Collins, John C. and Soper, Davison E., Ann. Rev. Nucl. Part. Sci. **37**, 383 (1987).

[3] Ellis, R. K. and Nason, P., Nucl. Phys. **B312**, 551 (1989).

[4] Smith, J. and van Neerven, W. L., Nucl. Phys. **B374**, 36 (1992).

[5] Frixione, Stefano and Mangano, Michelangelo L. and Nason, Paolo and Ridolfi, Giovanni, Adv. Ser. Direct. High Energy Phys. **15**, 609 (1998).

[6] Altarelli, Guido and Parisi, G., Nucl. Phys. **B126**, 298 (1977).

[7] Witten, Edward, Nucl. Phys. **B120**, 189 (1977);
Llewellyn Smith, C. H., Phys. Lett. **B79**, 83 (1978);
Bardeen, William A. and Buras, Andrzej J., Phys. Rev. **D20**, 166 (1979);
DeWitt, R. J. and Jones, L. M. and Sullivan, J. D. and Willen, D. E. and Wyld, H. W. , Jr., Phys. Rev. **D19**, 2046 (1979).

[8] Eidelman, S. and others, Phys. Lett. **B592**, 1 (2004).

[9] Gabareen Mokhtar, Arafat, Preprint hep-ex/0406036, 2004.

[10] ZEUS Structure Functions and Electroweak Physics working group, *Combined H1 and ZEUS proton PDF's* (unpublished), 2004, available on `http://www-zeus.desy.de/physics/sfew/PUBLIC/sfew_results/preliminary/moriond04/zeush1.php` .

[11] Sjostrand, Torbjorn et al. , Comput. Phys. Commun. **135**, 238 (2001).

[12] Von Weizsaecker, C. F., Z. Phys. **88**, 612 (1934);
Williams, E. J., Phys. Rev. **45**, 729 (1934).

[13] Peterson, C. and Schlatter, D. and Schmitt, I. and Zerwas, Peter M., Phys. Rev. **D27**, 105 (1983).

[14] Buskulic, D. et al. , Phys. Lett. **B357**, 699 (1995).

[15] Abe, K. and others, Phys. Lett. **B547**, 181 (2002);
Aubert, B. and others, Phys. Rev. **D67**, 031101 (2003).

[16] M. Corradi, M. Turcato, *Beauty production in dijet events* (unpublished). ZEUS-Note 04-005, 2004.

[17] Frixione, Stefano and Mangano, Michelangelo L. and Nason, Paolo and Ridolfi, Giovanni, Nucl. Phys. **B412**, 225 (1994);
Frixione, Stefano and Mangano, Michelangelo L. and Nason, Paolo and Ridolfi, Giovanni, Phys. Lett. **B348**, 633 (1995).

[18] Bardeen, William A. and Buras, A. J. and Duke, D. W. and Muta, T., Phys. Rev. **D18**, 3998 (1978).

[19] Kartvelishvili, V. G. and Likhoded, A. K. and Petrov, V. A., Phys. Lett. **B78**, 615 (1978).

[20] Herb, S. W. et al. , Phys. Rev. Lett. **39**, 252 (1977).

[21] Wohri, H. and Lourenco, C., J. Phys. **G30**, S315 (2004).

[22] Jansen, D. M. et al. , Phys. Rev. Lett. **74**, 3118 (1995).

[23] Alexopoulos, T. et al. , Phys. Rev. Lett. **82**, 41 (1999).

[24] Abt, I. et al. , Eur. Phys. J. **C26**, 345 (2003).

[25] Albajar, C. et al. , Phys. Lett. **B256**, 121 (1991).

[26] Acosta, D. et al. , Phys. Rev. **D65**, 052005 (2002).

[27] Albajar, C. et al. , Z. Phys. **C61**, 41 (1994).

[28] Nason, P. and Dawson, S. and Ellis, R. K., Nucl. Phys. **B303**, 607 (1988);
Nason, P. and Dawson, S. and Ellis, R. K., Nucl. Phys. **B327**, 49 (1989).

[29] Abe, F. et al. , Phys. Rev. **D53**, 1051 (1996).

[30] Abachi, S. et al. , Phys. Rev. Lett. **74**, 3548 (1995).

[31] Abbott, B. et al. , Phys. Lett. **B487**, 264 (2000).

[32] Cacciari, Matteo and Greco, Mario and Nason, Paolo, JHEP **05**, 007 (1998).

[33] Cacciari, M. and Frixione, S. and Mangano, M. L. and Nason, P. and Ridolfi, G., JHEP **07**, 033 (2004).

[34] Abe, F. et al. , Phys. Rev. Lett. **75**, 1451 (1995).

[35] Chen, C. for the CDF collaboration, presentation at *beauty 2003*, *Measurement of the b-hadron inclusive Cross-section in CDF Run II using* $Hb \to J/\psi X$ (unpublished), 2003, available on `http://www-cdf.fnal.gov/physics/new/bottom/030904.blessed-bxsec-jpsi/` ;
Bishai, M. for the CDF collaboration, presentation at *Fermilab, Dec 5. 2003*, *Beauty and Charm Production at the Fermilab Tevatron* (unpublished), 2003, available on `http://www-cdf.fnal.gov/~bishai/papers/wandc.pdf` .

[36] Frixione, Stefano and Nason, Paolo and Webber, Bryan R., JHEP **08**, 007 (2003);
Frixione, Stefano and Webber, Bryan R., JHEP **06**, 029 (2002).

[37] Chekanov, S. et al. , Phys. Lett. **B599**, 173 (2004).

[38] H1 Coll. , A. Aktas et al. , *Measurement of beauty Production in Deep Inelastic Scattering at HERA*. Paper 5-0165 submitted to the International Conference on High Energy Physics, ICHEP04, Beijing, China, August 16 2004, 2004.

[39] Harris, B. W. and Smith, J., Phys. Rev. **D57**, 2806 (1998);
Harris, B. W. and Smith, J., Nucl. Phys. **B452**, 109 (1995);
Harris, B. W. and Smith, J., Phys. Lett. **B353**, 535 (1995).

[40] H1 Coll. , A. Aktas et al. , *Measurement of Beauty Photoproduction at HERA Using Semi-Muonic Decays*. Paper 5-0164 submitted to the International Conference on High Energy Physics, ICHEP04, Beijing, China, August 16 2004, 2004.

[41] H1 Coll. , A. Aktas et al. , *Measurement of Beauty Photoproduction at HERA Using Inclusive Lifetime Tagging*. Paper 5-0760 submitted to the International Conference on High Energy Physics, ICHEP04, Beijing, China, August 16 2004, 2004.

[42] Chekanov, S. et al. , Preprint hep-ex/0312057, 2003.

[43] Bromley, J. et al. , *Hztool: A Package For Monte Carlo-Data Comparison At Hera (Version 1.0)* (unpublished). Prepared for Workshop on Future Physics at HERA (Preceded by meetings 25-26 Sep 1995 and 7-9 Feb 1996 at DESY), Hamburg, Germany, May 1996;
Brook, N. et al. , *HzTool: A Package For Monte Carlo-Data Comparison At Hera (Version 2.0)* (unpublished). http://www.desy.de/ carli/hztool/hztool.ps.gz .

[44] Butterworth, J. M. and Butterworth, S., Comput. Phys. Commun. **153**, 164 (2003).

[45] Adloff, C. et al. , Eur. Phys. J. **C25**, 13 (2002).

[46] Chekanov, S. et al. , Eur. Phys. J. **C23**, 615 (2002).

[47] Hamburg Desy - DESY HERA 81-10 (81,REC.AUG.) 292p.

[48] M. Bieler, private communication, 2004.

[49] Schneekloth, U. , (ed.). DESY-HERA-98-05.

[50] D. Bailey et al. , *Study of beam-induced backgrounds in the ZEUS detector from 2002 HERA running* (unpublished), 2002, available on `http://www-zeus.desy.de/~kuze/zeusbg/` . ZEUS-Note 02-018;
D. Bailey et al. , *Study of beam-induced backgrounds in the ZEUS detector from 2002 HERA running (Addendum 1)* (unpublished), 2002, available on `http://www-zeus.desy.de/~kuze/zeusbg/` . ZEUS-Note 02-020;
D. Bailey et al. , *Study of beam-induced backgrounds in the ZEUS detector from 2002 HERA running (Addendum 2)* (unpublished), 2003, available on `http://www-zeus.desy.de/~kuze/zeusbg/` . ZEUS-Note 02-027.

[51] Seidel, M. DESY-HERA-00-01.

[52] Saxon, D. H. Presented at DESY Theory Workshop, Hamburg, West Germany, Oct 12-14, 1987.

[53] ZEUS Coll. , U. Holm (ed.), *The ZEUS Detector*. Status Report (unpublished), DESY (1993), available on `http://www-zeus.desy.de/bluebook/bluebook.html` .

[54] Harnew, N. et al. , Nucl. Instrum. Meth. **A279**, 290 (1989);
Foster, B. et al. , Nucl. Phys. Proc. Suppl. **32**, 181 (1993);
Foster, B. et al. , Nucl. Instrum. Meth. **A338**, 254 (1994).

[55] R. Hall-Wilton et al. , *The CTD Tracking Resolution* (unpublished). ZEUS-Note 99-024, 1999.

[56] R. Hall-Wilton, private communication, 2004.

[57] Maddox, Erik, *Study of heavy quark production at HERA using the ZEUS microvertex detector* (unpublished). Thesis, 2004.

[58] The ZEUS Collaboration, *A Microvertex Detector for ZEUS* (unpublished). Tech. Report DESY-PRC 97/01, 1997.

[59] Chiochia, V., Nucl. Instrum. Meth. **A501**, 60 (2003);
Koffeman, E. N., Nucl. Instrum. Meth. **A473**, 26 (2001);
Petrucci, M. C., Int. J. Mod. Phys. **A16S1C**, 1078 (2001);
Koetz, U., Nucl. Instrum. Meth. **A461**, 210 (2001);
Koffeman, E. N., Nucl. Instrum. Meth. **A453**, 89 (2000);
Coldewey, C., Nucl. Instrum. Meth. **A453**, 149 (2000);
Coldewey, C., Nucl. Instrum. Meth. **A447**, 44 (2000);
Klanner, R. Prepared for International Europhysics Conference on High- Energy Physics (EPS-HEP 99), Tampere, Finland, 15-21 Jul 1999;
Garfagnini, A., Nucl. Instrum. Meth. **A435**, 34 (1999);
Dannheim, D. et al. , Nucl. Instrum. Meth. **A505**, 663 (2003).

[60] Derrick, M. et al. , Nucl. Instrum. Meth. **A309**, 77 (1991);
Andresen, A. et al. , Nucl. Instrum. Meth. **A309**, 101 (1991);
Caldwell, A. et al. , Nucl. Instrum. Meth. **A321**, 356 (1992);
Bernstein, A. et al. , Nucl. Instrum. Meth. **A336**, 23 (1993).

[61] Battistoni, G. et al. , Nucl. Instr. Meth. **217**, 429 (1983).

[62] Abbiendi, G. et al. , Nucl. Instrum. Meth. **A333**, 342 (1993).

[63] De Giorgi, M. et al. , Nucl. Instrum. Meth. **A378**, 472 (1996).

[64] Tomasz Jezynski et al. , Proc. SPIE **5484**, 180 (2004);
Krzysztof T. Pozniak et al. , Proc. SPIE **5484**, 186 (2004).

[65] Andruszkow, J. et al. , Acta Phys. Polon. **B32**, 2025 (2001).

[66] H. Bethe and W. Heitler, Proc. Roy. Soc. Lond. **A146**, 83 (1934).

[67] W. H. Smith, K. Tokushuku and L. W. Wiggers. *Proc. Computing in High-Energy Physics (CHEP), Annecy, France, 1992*, C. Verkerk and W. Wojcik (eds.), p.222. CERN, Geneva, Switzerland (1992). Also in pre print DESY-92-150B.

[68] S. Dhawan, *Proceedings of the Conference Real Time'03, Montreal*. (2003);
M. Sutton, *Proceedings of the Conference Real Time'03, Montreal*. (2003);
C. Youngman, *Proceedings of the Conference Real Time'03, Montreal*. (2003);
A. Polini, ECONF **C0303241**, MOGT005 (2003).

[69] S.M. Fisher and P. Palazzi, *ADAMO Reference Manual for Version 3.3*. CERN ECP, available on `http://adamo.web.cern.ch/Adamo/refmanual/Document.html` .

[70] Brun, R. and Bruyant, F. and Maire, M. and McPherson, A. C. and Zanarini, P. CERN-DD/EE/84-1.

[71] Kind, O. et al. , ECONF **C0303241**, MOLT002 (2003).

[72] Brun, R. and Rademakers, F., Nucl. Instrum. Meth. **A389**, 81 (1997).

[73] M. Ernst et al. , *dCache, a distributed storage data caching system*. Paper 4-005 submitted to the Conference: Computing in High Energy And Nuclear Physics, CHEP01, Beijing, China, 2001.

[74] Hartner, G. et al. (1997). ZEUS-Note 97-064;
Hartner, G. (1998). ZEUS-Note 98-058.

[75] Kalman, Rudolph, Emil, Transactions of the ASME–Journal of Basic Engineering **82**, 35 (1960);
Fruhwirth, R., Nucl. Instrum. Meth. **A262**, 444 (1987).

[76] Repond, J. (1996). ZEUS-Note 96-133.

[77] G. Abbiendi, *Global tracking of muons in the Barrel and Rear region* (unpublished). ZEUS-Note 99-063, 1999.

[78] Innocente, V. and Maire, M. and Nagy, E. In *Amsterdam 1991, Proceedings, MC91: Detector and event simulation in high energy physics* 58-78. (see HIGH ENERGY PHYSICS INDEX 30 (1992) No. 3237).

[79] M. Corradi, private communication, 2004;
L. Bellagamba, *MVMATCH: A package to match FMUON tracks with Central Detectors* (unpublished). ZEUS-Note 96-051, 1996.

[80] Kuzmin, V. A., Nucl. Instrum. Meth. **A453**, 336 (2000).

[81] G. Abbiendi et al. , *Observation of* $J/\psi \to \mu^+\mu^-$ *in the first* 273 nb^{-1} *of 1993 run* (unpublished). ZEUS-Note 93-120, 1993.

[82] L. Wai, *A muon separator* (unpublished). ZEUS-Note 93-12, 1993.

[83] A. Geiser et al. , *GMuon - A global muon reconstruction for ZEUS* (unpublished). ZEUS-Note *in preparation*, 2004.

[84] Marchesini, G. et al. , Comput. Phys. Commun. **67**, 465 (1992).

[85] Arneodo, M. and Lamberti, L. and Ryskin, M., Comput. Phys. Commun. **100**, 195 (1997).

[86] Kwiatkowski, A. and Spiesberger, H. and Mohring, H. J., Comp. Phys. Commun. **69**, 155 (1992).

[87] Abe, Tetsuo, Comput. Phys. Commun. **136**, 126 (2001).

[88] Briskin, Gennady M. DESY-THESIS-1998-036;
Tuning, N., *ZUFOs: Hadronic final state reconstruction with calorimeter, tracking and backsplash correction* (unpublished). ZEUS-Note 01-021, 2001.

[89] Longhin, A., *Misura delle sezioni d'urto di fotoproduzione di Open Beauty ad HERA. (In Italian)* (unpublished). PhD Thesis at the University of Padua, 2000;
Turcato, Monica, *Measurement of beauty photoproduction at HERA* (unpublished). DESY-THESIS-2003-039;
Chiochia, Vincenzo, *Measurement of beauty quark production in deep inelastic scattering at HERA* (unpublished). DESY-THESIS-2003-031.

[90] Berger, E. L. , (ed.). Singapore, Singapore: World Scientific (1992) 808 p.

[91] Catani, S. and Dokshitzer, Yuri L. and Webber, B. R., Phys. Lett. **B285**, 291 (1992);
Catani, S. and Dokshitzer, Yuri L. and Seymour, M. H. and Webber, B. R., Nucl. Phys. **B406**, 187 (1993);
Turcato, Monica, *Measurement of beauty photoproduction at HERA* (unpublished). DESY-THESIS-2003-039.

[92] Abramowicz, Halina and Caldwell, Allen and Sinkus, Ralph, Nucl. Instrum. Meth. **A365**, 508 (1995);
Sinkus, R. and Voss, T., Nucl. Instrum. Meth. **A391**, 360 (1997).

[93] F. Jacquet & A. Blondel. Proc. of the Study of an ep facility for Europe, ed U Amaldi, DESY 79/48, p391, 1979.

[94] Turcato, Monica, *Measurement of beauty photoproduction at HERA* (unpublished). DESY-THESIS-2003-039.

[95] James, F. and Roos, M., Comput. Phys. Commun. **10**, 343 (1975).

[96] ZEUS Coll. , S. Chekanov et al. , *First results on beauty production using HERA II data.* Paper 5-0354 submitted to the International Conference on High Energy Physics, ICHEP04, Beijing, China, August 16 2004, 2004.

[97] Lai, H. L. and others, Phys. Rev. **D55**, 1280 (1997).

[98] Lai, H. L. and others, Eur. Phys. J. **C12**, 375 (2000).

[99] Gluck, M. and Reya, E. and Vogt, A., Phys. Rev. **D46**, 1973 (1992).

List of Figures

2.1 Generic diagram of electron–proton scattering . . . 7
2.2 Feynman diagram of an electron–proton interaction in the QPM . . . 8
2.3 Diagrams for BGF and QCDC . . . 9
2.4 Diagrams for pointlike and hadronic components of ep photoproduction . . . 9
2.5 Differential CC and NC DIS cross sections . . . 12
2.6 Proton structure function as function of Q^2 and x . . . 13
2.7 Proton density functions from ZEUS NLO calculation . . . 14
2.8 PYTHIA: Leading order MC plus parton shower MC . . . 15
2.9 Spectator model of hadron decay . . . 18
2.10 Prompt and cascade decay of beauty quark . . . 18
2.11 dB/dp for the electron momentum in the B hadron centre–of–mass system . . . 19
2.12 PYTHIA predictions for electron and muon momentum distribution from B hadrons . . . 19
2.13 Differential NLO QCD cross sections in p_T^μ for varied scales and beauty quark mass . . . 21
2.14 Differential NLO QCD cross sections in η^μ for varied scales and beauty quark mass . . . 21
2.15 Differential NLO QCD cross sections for varied proton PDF . . . 22
2.16 Differential NLO QCD cross sections for varied fragmentation . . . 23
2.17 Differential NLO QCD cross sections for varied Λ_{CQD} . . . 23

3.1 $b\bar{b}$ cross section measurement from different experiments . . . 27
3.2 Inclusive single beauty quark cross section from UA1. . . . 28
3.3 Beauty quark correlation cross sections in $\Delta R_{b\bar{b}}$ and $\Delta\phi_{b\bar{b}}$ from UA1. . . . 28
3.4 Beauty quark cross sections of D0 and CDF . . . 29
3.5 Beauty quark cross section from D0 . . . 30
3.6 Improved NLO QCD calculation and recent beauty quark cross section by CDF . . . 30
3.7 Differential beauty quark jet cross sections in DIS ep collisions . . . 31
3.8 Differential beauty quark jet cross sections in PHP ep collisions by H1 . . . 32
3.9 Differential beauty quark cross sections in x_γ in PHP ep collisions by H1 . . . 32
3.10 Differential beauty quark cross sections in PHP ep collisions by ZEUS . . . 33
3.11 Beauty quark cross sections in muon regions and x_γ^{jets} in PHP ep collisions by ZEUS . . . 33
3.12 Differential beauty quark production cross section in ep collisions by ZEUS . . . 34

4.1 Differential dijet photoproduction cross sections for JetWeb-scale determination. . . . 36
4.2 JetWeb comparison of beauty quark cross sections differential p_T^μ and η^μ by ZEUS . . . 38
4.3 JetWeb comparison of differential jet beauty quark cross sections by ZEUS . . . 38
4.4 JetWeb comparison of beauty quark cross sections in muon regions and x_γ by ZEUS . . . 39
4.5 JetWeb comparison of beauty quark cross sections as a function of p_T^b by UA1 and D0 . 39
4.6 JetWeb comparison of beauty quark correlations cross sections by UA1 for $p_T^b > 11$ GeV 40
4.7 JetWeb comparison of beauty quark correlations cross sections by UA1 for $p_T^b > 6$ GeV . 40

5.1 Airplane view of the DESY laboratory . . . 41
5.2 Schematic view of the HERA accelerator complex . . . 42
5.3 HERA delivered luminosity for 1993-2000 and 2003-2004 . . . 43
5.4 The ZEUS coordinate system . . . 43
5.5 Cross section of the ZEUS detector along the beam axis . . . 44
5.6 ZEUS gated luminosity for 1993-2000 and 2003-2004 . . . 45
5.7 XY cross section of one octant of the CTD . . . 46

5.8 Schematic layout of the MVD . . . 47
5.9 Schematic view of the CAL along the beam axis . . . 48
5.10 A module of the forward calorimeter . . . 49
5.11 Schematic view of the forward muon detector along the beam axis . . . 50
5.12 Layout of the barrel and rear muon detector . . . 51
5.13 Schematic view of the lumi monitor system . . . 52
5.14 The ZEUS trigger and data acquisition system . . . 54

6.1 Client-server structure of the new ZeVis event display . . . 56
6.2 Server side layers . . . 57
6.3 Single event request . . . 58
6.4 Download event file request . . . 59
6.5 Online event request . . . 59
6.6 3D ZeVis event display . . . 60
6.7 2D projections of the 3D ZeVis event display . . . 61
6.8 3D external displays of an event by ZeVis . . . 61
6.9 Default display of an event by ZeVis . . . 62
6.10 Display of the complete header information . . . 62
6.11 Display of vertex fitted and non vertex fitted tracks. . . . 63
6.12 Display of CAL energy cell information . . . 63
6.13 Display of muon candidate in muon chambers and BAC . . . 64
6.14 Detailed hit information display of CTD and MVD . . . 64
6.15 Detailed hit information display of CTD and MVD in fish eye mode . . . 65

7.1 Helix in the XY view for a positively charged track . . . 68
7.2 Resolution of CTD–only and global track reconstruction . . . 69
7.3 Beamspot resolution for Kalman-fitted tracks . . . 70
7.4 Dimuon invariant mass spectra for efficiency correction data and MC samples . . . 78
7.5 Exemplary muon reconstruction efficiencies in p_T^μ bin . . . 79
7.6 Pre– and post–upgrade muon efficiency correction factors . . . 80
7.7 CTD and CAL resolutions . . . 81
7.8 Reconstruction of EFO's by a match between CAL cells and tracks . . . 82
7.9 Dead material map between interaction region and CAL . . . 83
7.10 Muonic energy in the CAL as a function of θ . . . 84

8.1 Comparison of true and reconstruction level for y_{jb} . . . 91
8.2 True photon virtuality after all selection cuts for pre–upgrade running periods . . . 92
8.3 True photon virtuality after all selection cuts for post–upgrade running periods . . . 92
8.4 Selected muons qualities and finder categories for pre–upgrade running periods . . . 93
8.5 Data-MC comparison for pre–upgrade muon finder categories . . . 93
8.6 Data-MC comparison for pre–upgrade muon finder categories normalised in muon regions 94
8.7 Data-MC comparison for p_T^μ and η^μ for pre–upgrade running periods . . . 94
8.8 Selected muons qualities and finder categories for post–upgrade running periods . . . 95
8.9 Data-MC comparison for reconstructed post–upgrade muon finder categories . . . 95
8.10 Data-MC comparison for p_T^μ and η^μ for post–upgrade running periods . . . 96
8.11 Comparison of true and reconstruction level for p_T^{jet} and η^{jet} . . . 97
8.12 Pre– and post–upgrade Data-MC comparison for $p_T^{\mu-jet}$ and $\eta^{\mu-jet}$ . . . 98
8.13 Pre– and post–upgrade Data-MC comparison for $p_T^{other-jet}$ and $\eta^{other-jet}$ . . . 99
8.14 Data-MC comparison for $mass_{\mu-jet}$ for pre– and post–upgrade running periods . . . 103
8.15 Data-MC comparison for p_T^μ/E_T^{jet} for pre– and post–upgrade running periods . . . 103
8.16 Data-MC comparison for x_γ for pre– and post–upgrade running periods . . . 104

9.1 p_T^{rel} definition . . . 105
9.2 p_T^{rel} distributions from data and signal and background MC samples . . . 106
9.3 $p_T^{rel,jet-\mu}$ distributions from data and signal and background MC samples . . . 106
9.4 $p_T^{rel,jet-\mu}$ fits for pre– and post–upgrade running periods . . . 107
9.5 Background $p_T^{rel,jet-\mu}$ shape comparison between data and MC simulation . . . 109

9.6 Background $p_T^{rel,jet-\mu}$ shape correction factors . . . 109
9.7 Comparison of true muon impact parameter from beauty and charm quarks . . . 110
9.8 Impact parameter definition . . . 111
9.9 Post–upgrade impact parameter distributions for the reduced data sample and MC samples 112
9.10 Comparison between impact parameter distributions from data and lighter flavours MC . 112

10.1 Pre–upgrade purity of η^μ . . . 115
10.2 p_T^{rel} fits for all 4 bins of the cross section η^μ distribution . . . 116
10.3 Pre–upgrade shape comparison between data and MC differential in η^μ . . . 116
10.4 Pre–upgrade shape comparison between data and MC differential in p_T^μ . . . 117
10.5 Pre–upgrade shape comparison between data and MC differential in $p_T^{\mu-jet}$ and $\eta^{\mu-jet}$. 117
10.6 Pre–upgrade shape comparison between data and MC differential in x_γ^{jets} . . . 118
10.7 Pre–upgrade shape comparison between data and MC differential in ΔR_{jj} and $\Delta\phi_{jj}$ . . . 118
10.8 Pre–upgrade MC comparison for cross sections differential in p_T^μ and η^μ . . . 120
10.9 Pre–upgrade MC comparison for cross sections differential in $p_T^{\mu-jet}$ and $\eta^{\mu-jet}$ . . . 121
10.10 Pre–upgrade MC comparison for the cross section differential in x_γ^{jets} . . . 121
10.11 Pre–upgrade MC comparison between cross sections differential in ΔR_{jj} and $\Delta\phi_{jj}$ . . . 122
10.12 Pre–upgrade cross section differential in p_T^μ compared to NLO . . . 124
10.13 Cross section differential in η^μ compared to NLO QCD predictions . . . 125
10.14 Post–upgrade shape comparison of data and MC differential in p_T^μ and η^μ . . . 126
10.15 Post–upgrade shape comparison of data and MC differential in $p_T^{\mu-jet}$ and $\eta^{\mu-jet}$ . . . 127
10.16 Post–upgrade shape comparison of data and MC differential in x_γ^{jets} . . . 127
10.17 Post–upgrade shape comparison between data and MC differential in ΔR_{jj} and $\Delta\phi_{jj}$ . . 128
10.18 Post–upgrade MC comparison of cross sections differential in p_T^μ and η^μ . . . 129
10.19 Post–upgrade MC comparison of cross sections differential in $p_T^{\mu-jet}$ and $\eta^{\mu-jet}$ . . . 129
10.20 Post–upgrade MC Comparison of cross sections differential in x_γ^{jets} . . . 129
10.21 Post–upgrade MC comparison of cross sections differential in ΔR_{jj} and $\Delta\phi_{jj}$ . . . 130
10.22 Cross section differential in p_T^μ and η^μ compared to NLO QCD predictions . . . 130
10.23 Pre– and post–upgrade comparison of cross sections differential in p_T^μ and η^μ . . . 131
10.24 Pre– and post–upgrade comparison of cross sections differential in $p_T^{\mu-jet}$ and $\eta^{\mu-jet}$ . . . 132
10.25 Pre– and post–upgrade comparison of cross sections differential in x_γ^{jets} . . . 132
10.26 Pre– and post–upgrade comparison of cross sections differential in ΔR_{jj} and $\Delta\phi_{jj}$ . . . 132
10.27 Impact parameter distributions for the reduced post–upgrade data sample . . . 134
10.28 Data–MC comparison of post–upgrade impact parameter spectrum . . . 134
10.29 Comparison of data mirrored-subtracted impact parameter to beauty and charm MC . . 135

A.1 JetWeb comparison of a generic differential cross section to different MC settings . . . 140
A.2 JetWeb comparison of a generic differential cross section to different MC generators . . . 140
A.3 JetWeb comparison of differential cross sections from different experiments to PYTHIA . 140

B.1 Response time of the ZeVis single event server . . . 142
B.2 Response time as a function of concurrent single event requests . . . 142
B.3 Graphical user interface of the ZeVis event display . . . 143
B.4 File, view and options menu of the ZeVis GUI . . . 144
B.5 Tabs for the different server modes in the ZeVis GUI . . . 145
B.6 Tabs for fast event and detector option switches in the ZeVis GUI . . . 145
B.7 Popup menu to steer the view mode in the current pad . . . 146
B.8 3D drawing capabilities of ROOT . . . 147
B.9 ZeVis ROOT implementation of the ZEUS geometry . . . 148
B.10 Interplay between hit and geometry information . . . 148
B.11 3D shape hierarchy of the forward MVD . . . 149
B.12 3D shape hierarchy of the barrel MVD . . . 150
B.13 2D shapes of the barrel MVD . . . 151
B.14 2D shapes of the forward MVD . . . 152
B.15 3D display of MVD hits . . . 153
B.16 2D display of MVD hits . . . 154

F.1 p_T^{rel} fit for comparison to previous results . . . 163

F.2 Muon control distributions for comparison to previous results 164
F.3 Comparison of $d\sigma/dp_T^{\mu}(ep \to eb\bar{b}X \to e\mu jjX$ to previous analysis 164
F.4 Comparison of $d\sigma/d\eta^{\mu}(ep \to eb\bar{b}X \to e\mu jjX$ to previous analysis 165

List of Tables

2.1 The elementary fermions of the *Standard Model* . . . 5
2.2 The fundamental interactions in the *Standard Model* . . . 6

3.1 Collection of $b\bar{b}$ production cross sections . . . 26
3.2 Tevatron running periods . . . 29

4.1 Summary of implemented cross section from UA1, DO and ZEUS . . . 37

5.1 HERA design parameters . . . 42
5.2 Angular coverage of the CAL parts and dimensions of the cells . . . 48
5.3 Summary of BAC modules . . . 52

7.1 CAL energy-correction factors . . . 70
7.2 Data samples used for the efficiency correction determination of the muon reconstruction 78
7.3 MC samples available for the efficiency correction determination of the muon reconstruction 78

8.1 Available data samples from the pre– and post–upgrade running periods . . . 87
8.2 Generator cross sections and luminosities of the available PYTHIA MC samples . . . 89
8.3 Third level trigger selection for the running period 96-00 and 03-04 . . . 89
8.4 Residual DIS contamination of photoproduction MC samples after event selection . . . 92
8.5 Number of selected events per running period . . . 102

9.1 Determined pre– and post–upgrade beauty fractions using $p_T^{rel,jet-\mu}$ . . . 108
9.2 Determined pre– and post–upgrade beauty fractions using p_T^{rel} . . . 108
9.3 Systematic influence of the charm $p_T^{rel,jet-\mu}$ background shape correction . . . 109

10.1 Binning in η^{μ} . . . 115
10.2 Calculation of the number of muons coming from beauty quarks . . . 115
10.3 Definition of the differential p_T^{μ} and η^{μ} beauty quark cross sections . . . 120
10.4 Definition of the differential $p_T^{\mu-jet}$ and $\eta^{\mu-jet}$ beauty quark cross sections . . . 120
10.5 Definition of the beauty quark photoproduction cross section differential in x_{γ}^{jets} . . . 121
10.6 Definition of the beauty quark photoproduction cross sections differential in ΔR_{jj} and $\Delta\phi_{jj}$ 122

B.1 Forward, barrel and rear tubes of the MVD . . . 149
B.2 Four wheels of the forward MVD . . . 149
B.3 Two different sized trapezoidal shaped sector . . . 149
B.4 Three cylinders of the barrel MVD . . . 150

C.1 Beauty MC sample parameters . . . 156
C.2 Charm MC sample parameters . . . 156
C.3 Lighter flavours MC sample parameters . . . 157

D.1 Pre–upgrade data event numbers for $p_T^{\mu} \geq 2.0$ GeV . . . 159
D.2 Pre–upgrade 96-97 MC event numbers for $p_T^{\mu} \geq 2.0$ GeV . . . 159
D.3 Pre–upgrade 98-99 MC event numbers for $p_T^{\mu} \geq 2.0$ GeV . . . 159
D.4 Pre–upgrade 99-00 MC event numbers for $p_T^{\mu} \geq 2.0$ GeV . . . 160
D.5 Post–upgrade data event numbers for $p_T^{\mu} \geq 1.5$ GeV . . . 160

D.6 Post–upgrade 03-04 MC event numbers for $p_T^\mu \geq 1.5$ GeV 160
D.7 Post–upgrade data event numbers for $p_T^\mu \geq 2.0$ GeV 160
D.8 Post–upgrade 03-04 MC event numbers for $p_T^\mu \geq 2.0$ GeV 160

G.1 Pre–upgrade systematic errors total and differential in p_T^μ and η^μ for $p_T^\mu \geq 2.0$ GeV . . . 167
G.2 Pre–upgrade systematic errors differential in $p_T^{\mu-jet}$ and $\eta^{\mu-jet}$ for $p_T^\mu \geq 2.0$ GeV 168
G.3 Pre–upgrade systematic errors differential in x_γ^{jets} and ΔR_{jj} for $p_T^\mu \geq 2.0$ GeV 168
G.4 Pre–upgrade systematic errors differential in $\Delta\phi_{jj}$ for $p_T^\mu \geq 2.0$ GeV 169
G.5 Post–upgrade systematic errors total and differential in p_T^μ and η^μ for $p_T^\mu \geq 1.5$ GeV . . . 169
G.6 Post–upgrade systematic errors differential in $p_T^{\mu-jet}$ and $\eta^{\mu-jet}$ for $p_T^\mu \geq 1.5$ GeV 170
G.7 Post–upgrade systematic errors differential in x_γ^{jets} and ΔR_{jj} for $p_T^\mu \geq 1.5$ GeV 170
G.8 Post–upgrade systematic errors differential in $\Delta\phi_{jj}$ for $p_T^\mu \geq 1.5$ GeV 171
G.9 Post–upgrade systematic errors total and differential in p_T^μ and η^μ for $p_T^\mu \geq 2.0$ GeV . . . 171
G.10 Post–upgrade systematic errors differential in $p_T^{\mu-jet}$ and $\eta^{\mu-jet}$ for $p_T^\mu \geq 2.0$ GeV 172
G.11 Post–upgrade systematic errors differential in x_γ^{jets} and ΔR_{jj} for $p_T^\mu \geq 2.0$ GeV 172
G.12 Post–upgrade systematic errors differential in $\Delta\phi_{jj}$ for $p_T^\mu \geq 2.0$ GeV 173

Acknowledgments

The results presented in this thesis are based on the constant efforts of the members of the ZEUS collaboration and would not have been possible without their help and support. I owe special thanks to the members of the *background task force* who solved the difficult problems of the high background conditions at the ZEUS interaction region in the beginning of the post–upgrade running periods.

I would like to thank my professor, Prof. Dr. Robert Klanner, for giving me the opportunity to work on my PhD in the ZEUS collaboration. Especially I want to thank him for the opportunity to spend half a year on a research stay at the University College London. I also want to thank Prof. Dr. Beate Naroska for her interest in my thesis and questions during my disputation.

Before all, I want to thank my supervisor, Dr. Achim Geiser. It has been a great pleasure to work with him on my PhD thesis. He always helped me with advice and support. Also his support during my technical task and my stay at London with his technical skills and his tremendous physical understanding has been invaluable.

I also want to thank my technical task supervisor, Dr. Rainer Mankel. The work with him and the event display team, especially with Oliver Kind, was encouraging and gave me invaluable insights in the process of software development and project management.

I owe great thanks to Massimo Corradi and Monica Turcato who carried out the previous analysis of beauty quark photoproduction cross section measurements in dijet plus muon events. They answered patiently all my questions and provided the starting point for this analysis. Especially the work done for the calculation of NLO QCD predictions from FMNR by Massimo Corradi was the basis for the next–to–leading order comparisons shown here.

I also want to thank Silvia Miglioranzi who I worked with on the impact parameter studies presented at ICHEP 04. I hope we will continue to work together on beauty quark topics in the future.

The research stay at the University College London, funded by the German Academic Exchange Service, was a fruitful experience and I hope that the results presented in this thesis will be extended in the future. I want to thank my supervising professor at UCL, Prof. Tegid Jones, for providing me with the support of the UCL HEP group and his flat in London. I also want to thank Jon Butterworth and especially Ben Waugh for their help with the JetWeb facility. And, thanks to all the people at UCL and especially to Stewart Boogert who welcomed me as a group member during my stay.

Large thanks go to my team, the *beauty team*, which joined me in analysing beauty quarks with the ZEUS detector. Headed by Achim Geiser, the team members Ingo Bloch, Benjamin Kahle and Ursula Meyer helped and encouraged me with their advice and ideas.

Ingo Bloch and Benjamin Kahle became more than colleagues during the time of my PhD. As well as the other PhD students at DESY, Raquel Santamarta, Liz “Mamma” Nuncio-Quiros, Amita Raval, Volker Adler, Chi-Nhan Nguyen, Joerg Stahl and many more, they became also friends who shared the exciting and sometimes long hours of work and research with me. I also want to thank John Loizides and Nicola Coppola for having a good time at DESY and in China. In the end, I want to thank Dominik Dannheim who became a close friend and who gave me big support and advice.

My family has a big share in what I achieved during the last years. I want to thank my parents, who supported me during the years of study and who encouraged me and guided my with their advice and example. And I want to thank my brother Dominic for being around and showing interest in everything I did.